

AD-A113 385 SCRIPPS INSTITUTION OF OCEANOGRAPHY LA JOLLA CA SHOR--ETC F/G 8/3
WAVE DIRECTIONAL CHARACTERISTICS ON A PARTIALLY SHELTERED COAST--ETC(U)
1982 S S PAWKA N00014-75-C-0300
NL

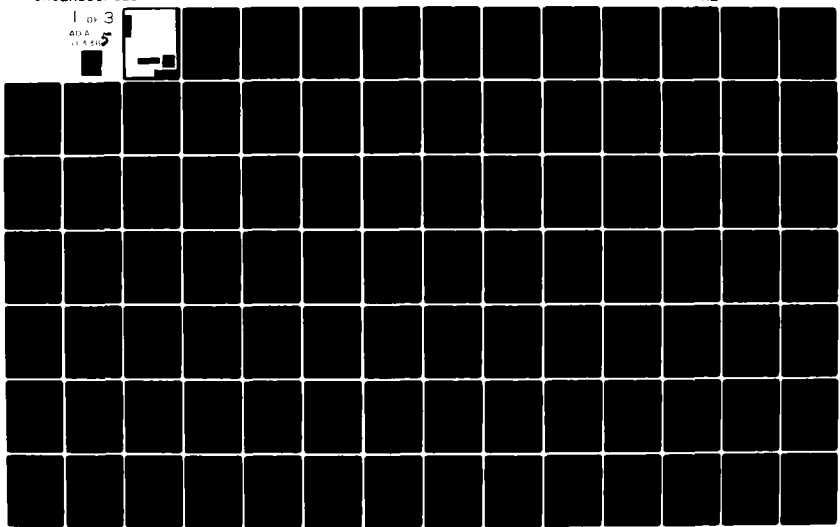
UNCLASSIFIED

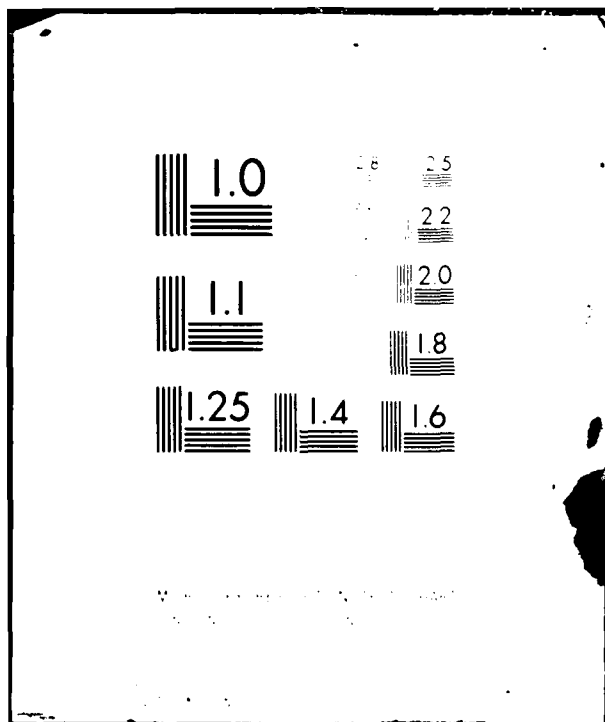
1 of 3

400A

015555

5





AD A113385

This document has been approved
for public release and unlimited
distribution is authorized.



82 04 09 026

REPORT DOCUMENTATION PAGE		READ INSTRUCTIONS BEFORE COMPLETING FORM
1. REPORT NUMBER	2. GOVT ACCESSION NO.	3. RECIPIENT'S CATALOG NUMBER
		AD-A113 385
4. TITLE (and Subtitle) WAVE DIRECTIONAL CHARACTERISTICS ON A PARTIALLY SHELTERED COAST		5. TYPE OF REPORT & PERIOD COVERED PhD Dissertation
7. AUTHOR(s) STEVEN SITTER PAWKA		6. PERFORMING ORG. REPORT NUMBER ONR Code 422CS Contract #N00014-75-C-0300
8. PERFORMING ORGANIZATION NAME AND ADDRESS Shore Processes Lab, A-009 Scripps Institution of Oceanography La Jolla, CA 92093		10. PROGRAM ELEMENT, PROJECT, TASK AREA & WORK UNIT NUMBERS
11. CONTROLLING OFFICE NAME AND ADDRESS		12. REPORT DATE 1982
14. MONITORING AGENCY NAME & ADDRESS (if different from Controlling Office)		13. NUMBER OF PAGES 246
16. DISTRIBUTION STATEMENT (of this Report)		15. SECURITY CLASS. (of this report) Unclassified
17. DISTRIBUTION STATEMENT (of the abstract entered in Block 20, if different from Report)		15a. DECLASSIFICATION/DOWNGRADING SCHEDULE
18. SUPPLEMENTARY NOTES		
19. KEY WORDS (Continue on reverse side if necessary and identify by block number) island sheltering, wave directional spectra, wave refraction, Maximum Likelihood Estimates, wind generated waves, radiation stress estimation, linear arrays, radiation stress statistics, SAR spectra		
20. ABSTRACT (Continue on reverse side if necessary and identify by block number) The sheltering effects of the Channel Islands on the wind generated surface gravity wave field at the Southern California coastline are studied with an extensive field experiment. Emphasis is placed on wave directional measurements sampled at Torrey Pines Beach with a linear array of pressure sensors. A linear model was implemented for the evaluation of wave transformations around the islands due to refraction over the shoals in the island region and blocking due to the island cross-sections. This model shows a strong (cont.)		

influence of refraction on waves with frequencies less than 0.10 Hz. Only limited confirmation of the model in the frequency range 0.08-0.11 Hz is obtained due to the variable quality of the deep ocean estimates of wave directionality.

Several estimation techniques were compared for their performance in directional spectrum analysis. Two methods developed here show significant improvement over the Maximum Likelihood Estimator in defining spectral gaps and in the partition of energy among spectral peaks.

The estimation problem of extracting accurate estimates of the onshore flux of longshore directed momentum, S_{yx} , from linear array data is addressed. A window shaping technique is developed and compared to the integration of the directional spectrum estimates. Using field data, the linear array methods are compared with a biaxial current meter and a "slope" array. The window shaping technique and integration of the IMLE spectra show excellent agreement with the results from the other two systems. The statistical nature of point measurements of S_{yx} in a directional wave field is also considered.

UNIVERSITY OF CALIFORNIA

SAN DIEGO

Wave Directional Characteristics on a Partially Sheltered Coast

A dissertation submitted in partial satisfaction of the
requirements for the degree of Doctor of Philosophy
in Oceanography

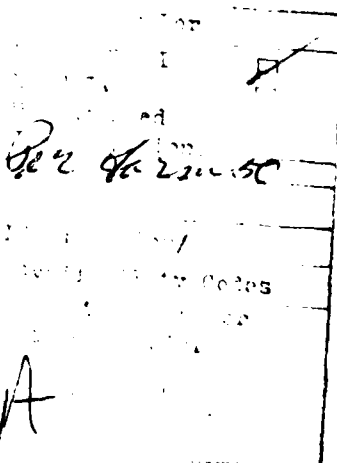
by

Steven Sitter Pawka

Committee in charge:

Professor Douglas L. Inman, Chairman
Professor Robert T. Guza
Professor Russ E. Davis
Professor Hugh Bradner
Professor Seibert Q. Duntley

1982



The dissertation of Steven Sitter Pawka is approved,
and it is acceptable in quality and form for
publication on microfilm:

P. T. Jaya

Leibert G. Dantley

J. Ferguson Bradner

Russ E. Davis

Douglas S. Druman

Chairman

University of California, San Diego

1982

To Dana, Mom, and Dad

TABLE OF CONTENTS

SECTION	PAGE
List of Symbols	vii
List of Figures	xiv
List of Tables	xx
Acknowledgments	xxii
Vita, Publications	xxiv
Fields of Study	xxvi
Abstract	xxvii
I. Introduction	1
I.1 Island Sheltering Experiment	1
I.2 Wave Directional Characteristics	8
II Theoretical Considerations	10
II.1 Physical Processes	10
II.1.1 Wave Refraction Models	10
II.1.2 Other Wave-Bottom Interactions	24
II.1.3 Island Edge Diffraction	32
II.1.4 San Clemente Island Shadow	36
II.2 Directional Spectrum Estimators	38
II.2.1 Maximum Likelihood Estimator (MLE)	38
II.2.2 Iterative Modifications to MLE	40
II.2.3 Minimum Square Window Error (MSWE) estimator	47
II.2.4 Estimation of Spectral Moments	53
III Experimental Set-up	61
III.1 In-situ Frequency Spectrum Measurements	61

TABLE OF CONTENTS

SECTION	PAGE
III.2 In-situ Directional Measurements	65
III.3 Remote Directional Characteristics	76
III.4 In-situ Wind Measurements	79
IV Nearshore Wave Directional Characteristics	80
IV.1 Island Sheltering Experiment	80
IV.1.1 Low Frequency	90
IV.1.2 Mid Frequency	95
IV.1.3 High Frequency	99
IV.2 San Clemente Island Shadow	107
IV.3 Northern Quadrant Window ($270\text{-}295^\circ\text{T}$)	119
IV.4 Refractive Banks Quadrant ($250\text{-}269^\circ\text{T}$)	125
IV.5 Inter-Island Fetch ($296\text{-}320^\circ\text{T}$)	132
IV.6 Southern Quadrant ($180\text{-}249^\circ\text{T}$)	136
IV.7 Conclusions	139
V Momentum Flux Estimation	144
V.1 Introduction	144
V.2 Field Comparison With a Slope Array	147
V.3 Field Comparison With a Current Meter	161
V.4 Conclusions	173
VI Statistical Properties of Momentum Flux	175
VI.1 Characteristic and Density Function of Cross-Spectral Estimates	176
VI.2 Comparison with Field Data	181
VI.3 Distribution Variability	190

TABLE OF CONTENTS

SECTION	PAGE
VI.4 Conclusions	195
References	197
Appendix A Comparisons of SAR and Linear Array	203
Appendix B Model Tests of MLE and IMLE Methods	212
Appendix C IMLE Approach Paths	236

List of Symbols

General Roman Alphabet

a_c	curvature of a caustic line
$a_{1m}, a_{1m}(\alpha)$	cross-spectrum weights
b	subscript denoting the "breakpoint"
c	phase velocity
C	phase speed ($= \underline{C} $)
c_f	quadratic friction coefficient
C_0	initial value of phase speed in refraction model
$C_{1m}(f)$	co-spectrum of sensors 1 and m
$C_{uv}(f)$	co-spectrum of horizontal velocity components
$C_{\eta_x \eta_y}(f)$	co-spectrum of orthogonal slope components
D	adjustable constant for MLE spectrum
D1,D2,D3	constants used in model directional spectra
E	wave energy
f	wave frequency
F_e	fetch length
$F(\cdot)$	general function of ...
F	angle transformation function
g	acceleration of gravity
h	mean water depth
i,j,k,l,m	indices used as subscripts
i	$(-1)^{\frac{1}{2}}$
I	function to be minimized
I_1	longshore transport of sand
K	vector wavenumber

K	magnitude of wavenumber ($= \underline{K} $)
\hat{M}	estimate of directional moment
$M(\alpha)$	directional moment weighting function
$M_{1m}(f)$	harmonic moments of the directional spectrum
n	ratio of group/phase speeds
$n(f)$	n as a function of frequency
n_0	initial value of n in refraction model
n_e	number of ensembles
P_1, P_2, P_3	cos powers used in directional spectrum models
$p(x)$	probability density function
$Q_{1m}(f)$	quad-spectrum of sensors 1 and m
r	correlation coefficient
s	distance along a wave ray
S_{yx}	onshore flux of longshore directed wave momentum
$S_{yx}(f)$	S_{yx} expressed as a function of frequency
$\hat{S}_{yx}, \hat{S}_{yx}(f)$	estimates of S_{yx} and $S_{yx}(f)$
t	time
T	superscript denoting the transpose of a vector
$T(\alpha)$	MLE response to a model directional spectrum
u, v	horizontal current components
U, V	complex Fourier transform of horizontal current components
U_r, V_r	real parts of U, V
U_i, V_i	imaginary parts of U, V
U_{10}	wind speed at 10 m height off the surface
$\langle \underline{u} \rangle$	average magnitude of horizontal velocity

V_a	variance-covariance matrix
$W(\alpha', \alpha)$	directional spectrum window
x, y	orthogonal spatial coordinates
x_{1m}, x_1	spatial lags in an array
x_0	minimum spatial lag in a sensor array
$X_{1m}(f)$	complex cross-spectrum of sensors 1 and m
z'	depth off bed

General Greek Alphabet

α	wave propagation direction
α_m	mode angle of directional spectrum
α_0	initial angle in refraction model
α_{tp}	wave angle at Torrey Pines Beach (deep water)
α_{do}	wave angle in deep ocean
$\alpha_1, \alpha_2, \alpha_3$	angle constants used in directional spectrum models.
$\Delta\alpha_m$	directional mode width
β	constant used in IMLE modifications
$\beta_{1m}(\alpha)$	complex cross-spectrum weights
∇	horizontal spatial gradient operator
Δ	finite differential
$\delta(l, K)$	Kronecker delta function
$\epsilon_i(\alpha)$	modifications used in IMLE scheme
γ	constant used in IMLE modifications
$\Gamma(x)$	gamma function
κ_u, κ_b	parameters used in directional spectrum models
λ	parameter used in IMLE modifications
Λ	moment parameter of directional spectrum

μ	Lagrange multiplier
n	sea surface elevation
n_x, n_y	orthogonal slope components
v	parameter to weight estimator variance
v_n	normalized value of v
$\phi_x(\theta)$	characteristic function of the variable x
ψ	moment parameter of directional spectrum
ρ	density of sea water
σ	radian frequency
σ_m	frequency maximum in spectrum
σ_n	normalized standard deviation
σ_x^2	variance of the variable x
θ	transform variable for characteristic functions
χ^2	Chi-square density function

Intermediate Variables Used In Derivations

Variables

a,b,c
 a', b', c'
A,B,C
 A_0, B_0, C_0
x
 u_{rj}, u_{ij}
 v_{rj}, v_{ij}

Functions

$h_{lm}(a, a'), h_{lm}(a')$

Vectors

A, C, S, θ

Matrices

B, Ω

Theoretical Spectra

$E(f, \alpha)$	frequency-directional spectrum
$E(K)$	wavenumber spectrum
$E(\alpha)$	directional spectrum
$\hat{E}(\alpha)$	directional spectrum estimate
$\hat{E}_0(\alpha)$	MLE directional spectrum estimate
$\hat{E}_i(\alpha)$	IMLE directional spectrum estimate
$E_{tp}(f, \alpha)$	frequency-directional spectrum at Torrey Pines Beach
$E_{do}(f, \alpha)$	frequency-directional spectrum in deep ocean
$E_{do}(\alpha)$	directional spectrum in deep ocean

Measured Spectra

$E_{xx}(f)$	frequency spectrum where xx=os is Oceanside, tp is Torrey Pines Beach, ib is Imperial Beach, br is Begg Rock, and tb is Tanner Bank
$E_r(\alpha)$	SAR directional spectrum
$E_u(\alpha)$	unimodal representation of SAR spectrum
$E_{tm}(\alpha)$	MLE directional spectrum at TPB
$E_{ti}(\alpha)$	IMLE directional spectrum at TPB
$E_{tw}(\alpha)$	MSWE directional spectrum at TPB

$E_g(f)$	gap energy density
$E_f(f)$	inter-island fetch spectrum ($296\text{-}320^\circ T$) at TPB
$E_w(f)$	window quadrant spectrum ($270\text{-}295^\circ T$) at TPB
$E_b(f)$	banks quadrant spectrum ($250\text{-}269^\circ T$) at TPB
$E_s(f)$	south quadrant spectrum ($180\text{-}249^\circ T$) at TPB

Operators

—→	array smearing (MLE) transformation
*	convolution

Abbreviations

CDS	continuous directional sample (days)
CM	biaxial current meter
DOF	degrees of freedom
FWHM	full width at half maximum
IMLE	iterative modification to MLE (estimator)
MLE	Maximum Likelihood Estimator
ME	moment estimator
MSWE	minimum square window error (estimator)
NRG	Nearshore Research Group
NSD	normalized square deviations
NSE	normalized square error
OS	Oceanside
RSE	relative square error
SAR	synthetic aperture radar
SIO	Scripps Institution of Oceanography
SCI	San Clemente Island

SWE	square window error
SYXE	S_{yx} (estimation) error
TPB	Torrey Pines Beach
VAR	variance
XSD	cross-spectrum deviations

LIST OF FIGURES

FIGURE		PAGE
1	Location map of West Coast Experiment.....	3
2	Hypothetical refractive transformations.....	13
3	Wave energy responses at coastal sites.....	17
4	Directional responses at Torrey Pines Beach.....	20
5	Energy ratios at Torrey Pines Beach and deep ocean	21
6	a. Cusp caustic at a circular shoal b. Appearance of a caustic in angle transformation.....	26
7	Numerical evaluation of diffractive effects....	33
8	MLE and IMLE response to unimodal test spectrum.	42
9	MSWE directional windows.....	51
10	MLE and MSWE response to a bimodal test spectrum.	54
11	IMLE, MLE, and MSWE directional spectra for 0.082 Hz on 5 March 1977.....	55
12	Performance of ME_0 method in estimation of $S_{yx}(f)$ with 1-2-4-5 array.....	58
13	Bathymetry and sensor locations at Torrey Pines Beach.....	67
14	Square window error of various linear arrays....	71
15	Average frequency spectra sampled during the West Coast Experiment.....	81
16	Ratio of band energy at Torrey Pines Beach to Begg Rock versus frequency.....	83

LIST OF FIGURES

FIGURE		PAGE
17	Frequency spectra at Torrey Pines Beach and Begg Rock for 25 and 28 March 1977.....	87
18	Sample directional spectra at Torrey Pines Beach.	89
19	Comparison of predicted and measured directional spectra at Torrey Pines Beach for 0.059 Hz on 25 March 1977.....	93
20	Comparison of predicted and measured directional spectra at Torrey Pines Beach for 0.090 Hz on 25 March 1977.....	97
21	Comparison of predicted and measured directional spectra at Torrey Pines Beach for 0.137 Hz on 25 March 1977 and 0.145 Hz on 28 March 1977....	103
22	Normalized gap energy as sampled by IMLE, MLE, and MSWE methods for various frequencies on 5 March 1977.....	109
23	Average MSWE estimates of normalized gap energy versus frequency.....	111
24	Comparison of directional spectrum models, model responses, and measured spectra for 0.067 Hz....	114
25	Average MSWE directional spectrum estimates for 0.114 Hz and 0.145 Hz.....	116
26	MSWE, IMLE, and MLE directional spectrum estimates for 0.145 Hz on 5 March 1977.....	121

LIST OF FIGURES

FIGURE		PAGE
27	MSWE, IMLE, and MLE estimates of peak energy ratios in Torrey Pines Beach directional spectra.	126
28	MSWE, IMLE, and MLE directional spectrum estimates for 0.137 Hz on 25 March 1977.....	134
29	Inter-island fetch energy versus frequency.....	135
30	IMLE estimates of southern quadrant directional spectra for various frequencies on 25 March 1977.	138
31	Performance of IMLE, MLE, and ME_0 methods in $S_{yx}(f)$ estimation for 1-2-4-5 and 1-2 linear arrays.....	149
32	Average frequency spectra for the $S_{yx}(f)$ estimation comparison data sets.....	151
33	IMLE and MLE directional spectrum estimates for 0.129 Hz and 0.059 Hz on 10 June 1977.....	153
34	Comparison of slope array and linear array estimates of $S_{yx}(f)$	156
35	Performance of the IMLE, MLE, and ME_0 methods in the estimation of $S_{yx}(f)$ with 2-2-2-5 array.....	163
36	IMLE and MLE directional spectrum estimates for 0.074 Hz on 18 Nov 1978 and 0.106 Hz on 6 Dec 1978.....	167
37	Comparison of linear array and current meter estimates of $S_{yx}(f)$ on 6 Dec 1978.....	169

LIST OF FIGURES

FIGURE		PAGE
38	Comparison of linear array and current meter estimates of $S_{yx}(f)$ on 18 Nov 1978.....	171
39	Analytic density functions for estimates of $S_{yx}(f)$	182
40	Comparison of analytic and sample distributions of $S_{yx}(f)$ estimates.....	185
41	Directional spectra associated with data plotted in Figure 40.....	186
42	Comparison of theoretical and sample variances of $\hat{S}_{yx}(f)$ distributions.....	189
43	Standard deviation and skewness of $\hat{S}_{yx}(f)$ distributions as a function of spectrum and averaging parameters.....	192
A.1	Location map of Torrey Pines Beach array.....	204
A.2	Frequency spectrum for 25 March 1977.....	204
A.3	MLE responses of 1-2-4-5 array.....	204
A.4	Measured and refracted directional spectra at Torrey Pines Beach.....	205
A.5	Schematic of SAR illuminating a patch of the ocean surface.....	205
A.6	SAR image.....	206
A.7	Two-dimensional FFT of SAR image.....	207
A.8	Schematic of SAR image distortion due to wave motion.....	208

LIST OF FIGURES

FIGURE		PAGE
A.9	Frequency spectrum on 28 March 1977.....	208
A.10	Comparison of linear array and SAR directional spectra on 25 March 1977.....	209
A.11	Comparison of linear array and SAR directional spectra on 28 March 1977.....	210
A.12	Directional spectrum discrepancies versus band energy and surface slope.....	211
B.1	Normalized square error and $S_{yx}(f)$ estimation error for IMLE and MLE methods versus frequency for unimodal deterministic tests.....	216
B.2	Normalized square error and $S_{yx}(f)$ estimation error for IMLE and MLE methods versus background spectral level for unimodal deterministic tests.	218
B.3	MLE and IMLE directional responses to a bimodal spectrum.....	219
B.4	Normalized square error for MLE and IMLE methods versus frequency for a unimodal test spectrum...	224
B.5	Normalized range of MLE and IMLE directional spectrum estimates in response to numerically simulated random cross-spectra.....	232
B.6	MLE and IMLE deterministic and random responses to a narrow and broad directional distribution.	234
B.7	Test directional spectra.....	235

LIST OF FIGURES

FIGURE	PAGE
C.1 Trends of normalized square error and cross-spectrum deviations versus iteration of IMLE method.....	238
C.2 Value of $S_{yx}(f)$ estimate versus iteration of IMLE method.....	239
C.3 IMLE directional spectrum estimates in response to a strongly bimodal spectrum.....	241
C.4 Normalized cross-spectral error versus iteration of the IMLE method for field data.....	246

LIST OF TABLES

TABLE		PAGE
1	Evaluation of bottom dissipation effects.....	31
2	Evaluation of island edge diffraction effects...	35
3	Bias and variance of $S_{yx}(f)$ estimators.....	59
4	Locations and depth of West Coast Experiment sensor sites.....	63
5	Low frequency square window error.....	73
6	Mode parameters for unimodal representations of SAR directional spectra.....	85
7	Comparison of measured and predicted band energy at coastal sites.....	92
8	Averaged comparisons of measured and predicted band energy at coastal sites.....	100
9	Correlation of wave energy and wind speeds.....	105
10	Mode parameters of window quadrant peak.....	122
11	Comparison of the predicted and measured values of the banks/window energy ratio.....	128
12	Statistics of mode parameters of banks quadrant peak.....	129
13	Quantitative comparisons of $S_{yx}(f)$ estimators...	158
14	Variances of $S_{yx}(f)$ estimates.....	172
15	Comparison of theoretical and sample values of skewness and kurtosis of $S_{yx}(f)$ distributions...	188
A.1	Mode parameters of SAR and linear array spectra.	208
A.2	Comparisons of spectral moments.....	209

LIST OF TABLES

TABLES	PAGE
B.1 Normalized square error of IMLE estimates.....	214
B.2 Relative square error of IMLE and MLE estimates.	221
B.3 $S_{yx}(f)$ estimation errors.....	227
B.4 Relative estimation errors for random tests.....	229
B.5 $S_{yx}(f)$ estimation errors for random tests.....	230
C.1 Errors in estimation of harmonic moments.....	243
C.2 IMLE estimates of $S_{yx}(f)$	244

ACKNOWLEDGMENTS

Professor Doug Inman guided me into this general field, taught me the basics, helped initiate the specific topic, and maintained positive critical and financial support for over a decade. Without him, this work would never have been done. Professor Bob Guza provided substantial guidance, both as a friend and boss, and sacrificed an uncountable number of hours working on the various drafts. Without him, this work would never have been reduced to a readable document. Professor Russ Davis contributed a large amount of original ideas, provided excellent critical review, and his work was drawn on heavily. Mike Freilich (now a professor also) contributed daily (for years) as a friendly advisor, provider of the "opposing point of view", and computer wizard. Mike's presence enhanced the quality of work of everyone in the lab.

There is a substantial amount of field work discussed in this dissertation that would not have been possible without the efforts of the staff of the Shore Processes Lab. All of the data were retrieved through systems that were designed by Bob Lowe. Bob thoroughly supervised all of the field work, served as a personal friend and advisor, and contributed much original thought to the research. Chuck Nordstrom did valuable work in helping set up the West Coast Experiment, as did Omar Shemdin and Vincent Hsiao (of JPL). Omar and Vincent also did excellent work with the radar systems. It would be impractical to list every person that helped in the field work, but substantial contributions were made by Mike Kirk, J.C. Boylls, and

Walt Waldorf.

There was a lot of cooperative effort on the various projects by the students at SPL. My projects were helped by many, but particularly strong support was supplied by Dave Aubrey and Greg Geehan.

Mike Clark drafted the figures and displayed remarkable patience with my crude originals and numerous changes. Dana, my wife, helped me put together the final manuscript. We drew heavily on her technical skills (tables and equations). She unselfishly sacrificed her spare time to accomplish this task while maintaining a normal routine at her job at Scripps and running our household.

The Jet Propulsion Laboratory and Sea Grant, through the National Sediment Transport Study, sponsored the field work. The Office of Naval Research, Code 422CS (Coastal Sciences), Contract No. N00014-75-C-0300, provided the financial support for the data analysis and interpretation.

VITA

Born: 14 January 1949 - San Diego, California.

1971 B. A. Physics, University of California, San Diego.
1971 Physicist, Naval Electronics Laboratory, San Diego, California.
1971-1978 Research Assistant, Scripps Institution of Oceanography, University of California, San Diego.
1978-present Research Associate, Scripps Institution of Oceanography, University of California, San Diego.

PUBLICATIONS

Taylor, H. F., V. N. Smiley, W. E. Martin and S. S. Pawka, 1972, "Fluorescence of graded-band-gap Cd S_x Se_y crystals produced by diffusion," Physical Review, Series B, vol 5, no 4, p 1467-73.

Inman, D. L., C. E. Nordstrom, S. S. Pawka, D. G. Aubrey and L. C. Holmes, 1974, "Nearshore processes along the Silver Strand Littoral Cell," unpublished report prepared for the U. S. Army Corps of Engineers, Los Angeles District.

Pawka, S. S., 1974, "Study of wave climate in nearshore waters," Proc. Int. Symp. on Ocean Wave Measurement and Analysis, Amer. Soc. Civil Eng., vol 1, p 745-60.

Pawka, S. S., D. L. Inman, R. L. Lowe and L. C. Holmes, 1976, "Wave climate at Torrey Pines Beach, California," U. S. Army Corps of Eng., Coastal Eng. Res. Center, Tech Paper 76-5, 372 pp.

Inman, D. L., D. G. Aubrey and S. S. Pawka, 1976, "Application of nearshore processes to the Nile Delta," p 205-255 in Proc. of Seminar on Nile Delta Sedimentology, held in Alexandria 25-29 Oct 75 by UNDP/UNESCO Project for Coastal Studies, Publ. by the Project under Academy of Scientific Research and Technology, 257 pp.

Pawka, S. S., 1977, "Linear arrays," Nearshore Sediment Transport Study Workshop on Instrumentation for Nearshore Processes, University of California Sea Grant Program, IMR Ref. 78-102.

Pawka, S. S., V. Hsiao, O. H. Shemdin, and D. L. Inman, 1978, "Comparison of wave directional spectra from SAR and pressure sensor array," Transactions, American Geophysical Union, Vol. 59, no 12, p. 1100 (abstract only).

- Pawka, S. S. and D. L. Inman, 1978, "Effect of islands on coastal wave conditions," Transactions, American Geophysical Union, Vol. 59, no. 12, p. 1100 (abstract only).
- Pawka, S. S., S. V. Hsiao, O. H. Shemdin, and D. L. Inman, 1980, "Comparisons between wave directional spectra from SAR and pressure sensor arrays," Jour. of Geophys. Res., vol 85, no C9, pp 4987-4995.
- Vesecky, J. F., S. V. Hsiao, C. C. Teague, O. H. Shemdin, and S. S. Pawka, 1980, "Radar Observations of Wave Transformations in the Vicinity of Islands," Journal of Geophysical Research, vol 85, no C9, pp 4977-4986.
- Higgins, A. L., R. J. Seymour, and S. S. Pawka, 1981, "A compact representation of ocean wave directionality," Applied Ocean. Res., vol 3, no 3, pp 105-112.

FIELDS OF STUDY

Major Field: Oceanography

Studies in Nearshore Processes

Professors D. L. Inman and R. T. Guza

Studies in Physical Oceanography

Professors R. S. Arthur, R. E. Davis, M. C. Hendershott,
W. H. Munk, J. L. Reid, and C. D. Winant.

Studies in Marine Geology

Professors J. R. Curray, D. L. Inman, and H. W. Menard

Studies in Chemical Oceanography

Professor J. M. Gieskes

Studies in Biological Oceanography

Professors J. A. McGowan, M. M. Mullin, R. H. Rosenblatt,
and W. A. Newman

Studies in Time Series Analysis

Professors R. E. Davis and R. A. Haubrich

ABSTRACT OF THE DISSERTATION

Wave Directional Characteristics on a Partially Sheltered Coast

by

Steven Sitter Pawka

Doctor of Philosophy in Oceanography
University of California, San Diego, 1982
Professor Douglas L. Inman, Chairman

The sheltering effects of the Channel Islands on the wind generated surface gravity wave field at the Southern California coastline are studied with an extensive field experiment. Emphasis is placed on wave directional measurements sampled at Torrey Pines Beach

with a linear array of pressure sensors. Problems in the estimation of wave directional spectra and momentum flux are addressed and solutions are proposed. Finally, the statistical fluctuations of the wave momentum flux estimators are examined and compared to approximate analytic relationships.

A linear model was implemented for the evaluation of wave transformations around the islands due to refraction over the shoals in the island region and blocking due to the island cross-sections. This model shows a strong influence of refraction on waves with frequencies less than 0.10 Hz. Extensive sets of field measurements were taken as part of the Seasat West Coast Experiment to test the validity of this approximation to the wave transformations from the deep ocean to the coast. The variable quality of the deep ocean estimates of wave directionality, obtained from synthetic aperture radar (SAR) images, led to a limited confirmation of the island refraction/blocking model.

The high resolution of the Torrey Pines Beach array measurements allowed for the definition of the island shadows in the directional spectrum. For example, the 0.07 Hz spectra resolve narrow peaks with separation of 8° while the 0.15 Hz resolution is about 4° . A characteristic bimodal directional structure of the north swell is observed in the directional spectra. The statistical characteristics of the two directional modes are consistent with the refractive modeling of wave transformations around the islands. Frequent south swell and occasional local generation further complicate the coastal wave directionality.

Several estimation techniques were compared for their performance in directional spectrum analysis. An existing data adaptive technique, the Maximum Likelihood Estimator, was chosen for the initial data reduction. A modified form of this method (IMLE) and an alternative minimum square window error technique are proposed and implemented. The two methods developed here show significant improvement in the definition of gaps in the spectrum and in the partition of energy amongst the spectral peaks. Although none of these methods is considered a sole solution to the estimation problem, much information on the wave directional characteristics is derived from the comparative results. For instance, a near zero energy density estimate for the shadowed quadrants of the spectra in the frequency range 0.08-0.10 Hz is indicated by the comparative study of the estimators.

The complicated directional spectrum forms commonly observed at Torrey Pines Beach present difficulties in the estimation of sensitive directional moments. The estimation problem of extracting accurate estimates of the onshore flux of longshore directed momentum, S_{yx} , from linear array data is addressed. A window shaping technique is developed and compared to the integration of the directional spectrum estimates. Using field data, the linear array methods are compared with a biaxial current meter and a "slope" array. The window shaping technique and integration of the IMLE spectra show excellent agreement with the results from the other two systems.

The statistical nature of point measurements of S_{yx} in a directional wave field is related to previous work on probability

density functions of the co-spectrum in a bivariate Gaussian random process. A family of distributions is developed from the statistical theory. These distributions are compared with the observed variability of linear array estimates of S_{yx} . The theory describes well the basic trends in the field data. Finally, the S_{yx} sampling problem is addressed in light of these theoretical distributions. The sampling time required for stable estimates of S_{yx} is shown to be a strong function of the directional spectrum. Very stable estimates of S_{yx} are associated with narrow unimodal distributions while near zero estimates have relatively large absolute variability when the directional spectrum is dispersed or bimodal. Examples given show that for a stated quantification of the desired estimate stability, the sampling time required for this stability can easily vary by a factor of 2.

I INTRODUCTION

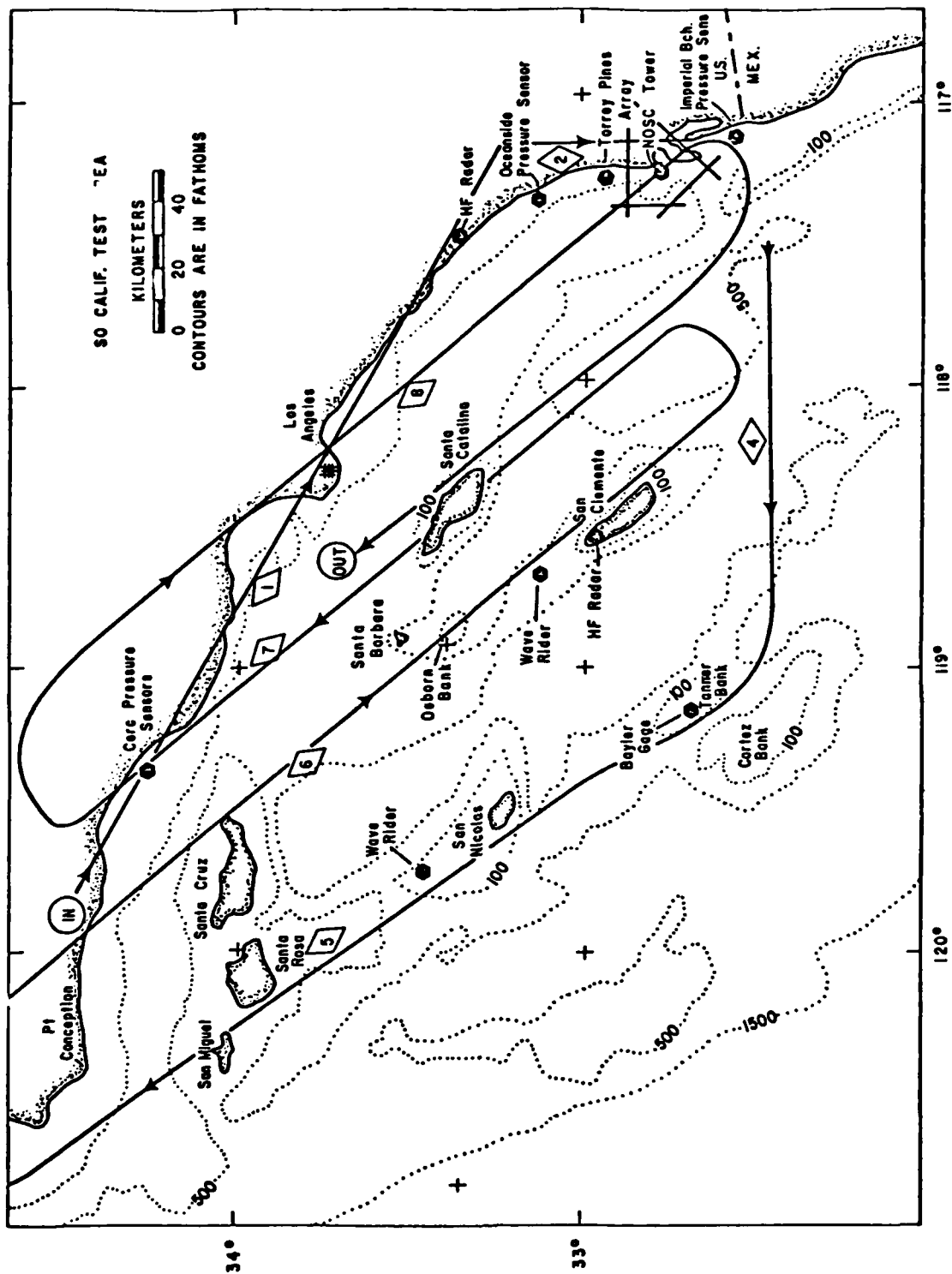
Wind generated surface gravity waves are often the dominant driving force for nearshore processes (Inman and Brush, 1973). The energy supplied by these waves has been linked to longshore currents, nearshore circulation, edge waves, set-up, and longshore and on-offshore sediment transport. Many of these processes are interrelated and together form the complex dynamical system of the air-sea-land interface. Investigation into the dynamics of the nearshore requires a detailed specification of the frequency and directional characteristics of the wave field. The presence of the Channel Islands has been long recognized as a dominant factor in the Southern California wave climate (Arthur, 1951). An extensive field experiment was conducted to quantitatively evaluate the island sheltering effects. Additionally, a detailed study was made of the persistent features in the frequency-directional spectra measured at Torrey Pines Beach (TPB). The same basic data set was used for all of the analysis.

The onshore flux of longshore directed wave momentum, S_{yx} , is an important parameter of the wave field. On-offshore gradients in S_{yx} have been shown to be a dominant force in the driving of longshore currents and the resulting transport of sediment. The S_{yx} estimation problem and a statistical treatment of this wave field parameter are addressed in later sections of this dissertation. The associated motivation and background are also presented there.

I.1 Island Sheltering Experiment

The Southern California coast is bordered by a number of islands of complicated geometry (Figure 1). The basic effect of the

Figure 1. Location map of the West Coast Experiment sensor sites. The arrowed line indicates the flight path of the CV-990 which carried the L-band SAR (the diamonds indicate the leg number). The hexagonal dots show the positions of the various surface sensors.



islands should be blockage of certain quadrants of possible wave approach in the lee of the islands. The complicated cross-section due to the numerous islands and their shoals leaves only a few "windows" of exposure to deep ocean waves at a given coastal location.

The sheltering effects of islands have been studied previously. Arthur (1951) used visual observations along the Southern California coast to indicate the shadows of the Channel Islands in the presence of south swell. Arthur's primary conclusion was that wave refraction over the island shoals and width of the deep ocean directional spectrum were the dominant factors in spreading wave energy into the lee of the islands. He dismissed the importance of diffraction and wave interactions with large scale currents on a theoretical basis. Arthur did not attempt to completely evaluate the refraction effects for the island topography. Additionally, the deep ocean wave statistics were unknown. Therefore, his results were a qualitative description of the sheltering process.

Emery (1958) visually observed the wave field in the Southern California borderland region from an aircraft. There were multiple "wave trains" present in the field, but the dominant swell was around 0.10 Hz. Emery observed reduced wave heights in the islands' lee. However, he saw generally negligible directional control of the islands (or associated shoals) over the wave field. Also, Emery found little evidence of cross swell, which can be produced by either refraction around the island edges or by the existence of relatively broad deep ocean directional spectra.

Pawka et al (1976) used a linear array of length 120 m at TPB

for the study of the local directional wave climate. The measurements indicated restrictions on the local directional spectra due to the presence of the Channel Islands. However, the low directional resolution of this array did not allow for the definition of shadows of individual islands.

The sheltering effects of Sado Island on the wave field at the Niigata coast (Japan) were investigated by Hom-ma et al (1966). This experiment included measurements of the frequency spectrum offshore of the island and on the coast. A mean wave direction was deduced from the local weather patterns and a broad (\cos^2) offshore directional distribution was assumed. Refraction effects at the island edge were computed for the "significant" wave frequency and direction on each sample day. The authors found a positive correlation between the predicted (using offshore statistics) and measured values of coastal significant wave height. However, there was a large amount of scatter in the comparative data. The suitability of the assumed directional distributions was questioned. However, they concluded that both refraction and finite directional spread are important factors in determining the wave field at that coast.

Wilson et al (1973) demonstrated that wave refraction through the Mona Passage redirects low frequency energy from the North Atlantic to the western reaches of the Caribbean. Frequency spectra and wave direction were measured with a pair of sensors in shallow water off Aruba Island (Venezuela). These measurements , along with the appropriate timing of the swell arrival with the storm occurrence, fit the refracted source hypothesis. The required refraction in the

passage alters the wave propagation angle by 90°. No attempt was made to quantitatively evaluate the refraction at the passage.

Fett and Rabe (1976) compare simulated wave propagation around model island topography with observed satellite radar return from the ocean near several islands. They conclude that the qualitative structure of the calm sea patches in the island lee are consistent with the wave refraction process.

The work mentioned above displays a varying degree of quantification of the island sheltering effects. Several of the studies indicate that wave refraction is an important mechanism in determining the wave energy level in the lee of islands. However, the ability to quantitatively account for the refraction process has not been demonstrated. The primary information that is lacking is the synoptic measurement of the frequency-directional spectrum in the exposed (deep ocean) and sheltered regions.

An extensive field measurement program to quantify the island sheltering processes in the Southern California region was undertaken as part of the Seasat West Coast Experiment. The measurements included numerous in-situ (surface) estimates of the wave frequency spectrum along the coast and in the "deep ocean" (relatively unsheltered region offshore of the islands). An airborne L-band synthetic aperture radar (SAR) was used to sample the deep ocean estimates of the wave directional distributions. High quality SAR data were sampled on only 2 days of the month long experiment. Wave directional spectra were measured at TPB with a 400 m length linear pressure sensor array located in a mean depth of 9.6 m.

The refraction process over the island topography was studied with the use of a numerical model. Wave diffraction around the island edges with continuous directional spectra was also modeled and found to be roughly negligible, a result which is consistent with Arthur (1951). The primary aim of this measurement program was a quantitative evaluation of the refractive modeling of the sheltering effects. The ultimate goal of this research was a tool for first order coastal wave prediction in terms of deep ocean statistics.

The deep ocean estimates of the frequency-directional spectrum were transformed by the island refraction model to yield deep water predictions at the TPB and Oceanside coastal sites and in an area near the northern tip of San Clemente Island (Figure 1). The array measurements of the frequency-directional spectrum at TPB were refracted out over the local shelf topography for direct comparison with the predicted spectrum in "local deep water". The predicted and observed spectra are in good agreement for the limited range of frequencies which have reasonably accurate deep ocean directional spectra. Only frequency spectral comparisons were made at Oceanside and San Clemente Island due to the lack of surface directional measurements. Approximations of the deep water directional spectra at Oceanside were necessary for the estimation of the local shelf refraction effects. The predicted directional spectra obtained from the island refraction model was used for this approximation. As a result, the model-data comparisons at this site are inconclusive.

There are several other mechanisms which may be of importance in island sheltering. These include nonlinear wave-wave interactions,

wave-current interactions, and local wave generation. The framework of the wave measurements and the lack of background information (e.g. the current field) did not allow for a detailed investigation of these processes. Information on only their integrated effect is deduced from the inadequacies of the refractive modeling of the wave transformations around the islands.

I.2 Wave Directional Characteristics

The second part of this work was a detailed study of the frequency and directional characteristics of the wave field at TPB. Persistent features in the local directional spectra were identified with the physical setting of the borderland region (patterns of islands and windows). The location, shape, and energetic level of the peaks and valleys in the spectra are statistically described for the West Coast Experiment data set. This detailed study generated much information on the processes which govern the local wave climate.

There have been many previous investigations of wave characteristics on the Southern California coastline. Powers et al (1960), Seymour et al (1977), and Thompson (1980) describe some of the studies which have measured only the wave frequency spectrum. Several studies of the directional wave field have been made with limited resolution systems. Panicker (1971) discusses the CERC 5 gage star array located at Pt. Mugu. Pawka et al (1976) performed a wave climate study at TPB with the use of a linear array. Seymour and Higgins (1977) used short sensor lags to investigate wave directional properties. All of these studies have emphasized the importance of low frequency (0.05-0.10 Hz) swell which is generated by distant

storms. However, none of the measurement systems had the resolution to define the details of the expected shadows of the islands. This requires a deep water directional resolution of roughly 5-10°. The high resolution array measurements taken during the West Coast Experiment were of sufficient quality to perform this investigation.

Barber (1954) first employed a sensor array for the measurement of ocean wave directionality. Since that time, many methods have been introduced for the enhanced estimation of the wave directional spectrum. No attempt is made here to review the evolution of this topic or the various techniques presently employed. Comprehensive reviews are included in Panicker (1974) and in Davis and Regier (1977).

Three directional spectrum estimators are employed in this study of nearshore wave characteristics. The first method, the Maximum Likelihood Estimator (MLE), has been widely used and discussed in the literature. The other two methods are developed in this work and in some applications show superior performance relative to the MLE method. None of these methods is recommended for unqualified use as an "optimal" estimator. Each has its own advantages and drawbacks. However, the intercomparison of the results of all three methods proves to be a useful technique in the study of directional wave properties. Tests with model spectra (Appendix B) and intercomparison of the methods does yield valuable information on their relative performance in specific applications.

II THEORETICAL CONSIDERATIONS

II.1 Physical Processes

A numerical model is used to evaluate wave refraction over the shoals in the island region. This model is also used to account for the local shelf refraction effects in the conversion of shallow water coastal measurements into local deep water estimates. A crude model of continuous spectrum diffraction by the island edges is used to estimate the importance of this process. Lastly, the processes which affect the wave energy level in the shadowed quadrants of the coastal directional spectra are briefly discussed.

II.1.1 Wave Refraction Models

Refraction has long been recognized as a process which alters the direction of surface gravity wave propagation. Arthur (1951) identified refraction as a possible first order mechanism for the spreading of wave energy into the lee of islands. His conclusion, based primarily on the study of smooth model island configurations, was that the slope of the offshore bathymetry is of considerable importance in the determination of the level of refracted wave energy in the island lee. A crude representation of the Channel Island bathymetry is shown in Figure 1. The islands are the surface expression of elongated submarine ridges. There are broad shoals in the depth range 50-100 m, particularly in the area between Santa Rosa and San Nicolas Islands and in the vicinity of Cortez and Tanner Banks. This topography should significantly affect the low frequency waves.

The method of refraction of a continuous wave spectrum was employed for this study. This method has been used by numerous investigators, e.g. Munk et al. (1963) and Collins (1972), for the theoretical description of the refraction process. The method is based on the conservation of $E(\underline{K})$, the wavenumber spectrum, along a ray. Longuet-Higgins (1957) derived this result for energy contained in a small region of wavenumber space, $\Delta \underline{K}$, using the conservation of energy flux. This result requires the linearity of the wave field and the general validity of the ray solution. The conservation of $E(\underline{K})$ is more routinely arrived at through the radiative transfer equation

$$\frac{\partial E}{\partial t} + \nabla \cdot E \underline{C} n = 0 \quad (\text{II.1})$$

where E is a measure of wave energy ($E = E(\underline{K})\Delta \underline{K}$), \underline{C} is the phase velocity, n is the (group/phase) speed ratio, ∇ is the spatial horizontal gradient operator, and there are no sources or sinks of wave energy, see e.g. Phillips (1966). This equation is combined with the conservation of crests equation

$$\frac{\partial \underline{K}}{\partial t} + \nabla \sigma = 0 \quad (\text{II.2})$$

where σ is the radian frequency, to yield

$$\frac{\partial E(\underline{K})}{\partial t} + \underline{C} n \cdot \nabla E(\underline{K}) = 0 \quad (\text{II.3})$$

The steps in this derivation are somewhat subtle and are included in Phillips (1966). With steady wave conditions and employing the transformation to the variables α (propagation direction) and f (frequency) this reduces to

$$c^2 n E(f, \alpha) = \text{constant} \quad (\text{II.4})$$

for evaluation of the spectrum along a ray.

Functionally, the refraction effects are represented by a map of angles

$$c^2 n E(f, \alpha) = c_{do}^2 n_{do} E_{do}(f, \alpha_{do}) \quad (\text{II.5})$$

where the subscript do implies evaluation in the deep ocean (homogeneous) region. Figure 2a shows the refractive transformation of a rectangular spectrum which is incident to a plane beach. The energy density is adjusted by the factor $c^2 n / c_{do}^2 n_{do}$ while the directional bandwidth, $\Delta\alpha$, is decreased. The net effect in this example is an increase in the band energy, $E(f)$

$$E(f) = \int_{\alpha} E(f, \alpha) d\alpha \quad (\text{II.6})$$

Reference will often be made to the directional spectrum, $E(\alpha)$, which is an implied evaluation of $E(f, \alpha)$ at a particular frequency.

A hypothetical example of refraction around an island edge is shown in Figure 2b. The sheltered site is in deep water which yields $c^2 n = c_{do}^2 n_{do}$. However, the refraction and blocking effects severely reduce the directional spread ($\Delta\alpha << \Delta\alpha_{do}$). The sheltered band energy is a small fraction of the deep ocean value.

The ray paths were calculated over a digital representation of the topography with the use of a numerical program developed by Dobson (1967). This program integrates the fundamental ray equations for solution of the ray paths. These equations are

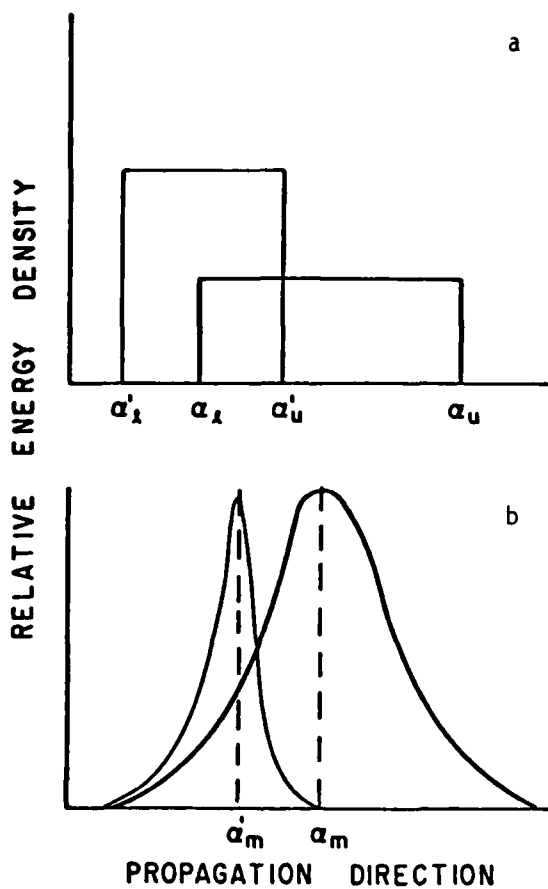


Figure 2. Refractive transformations of continuous directional spectra.

Examples shown are a) rectangular spectrum incident on a plane beach with $C^2 n = 0.5 C_{do}^2 n_{do}$ (equation II.5) and b) unimodal spectrum refracted around a hypothetical island edge with $C^2 n = C_{do}^2 n_{do}$, a deep water to deep water transformation. α_I , α_u , and α_m are reference angles where α_m transforms to α'_m and so forth.

$$\begin{aligned}\frac{dx}{ds} &= \cos\alpha \\ \frac{dy}{ds} &= \sin\alpha \\ \frac{d\alpha}{ds} &= \frac{1}{C} \left[\sin\alpha \frac{\partial C}{\partial x} - \cos\alpha \frac{\partial C}{\partial y} \right]\end{aligned}\quad (\text{II.7})$$

where x and y are horizontal coordinates and s is the distance along the ray, see Munk and Arthur (1952). Coarse grids with 480 m spacing covered the broad regions between San Nicolas and Santa Rosa Islands and the Cortez and Tanner Banks. The topography at Osborne Bank and both edges of San Clemente Island were simulated with grids of ~250 m spacing. All of the grids covered the depths from 0 m to 250 m.

The method of refraction of continuous spectra described above has particular advantage over the monochromatic method when patching together results from many grids. The final result of the refraction analysis was a map of local directions into deep ocean directions for each coastal location. The analysis was carried out for local directional bandwidths of 0.1° for rays projecting to relatively shallow portions of the island topography and 0.2° for the remaining sectors. An angle difference of 0.1° at TPB projects to a horizontal separation of 150–300 m at the island grids. The fine resolution spectrum at TPB is obtained

$$E_{tp}(f, \alpha_{tp}) = \frac{1}{2\Delta} \int_{\alpha_{tp}-\Delta}^{\alpha_{tp}+\Delta} E'_{tp}(f, \alpha'_{tp}) d\alpha'_{tp} \quad (\text{II.8})$$

$$\begin{aligned}&= \frac{1}{2\Delta} \int_{F^{-1}(\alpha_{tp}-\Delta)}^{F^{-1}(\alpha_{tp}+\Delta)} E_{do}(f, \alpha_{do}) \frac{d\alpha_{tp}}{d\alpha_{do}} d\alpha_{do} \\ &\quad (\text{II.9})\end{aligned}$$

and is approximated by

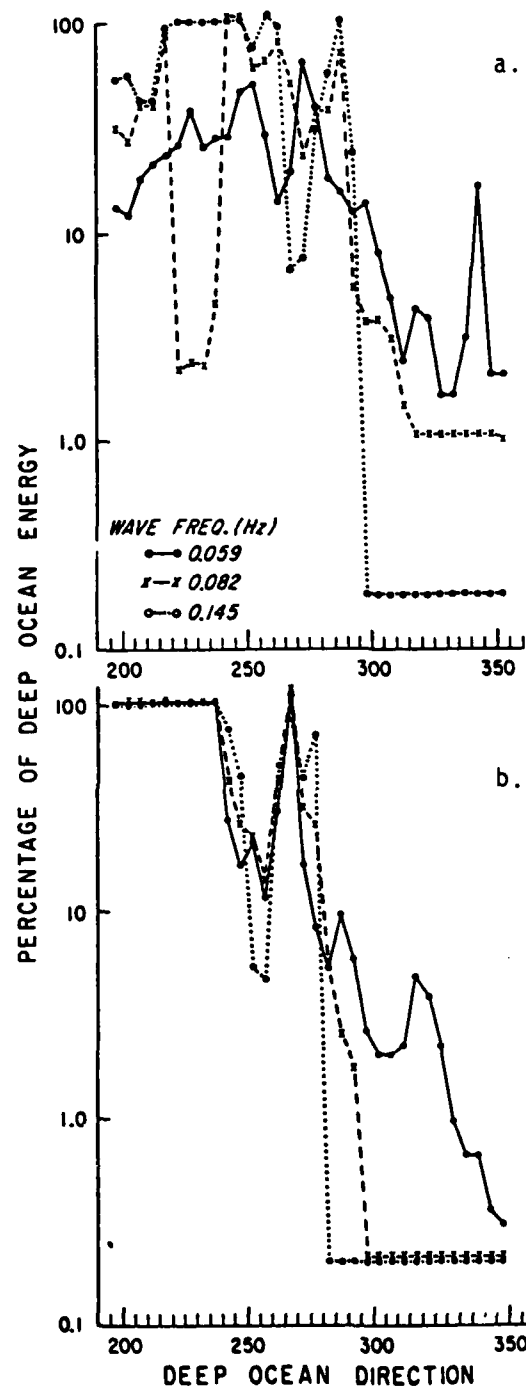
$$\frac{1}{\Delta_{do}} \int_{F^{-1}(\alpha_{tp}-\Delta)}^{F^{-1}(\alpha_{tp}+\Delta)} E_{do}(f, \alpha_{do}) d\alpha_{do} \quad (\text{II.10})$$

where $E_{tp}(f, \alpha_{tp})$ is the TPB spectrum, $E_{do}(f, \alpha_{do})$ is the deep ocean spectrum, 2Δ is the fine resolution bandwidth at TPB, the angles α_{tp} and α_{do} are related by the transformation $\alpha_{tp} = F(\alpha_{do})$ and $\Delta_{do} = |F^{-1}(\alpha_{tp}+\Delta) - F^{-1}(\alpha_{tp}-\Delta)|$. The limitations of this approximation will be discussed later. $E_{tp}(f, \alpha_{tp})$ is then block averaged and decimated into 1° directional bands. All discussion of theoretical coastal spectra (or coastal response) will be in reference to the local deep water conditions. Rays which intercept the islands are terminated which leaves gaps in the coastal directional spectra. Therefore, the "blocking" effects of the islands is imbedded in the refraction model.

The energy response at the sheltered sites as a function of deep ocean direction is shown for several wave frequencies in Figure 3. There is a marked difference in the response functions at the two sites. The variation of the response with wave frequency at a particular site is due to the wavelength dependence of the refraction process. The large variance of the TPB response functions indicates the relative importance of refraction at the site.

The low frequency response at TPB is made fairly smooth by the refraction process. Nearly all of the low frequency directional spectrum at TPB is affected to some extent by the topography either in the Channel Islands or Pt. La Jolla regions. There are no large "open windows" to the deep ocean directional spectrum. On the other hand, there is a fairly significant response to all sectors of the deep

Figure 3. Wave energy response at a) Torrey Pines Beach and b) Ocean-side versus deep ocean direction. The values given are the wave energy ratio coastal/deep ocean for 5 rectangular spreads in deep ocean directions. The flat segments of the curves at high north angles ($300-350^{\circ}$ T) are an artifact of the averaging in the refraction model. The variability between the curves of different frequency is due to the wavelength dependence of the refraction process.

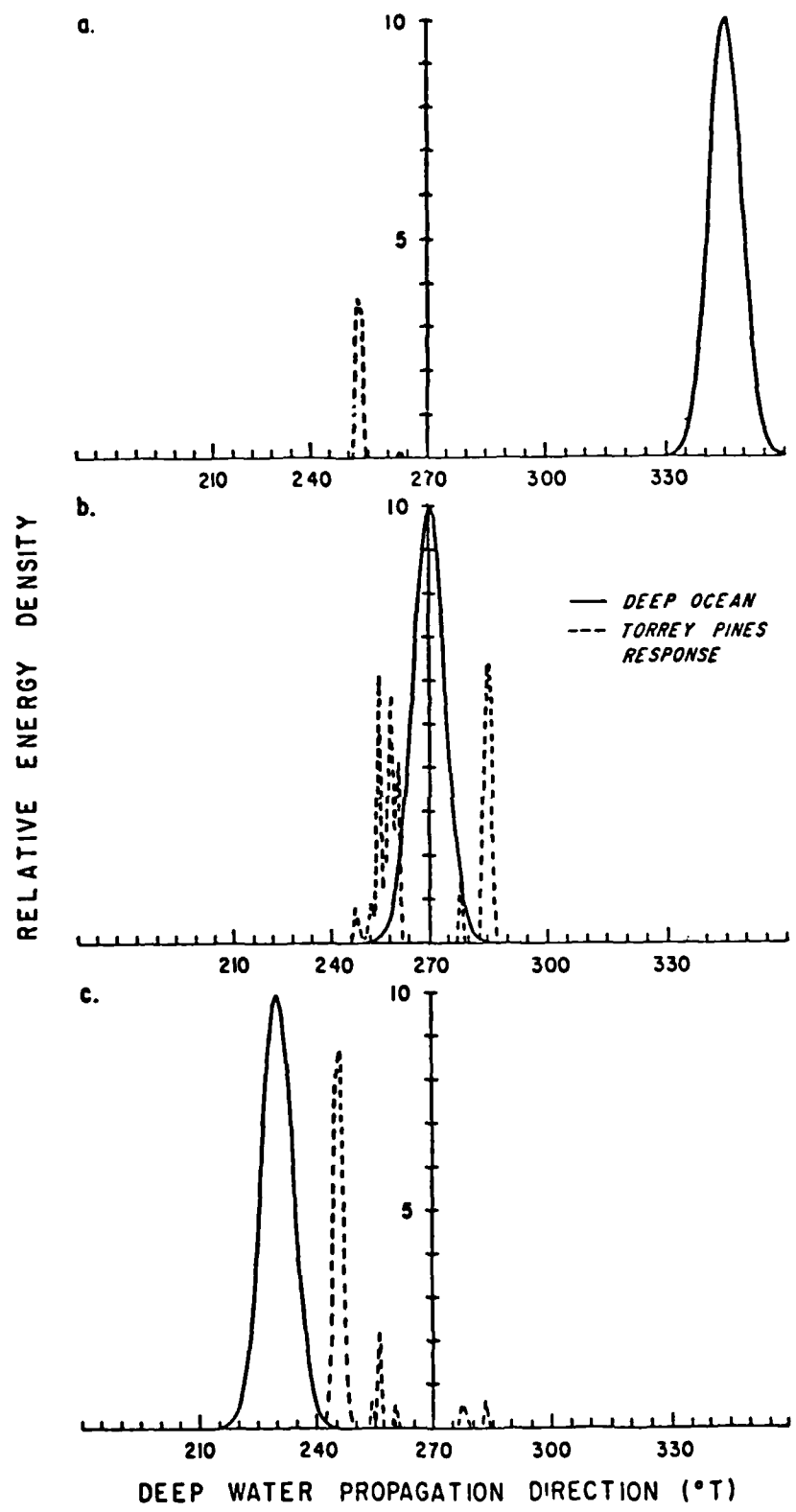


ocean spectrum, even the high angle northern ("northern" defined as $\alpha_{do} > 270^\circ T$) quadrant waves. The higher frequency response at TPB has much sharper delineation of the windows to the deep ocean. For example, the definition of the northern quadrant window, centered on $285^\circ T$, sharpens with increasing wave frequency. Also, a significant spread of southerly directions are completely open at high wave frequencies. The energy refracted to TPB for waves with $\alpha_{do} > 295^\circ T$ is insignificant for frequencies greater than 0.10 Hz.

The characteristics of the directional spectrum at the coast are significantly affected by the presence of the borderland islands and shoals. The 0.059 Hz directional responses to a variety of unimodal deep ocean directional spectra are shown in Figure 4. Energy from a large range of deep ocean directions refracts into the coastal angles which point to the shoals (shoal apertures). In this way, these shoal regions appear as "diffuse sources" of wave energy, regardless of the structure of the deep ocean directional spectrum. The major refractive sources are Cortez Bank ($252-255^\circ T$), Tanner Bank and the southern shoals of SCI ($261-263^\circ T$), and the shoals of the northern quadrant window ($278-290^\circ T$).

The relative sizes of the refractive sources vary as a function of the deep ocean directional spectrum. Figure 5a,a' shows the relationship of the band energy at TPB, $E_{tp}(f)$, to the deep ocean values for various unimodal north swell conditions. Figure 5b,b' shows the ratio of the refractive sources which contribute to the total band energy. The northern quadrant peak and the banks quadrant peaks are comparable in energy level for a wide range of deep ocean spectral

Figure 4. Theoretical directional response at Torrey Pines Beach for 0.059 Hz waves and several deep ocean spectrum forms. The transformations were computed using the island refraction model. A null result for energy density is predicted for the shadowed quadrants (for example, the San Clemente Island shadow centered on about 270° T).



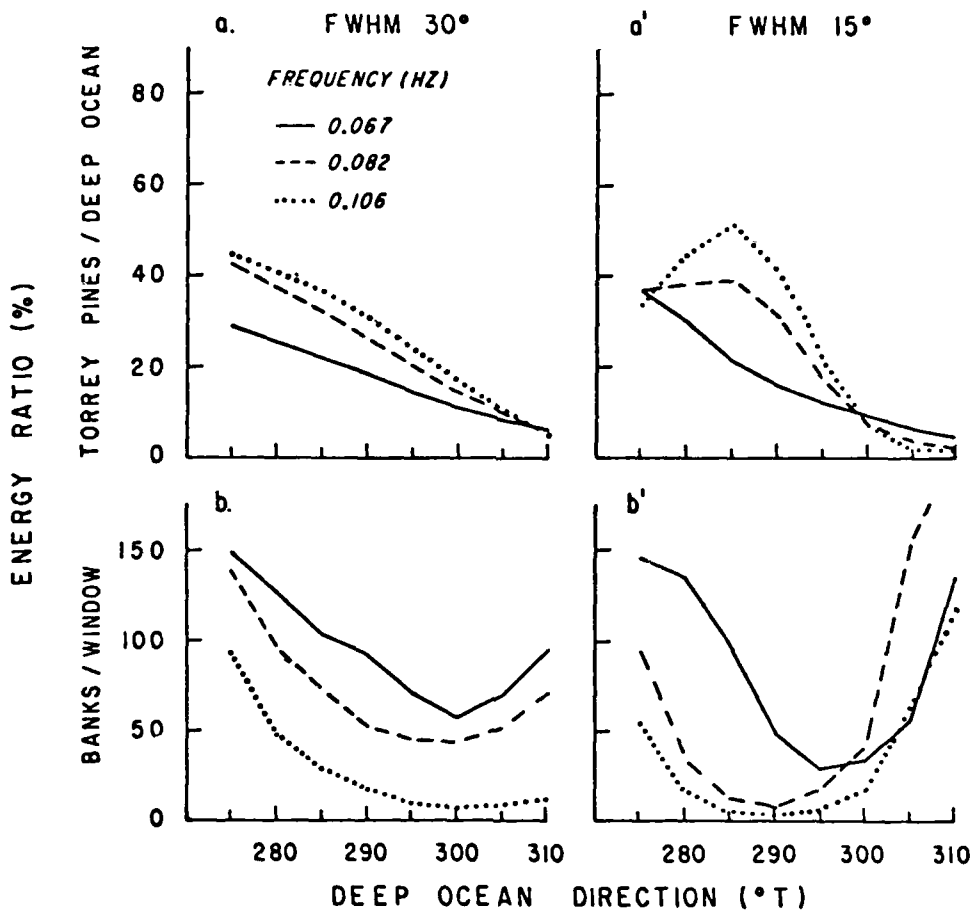


Figure 5. a,a') Ratio of band energy at Torrey Pines Beach to the deep ocean value. b,b') Ratio of banks quadrant ($250-269^{\circ}$ T) energy to the window quadrant ($270-295^{\circ}$ T) energy at Torrey Pines Beach. These ratios are theoretical results obtained from the island refraction model and are expressed as a function of mode direction for two unimodal (cos power) deep ocean spectral forms. FWHM denotes the full width at half maximum of the distribution modes.

conditions. Very high angle north swell ($\alpha_{d0} > 305^\circ T$) is seen to approach the TPB site primarily from southern angles (Figure 5b,b'), although this involves only a small percentage of the unsheltered energy (Figure 5a,a'). This is due to the strong refraction over Cortez Bank.

The refraction over the shoals off Pt. La Jolla plays an important role in the sheltering of south swell energy at TPB. Again, the response is seen to be highly frequency dependent. The sharp gap in the response at 0.082 Hz ($230^\circ T$ in Figure 3) is due to refraction by relatively irregular topography in this shoal region. This feature in the response functions does not vary smoothly with wave frequency. Pt. La Jolla has the effect of imposing a southern limit to the local directional spectra at TPB (Figure 4). This limit shifts progressively to the south for increasing wave frequency.

The presence of the borderland islands restricts the possible wave approach angles at the coast. In fact, the wave energy at TPB should be contained in a few relatively narrow directional sectors. This reduces the potential randomness of the coastal directional spectrum. On the other hand, the blocking and refraction may also complicate the coastal wave conditions. The examples shown in Figure 4 illustrate a common bimodal or even trimodal directional response at TPB to unimodal deep ocean spectra. The only unimodal coastal response occurs in response to very high angle north swell.

The refraction process appears to be important to the response functions at Oceanside only for the lowest frequency waves. As with TPB, the theoretical response at this site to high angle north swell

waves is primarily due to refraction over the Cortez and Tanner Banks. The refraction model predicts a coastal band energy greater than the deep ocean value for much of the southern quadrant. This is due to the fact that energy refracted to the site from various shoals in the island region adds to the primary source, which is received with full exposure. This is not a coherent focusing effect, however, and only slightly elevated values are expected.

Wave refraction analysis was also used to transform the shallow water coastal measurements into local deep water estimates. Refraction grids with spacings of ~50 m were developed for the coastal sites at TPB and Oceanside. The ray paths were constructed from the sensor locations out into local deep water. Ray path information was obtained for Imperial Beach from the L.A. Corps of Engineers. The method of continuous refraction was used to estimate the wave transformations over the shelf.

The directional spectra analyzed from the linear array at TPB were used directly in the transformation of finite depth measurements into local deep water values. Figure A.4 shows a sample directional spectrum obtained from the array along with the corresponding deep water estimate. Limits to the range of deep ocean directions were imposed by practical limits to the total refraction grid. The limits were chosen to include all possible directions of wave approach considering the orientation of the coastline. The linear array directional spectra were normalized so that all of the band energy was contained in the directional range which corresponded to the deep water limits.

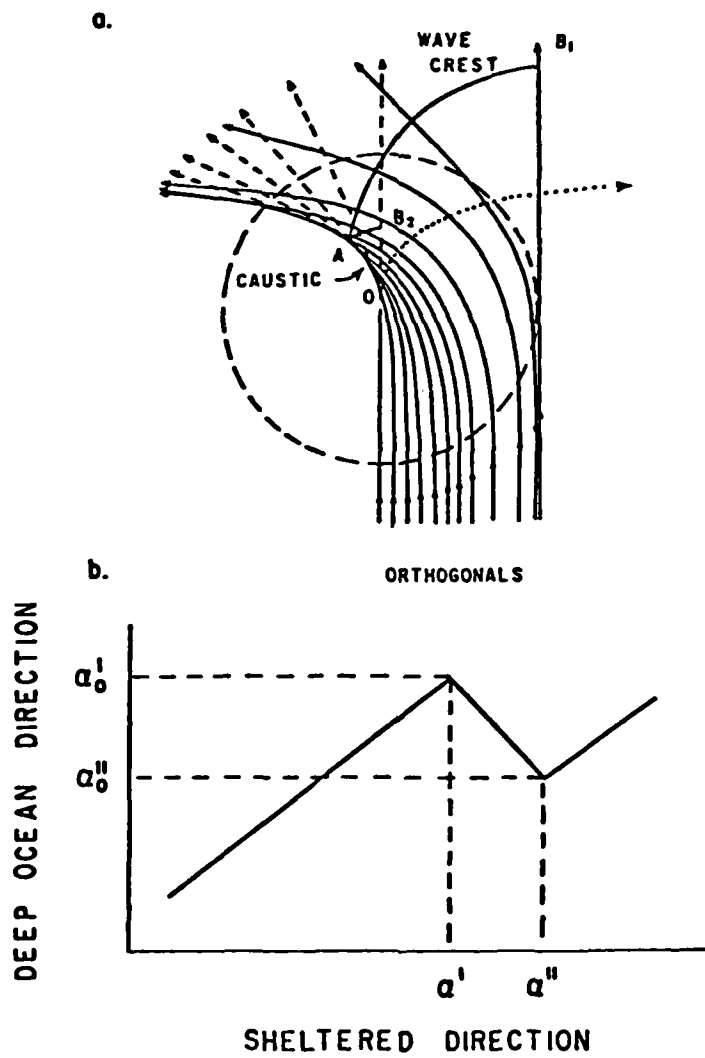
II.1.2 Other Wave-Bottom Interactions

There are several wave interactions with bottom topography which invalidate the energy density conservation along a ray, equation II.4. These include scattering, bottom friction effects, and the formation of caustics. These mechanisms were not integrated into the island transformation model. The possible consequences of this simplification are briefly discussed.

A caustic is an envelope of a family of rays (Figure 6a) and may be formed by wave refraction over spatially varying currents or bottom topography. Caustics cause a discontinuity in the slope of the relationship $\alpha = F(\alpha_{d0})$, see Figure 6b. Monochromatic ray theory gives an infinite solution for wave amplitude at a caustic. Large wave amplitudes can be associated with caustics, see e.g. Pierson (1951), but the infinite value given by ray theory is not physically realizable.

Ludwig (1966) solved for the wave field near a smooth caustic using an asymptotic expansion of the wave equations. Terms of the equations are grouped in powers of an appropriate small parameter and the wave amplitude and phase are allowed to slowly vary. No progressive wave components are allowed to propagate into the shadow side of the caustic. The resulting solution has an exponential decay in the shadow region and a finite maximum near the caustic in the illuminated region. The field in the illuminated region is composed of an incident and reflected progressive components which in the far field asymptotically approach the geometric ray solution. This is equivalent to the assumption that equation II.4 can be used for rays

Figure 6. a) Caustic generated by a circular shoal, from Arthur (1946).
The dashed rays have passed "through" (tangent to) the caustic line. Only the rays entering the right hand side of the shoal are shown. Another caustic line (dotted line) is generated by the left hand side rays. The structure of the caustic near the shoal center (0) is termed a cusped caustic.
b) Appearance of two caustics (at α' and α'') in a directional transformation map (equation II.5). Rays with sheltered directions $\alpha' < \alpha < \alpha''$ have passed through a caustic.



in the far field. However, as pointed out by Peregrine and Smith (1979), strong focusing of the wave field near a caustic may result in nonlinear interactions. These effects are of particular concern near a cusped caustic (Figure 6a), such as that set up by a circular shoal, where there are dramatic increases in the wave amplitude. Pierson (1951) demonstrated that the waves may even break near a caustic. These mechanisms would obviously invalidate the use of the linear conservation equation.

Numerous caustics were encountered in the island refraction model. There were no caustics generated by the local shelf topography. Figure 6b shows the effect of a hypothetical caustic on the angle transformations. Two caustics (at α' and α'') stem from a shoal in the island region which has typical dimensions of 2-10 km.

Ludwig (1968) worked from approximate relationships to investigate the focusing near convex (rays contained by an envelope that bends away from the illuminated region) caustics. His numerical examples show the caustic to be weak, no strong intensifications, if $a_c K > 4 \cdot 10^3$, where a_c is the caustic curvature. The ray equations were used to map a caustic line in the deep water region away from a circular shoal. For shoal radii in the range $R_0 = 2-10$ km and corresponding distances to the coast of $10-50 R_0$, $a_c K$ should have a minimum value of 10^7 . Therefore, it is very unlikely that any noticeable focusing will occur at the coast due to a caustic that stems from island topography.

Equation II.10 was used for the estimation of the coastal directional spectrum even in the neighborhood of caustics. This

method was used by Dorrestein (1966) and assumes that the singularities in $d\alpha_{tp}/d\alpha_{do}$ (equation II.9) are localized and integrable. However, the weighting of the spectrum in equation II.10 is not correct and may cause considerable error if there is significant curvature in the map $\alpha = F(\alpha_{do})$. The possible errors are a function of the smoothness of $E_{do}(\alpha_{do})$ over Δ_{do} (which is related to Δ_{tp} by the transformation curve). The expected errors due to the approximation ranged from 10-20%, for smooth caustics associated with a single shoal, to 200-300% for complicated refraction over multiple shoals. However, less than 1% of the total aperture is expected to have these large errors. The error analysis was performed assuming smooth-rounded functions for the structure of the caustic in the angle maps.

Another problem arises for geometric optics when waves propagate over strong depth variations that are on a horizontal scale which is comparable to the wavelength (or smaller). The assumptions associated with a slowly varying bottom are not valid when this occurs. The boundary conditions at sharp or step-like bottom features may only be satisfied with the addition of reflected and trapped waves that are not accounted for in slowly varying refraction analysis, see e.g. Newman (1965). Additionally, sharp lateral (orthogonal to wave direction) bottom changes will scatter wave energy into different directions, (Long, 1973).

The bathymetry of the shoals between Santa Rosa and San Nicolas Islands (northern quadrant window) is relatively smooth. Less than 10% of the cross-section to this topography contains features

which should scatter waves in the frequency range of interest. Most of the reefs indicated on the charts are very near to shore. However, approximately 25% of the aperture to Cortez and Tanner Banks does contain complex reef topography. Although the details (scales less than 0.5 km) are not shown on the available charts, it is assumed that some of this reef topography will scatter wave energy. Most of the reefs are in the depth range 20-40 m and therefore will not seriously affect higher frequency waves.

Dissipation due to bottom friction may also significantly alter the ray conservation equation. A substantial amount of theoretical, laboratory (see e.g. Putnam and Johnson, 1948), and field work (see e.g. Collins, 1972) has been devoted to this problem. Shemdin et al. (1978) used a nonlinear approach to analyze several data sets. Their results showed a quadratic friction coefficient, C_f , up to the size 0.01 for fine sand (the expected grain size in the island shoals and local shelves). However, coarse material can increase this coefficient up to 0.05 or more (Tunstall and Inman, 1975).

The decoupled dissipation model given by Collins (1972) was used for the crude approximation of the scale of bottom dissipation. This model takes the form

$$\frac{d}{ds} C_f^2 n E(f, \alpha) = \frac{-C_f g K E(f, \alpha) \langle |u| \rangle}{\sigma \cosh^2 Kh} \quad (\text{II.11})$$

where h is the local depth and $\langle |u| \rangle$ is the average magnitude of the currents. $\langle |u| \rangle$ is obtained from linear theory and integration over

the total spectrum.

Ray paths which cross the shallowest depths of the shoal topography were selected for the analysis. Table 1 shows the results for several shoals, frequency spectrum shapes, and assumed values of C_f . The dissipation result was a maximum for the lowest frequency waves. The results show that it takes large values of C_f or very large wave energy levels to make the dissipation effect greater than 10%. Most ray paths through the shoals will encounter much less integrated effect than these results. Therefore, the results of bottom friction were ignored for first order comparisons of the refraction model with the field data.

The combined effects of caustics, scattering, and bottom dissipation should be small relative to the general refraction process for broad banded deep ocean spectrum because of the limited cross-section of the shallow complex topography. However, much of the strong refraction, such as that responsible for the 0.059 Hz response to 345°T (Figure 3), is over the regions of complicated topography. The coastal energy predictions which involve strong refraction are therefore suspect. In these cases, the effects of these other mechanisms (which may involve wave breaking) could play a dominant role in the quantitative analysis of the energy received in the associated directional apertures. However, these processes should not alter the qualitative role of the shoal regions as diffuse sources of wave energy.

SHOAL

Spectrum	Frequency (Hz)	Tanner		San Nicolas Isl.		Cortez	
		$C_f = 0.01$	0.05	$C_f = 0.01$	0.05	$C_f = 0.01$	0.05
25 Mar 77	0.043	99.4	97.2	97.7	89.2	93.7	70.8
	0.074	99.6	98.0	98.4	92.2	94.0	72.1
	0.145	100.	100.	100.	100.	95.7	79.4
28 Mar 77	0.043	99.4	97.0	97.8	89.7	92.2	64.1
	0.074	99.6	97.5	98.4	92.4	92.5	65.5
	0.145	100.	100.	100.	100.	94.6	74.1
Rectangular	0.043	98.7	93.8	95.0	78.0	87.8	47.6
	0.074	99.1	95.5	96.4	83.8	88.3	49.8
	0.145	100.	100.	100.	97.8	92.0	62.0

Table 1. Evaluation of bottom dissipation effects for the integration of equation II.11 along ray paths through the various shoals. The values given are % coastal/deep ocean ray energy density. The path that crossed the minimum depth of each shoal was chosen for the analysis. The spectrum labeled "rectangular" has a constant energy density of $6.4 \cdot 10^4 \text{ cm}^2 \text{ sec}$ from 0.043-0.153 Hz (which yields a significant height of about 3.5 m). The 25 and 28 March spectra are averages of the sampled deep ocean spectrum for the experimental runs and both are shown in Figure 3.

II.1.3 Island Edge Diffraction

Wave diffraction occurs when a family of rays is intercepted by a boundary in such a way that the rays graze tangent to the boundary or strike an edge of the boundary, Keller (1978). Although geometric optics yields a total shadow region, this result is not a solution to Laplaces equation for wave motion. That is, the equations cannot support discontinuties in the velocity potential.

Penny and Price (1952) worked out the Sommerfeld solution for deep water gravity waves incident on a semi-infinite barrier. This solution was discussed in detail and experimentally verified by Putnam and Arthur (1948). Although the borderland islands generally are not steep walled (depth varying from zero to "deep" in lateral space scale on the order of wavelengths) for most wave frequencies, the general scale of the diffraction process and the qualitative features of the diffractive wave field can be investigated from these solutions. Arthur (1951) used the monochromatic soltions to dismiss diffraction as a possible first order mechanism in the spreading of wave energy into the island lee. However, a re-examination of the diffaction process with a continuous wave spectrum is warrented. In particular, the effects on the directional spectrum at the coastal locations are considered.

The importance of diffraction with a continuous wave spectrum can be viewed in terms of a bandwidth of offshore directions (which to refraction alone are sheltered) producing a significant response at a given site. Figure 7 shows this bandwidth as a function of spatial coordinates in the lee of a semi-infinite barrier. At large distances

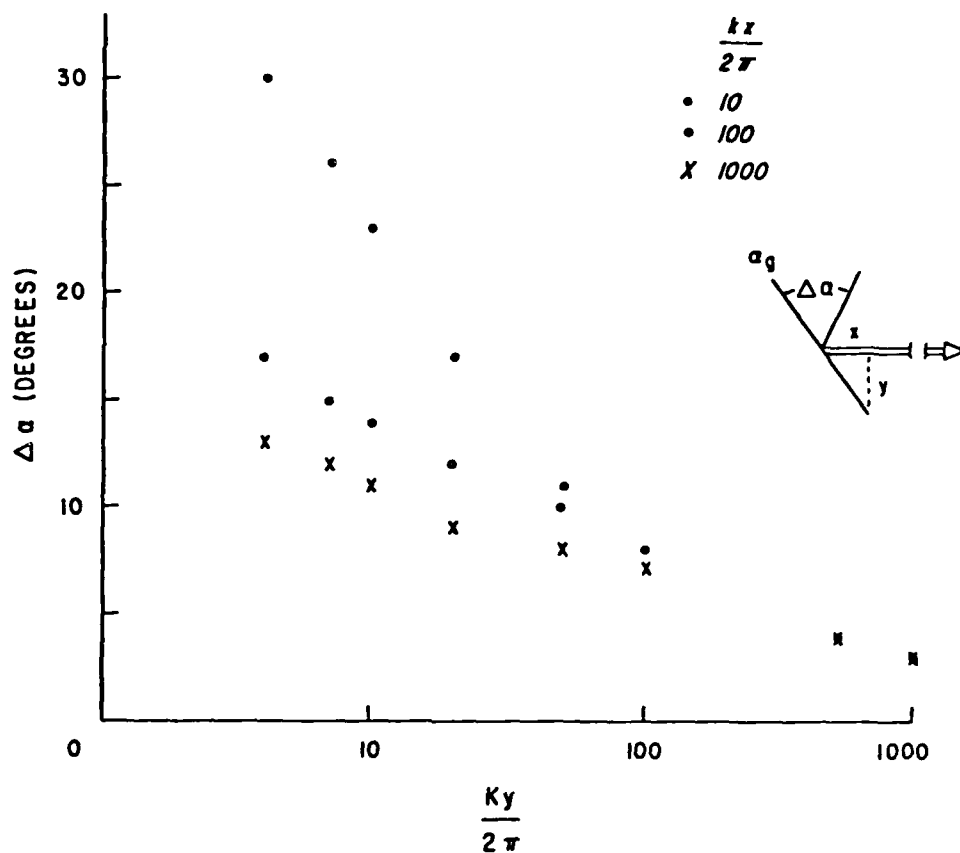


Figure 7. Directional bandwidth of significant diffractive wave energy as a function of position in the lee of a semi-infinite barrier. The spatial coordinates are defined in the insert. The bandwidth is defined as the spread in directions from grazing incidence, α_g in the insert, for which there is a significant response (greater than 10% of the unsheltered energy density) at the sheltered site.

from the barrier, the diffractive response is only significant for a very narrow range of directions.

A numerical analysis was performed for the physical setting of the sheltering of TPB by San Clemente Island and Santa Rosa Island (includes San Miguel, etc.). In each case, the width of the blocking island(s) is greater than 50 wavelengths (for the longest waves of interest) and therefore the semi-infinite approximation is valid. The results are listed in Table 2 and include comparisons to the energetic level of the refraction process. The absolute level of the diffractive wave energy increases with decreasing wave frequency, but the level relative to refracted energy trends in the opposite direction. The results show the diffracted energy to be 10-20% of the refracted energy for the lower frequency waves. In fact, the diffraction involved with the more distant (Santa Rosa) islands is less than 20% of the refraction level for all wave frequencies. The analysis for 0.145 Hz waves indicates diffraction may be relatively important for waves sheltered by SCI, but the portion of the deep ocean directional spectrum involved with this shadow ($265^{\circ}T-277^{\circ}T$) is small and relatively unimportant in the general wave climate (National Marine Consultants, 1960). Therefore, diffraction should be roughly negligible. The more complex problem of the combined effects of refraction and diffraction has to be addressed for a complete quantitative solution at the higher wave frequencies. It will be shown later, however, that local generation far outweighs the bottom interaction effects at these frequencies.

The directional distribution of diffractive wave energy at a

ISLAND

Frequency (Hz)	San Clemente Isl.	Santa Rosa (10°)	Santa Rosa (60°)
0.059	6.5 [15.2]	3.2 [24.2]	0.7 [12.0]
0.098	4.5 [17.8]	2.3 [20.2]	0.4 [18.3]
0.145	3.4 [47.2]	1.8 [14.8]	0.3 [14.3]

Table 2. Evaluation of diffractive effects around the two edges of San Clemente Island and around the southern edge of Santa Rosa Island. The values given are in % of deep ocean wave energy diffracted to Torrey Pines Beach. Also given in [] are the % normalized by the refractive wave energy for the same spectral conditions. Rectangular shaped directional distributions were used for the analysis. The limits of the deep ocean spectra were $265-275^{\circ}T$ for the SCI model, and $290-300^{\circ}T$ (10° spread) and $290-50^{\circ}T$ (60° spread) for the Santa Rosa model. These limits represent quadrants that are completely blocked by the island configuration. The narrow spectrum for the Santa Rosa model shows the response to north swell sources observed in this experiment while the wide spectrum shows the average values for the total exposure to the North Pacific.

sheltered location is concentrated in narrow bands around the direction to the edges of the barrier. The width of this directional band was in the range 0.5-1.0° for the numerical examples simulating the sheltering at TPB. The diffraction process does not produce waves which appear to be coming from directions interior to the angle grazing the island's edge. This result should not be altered by the consideration of the refraction process in the island vicinity.

II.1.4 San Clemente Island Shadow

Directions in the range 264.5-277.0°T project from TPB to the edges of or interior to SCI. Wave interactions with the island topography or associated shoals do not spread directional energy into this blocked quadrant. Actually, ray capture by the shoals at the island edges increases this 12.5° sector to 13° at 0.106 Hz and 14.7° at 0.059 Hz. The resulting prediction from the island refraction model has zero energy density in this sector (gap) of the local (deep water) directional spectrum.

There are several processes which can spread energy into this directional gap. These processes include wave-current interactions, wave-wave interactions, and wave generation by local wind. Additionally, wave scattering on the local shelf and reflection off the beach may spread energy into this quadrant (or opposing directions which are spacially aliased by an alongshore array). No attempt was made to quantitatively evaluate the relative strengths of these processes. The spatial current field or details of the wind field were generally not known for the period of this experiment. There is no theory for nonlinear wave evolutions in this region, which has

strong spatial inhomogeneities over interaction scales. Only a few arguments concerning these processes will be considered.

Arthur (1951) considered wave interactions with large scale currents, which include refraction and advection of wave energy. He concluded that the required current speeds (or shear) for a significant effect on long wind generated waves was so great (1-2 m/sec) that these processes would be generally negligible in the Southern California region. Although the theory for scattering off small scale currents is generally lacking, it is safe to assume that low current speed discontinuities produce only a second order effect.

The wind generation of waves in a limited fetch has been addressed by many investigators. Most of the previous work has been concerned with generation away from an infinite wall. The frequency spectrum in a limited fetch is approximated by the Jonswap spectrum (Hasselmann et al., 1973). σ_m , the frequency of maximum energy density, is obtained from the Kitaigorodskii (1962) similarity law

$$\sigma_m U_{10}/g = 3.5 (F_e g/U_{10}^2)^{-0.33} \quad (\text{II.12})$$

where U_{10} is the wind speed at 10 m and F_e is the fetch length. The nondimensional constants in this semi-empirical relationship were obtained from curve fits to field data.

The physical situation in the Southern California borderland does not resemble an idealized limited fetch. Only quadrants of the deep ocean directional spectrum are blocked by the islands. These quadrants taper with increasing distance east of the islands. Therefore, there is a significant background spectrum present which

may interact with the generation in the blocked sectors. Since the generation process is probably nonlinear, see e.g. Hasselmann et al.(1973), this case may differ markedly from the normal limited fetch.

II.2 Directional Spectrum Estimators

Results from the island refraction model indicate that complicated directional spectra are expected at the TPB site. High resolution-unbiased estimates of this directional structure are desired for the investigation of island shadows. Three estimators are employed in this study for the analysis of the directional spectrum. The Maximum Likelihood Estimator was chosen for the initial reduction of the data because it is an high resolution technique that has been widely used in the field. Also employed here is a modified form of this data adaptive technique. A third directional spectrum estimator considered is a minimum square window error technique. The latter two estimators were developed in this work.

A method designed for the accurate estimates of the moments of the directional spectrum is also developed in this section. This analysis technique is used in the later work concerned with momentum flux estimation.

II.2.1 Maximum Likelihood Estimator (MLE)

The MLE method was first applied to wavenumber spectrum estimation by Capon (1969) in an investigation of seismic waves. The method assumes that the measured time series is made up of a plane wave imbedded in noise. The methodology employed includes the

minimization of the estimate variance subject to the constraint that the amplitude of a pure plane wave (no noise) is estimated without bias. A complete treatment of one derivation of the estimator is given in Regier (1975). For a linear array, the MLE estimate takes the form

$$\hat{E}_0(\alpha) = D \left[\sum_{l=1}^N \sum_{m=1}^N x_{lm}^{-1} e^{iK x_{lm} \sin \alpha} \right]^{-1} \quad (\text{II.14})$$

where $\hat{E}_0(\alpha)$ is the directional spectrum estimate, x_{lm} is a component of the cross-spectral matrix, l and m are indices which refer to the sensors, x_{lm} are the lag spacings, and D is an adjustable constant required to obtain the correct integrated area under the curve.

The MLE method generally performs well with narrow unimodal sources. Examples given by Regier (1975), Pawka (1977), and review of the model testing described in Appendix B show that the MLE yields good estimates of the location and width of a narrow mode which is dominant in the spectrum. Regier (1975) encountered "over-resolution" problems with the MLE in response to broad directional spectra. However, relatively narrow directional distributions are expected because of the island windowing, distance to storms, and refraction over the shelf. Extensive model testing with bimodal spectra indicates no over-resolution problems for narrow forms (width $\leq 50^\circ$).

Deterministic and random model tests and field comparisons with the other estimators presented in this study show the MLE method is deficient in the estimation of certain quantitative features of bimodal spectra. In particular, the MLE results appear to bias low the estimate of S_{yx} and yield poor values for the ratio of energy

content of the two peaks. These results are detailed where applicable in the text and also in Appendix B.

II.2.2 Iterative Modifications to MLE

This method modifies the MLE directional spectrum estimates in an iterative fashion to yield a spectrum which is more consistent with the cross-spectral moments. Additionally, the modified estimate, IMLE, is a possible solution for the true directional spectrum. This is generally not true for the MLE estimate.

An estimate of the directional spectrum can be obtained from a linear combination of the measured cross-spectrum from a linear array (Davis and Regier, 1977)

$$\hat{E}(\alpha) = \sum_l \sum_m \beta_{lm}(\alpha) X_{lm} \quad (\text{II.15})$$

where β_{lm} are the complex weights for the array element pair l and m. The directional spectrum estimate is related to the true spectrum, $E(\alpha)$, by the convolution integral

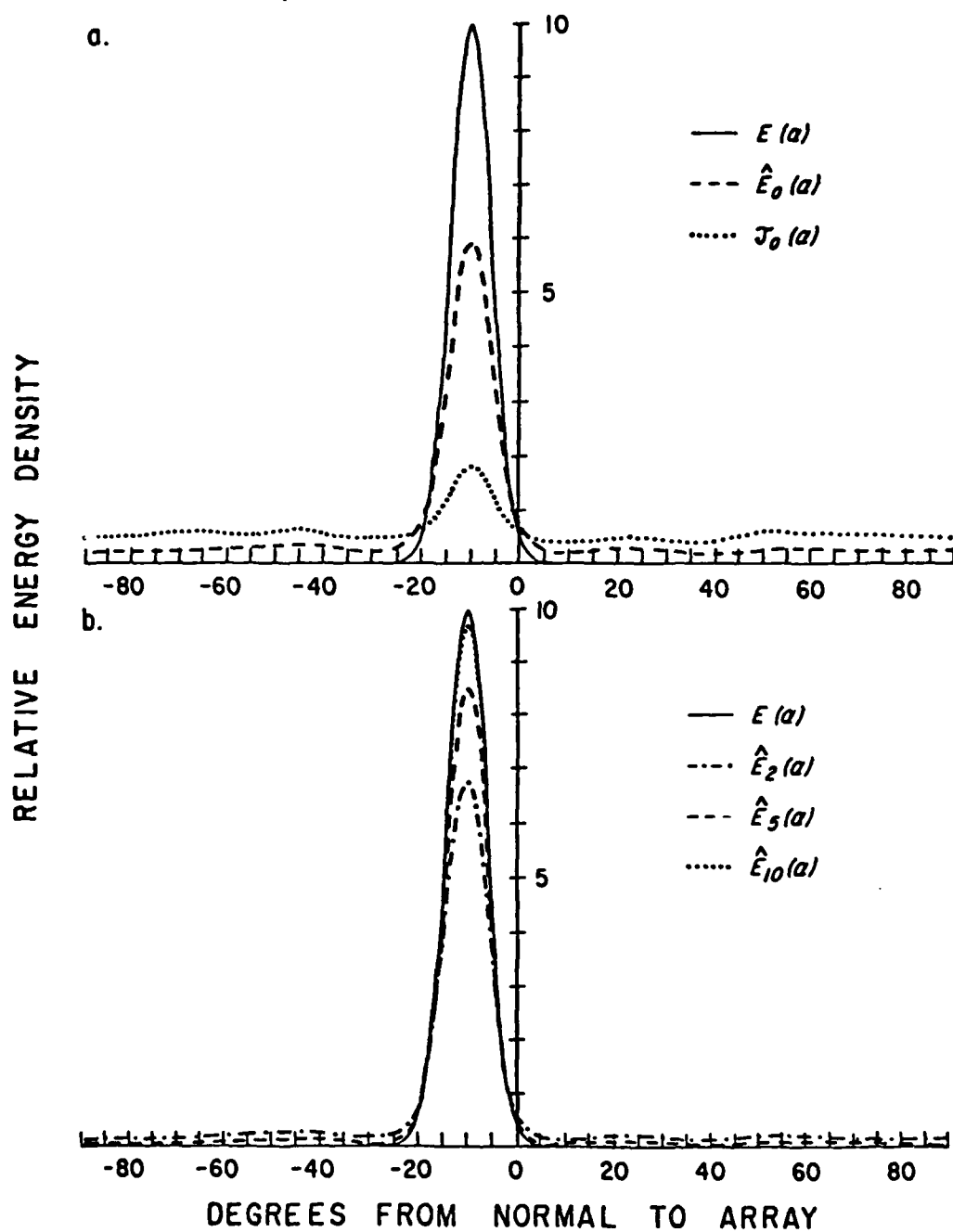
$$\hat{E}(\alpha) = \int_{\alpha'} W(\alpha, \alpha') E(\alpha') d\alpha' \quad (\text{II.16})$$

where $W(\alpha, \alpha')$ is the complex spectral window. The shape of the window is dependent on the weights chosen for equation II.15

$$W(\alpha, \alpha') = \sum_l \sum_m \beta_{lm}(\alpha) e^{iK x_{lm} \sin \alpha'} \quad (\text{II.17})$$

Figure 8a is a plot of a very narrow unimodal directional spectrum and the response of a 5 gage linear array using the MLE

Figure 8. Simulated response of the MLE method, $\hat{E}_0(\alpha)$, to a unimodal directional spectrum model, $E(\alpha)$, with the 1-2-4-5 array. Also shown is the simulated response, $F_0(\alpha)$, assuming a test directional spectrum equal to $\hat{E}_0(\alpha)$. b) IMLE modified directional spectrum estimates for the same test distribution. The estimates, $\hat{E}_i(\alpha)$ are for i iterations with a slow approach method ($\beta=1.0, \gamma=5.0$).



method. Although the directional estimate obtained from the array analysis is very well behaved in form, it is not well suited for the calculation of some spectral moments.

The fact that the MLE estimate shown in Figure 8a can not be the true spectrum can be demonstrated, even if the true spectrum is not known, by making the assumption that the estimate is the true spectrum and calculating the resulting response of the array. This response, $T_0(\alpha)$, is also plotted in Figure 8a and is seen to be even more smeared than the first estimate, $\hat{E}_0(\alpha)$.

The relationship between the spectral input to the array and the array's response can be thought of as a smoothing transformation and will be referred to by the operator \longrightarrow . The similarity of the transformations $E(\alpha) \longrightarrow \hat{E}_0(\alpha)$ and $\hat{E}_0(\alpha) \longrightarrow T_0(\alpha)$ suggests that the latter may be used to modify the original estimate, $\hat{E}_0(\alpha)$, to more closely resemble the true spectrum. A scheme is proposed to modify $\hat{E}_0(\alpha)$ in an iterative fashion to yield a spectrum which will transform to the original estimate. The general procedure is to modify the estimate upward for angles where $\hat{E}_0(\alpha) > T_0(\alpha)$ and vice-versa. The modified estimates take the form

$$\hat{E}_i(\alpha) = \hat{E}_{i-1} + \epsilon_i(\alpha) \quad (\text{II.18})$$

$$\epsilon_i(\alpha) = F \left[\hat{E}_0(\alpha)/T_{i-1}(\alpha), \hat{E}_{i-1}(\alpha) \right]$$

where F is a function to be specified later, $\epsilon_i(\alpha)$ is the modification on the i 'th iteration, $\hat{E}_0(\alpha)$ is the original MLE estimate, $\hat{E}_i(\alpha)$ is the i 'th ($i > 0$) iterative modified estimate and $\hat{E}_i(\alpha) \longrightarrow T_i(\alpha)$.

The spectral modifications are stepped forward until $T_i(\alpha)$ is sufficiently close to $\hat{E}_0(\alpha)$ for all α . To the approximation that $\hat{E}_i(\alpha) \rightarrow \hat{E}_0(\alpha)$, the modified estimate will be a possible solution for the true spectrum. Unfortunately, due to the convolution involved in the smoothing transformation, there are an infinite number of possible solutions for the true spectrum. Several functional forms for $\epsilon_i(\alpha)$ were tested including

$$\epsilon_i(\alpha) = \frac{|\lambda|^{\beta+1}}{\lambda} \frac{\hat{E}_{i-1}(\alpha)}{\gamma} \quad (\text{II.19})$$

$$\lambda = 1.0 - (T_{i-1}(\alpha)/\hat{E}_0(\alpha))$$

where several values were tried for β and γ . Although convergence rates varied significantly, the basic form of the solution spectrum was not found to be strongly dependent on the various parameters as long as $\epsilon_i(\alpha)$ is small relative to $\hat{E}_{i-1}(\alpha)$ for each iteration. A discussion of the various iterative approach paths and their "convergence" rates is included in Appendix C. A relatively slow approach method ($\beta=1.0, \gamma=5.0$) with 50 iterations was used for the data analysis in this experiment.

Figure 8b is a plot of successive IMLE modified spectra for 2, 5, and 10 iterations ($\beta=1.0, \gamma=5.0$) of the MLE estimate shown in Figure 8a. The IMLE estimates rapidly approach the true spectrum for this example. The normalized square error (NSE) of the estimates defined as

$$\text{NSE} = \frac{\sum_{\alpha} (\hat{E}_i(\alpha) - E(\alpha))^2}{\sum_{\alpha} E^2(\alpha)} \quad (\text{II.20})$$

drops from 0.153 for the MLE estimate to 0.0001 for $E_{10}(\alpha)$.

The basic directional data that is available from an array of sensors are the moments obtained from the cross-spectrum

$$\begin{aligned} C_{1m}(f) &= \int_{\alpha} E(f, \alpha) \cos(K x_{1m} \sin \alpha) d\alpha \\ Q_{1m}(f) &= \int_{\alpha} E(f, \alpha) \sin(K x_{1m} \sin \alpha) d\alpha \end{aligned} \quad (\text{II.21})$$

where $C_{1m}(f)$ is the co-spectrum and $Q_{1m}(f)$ is the quad-spectrum obtained from the sensor pair 1 and m. Estimates of $C_{1m}(f)$ and $Q_{1m}(f)$ ($\hat{C}_{1m}(f), \hat{Q}_{1m}(f)$) can be made with the integration of the estimated directional spectrum. The squared deviation (XSD) of the estimated cross-spectrum from the true (measured) values can be calculated for any of the directional spectrum estimates

$$XSD = \sum_1 \sum_m (\hat{C}_{1m}(f) - C_{1m}(f))^2 + (\hat{Q}_{1m}(f) - Q_{1m}(f))^2 \quad (\text{II.22})$$

Thus, it is always possible to insure that the IMLE estimates are increasingly consistent with the measured cross-spectrum with added iteration. Analysis of both simulated and field data has demonstrated that for the approach methods employed here there is generally a decrease in XSD with iteration, see Appendix C. No analytic relationship between the IMLE estimate and the true spectrum has been developed. This is also true for the MLE method. Therefore, the MLE and IMLE methods have been subjected to an extensive set of deterministic and random simulation tests to observe their behavior as a function of the characteristics of the true directional spectrum. The testing procedures and results are discussed in detail in Appendix

B. A total of 960 unimodal and 800 bimodal spectral shapes were tested for the deterministic response of the two methods. The values of NSE, equation II.20, were used as a general basis of comparison. The IMLE method improved the performance of the IMLE in all but 3.5% of the unimodal cases and 0.1% of the bimodal cases. The MLE method had better relative performance only with very narrow sources imbedded in very low background spectral levels. The improvement afforded by the modifications was particularly dramatic with broader directional forms and at higher wave frequency.

The relative performance of the estimators in the calculation of $S_{yx}(f)$ was also considered. The IMLE method consistently outperformed the MLE across the test space of variable wave frequency and spectral shape. The average magnitude of $S_{yx}(f)$ estimation error for the IMLE and MLE methods with the unimodal test spectra was 2.4% and 34.4% respectively. The values for the bimodal testing were 4.2% for the IMLE and 44.7% for the MLE. Also, the MLE estimates of $S_{yx}(f)$ were biased low in 98% of the test cases (100% of the unimodal). There was no consistent bias in the IMLE estimates.

The estimators were also tested in response to random cross-spectra with several different forms of base directional spectra. The results showed stability problems with both methods at low numbers of ensembles averaged ($n_e < 6$). The stability problems were greatest with the IMLE estimates. Stability of the IMLE spectral estimates requires roughly 6-10 ensembles averaged depending on the form of the base spectrum. The good relative performance of the IMLE method in the resolution of the true spectrum and estimation of $S_{yx}(f)$ is preserved

when the data is sufficiently averaged.

One spectral problem of the IMLE method evidenced by the model testing was over-resolution of spectral peaks. This problem is particularly severe when the dominant peak is surrounded by an extremely low background spectral level. However, this condition was evidenced in less than 10% of the total test cases. Also, the existence of the over-resolved peaks does not degrade the relative improvement offered in the estimation of low order spectral moments, see Appendix C.

The over-resolution problems of the IMLE method limit its application in the investigation of energy sources in the local directional spectrum. Care must be taken to compare the IMLE results with the other spectrum estimates. Also, it is important that the MLE estimate be a good first guess for the successful operation of the IMLE. However, it is concluded that for some applications, treated in the text, the IMLE method presents a useful representation of the directional spectrum.

II.2.3 Minimum Square Window Error (MSWE) Estimates

The analysis from the previous section showed the MLE method to be a relatively poor estimator, particularly when dealing with bimodal spectral forms. The lack of theoretical justification of the IMLE method creates uncertainty about its use in the quantification of spectral properties. Therefore, another estimator, with a more concise mathematical derivation, was developed for use in this experiment. The derivation of this estimator closely follows the general design and mechanics used for the Steered Appriori Optimal

Estimator by Regier (1975). A comprehensive treatment of the methodology of spectral estimation is given by Davis and Regier (1977).

The basic design of the estimator is in the minimization of the square window error, SWE, at estimate angle α .

$$\text{SWE}(\alpha) = \int_{\alpha'} |W(\alpha, \alpha')|^2 G(\alpha') E(\alpha') d\alpha' \quad (\text{II.23})$$

where $G(\alpha')=0.0$ for $|\alpha-\alpha'| < \Delta\alpha/2$ and 1.0 otherwise. The form of this function is somewhat arbitrary. $\Delta\alpha=1^\circ$ was used in the analysis but values ranging from 0-3° did not significantly alter the results. The minimization of $\text{SWE}(\alpha)$ is done subject to a constraint that the window values must be relatively large near $\alpha'=\alpha$. Regier (1975) discusses integral forms of this constraint. However, the condition that $W(\alpha, \alpha'=\alpha) = 1.0$ is sufficient with the anticipated narrow spectral forms. This constraint is imposed through the use of a Lagrange multiplier.

The window can be expressed in the form

$$\begin{aligned} W(\alpha, \alpha') &= \sum_l \sum_m a_{lm}(\alpha) e^{ikx_{lm}(\sin\alpha' - \sin\alpha)} \\ &= \sum_l \sum_m h_{lm}(\alpha, \alpha') e^{ikx_{lm}(\sin\alpha')} \end{aligned} \quad (\text{II.24})$$

and the function I to be minimized with respect to the $a_{lm}(\alpha)$ s is

$$I = \sum_{\alpha'} E(\alpha') |W(\alpha, \alpha')|^2 + \mu (1.0 - W(\alpha, \alpha'=\alpha)) \quad (\text{II.25})$$

where μ is a Lagrange multiplier. It was observed that the solution

for the coefficients was not necessarily stable with this form of I. The estimate variance is proportional to $\sum_m \sum_\alpha a_{1m}^2(\alpha)$. Therefore, the term $v \sum_m \sum_\alpha a_{1m}^2(\alpha)$ (following Davis and Regier, 1977), was added to the function. Differentiation yields

$$\frac{\partial I}{\partial a_{1m}} = 0 = \sum_j \sum_k a_{jk}^*(\alpha) \sum_\alpha h_{1m}(\alpha, \alpha') h_{jk}^*(\alpha, \alpha') E(\alpha') + v a_{1m}^*(\alpha) - \mu h_{1m}(\alpha, \alpha') \quad (\text{II.26})$$

where * is the complex conjugate and v is adjusted to reject noise. This set of equations can be expressed in the matrix form

$$\underline{B} \cdot \underline{A} = \underline{C} \quad (\text{II.27})$$

where A and C are N^2 (N =number of sensors) column vectors with elements $A_{(1m)} = a_{1m}(\alpha)$, $C_{(1m)} = h_{1m}(\alpha, \alpha')$, $(1m)$ has the value $1+(N-1)m$, and B is the N^2 by N^2 matrix with elements

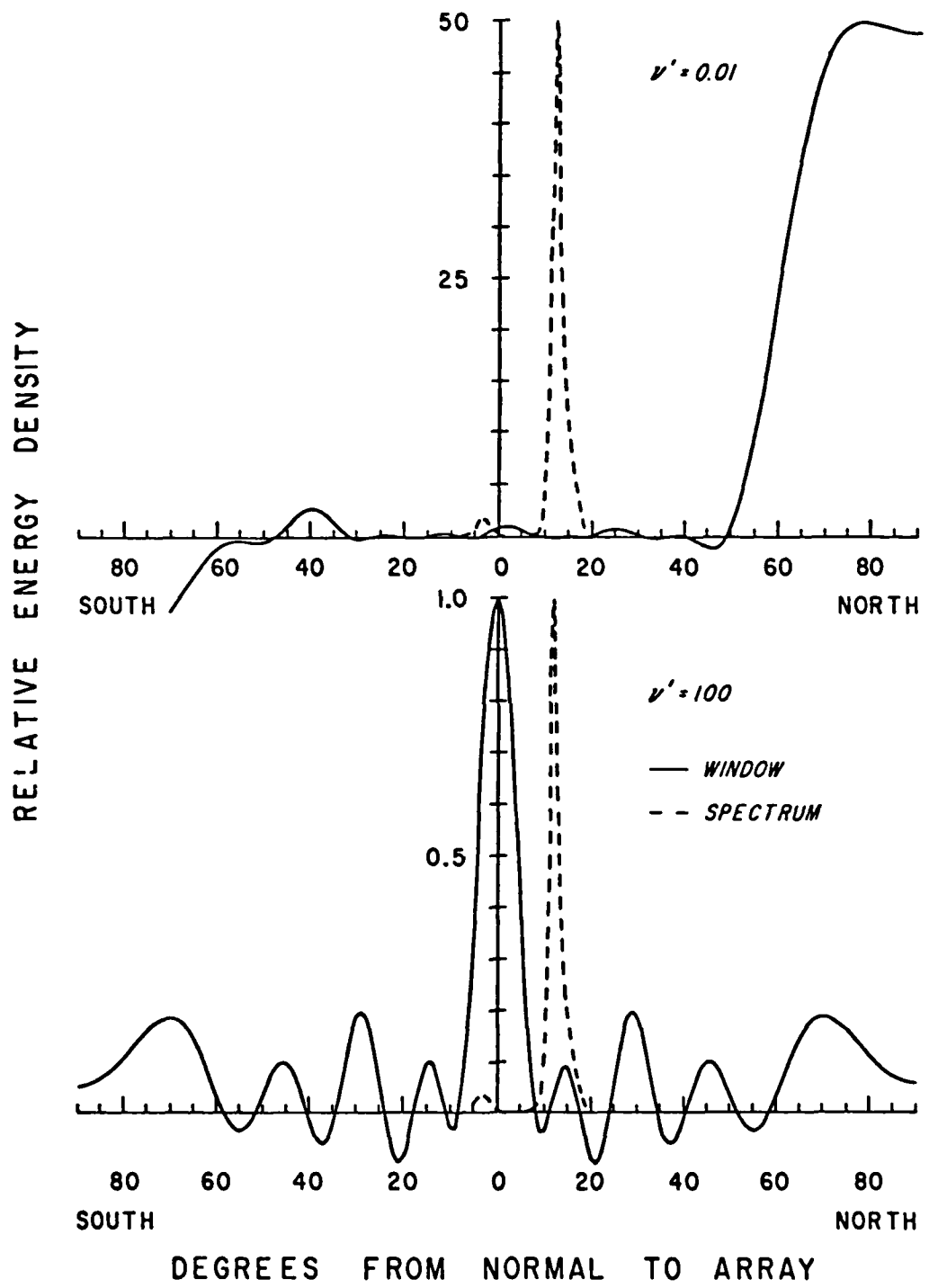
$$B_{(1m)(jk)} = \sum_\alpha h_{1m}(\alpha, \alpha') h_{jk}^*(\alpha, \alpha') E(\alpha') + \delta(1m, jk)v \quad (\text{II.28})$$

where $\delta(1m, jk)=1.0$ if $(1m)=(jk)$ and 0.0 otherwise

The coefficients must satisfy the condition $a_{1m}(\alpha) = -a_{m1}^*(\alpha)$ to insure real valued spectrum estimates. Also, the coefficients $a_{11}(\alpha), 1=(1, N)$, may be set equal with no loss of generality. These conditions reduce the order of the equivalent real valued matrix to be inverted to the size $2N_1+1$ where N_1 =the number of non-redundant lags.

Values of the parameter v represent a tradeoff in estimator resolution and noise sensitivity. Figure 9 shows the windows associated with the estimate at a direction located between two narrow

Figure 9. Spectral windows for the zero angle directional spectrum estimate with the MSWE method. v is a normalized noise rejection term (equation II.26) where $v' = v(\sum_{\alpha} E(\alpha) \Delta \alpha)^{-1}$. The windows are constrained to equal 1.0 at $\alpha=0.0$.



peaks. The window calculated with values of $v=0.01\sum_{\alpha}E(\alpha)\Delta\alpha$ shows high resolution and roughly complete rejection of the assumed spectral energy. However, the very large lobes at high angles make the estimate sensitive to even low noise levels. The result with large v ($v=100\cdot\sum_{\alpha}E(\alpha)\Delta\alpha$) is also shown. All of the coefficients converge to the same constant (not a function of the assumed spectrum) value for this condition. The resultant window is close in form to the one suggested by Barber (1963)

$$W(\alpha, \alpha') = (2N_1+1)^{-1} \left[1 + 2 \sum_{m=1}^{N_1} \cos(K x_m (\sin\alpha' - \sin\alpha)) \right] \quad (\text{II.29})$$

where x_m is the separation of the lag denoted by m . This window has fairly low side lobes but a broad central peak.

The variance of the spectral estimates reduced from field data was calculated as a function of trial values of v . The cross-spectra were averaged over 8 ensembles. These results showed a rapid decrease in estimate variance with increasing v for low values of v . The trend flattened out in the vicinity of $v=0.02\sum_{\alpha}E(\alpha)\Delta\alpha$. This value of v was used in the routine data analysis. The subject of the relative variance of the various spectrum estimators is further detailed in the discussion of the experimental results.

Another judgement which enters the estimator design is the representative form chosen for $E(\alpha)$. There is an expected gap in the directional spectrum due to the presence of SCI. It is desired that the estimator make high resolution, low bias estimates of the wave energy density in this spectral regions. Equations II.26 were solved with the use of MLE and IMLE estimates as representations of the true

spectrum. Also used were the MLE spectra with an artificial gap imposed in the directions associated with SCI. There was no substantial difference between the results of the method with these various assumed forms of $E(\alpha)$. The MLE estimates were routinely used as $E(\alpha)$ in equation II.26 for the data analysis.

The simulated deterministic response of the MLE and MSWE methods to a typical bimodal form is shown in Figure 10. The MSWE estimates show an excellent representation of the energy density in the gap between the peaks. Figure 11 is a plot of the average directional spectra obtained from the MLE, IMLE, and MSWE methods for 0.082 Hz waves on 5 March 1977. Although the spectra are similar in form, the gap energy density level varies significantly. The MSWE method shows the sharpest resolution of the peaks. The MLE and IMLE estimates are necessarily positive for all angles while the MSWE estimates can take on negative values. The intercomparison of the methods is discussed in detail later.

II.2.4 Estimation of Spectral Moments

An estimate of an arbitrary moment of the directional spectrum is

$$\hat{M} = \int_{\alpha} \hat{E}(\alpha) M(\alpha) d\alpha \quad (\text{II.30})$$

where $M(\alpha)$ is the desired weighting function. As discussed previously, the smearing inherent in $\hat{E}(\alpha)$ may cause this integration technique to be a poor estimator of some moments. The smearing of equation II.16 may be represented

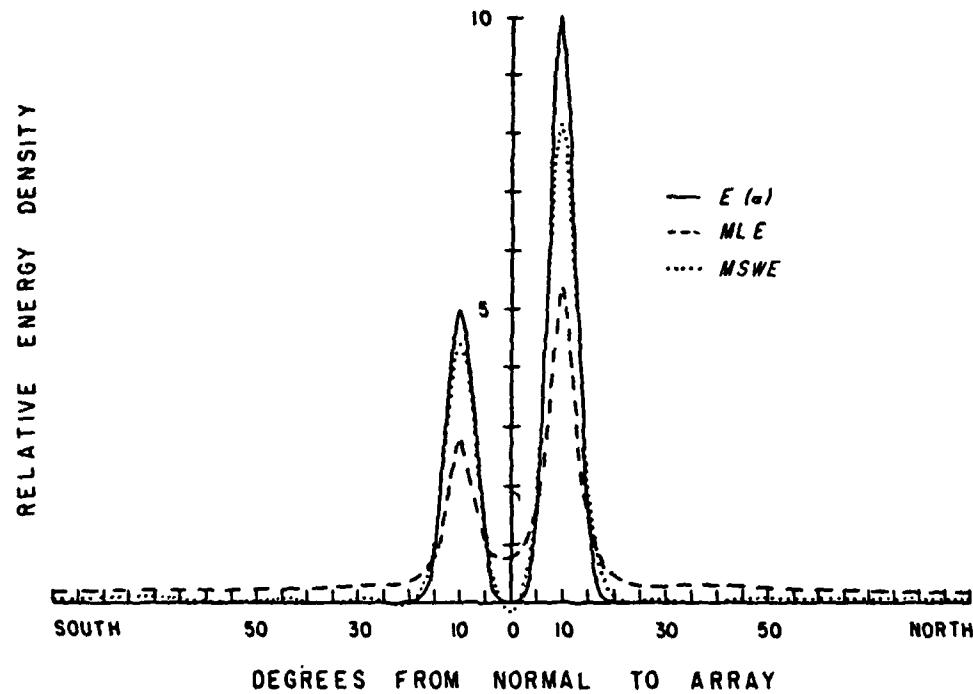


Figure 10. Response of the MLE and MSWE ($v = 0.02 \sum_{\alpha} E(\alpha) \Delta \alpha$) methods to a strongly bimodal deterministic test spectrum, $E(\alpha)$. The analysis is for the 1-2-4-5 array. The curves are normalized to the same integrated area.

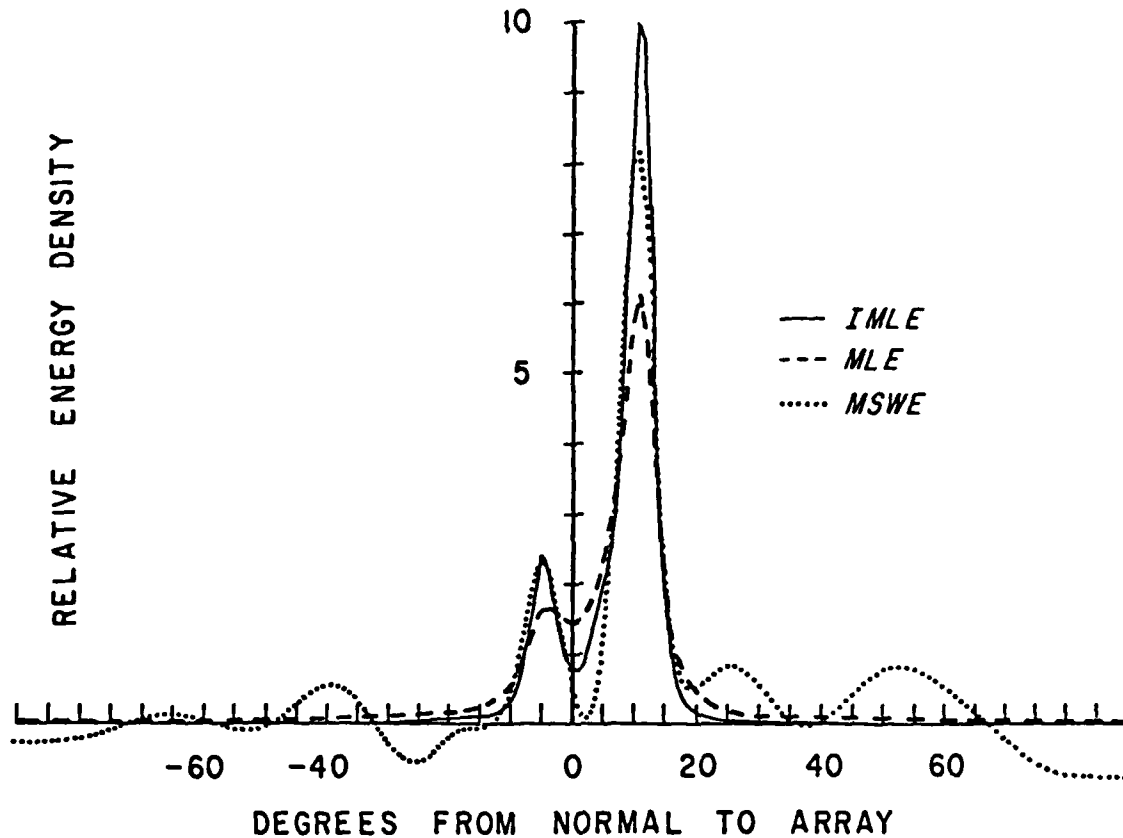


Figure 11. Various estimates of the directional spectrum for 0.082 Hz waves on 5 March 1977. The spectra were averaged over 50 consecutive 17.1 minute data runs. The 1-2-4-5 array, located in a mean depth of 9.6 m, was used for the analysis. The MSWE estimates were calculated with a value of $v = 0.02 \sum_{\alpha} \hat{E}(\alpha) \Delta \alpha$ (equation II.26).

$$\hat{M} = \int_{\alpha'} E(\alpha') W(\alpha') d\alpha' \quad (\text{II.31})$$

where the coefficients β_{1m} are now constants over the look angle α .

It was suggested by R.E. Davis (personal communication) that $W(\alpha')$ be shaped, by manipulation of the coefficients to resemble the function $\sin\alpha' \cos\alpha'$ for the estimation of S_{yx} . In general, any moment can be estimated by shaping $W(\alpha')$. With a limited number of sensors it may be difficult to accurately shape $W(\alpha')$ for all angles. However, it is only necessary to make the window approximate the function $\sin\alpha' \cos\alpha'$ for angles where the spectrum is relatively large. Therefore, the shaping of the window requires the minimization of the parameter

$$I = \sum_{\alpha'} (W(\alpha') - \frac{1}{2} \sin 2\alpha')^2 E(\alpha') \quad (\text{II.32})$$

The MLE estimate of the directional spectrum should be of sufficient quality to provide the weighting function in equation II.32. The problem is then reduced to solution by the method of least squares.

The mechanics of the solution to this problem are identical to those used in the development of the MSWE method. Again, a term must be added to reject noise. The system of equations analogous to those in equation II.26 take the form

$$\frac{\partial I}{\partial a_{1m}} = 0 = \sum_j \sum_k a_{jk}^* \sum_{\alpha'} h_{1m}^*(\alpha') h_{jk}^*(\alpha') E(\alpha') + v a_{1m}^* \quad (\text{II.33})$$

$$- \frac{1}{2} \sin 2\alpha' E(\alpha') h_{1m}^*(\alpha')$$

The matrix reduction of this set of equations follows that outlined

for the MSWE method. The solution is referred to as the moment estimator, ME_v , where the parameter v is a variable of the estimator design.

The performance of the $ME_v (v=0.0)$ method in the estimation of S_{yx} was tested in response to several deterministic directional spectrum forms. A 1-2-4-5 configuration linear array (unit lag=33.0m) was used in the test analysis. This is the linear array configuration used in the West Coast Experiment. The results, shown in Figure 12, are excellent for wave frequencies 0.05-0.13 Hz. The performance of the ME_v method drops off at 0.13 Hz for the broad test spectrum. The high frequency estimates are the most accurate in response to the narrow directional forms and fall off only with the onset of spatial aliasing.

The various estimators were subjected to simulated random cross-spectra. As anticipated, the ME_0 estimates were relatively noise sensitive. The values of v_n are normalized by the spectrum

$$v_n = 10 v \left(\sum_{\alpha} E(\alpha) \Delta \alpha \right)^{-1} \quad (II.34)$$

to compare the results with different spectral forms. Table 3 shows the bias and variance of the ME_v estimates as a function of v_n . This analysis was done with a relatively noise sensitive 2-2-2-5 array (due to side lobe problems) which was used for some of the momentum flux comparison experiments. The results are shown to be frequency dependent. A drop in variance occurs with values of v_n between 0.01-0.05. The location of this jump varies as a function of directional spectrum form and frequency. The estimator bias also varies but

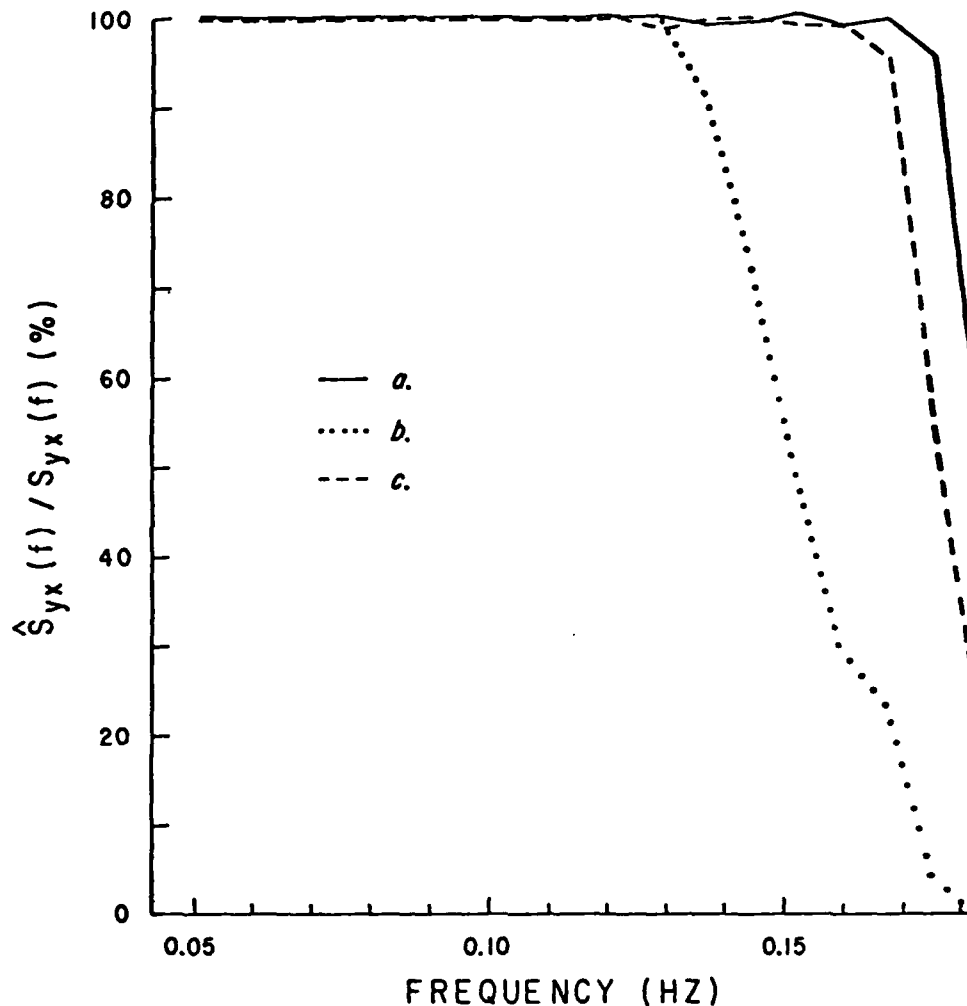


Figure 12. Estimate/model ratios for $S_{yx}(f)$ obtained from the ME_0 method in response to deterministic test spectra. The 1-2-4-5 array of length 400 m was used for the analysis. The curves are for the distributions: a) narrow, $\cos^{200}(\alpha+20^\circ)$, b) broad, $\cos^4(\alpha+20^\circ)$, c) bimodal, $\cos^{200}(\alpha+10^\circ) + 2.0 \cos^{200}(\alpha-10^\circ)$.

	Frequency (Hz)	v=0.0	0.1	0.5	1.0	MLE	IMLE	ME _v
$\hat{S}_{yx}(f)/S_{yx}(f) \text{ (%)}$	0.067	96.3	95.4	92.7	91.3	56.4	100.9	ME _v
	0.098	107.8	105.5	98.6	91.7	50.5	92.9	
σ_n	0.067	0.68	0.60	0.58	0.58	0.41	0.67	ME _v
	0.098	0.82	0.79	0.70	0.62	0.27	0.54	

Table 3. Bias and standard deviation of the $S_{yx}(f)$ estimators in response to numerically simulated random cross-spectra. The analysis was performed with a 2-2-2-5 array configuration (unit lag = 33 m). This array was used in the Nov. 1978 NSTS experiment. The bias is given as the ratio of the mean estimate value, $\hat{S}_{yx}(f)$, to the true value, $S_{yx}(f)$. σ_n is the standard deviation of the estimates normalized by the true value. A set of 50 cross-spectra were averaged over 8 ensembles each with a model directional spectrum of the form: $\cos^{500}(\alpha-10^\circ) + 2.0 \cos^{500}(\alpha+10^\circ)$.

remains in the 10% range for the tested values of v_n . These expected errors compare well with the tested accuracy of the IMLE estimates. The MLE estimates of S_{yx} are biased low in magnitude. The ME_v estimates at 0.098 Hz are biased high at low values of v_n . The bias drops with increasing values of v_n . This effect is seen in the comparative field data. The problem of determining the design values of v_n is further discussed in Section V.

III EXPERIMENTAL SETUP

The measurements applicable to the island sheltering study were made in March 1977 during the Seasat West Coast Experiment. Widespread coverage of the wave field in the borderland region was obtained through the use of both in-situ and remote sensors. Crucial to the success of the experiment were accurate measurements of the frequency and directional spectra in the unsheltered region west of the islands and in several coastal locations. The deep ocean and coastal measurements were necessary to test the validity of the wave transformations obtained from the island refraction model. "Point" measurements of $E(f)$ were sampled along the coast to test the directionally integrated effects of blocking and refraction. The coastal directional measurements allowed detailed comparisons with the directional structure of the model predictions.

The West Coast Experiment was a multi-organizational effort which had many research goals. These goals included the investigation of surf zone dynamics, wind stress on the sea surface, and the ground truth verification of the Seasat I remote sensors. A discussion of these scientific investigations and a list of the associated research organizations are included in Shemdin (1980). Only the measurements used in the present study will be discussed here.

III.1 In-situ Measurement of the Frequency Spectrum

Surface (or subsurface) measurements of the wave frequency spectrum were made using pressure sensors, Datawell Waveriders, and a Baylor gage. All of these instruments have been widely used in the

field for wave height measurement. This variety of sensors provided for accurate measurements in the relatively shallow coastal waters and the deep water locations near the borderland islands. The locations and local water depth of all the surface stations are indicated in Table 4. All of the frequency spectra were smoothed to yield a resolution of 0.0078 Hz. Varying lengths of data runs from different stations caused differences in the confidence limits of the associated spectra.

Bottom mounted pressure sensors were used to sample the wave field at the coastal sites. The pressure gages were in depths varying from 7-10 meters. It was necessary to account for local refraction, described in Section II, to convert the shallow water measurements into local deep water estimates. The coastal sites employed all have relatively smooth bottom topography.

The Oceanside and Imperial Beach (IB) sites are part of the California Coastal Data Collection Program. The Nearshore Research Group (NRG) at SIO designed and maintains this network of coastal wave stations. The description of the data network and the sensors employed is included in Seymour et al. (1977). These stations were sampled consecutively for data runs of 17.1 minute duration. The normal sampling frequency of two runs per day was increased to about 6-10 during the days of overflights. The raw data was reduced by NRG. The station at Oceanside was the most sheltered from Northern Hemisphere swell, but is completely exposed to southern swell. The Coronado Islands, which lie southeast of San Diego, partially block the southern quadrant at IB. No attempt was made to model the wave

SITE	LATITUDE (°)	LONGITUDE (°)	DEPTH (m)
Begg Rock	33.48	119.67	110
Tanner Bank	32.67	119.13	61
San Clemente Island	33.17	118.05	650
Oceanside	33.19	117.39	7.4
Torrey Pines Beach	32.90	117.26	9.6
Imperial Beach	32.58	117.15	9.3

Table 4. Physical coordinates and mean depth for the surface sites in the West Coast Experiment.

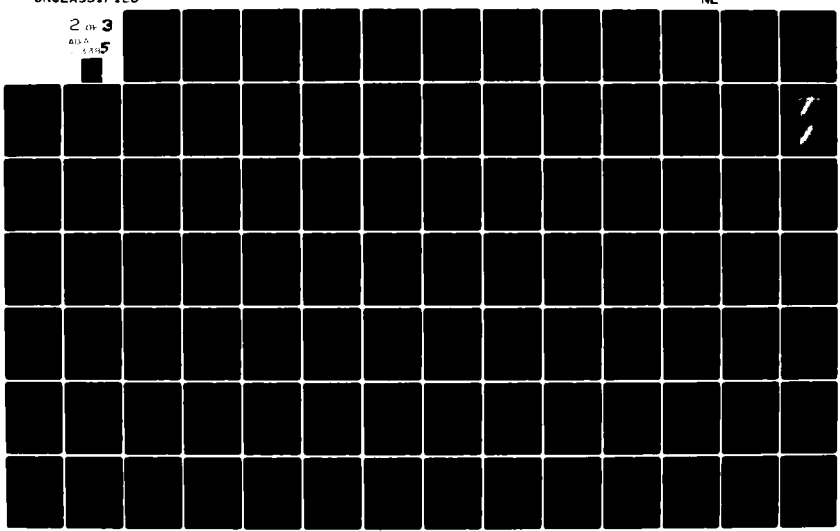
AD-A113 385 SCRIPPS INSTITUTION OF OCEANOGRAPHY LA JOLLA CA SHOR--ETC F/6 8/3
WAVE DIRECTIONAL CHARACTERISTICS ON A PARTIALLY SHELTERED COAST--ETC(U)
1982 S S PAWKA N00014-75-C-0300

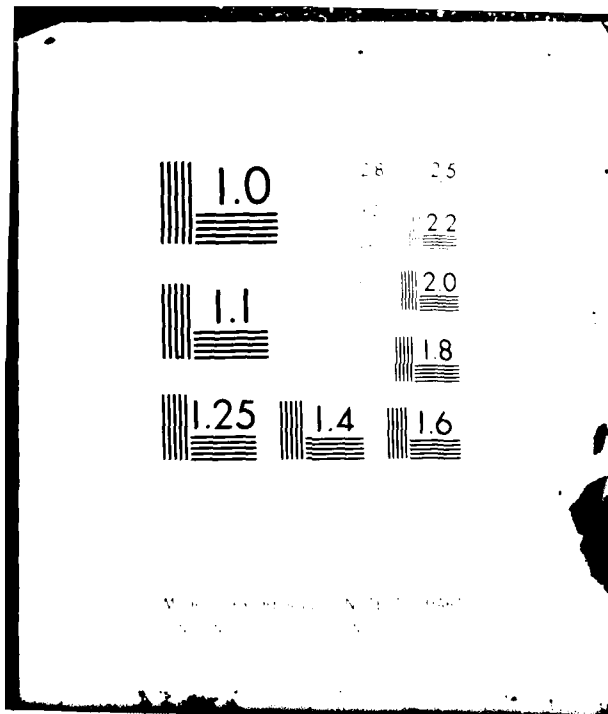
UNCLASSIFIED

2 on 3

03.5

5





propagation around these islands. Since there was significant south swell during the intensive sampling days, the station at IB was not of general use in the data comparisons. There were no in-situ directional measurements at Oceanside or IB. Therefore, the predicted local directional spectrum obtained from the island refraction model was used for the calculation of local shelf refraction effects at these sites.

A linear array of pressure sensors was used for the frequency spectral measurements at TPB. The details of the data aquisition and recording systems and the sensor specifications are given in Pawka et al. (1976). The TPB estimates of the local deep water frequency spectrum are considered the most reliable of the coastal sites because of the high resolution directional spectra available from the array which were used in the local shelf refraction calculations. Data were sampled continuously for roughly 6-8 hours each day and processed in consecutive 34.1 minute segments.

Two Datawell Waveriders were used for the measurement of the wave frequency spectrum in the island vicinity. These buoy systems have been used extensively in the field for wave height measurement and several comparative studies show them to yield unbiased spectral estimates in the frequency range of interest in this experiment (Blair, 1974).

One waverider was moored in a position approximately 24 km northwest of San Nicolas Island (near Begg Rock) in a depth of 110 m. The bottom topography in this area is a relatively smooth portion of a broad submarine ridge which extends northwest from San Nicolas Island.

This site is fully exposed to deep ocean waves with directions 180-320°T. Therefore, the Begg Rock buoy measurements represent a relatively unsheltered sample of the deep ocean wave intensity. The Pacific Missile Test Center maintained this buoy, collected the data, and performed the spectral analysis. Twenty minute data runs were sampled each day at 0100 and 1130 PST.

JPL maintained a waverider roughly 10 km northwest of SCI. The local depth near this site is in the range 600-700 m. This site is partially sheltered by the borderland islands and is approximately midway between Begg Rock and the coastal stations. Data from the buoy were sampled continuously by SPL during periods of intense experimental activity. The data were then processed in segments of 34.1 minutes length.

A Baylor gage was operated by the Shell Development Company on a drilling platform located over Tanner Bank. This site has roughly the same deep ocean exposure as the Begg Rock waverider site. The details of the data analysis, which include the subtraction of the platform motion out of the wave height signal, are discussed by Forristall et al. (1979). The platform was in a mean water depth of 61 m. A fairly complex system of reefs, with depths in the range 75-100 m, lie west of the platform site. Thus, there are significant refraction effects expected for waves with frequencies less than about 0.08 Hz. No attempt was made to perform the detailed analysis necessary to account for these effects.

III.2 In-Situ Directional Measurements

High resolution estimates of the directional spectrum at the coast are necessary to confirm the details of the island refraction model. The primary system for the coastal directional wave measurements was a linear array of 5 pressure sensors at TPB. The site at TPB was selected because of its proximity to SIO, plane bottom contours, lack of offshore reefs or kelp, and narrow shelf.

The site at TPB has relatively plane topography, as shown in Figure 13. A numerical evaluation of the refraction effects indicates a maximum variation of wave angle (for unidirectional waves) of approximately 2° over the space of the array. A sensor array with three redundant 66 m lags was operated at this site during the NSTS experiment of Nov. 1978, see Section V. Comparisons of the average phase angles of these lags support the conclusion of a nearly homogenous directional wave field.

There are numerous factors involved in the design of directional wave arrays. The factors which had some degree of flexibility in this experiment were the depth of the sensors, the sensor spacings, and the array length. The number of sensors was set by practical limits, as was the depth of the sensors off the bottom. The sensors were mounted roughly 20 cm off the bed. The maximum length of an array, with minimum spacings, is attained with a linear array. In order to sample a homogeneous wave field, it is desired to orient the linear array along a straight bottom contour. The direction normal to the array alignment was $264.5^{\circ}T$. The depths of the sensors were all within a range of 60 cm. There is a 180° ambiguity associated with a linear array but the coastline was judged

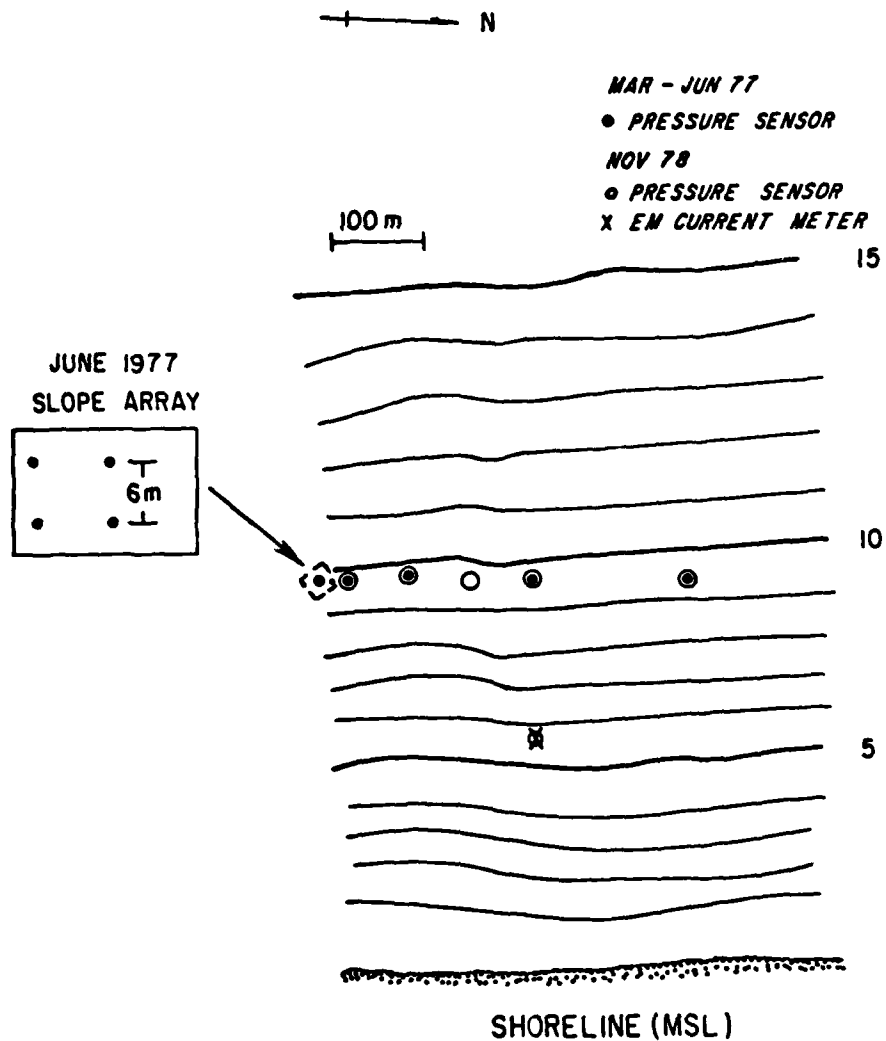


Figure 13. Local bathymetry of Torrey Pines Beach and sensor locations for the two experiments. The contours were sampled in November 1978 and reported in Gable (1980).

effective in blocking two quadrants of possible wave approach. This assumes that there is negligible wave reflection or surf zone "generation".

The mean depth of the pressure sensors was the first factor considered in the array design. A linear array aligned with the depth contours on a plane beach measures only the longshore wavenumber, k_y , which is conserved on a plane beach. Therefore, the required array length to resolve the structure of the island shadow does not vary with depth. However, there were some constraints to the design depth due to the nature of the data recovery system. The primary field unit of this system is an anchored spar (Lowe et al., 1972) which operates in the depth range 9-20 m. The minimization of total underwater cable length was of considerable practical concern. This necessitated the location of the array sensors in the same approximate depth as the spar.

Positioning the array at greater depth reduces the finite depth propagation that the waves undergo before measurement. This decreases the errors in the conversion of the shallow estimates to deep water values due to uncertainties in refraction or bottom dissipation. Also, the waves in the deeper region are less steep and are more likely to be linear. Although no comprehensive study of possible nonlinear effects has been undertaken, it has been observed that significant harmonic peaks are not generally evident in the 10 m depth spectra at this site.

The depth attenuation of the pressure signal requires a correction factor to make estimates of the wave energy spectrum. This

correction factor increases exponentially with frequency and must be cut off because the signal at high frequency is reduced to the noise level. Close examination of many data runs (Pawka et al., 1976) established this cutoff at 0.25 Hz for the 10 m array at TPB. This would correspond to roughly 0.18 Hz for these pressure sensors in 20 m depth. Waves in the frequency range 0.18-0.25 Hz are an important part of the locally generated wave spectrum. Therefore, in support of the surf zone work which was coincident with this project, a decision was made to place the array in a mean depth of 10 m.

A relatively long array is required to resolve low frequency waves coming around the edges of SCI. The refraction model indicates that the required resolution is about 8° for 0.067 Hz waves, climatologically the most energetic low frequency band. The separability of two spectral peaks is a function of the peak shapes, the relative peak amplitudes, the level and distribution of background energy, and the estimation technique employed. The response of the MLE method with a 400 m array was tested with computer simulated spectra which contained two narrow peaks. The results show clear resolution of the peaks at 0.067 Hz for 8° separation and secondary peak amplitudes as low as 25% of the primary. This peak ratio is close to the lowest expected value for low frequency waves (determined by the island refraction analysis). The 400 m length was considered to be roughly the maximum practical length.

The design of the array is then reduced to the relative configuration of 5 sensors within a total length of 400 m. Unless an array is designed to provide very specific information about the wave

field, it does not appear that there is an "optimal" configuration with 5 sensors. This array was required to resolve the low frequency directional peaks, avoid aliasing for frequencies up to at least 0.145 Hz, and provide good spectral response for the frequencies in between. This aliasing requirement insured quality data at the wave frequency sampled by the Stanford HF radar, which is discussed below.

Many 5 sensor array configurations were tested for their window properties in the frequency range 0.067-0.168 Hz. The array configurations of total length Nx_0 , where N is an integer from 9-14 and x_0 is the length of the shortest lag, with the least missing lags were studied. The square window error is defined

$$\text{Square Window Error} = \sum_{j=-90}^{90} \sum_{k=-45}^{45} W^2(\alpha_j, \alpha_k) (1 - \delta(\alpha_j, \alpha_k)) \quad (\text{III.1})$$

where the angles are defined from normal to the array, the indices j and k increment α by 1° , $\delta(\alpha_j, \alpha_k)$ is the Kronecker delta function, and the Barber window (equation II.29) was used as $W(\alpha_j, \alpha_k)$. The summation represents the square window error associated with the estimates in the directional range $\pm 90^\circ$. The error due only to the window values in the range $\pm 45^\circ$ is computed. This range was chosen to account for the expected limits of the true directional spectrum due to refraction over the shelf. Although several other estimators were eventually used in the data reduction, the Barber window does give a good general description of the properties (Regier, 1975). Figure 14 shows the mean square window error as a function of wavenumber for several sensor arrays. The frequency averaged results for the 1-2-4-5 and the 1-3-3-2 configurations were within a few percent of each

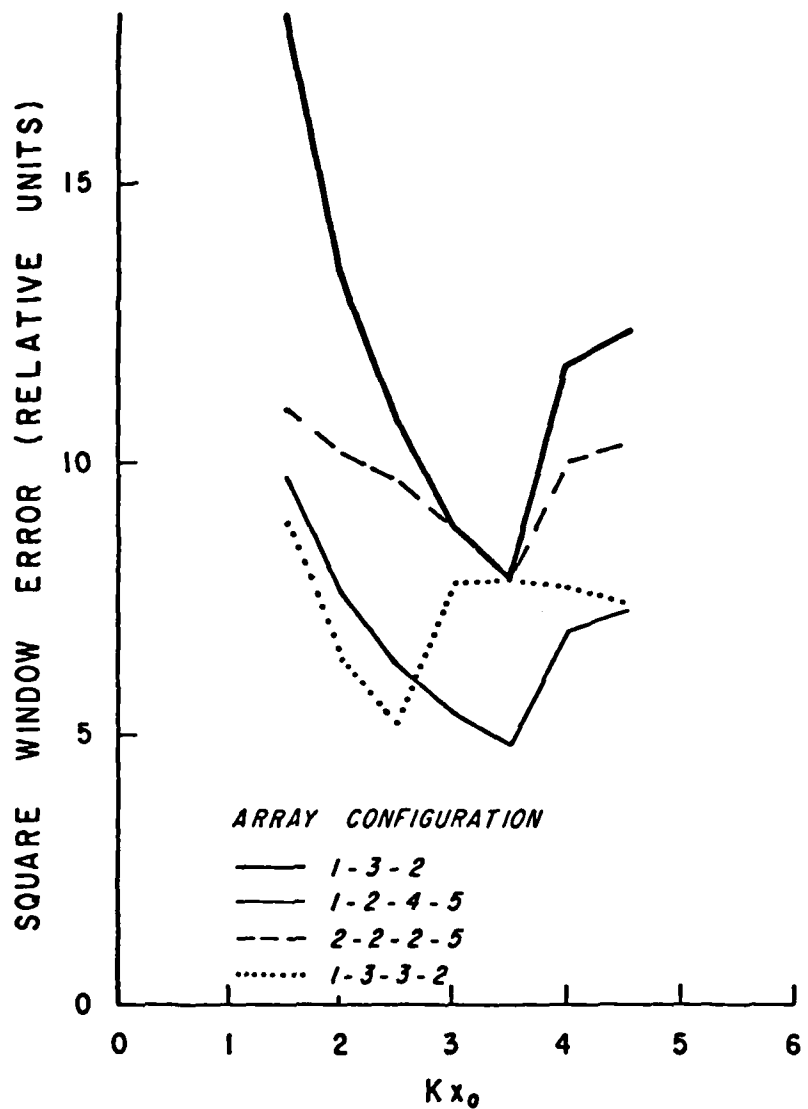


Figure 14. Square window error (equation III.1) versus normalized wavenumber for various array configuration. x_0 is the unit spacing of the arrays.

other. For comparison purposes, a poorly designed 5 sensor and a well designed 4 sensor array are shown to have generally much higher error results. Barber (1958) recommended a 1-3-3-2 configuration because it maximizes the number of consecutive lags. The 1-3-3-2 array outperforms the 1-2-4-5 array at lower wave frequencies because of its generally lower side lobes. However, the 1-3-3-2 array encounters aliasing at a lower frequency because its shortest lag must be greater than the unit lag of the 1-2-4-5 array to achieve the same total length.

The sharp rise in the errors at high frequency for all the curves in Figure 14 is due to the onset of aliasing. It should be noted that the effect of aliasing can be more dramatic with differently weighted versions of "spectral error". Pawka (1977) showed that the onset of aliasing can easily change the sign of the estimated wave momentum flux, S_{yx} .

The 0.067 Hz window errors and the initial aliasing frequency for several "reasonable" array designs are shown in Table 5 to roughly trend with each other. Any of these arrays listed would have done an adequate job in this experiment. The 1-2-4-5 configuration was chosen because a 1-2 array with the desired unit length had been previously established at this site. It was considered that the extension of the 1-2 design into a 1-2-4-5 array was the simplest modification yielding an array with a reasonable directional response. Additionally, the 1-2 sub-array was used to look at spectral properties in a very local, spatially homogeneous medium. This work is discussed in Section V.

A mini-ranger positioning system was used aboard the R/V Meter

ARRAY CONFIGURATION	M	x_0	SWE (0.067 Hz)	f (aliasing)
1-3-3-2 (1-1-4-4)	9	44.0	9.82	0.129
3-4-1-2	10	40.0	10.42	0.141
2-5-1-3	11	36.0	10.30	0.153
1-2-4-5	12	33.0	10.72	0.160
2-1-6-4	13	30.5	11.07	0.172
2-1-6-5	14	28.3	10.85	0.182

Table 5. Low frequency square window error (SWE, defined in equation III.1) and aliasing frequency for various linear arrays. x_0 is the unit spacing and $Mx_0 = 400$ m is the array length.

Maid for the establishment of the two most northern sensors, adding the 4 and 5 lags. This positioning system was calibrated so that smoothed readings gave results to within a radius of 1-2 m. Vertical photographs taken at several altitudes from a light aircraft were used to image the sensor locations. Highly visible buoyant spheres were pulled taut over each sensor position. The various photographs were intercompared for consistency and averaged to yield sensor positions to within 1 m. This position uncertainty corresponds to an orientation error of roughly 2° for the shortest lag and less than 1° for the longer lags. The absolute orientation of the array was based on the sensor positions relative to 2 upper beach bench marks. Discrepancies of $\pm 1^\circ$ in the magnetic heading of the line between these bench marks causes an uncertainty of $\pm 1.5\text{-}3.0^\circ$ in deep water wave directions.

The directional spectra obtained from the 1-2-4-5 array are useful in the frequency range 0.051-0.160 Hz. Resolution problems establish this lower limit and actually cause quantitative problems in the spectrum up to 0.067 Hz. The high frequency limit is due to the onset of aliasing. The spectra were refracted to local deep water using the refraction model discussed in Section II. There was no independent check on the local deep water energy spectra derived in this manner. However, due to the high directional resolution of the array, the TPB estimates of local deep water frequency spectra are considered more accurate than those at the other coastal stations. The estimates of deep water directionality were verified to some degree by comparisons to the SAR spectra imaged at this site. These results (Appendix A) show that the modal wave directions obtained from

the array, which have uncertainty due to both array orientation and refraction analysis, are consistent with the SAR results to within 2-3°.

An Endeco electromagnetic current meter was operated by the Shell Development Company at the Tanner Bank site. The performance of these current meters is discussed by Branaird and Lukens (1975). This current meter was placed in a depth of roughly 60 m and therefore responded only to waves with frequencies less than approximately 0.1 Hz. As discussed above, there are significant refraction effects expected for frequencies less than 0.08 Hz at the Tanner Bank site. Therefore, the expected range of accurate estimates of deep ocean properties is very limited.

The current meter signals were not synchronized with the output of the Baylor gage at this site. The only available directional moments are

$$\int_{\alpha} \cos^l(\alpha) \sin^m(\alpha) E(\alpha) d\alpha \quad (\text{III.2})$$

where the integers $l+m=2$. The angle obtained from the ratio of the energy densities of the velocity components will be close to the true mean wave direction only for well directed swell. A very high coherence between the sensors would indicate that this condition exists. However, low coherence may be due to a wide directional spread of a single mode, multiple modes, or the presence of noise. The generally low coherence values measured between the velocity components of this sensor limited its utility as a source of accurate directional data. Therefore, this data was primarily used as

background information in support of other observations. It should be noted that the current meter directions at the frequency spectral peaks compared well with angles deduced from aerial photographs. Comparative data from 10,11, and 14 March showed angular agreement to within 5°.

III.3 Remote Directional Measurements

The primary remote sensor used for the directional wave measurements was the L-band SAR flown by JPL aboard a CV-990 aircraft. The aircraft flight pattern, shown in Figure 1, was designed to cover the entire study region. The most important use of the SAR was the sampling of the deep ocean directional spectrum. The success of the data-model comparisons relied heavily on accurate directional resolution by this system in the deep ocean. Additionally, SAR images were taken at the TPB site and compared with the SPL array spectra (refracted into local deep water) to provide high resolution ground truth verification of the SAR system.

Wave patterns have been widely observed in sea scatter return from centrimetric radar systems. Previous work has been done with X and L-band SAR systems in the investigation of long period ocean waves, see e.g. Ross et al.(1974). The L-band SAR radiation is in Bragg resonance with the 23 cm surface waves. The radar return is a function of both the short wave amplitude and the local tilt due to the presence of longer waves. The long waves also modulate the short wave amplitude which enhances the imaging process. The sources of this modulation, such as straining due to the long wave orbital velocity field or the effects of wave induced airflow, are under

active investigation (Evans and Shemdin, 1980). Previous ground truth experiments, reported in Mcleish et al.(1980), indicate that the SAR system yields accurate estimates of modal wave direction but have not yet solved for an "image transfer function" to yield wave frequency spectra.

The SAR images were processed in sections which represented $5.5 \times 5.5 \text{ km}^2$ patches of the ocean surface. The estimated surface resolution of the system was 25 m. JPL operated the SAR, processed the images, and reduced the data to yield directional distributions at the various wave frequencies. The details of this analysis are included in Appendix A and in Vesecky et al.(1980). The analysis and results of the directional intercomparisons of the SAR and SPL array are also contained in Appendix A. The principal conclusions which pertain to the present study are: 1) the SAR provides good estimates of the location and width of the primary mode in the spectrum; 2) small secondary peaks evident in the array spectrum are not reliably imaged by the SAR; 3) the inherent noise level is much greater in the SAR spectra. The sampling problems evident in the SAR spectra severely limit their intended use as inputs into the refraction model of wave transformations around the islands.

The Stanford group utilized a synthetic aperture technique to receive HF (1.95 MHz) sea return from a Loran-A station. This radio frequency is in Bragg resonance with a deep water wave frequency of about 0.143 Hz. This measurement results in a spacial map (covering the entire operating area) of the relative energy densities of the wave components travelling radially toward or away from the site at

San Mateo Point.

The theory of this radar technique has been well established and is reviewed by Barrick (1978) and there has been significant practical application , see e.g. Tyler et al.(1974). The details of the HF measurements taken during this experiment are reported in Veseycky et al.(1980). The estimated directional resolution of the synthesized array was roughly 4°. Time averaging of the recorded signal yielded a range resolution of 5 km.

The estimates obtained from this method are very different from the SAR and SPL array results which represent the directional energy distribution at a single location. The HF directional maps are well suited to follow the energetic evolution of a single directional wave component as it propagates through the study region.

Aerial photography was taken from several aircraft during periods of intense experimental activity. Black and white photography was taken from a CV-990 and a P-3 which were flown at altitudes of 8-10 km. High resolution color photography was taken from a U-2 at 18 km elevation. Descriptions of the flight patterns, aircraft, and camera systems are given in Shemdin et al.(1977).

Wave directional spectra can be obtained from vertical photographs taken under very controlled situations. Stillwell and Pilon (1974) describe the theory and limitations of this measurement technique. However, the waves were primarily imaged in the glitter region of the photographs during this experiment. This does not lead to meaningful linear analysis. Therefore, the photographs were primarily used as indications of "principal wave direction". This

type of data was used as background information and in comparison to the other systems.

III.4 In-situ Wind Measurements

Surface anemometers were located at the Naval Ocean Systems Center (NOSC) tower in Mission Beach, San Nicolas Island, and SCI (Shemdin, 1980) to sample the wind field. Hourly averages of wind speed and direction were obtained from each site. The wind information was primarily used for correlation with various parameters of wave intensity to evidence the importance of local wind generation.

IV ISLAND SHELTERING RESULTS

IV.1 Island Sheltering Experiment

The airborne SAR system was relied upon for the estimation of the deep ocean directional spectrum. These estimates were necessary for the meaningful comparisons of the coastal data with the theoretical wave transformations developed from the island refraction/blocking model. The SAR spectra were sampled on only two of the experiment days. Frequency spectra were obtained at all the sites on 16 days. On 10 of these days, long data runs (2.5-14 hours) of high quality directional data were sampled at TPB.

The intercomparison of frequency spectra sampled throughout the study region is not adequate alone for the verification of the island refraction/blocking model. However, these comparisons do indicate the magnitude of the island shadowing effects. Figure 15 is a plot of the 16 day average frequency spectra measured synoptically at the various sites. The coastal spectra have been refracted into local deep water estimates. These spectra show that the relatively unsheltered offshore stations, Begg Rock and Tanner Bank, have approximately an order of magnitude greater energy level than the coastal sites. The spectral values at the two offshore sites do not agree well except in the high frequency tail of the spectrum. This is most likely due to the slightly different exposure and complex topography at Tanner Bank.

There is also a significant variation in the average spectral levels amongst the coastal stations. This is an expected feature of the sheltering process. However, the remarkable similarity between

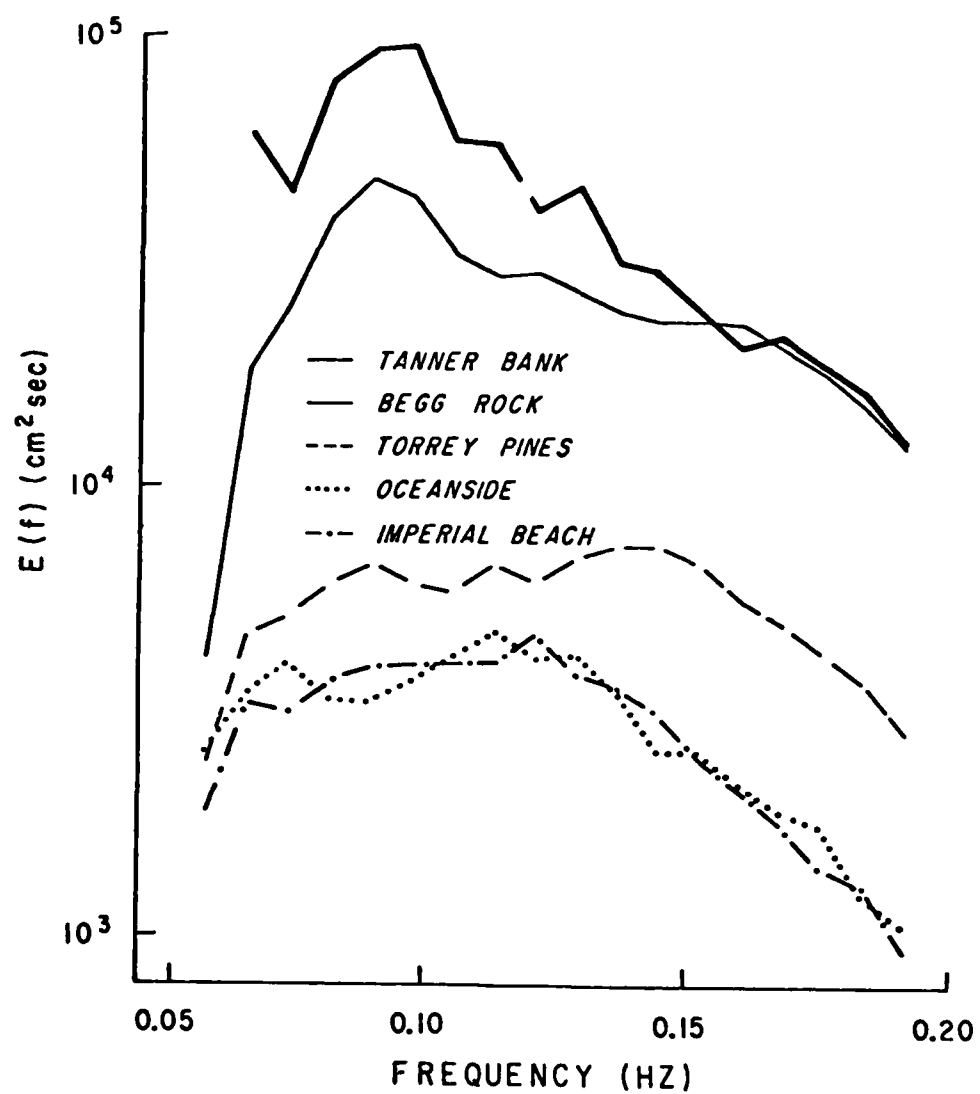


Figure 15. Average frequency spectra sampled at the various sites in the West Coast Experiment. The data were sampled synoptically on 16 days.

the spectra at Oceanside and IB may be an artificial result. Due to the lack of local directional spectra, the frequency spectra at these two sites were shoaled into deep water using an average of the refraction results for all of the sectors not blocked by the islands. These deep water estimates would be significantly altered if only the refraction values for the northern quadrant exposure were employed. The high frequency spectral values at Oceanside and IB would increase by 63% and 25% respectively under these conditions.

The ratio of the frequency spectral values at TPB to Begg Rock, $E_{tp}(f)/E_{br}(f)$, is plotted as a function of frequency in Figure 16. The average ratio drops sharply from the low to mid frequencies. This result is consistent with the island refraction/blocking model which indicates an emphasis of lower frequency energy at the coast in response to deep ocean north swell. Additionally, there is a greater percentage of south swell, which is relatively unsheltered, in the lower frequency bands. As a result of this filtering, the average coastal frequency spectra do not exhibit the strong mid frequency peak which is evident in the offshore spectra (Figure 15). The subsequent rise in the ratio $E_{tp}(f)/E_{br}(f)$ for frequencies greater than 0.098 Hz will be discussed later.

The extreme measured values of $E_{tp}(f)/E_{br}(f)$ are also indicated in Figure 16. These values generally lie significantly outside the expected 90% confidence range for a stationary process. This result is indicative of significant variations in the measured values of this ratio and hence the transformations of deep ocean to coastal wave conditions.

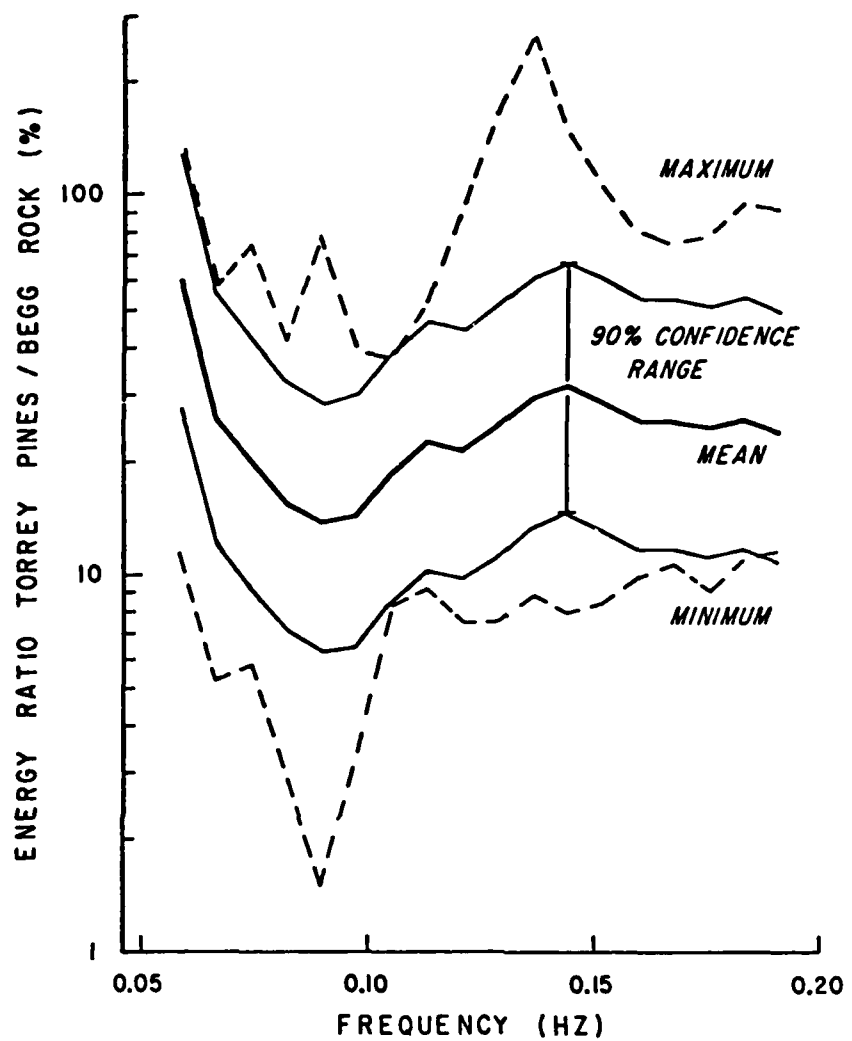


Figure 16. Average value of the ratio of band energy at Torrey Pines Beach to Begg Rock for 16 sample days. Also indicated are the maximum and minimum sampled ratio (dashed lines) and the 90% confidence range for a stationary process.

All of the ground based sensors were functioning on 25 March and 28 March. This excludes the gages at Tanner Bank which were permanently out at this time. The operations on these two days included a full flight pattern of the CV-990 which carried the SAR. Approximately 6 hours of continuous data were sampled at SCI and TPB. Discreet but numerous 17.1 minute data runs were obtained at the other coastal locations.

The average Begg Rock frequency spectra, shown in Figure 17, indicate a basically different deep ocean wave environment on the two days. The 25 March spectrum has a distinct bimodal form with peaks at 0.082 Hz and 0.0161 Hz. The spectrum on 28 March is broader with relatively high values of band energy in the frequency range 0.098-0.180 Hz. The total wave energy in the Begg Rock spectrum on 28 March is roughly twice the value on 25 March. The modal directions of the SAR spectra are summarized in Table 6. These directions show some indication of south swell in the low frequency regime on both experimental days. The primary energetic mode has directions in the range 280-305°T and has a full width at half maximum (FWHM) of 10-30°. This peak tends to broaden frequencies higher than about 0.13 Hz.

The average frequency spectra for TPB (local deep water) are also shown in Figure 17. These spectra show similar form to the deep ocean spectra but have a much lower energy level. The total wave energy at TPB is roughly twice as great on 25 March as on 28 March. This result is opposite of the trend at Begg Rock. A sample set of 10 m depth directional spectra measured at TPB is shown in Figure 18.

Frequency (Hz)	MARCH 25, 1977			MARCH 28, 1977		
	α_m	$\Delta\alpha_m$	Residual	α_m	$\Delta\alpha_m$	Residual
0.059	248	10	51.4	280	14	48.9
0.067	282	14	41.7	220	16	57.0
0.074	299	65	20.8	320	10	51.3
0.082	306	10	42.2	294	12	50.8
0.090	302	35	25.5	297	14	33.3
0.098	298	50	20.4	297	22	32.8
0.106	292	30	22.3	289	30	36.1
0.114	283	10	41.3	295	12	45.7
0.121	280	35	33.1	297	20	37.3
0.129	302	90	9.8	281	35	30.7
0.137	299	90	5.8	290	90	13.5
0.145	298	90	6.8	280	90	18.1

Table 6. Mode parameters for the unimodal distribution representations of the SAR spectra. α_m is the best fit mode direction while $\Delta\alpha_m$ is the full width at half maximum of the cos power distribution (both in degrees). The residual (given in percent) is defined

$$\text{residual} = \frac{\sum (\mathcal{E}_u(\alpha) - \mathcal{E}_r(\alpha))^2}{\sum \mathcal{E}_r^2(\alpha)}$$

Figure 17. Average frequency spectra for the Begg Rock waverider and the Torrey Pines pressure sensor array for the 2 sample days which had full coverage by SAR imagery. The Torrey Pines spectra have been refracted out into "local" deep water. DOF indicates the degrees of freedom of the spectral estimate.

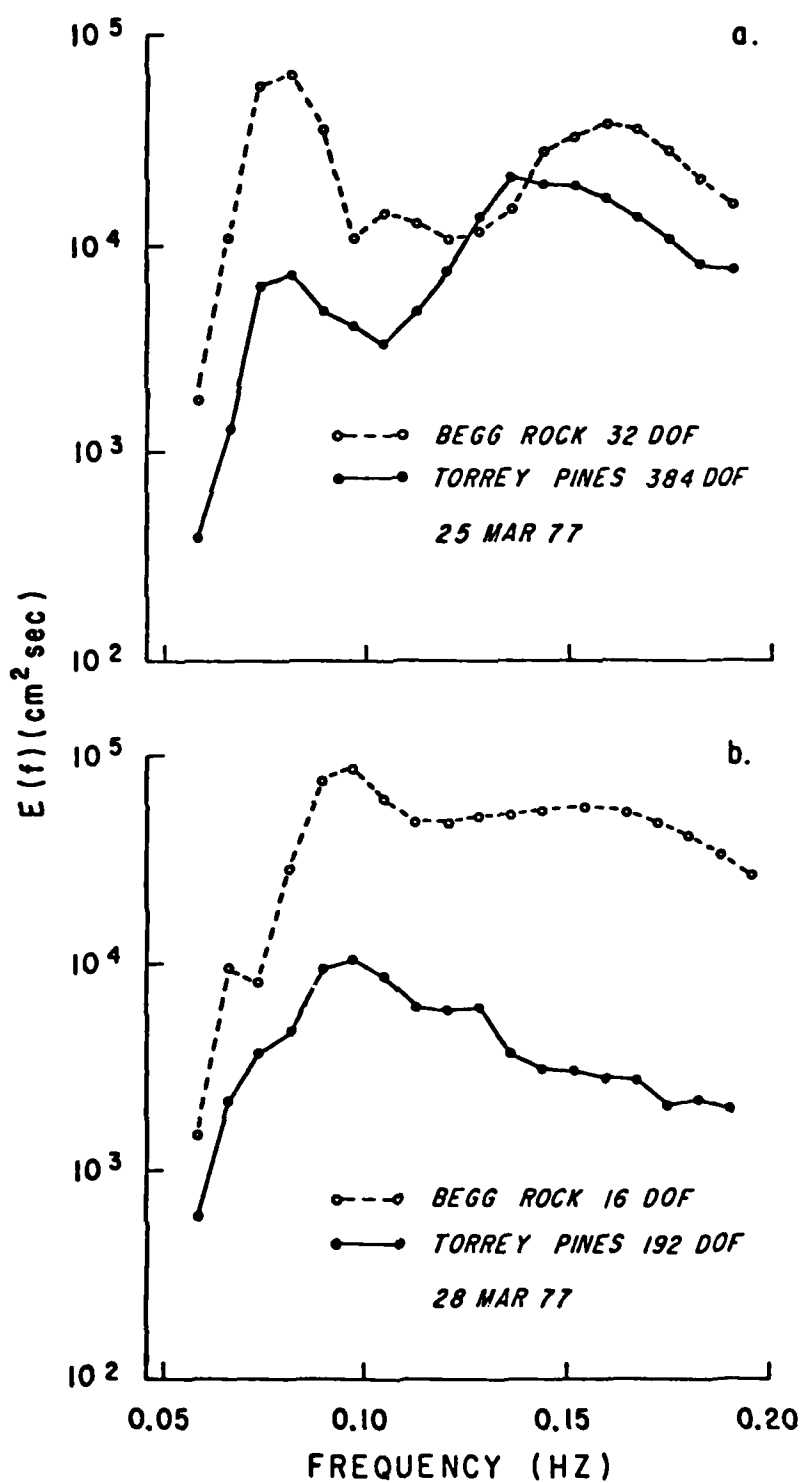
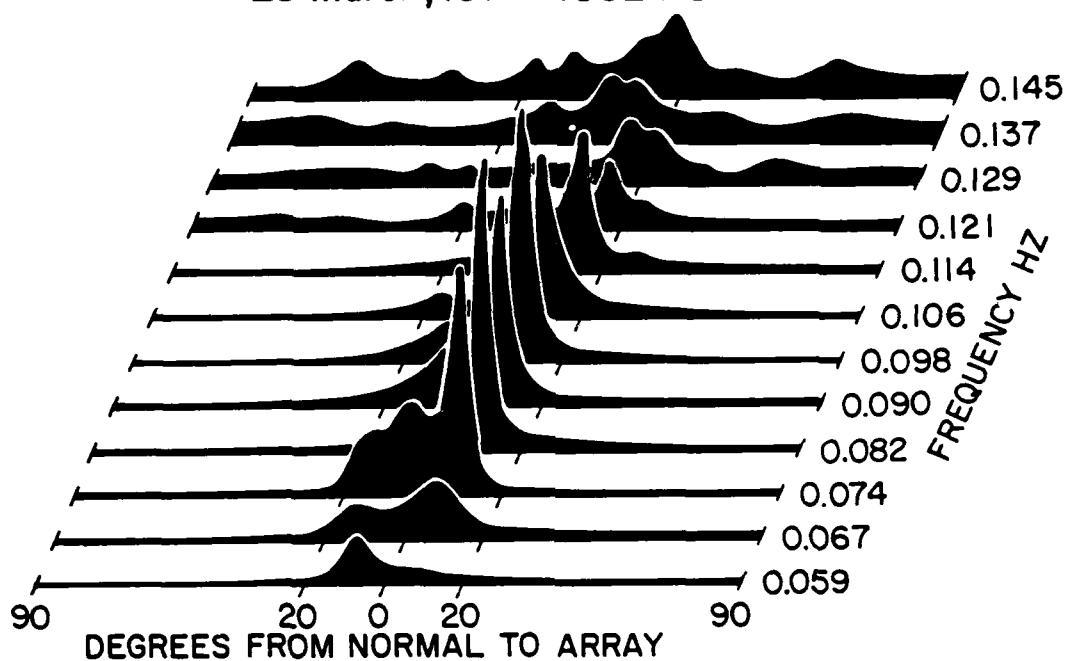
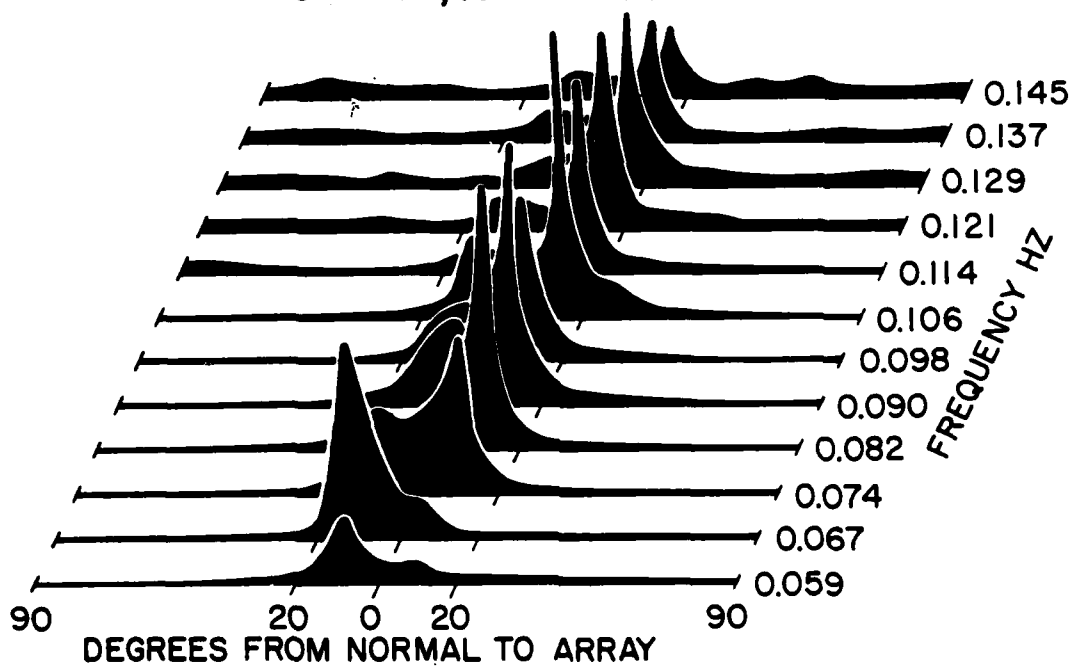


Figure 18. Directional spectra analyzed from the Torrey Pines array using the MLE method. The estimates are for 10 m water depth and the abscissa is equal to log (energy density). Each sample represents a 32.1 minute run.

25 March, 1977 1032 PST



28 March, 1977 1338 PST



These spectra show a wide variety of directional form. There are strong southern components in the low frequency regime. Above wave frequencies 0.082 Hz the spectra are dominated by a narrow mode with slight northerly directions. A secondary peak exists in the southern quadrant which produces a characteristic bimodal form. The spectra become more irregular at frequencies above 0.13 Hz, particularly on 25 March.

The frequency spectra obtained from the Begg Rock waverider and the SAR directional spectra, $E_r(\alpha)$, sampled in this location were combined to yield estimates of the deep ocean wave conditions. The SAR spectra were sampled west of the Begg Rock waverider (~10° more deep ocean exposure). This sheltering was accounted for by the refraction model 10-20% effect) to yield a "deep ocean" frequency spectrum. These spectra were then transformed by the island refraction/blocking model to give predictions of coastal wave statistics. Due to the high noise level in $E_r(\alpha)$, see Appendix A, a unimodal fit to the SAR directional distributions, $E_u(\alpha)$, was also used as an input for coastal predictions. The comparisons of the predicted and measured frequency spectra for 25 March and 28 March are listed in Table 7. The comparisons are quite variable and are discussed below in terms of three frequency ranges.

IV.1.1 Low Frequency

The low frequency range (0.059-0.074 Hz) is characterized by significant southern and northern components in the deep ocean spectrum. The 0.059 Hz SAR directional spectrum sampled at Begg Rock on 25 March is shown in Figure 19. The band energy is normalized by

Table 7. Ratio (%) of measured band energy at the coastal sites (deep water) to the values predicted with the island refraction/blocking model. The comparisons with the SAR spectrum, $E_r(\alpha)$, and the unimodal approximation, $E_u(\alpha)$, as estimates of the deep ocean directional spectrum are listed.

Frequency (Hz)	OCEANSIDE						SAN CLEMENTE ISLAND					
	E_r (a)	25 Mar	28 Mar	E_u (a)	25 Mar	28 Mar	E_r (a)	25 Mar	28 Mar	E_u (a)	25 Mar	28 Mar
0.059	110.	209.	49.6	133.	198.	224.	400.	690.	148.	324.	87.6	535.
0.067	51.5	111.	40.6	64.1	11.3	93.5	49.8	32.4	103.	157.	161.	52.5
0.074	42.0	163.	58.6	150.4	30.6	372.	86.8	1000.	100.	330.	144.	2050.
0.082	52.9	54.8	240.	87.7	30.3	86.7	565.	1270.	147.	230.	251.	177.
0.090	60.1	60.2	101.	97.8	40.9	29.6	157.	266.	115.	90.1	153.	72.3
0.098	123.	41.4	175.	58.8	91.8	23.9	283.	323.	246.	78.5	340.	84.3
0.106	73.	40.0	85.4	45.0	60.7	18.7	174.	44.9	173.	111.	180.	114.
0.114	97.4	42.8	62.8	70.5	48.3	24.6	128.	712.	128.	101.	145.	73.2
0.121	228.	37.6	178.	68.1	111.	16.3	134.	305.	244.	89.4	197.	79.5
0.129	330.	32.4	464.	29.6	253.	24.6	447.	30.9	287.	73.8	354.	58.3
0.137	433.	17.9	492.	19.7	249.	32.7	380.	50.6	387.	58.8	454.	63.8
0.145	232.	13.9	243.	12.9	98.7	11.0	145.	13.5	268.	45.5	281.	42.1

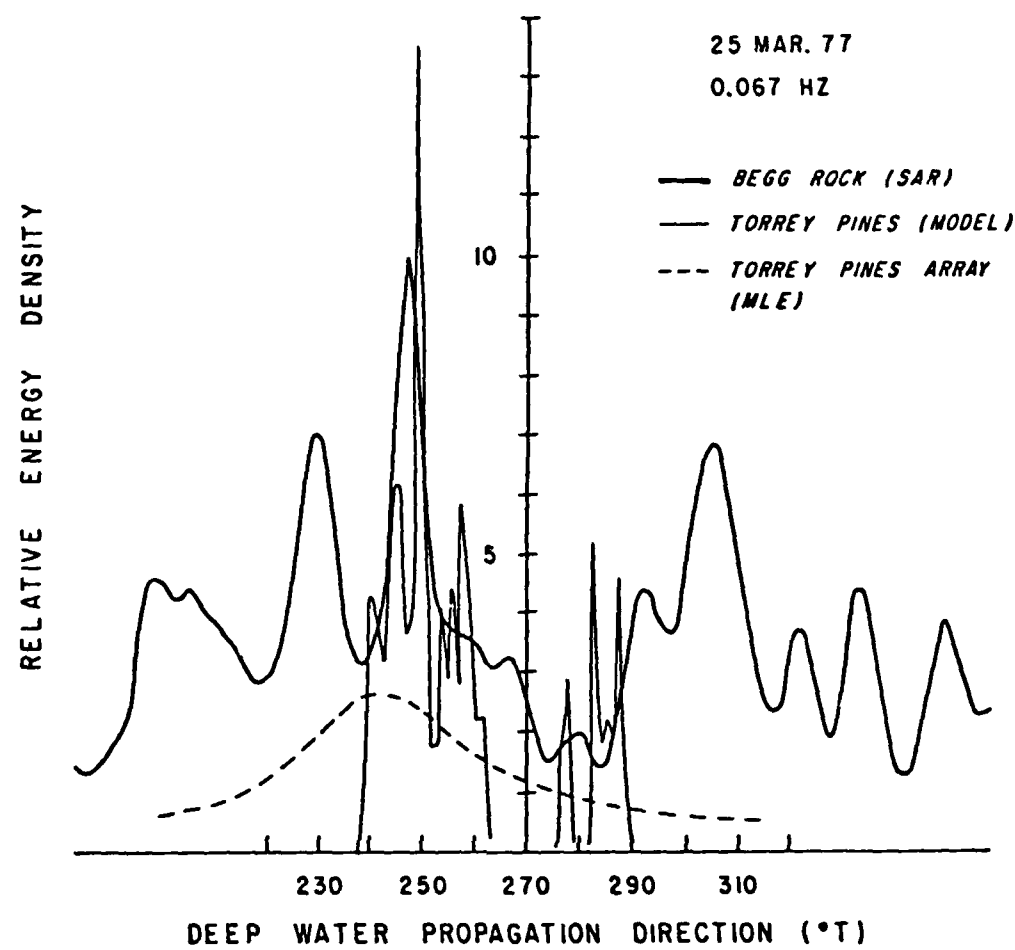


Figure 19. Comparison of predicted and measured (MLE) directional spectra at Torrey Pines Beach. The predicted spectrum was generated using SAR directional inputs into the island refraction/blocking model. The measured spectrum has been refracted into local deep water for the comparisons. The curves are normalized by their relative band energy.

the frequency spectrum obtained from the waverider in the area. This spectrum is transformed by the island refraction model to yield a predicted response, $P_{tr}(\alpha)$, at TPB. This response is compared in Figure 19 with the local deep water directional estimate, $E_{tm}(\alpha)$, analyzed with the MLE method. The disordered appearance of $E_r(\alpha)$ is typical of these low frequencies. The predicted band energy at TPB, $P_{tr}(f)$, is within 10% of the measured value for this case. Note that $E_{tm}(\alpha)$ does not resolve the two modes indicated in the predicted spectrum. This will be discussed at length later in this work.

The average value of the ratio $E_{tp}(f)/P_{tr}(f)$ for the low frequency bands was 1.18 (compare to the value of $(E_{tp}(f)/E_{br}(f))$ of 0.35). Although this result alone is not discouraging, there is a tremendous amount of scatter in the data. The normalized standard deviation is defined

$$\sigma_n = \frac{\langle (x - \langle x \rangle)^2 \rangle^{1/2}}{\langle x \rangle} \quad (\text{IV.1})$$

as a measure of the variability of the variable x . $\sigma_n(E_{tp}(f)/P_{tr}(f))$ is about 0.6 in the low frequency range. This value is roughly the same as $\sigma_n(E_{tp}(f)/E_{br}(f))$ calculated for the same data set. That is, accounting for the refraction transformation does not remove any of the scatter in the data. Assuming a stationary process and that the frequency spectra are χ^2 distributed, the expected value of $\sigma_n(E_{tp}(f)/P_{tr}(f))$ with the averaging employed is about 0.4.

The data-model comparisons at Oceanside show larger scatter than the TPB results. This is undoubtedly due to the increased sensitivity of the Oceanside site to south swell. The modeling of the

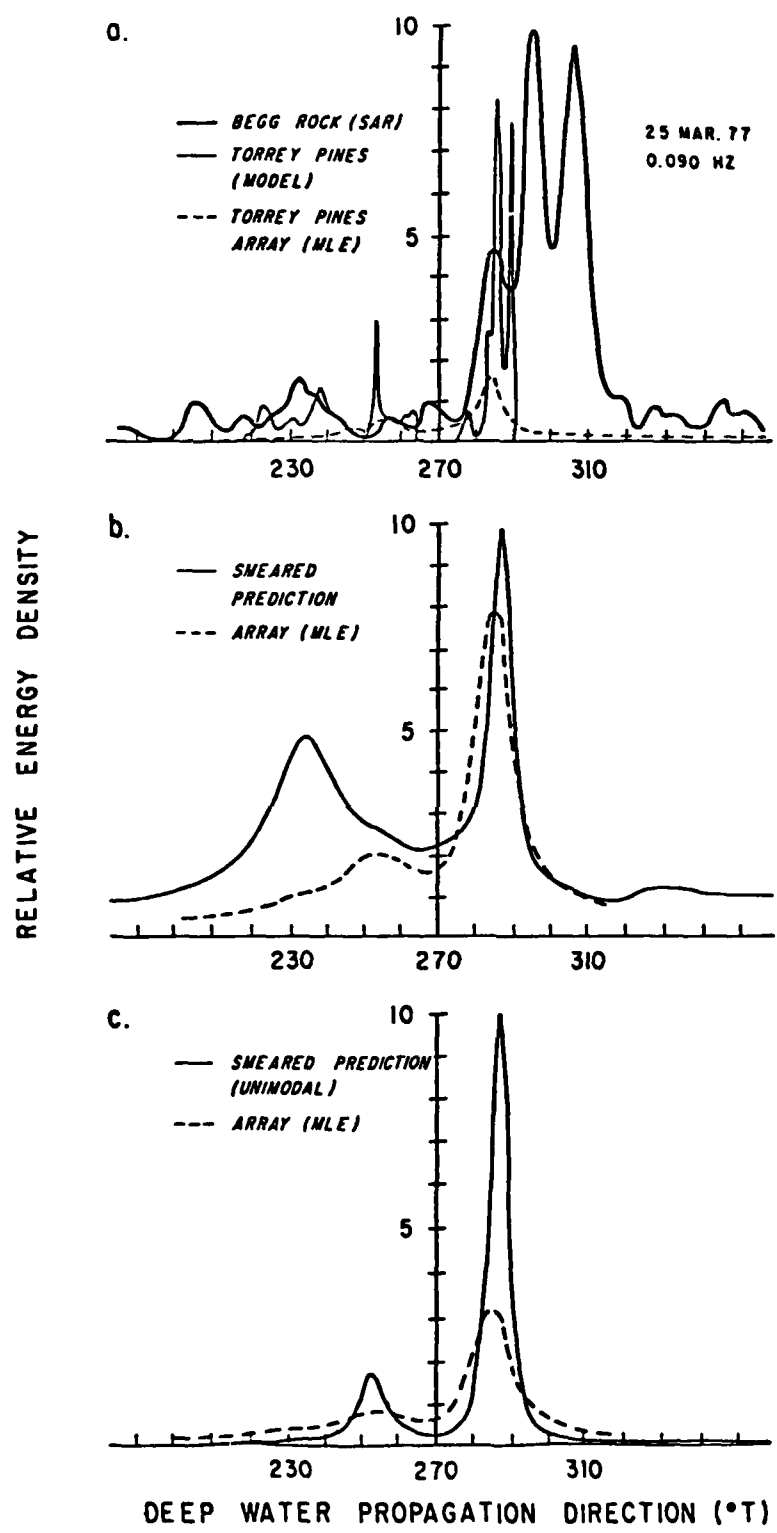
deep ocean directional spectrum with a unimodal directional distribution produces even worse results at both sites. This is expected due to the general indication of bimodal directional forms (north and south swell) at these frequencies.

The refraction process was shown theoretically to be the most significant in this low frequency range. It is felt that the poor quality of $E_r(\alpha)$ did not allow for a valid test of the refraction model. The peak in $P_{tr}(\alpha)$, shown in Figure 19, was roughly consistent with the structure of $E_{tm}(\alpha)$. This was often not the case in the low frequency comparisons.

IV.1.2 Mid Frequency

$E_r(\alpha)$ in the mid frequency range (0.082-0.114 Hz) is dominated by a relatively narrow (10-30° FWHM) peak around 280-305°T. The refraction model tends towards overprediction of the coastal energy values with the use of $E_r(\alpha)$ as the deep ocean directional spectrum. However, the model significantly reduces the variance in the data. $\sigma_n(E_{tp}(f)/P_{tr}(f))$ is roughly 0.4 (the value for a stationary process) as compared to a value of -0.6 for $\sigma_n(E_{tp}(f)/E_{br}(f))$. A plot of $E_r(\alpha)$ and the computed predictions at TPB for 0.090 Hz waves on 25 March is shown in Figure 20. The MLE response of the 1-2-4-5 array to $P_{tr}(\alpha)$ was calculated for direct comparisons with $E_{tm}(\alpha)$, also shown in Figure 20. The "smeared prediction", $\tilde{P}_{tr}(\alpha)$ where $P_{tr}(\alpha) \rightarrow \tilde{P}_{tr}(\alpha)$, agrees well with $E_{tm}(\alpha)$ for angles greater than 250°T. However, there is an excess of predicted energy in the sector $180^\circ T < \alpha_{tp} < 250^\circ T$. Again, this is most likely due to the relatively high noise level in the SAR spectrum. This bias in the southern quadrant is seen in

Figure 20. Comparison of predicted and measured spectra at Torrey Pines Beach. The predicted spectra were generated by SAR directional spectra inputs into the island refraction/blocking model. Shown are the comparisons of Torrey Pines array spectra with: a) raw prediction with the full SAR spectrum as the input, b) smeared prediction (MLE filter) with the full SAR spectrum as the input, c) smeared prediction with the unimodal SAR spectrum representation as the input. The spectra are normalized by their relative energy content.



$P_{tr}(\alpha)$ throughout the mid frequency range.

The unimodal distribution which best fits the SAR spectrum and its smeared coastal response, $P_{tu}(\alpha)$, are also shown in Figure 20. The predicted band energy is within 5% of the measured value for this case. Also, $P_{tu}(\alpha)$ locates well the two primary directional modes. The more "smeared" appearance of the measured spectrum may be due to a low background level in the southern quadrant that is not accounted for by the unimodal distribution. The unimodal model generally underpredicts the southern quadrant energy density. The average value of $E_{tp}(f)/P_{tr}(f)$ for in this frequency range is 1.03 which indicates that the mishandling of the southern quadrant is not serious at TPB. It is expected that the unimodal deep ocean approximation would be most appropriate in the mid frequency range due to the absence of south swell or local wind effects (both discussed later) in this range.

The use of $E_u(\alpha)$ as inputs to the island refraction/blocking model causes significant prediction problems at Oceanside. The data comparisons listed in Table 7 show that there is severe overprediction of band energy at Oceanside with $E_r(\alpha)$ inputs while the use of $E_u(\alpha)$ causes a strong underprediction. The differential response to the southern and northern quadrants is much more dramatic at Oceanside than at TPB, so problems with low background levels are magnified. Also, it should be restated that the Oceanside transformations to deep water are suspect.

There is quite a bit of variability of the unimodal parameters (Table 7) and the data-model comparisons ($\sigma_n(E_{tp}(f)/P_{tu}(f)) \sim 0.57$) in

the mid frequency range. The mode parameters were averaged over the entire range for each day in an attempt to suppress errors induced by this scatter. The average value of $E_{tp}(f)/P_{tu}(f)$ for the smoothed unimodal inputs was 0.95 with a normalized standard deviation of 0.45.

A transformation model which accounts only for island blocking effects (no refraction) was also tested in the mid frequency range. The performance of this model is compared with the island refraction/blocking model in Table 8. The blocking model has increased errors (bias towards overprediction) relative to the refraction model. The response of the blocking model with unsmoothed unimodal deep ocean directional estimates shows wild fluctuations in the comparisons to the measured spectra. The discrepancy between the results of the two models decreases at the high frequency end of this range showing the declining theoretical importance of the refraction process.

IV.1.3 High Frequency

The high frequency range (0.121-0.145 Hz) is characterized by a very large discrepancy in the results for the two days (Table 7). Both $P_{tr}(f)$ and $P_{tu}(f)$ show a significant underprediction of the band energy values in the high frequency on 25 March. The data comparisons on 28 March show an even larger discrepancy, but with a overpredicted bias. The deep ocean high frequency energy level on 28 March is approximately twice as large as on 25 March. However, roughly the reverse is true of the coastal wave field.

The wind speeds averaged 7-8 m/sec throughout the borderland region on 25 March. Each site had a maximum recorded hourly wind

MEASURED/PREDICTED BAND ENERGY

Frequency (Hz)	REFRACTION			BLOCKING			$E_{tp}(f)/E_{do}(f)$
	$E_r(\alpha)$	$E_u(\alpha)$	$E_{\bar{u}}(\alpha)$	$E_r(\alpha)$	$E_u(\alpha)$	$E_{\bar{u}}(\alpha)$	
0.082	54.9	164.	73.0	42.1	626.	48.4	13.5
0.090	60.1	100.	95.0	45.8	84.8	48.5	13.4
0.098	82.2	117.	108.	67.2	110.	92.3	25.0
0.106	56.5	65.0	86.0	48.1	49.6	69.3	19.0
0.114	70.0	67.0	114.0	60.5	52.5	92.5	25.0

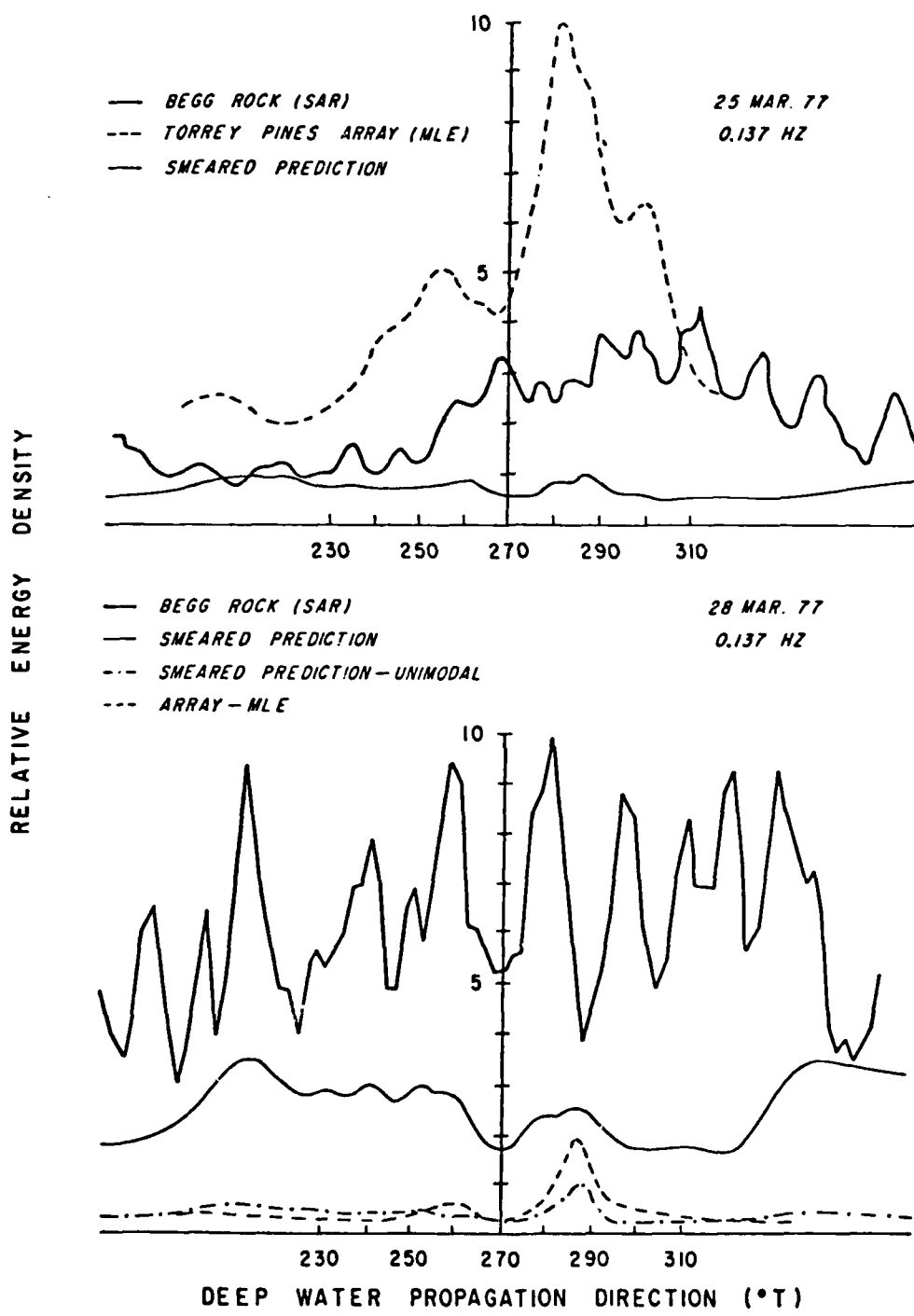
Table 8. Ratio (%) of measured band energy at Torrey Pines Beach to the predicted values. The results are averaged over the data from 25 and 28 March. The predictions were made with the island refraction/blocking model. The SAR spectrum, $E_r(\alpha)$, a unimodal approximation, $E_u(\alpha)$, and an averaged unimodal spectrum for the frequency range, $E_{\bar{u}}(\alpha)$, are used as deep ocean inputs to the models. Also given is the ratio (%) of Torrey Pines band energy to the deep ocean value, $E_{tp}(f)/E_{do}(f)$.

speed of about 10 m/sec. The mean wind direction varied slightly from 300°T at San Nicolas Island to 280°T at the NOSC tower. The measured band energies at TPB were significantly higher than the predicted values for the entire high frequency range. The size of this underprediction peaked at 0.137 Hz, with values of $E_{tp}(f)/P_{tr}(f) \sim 4-5$. This frequency was also the spectral maximum at the coastal sites.

The Begg Rock SAR spectrum, the smeared response at TPB, and the MLE spectrum from the TPB array ($E_r(\alpha)$, $P_{tr}(\alpha)$, $E_{tm}(\alpha)$) for 0.137 Hz on 25 March are shown in Figure 21. $E_{tp}(f)$, $f=0.137$ Hz, is actually greater than $E_{br}(f)$ on this day. $P_{tr}(\alpha)$ shows mild peaks at 260°T and 288°T which correspond roughly with modes in $E_{tm}(\alpha)$. The flatness of the smeared prediction curve is most likely due to the anomalously high energy level in the extreme southern quadrant of $E_r(\alpha)$. This wide distribution of energy density severely effects the theoretical MLE response. Measurements by Regier (1975) suggest that the directional spectrum in the vicinity of a wind generated peak is much more narrow than $E_r(\alpha)$ displayed in Figure 21. Narrowing of the assumed deep ocean directional spectrum would further decrease the size of the coastal predictions. The peak in $E_{tm}(\alpha)$ near 305°T is associated with the inter-island fetch which is totally blocked from deep ocean exposure at TPB. This feature of the coastal directional spectrum is due to local wind generation and is discussed at length later in this section.

The winds measured at Begg Rock are very consistent throughout the experiment. The wind speeds are greater than 5 m/sec on 20 of the 31 sample days with directions in the range 300-330°T. The wind

Figure 21. Comparisons of smeared predictions of the directional spectrum with the measured spectrum at Torrey Pines Beach. The comparisons are for: a) 0.137 Hz on 25 March, and b) 0.145 Hz on 28 March. Also shown are the deep ocean SAR (Begg Rock) estimates. The spectra are normalized by their relative energy content.



speeds and directions at SCI and NOSC are much more variable. The average speeds exceed 5 m/sec on 10 sample days at SCI and only 6 days at NOSC. The coastal winds correlate only mildly with the deep ocean values. The only events of relatively uniform wind conditions throughout the borderland region are associated with local frontal activity (includes 25 March).

The correlation of the band energy values sampled at the various sites with the wind speeds are listed in Table 9. The correlation of coastal band energy with coastal wind speeds increases almost monotonically with wave frequency. The results indicate relatively strong local control over the very high frequency region of the spectrum. However, the band energy values in the frequency range 0.082-0.145 Hz follow the deep ocean winds more closely than the coastal winds. This is not surprising because the lower frequency wave generation requires relatively strong winds over larger fetches. It is interesting to note that the mid frequency coastal band energy actually correlates better with the San Nicolas Island winds than do the estimates at nearby Begg Rock. The island sheltering of high angle north swell should increase the relative sensitivity of the coastal sites to local wind generation.

As mentioned previously, the high frequency coastal energy level is grossly overpredicted on 28 March. There is an apparent systematic drop in energy with propagation as the coastal band energy is overpredicted by a factor of five while band energy at SCI is roughly 50-60% of the predicted value. An example of $E_r(\alpha)$ for the high frequency range on 28 March is plotted in Figure 21b. This

		Wave Frequency Range (Hz)				
Sites		{ 0.059}	{ 0.082}	{ 0.121}	{ 0.153}	{ 0.206}
Wave	Wind	{ 0.074}	{ 0.114}	{ 0.145}	{ 0.192}	{ 0.231}
TPB	SNI	0.223	0.521	0.600	0.551	0.482
TPB	SCI	0.171	0.505	0.546	0.654	0.684
TPB	NOSC	-0.017	0.304	0.492	0.735	0.705
OS	SNI	0.235	0.562	0.585	0.468	0.382
OS	SCI	0.378	0.517	0.648	0.710	0.763
OS	NOSC	0.188	0.403	0.670	0.775	0.751
IB	SNI	0.201	0.498	0.578	0.604	0.497
IB	SCI	0.254	0.482	0.638	0.634	0.718
IB	NOSC	0.030	0.232	0.592	0.587	0.720
BR	SNI	0.149	0.413	0.460	0.567	-

Table 9. Correlation of band energy measurements at ground truth sites with wind speeds at San Nicolas Island (SNI), San Clemente Island (SCI), and the NOSC Tower. The ground truth sites are Torrey Pines Beach (TBS), Oceanside (OS), and Imperial Beach (IB). The correlations are over data sampled on 26 days. The correlation is defined for the variables x and y

$$r = \frac{\sum (x - \langle x \rangle)(y - \langle y \rangle)}{(\sum (x - \langle x \rangle)^2 \sum (y - \langle y \rangle)^2)^{\frac{1}{2}}}$$

directional spectrum shows little organized form and there is no agreement between $P_{tr}(\alpha)$ and $E_{tm}(\alpha)$. In particular, $E_{tm}(\alpha)$ shows relatively low energy density in the quadrants 230-250°T and 278-285°T which are completely exposed to the deep ocean. $E_{tm}(\alpha)$ peaks relatively sharply near the boundary to the north quadrant window (290°T). This is in contrast to directional spectrum sampled on 25 March.

The winds measured at San Nicolas Island on 28 March average 9 m/sec with directions near 320°T. The coastal winds are significantly lighter (4 m/sec) and have a shifting direction during the experimental run. Regier (1975) showed that the directional spectrum in a wind generated spectral peak is relatively narrow (FWHM~40°) with the mode being roughly colinear with the wind. This distribution was used as an input to the refraction model and the resulting smeared prediction (Figure 21) closely matches $E_{tm}(\alpha)$. Additionally, the predicted coastal energy values are within 20% of the measured values. However, this distribution underpredicts the band energies at SCI by a factor of 2. The true high frequency directional spectrum is most likely made up of components following the wind and "swell" near the mid frequency mode at 295-300°T. The SAR system is not expected to perform well under these spectral conditions.

The Stanford HF radar measurements, which map the 0.143 Hz waves travelly radially toward San Mateo Pt., show a sharp cutoff in energy density for deep ocean angles less than 256°T. These maps show roughly equivalent energy density values in the ranges 256-262°T and 277-284°T, which are open quadrants at this site. This information

does not help resolve the ambiguity in the deep ocean spectrum. However, the energy density in the open quadrant does not decrease along the propagation path from the deep ocean to the site. Therefore, the explanation of the 28 March observations as apparent spectral "dissipation" is unjustified.

IV.2 San Clemente Island Shadow

The presence of SCI should produce a relative gap in the directional spectrum at the coastal locations. The island refraction/blocking model predicts a coastal directional spectrum that has no energy density in this gap (Figure 4). Investigation into this characteristic feature of the refraction model does not require knowledge of the deep ocean directional spectrum.

SPL has operated various linear arrays at the TPB site. These arrays all had a total length of roughly 100 meters. The cumulative statistics from these arrays, see Pawka et al. (1976), showed a small directional gap associated with SCI. However, the poor resolution of these short arrays severely hampered the quantitative investigation of the gap, particularly at low wave frequencies. There were 3 independent high resolution directional measurement systems operating at the coast during this experiment. These systems were the SPL array, the SAR system, and the Stanford HF radar system. As discussed in Section II, the SAR spectra had noise level problems which effectively masked small secondary directional modes. Both the HF radar and the linear array had sufficient quality and resolution to investigate the directional gap.

The treatment of the various spectral estimators in Section II indicated that the MLE yields biased- high estimates of the energy in a trough between two spectral peaks. Forty-five consecutive 17.1 minute data records from the linear array on 5 March 1977 were analyzed for directional spectra using the MLE, IMLE, and MSWE method. The integrated energy density of a 1° band in the center gap direction, $E_g(f)$, was normalized by the band energy to yield a quantification of the gap definition. The comparative results as a function of frequency are shown in Figure 22. A sample plot of these directional spectra was shown in Figure 11.

All three estimators show (Figure 22) the same trends of gap definition, $E_g(f)/E_{tp}(f)$, with frequency. The MLE estimates are biased high relative to the results of the other two methods for all wave frequencies. The IMLE results also show a bias (high) tendency relative to the MSWE estimates in the frequency range 0.074-0.121 Hz. However, the IMLE estimates are in much closer agreement with the MSWE estimates than with the MLE results. The IMLE estimates show the sharpest gap definition at the lowest wave frequencies. Estimates from all three methods are in closest agreement for the highest frequencies analyzed.

The suppression of variance in the MSWE directional spectra was a consideration in the estimator design. However, the MSWE estimates of gap energy level were still much less stable than those of the IMLE and MLE methods. The directional spectra of 5 March were smoothed by averaging over N adjacent 17.1 minute runs. The value of N was increased until the average gap energy level of the 45/N groups

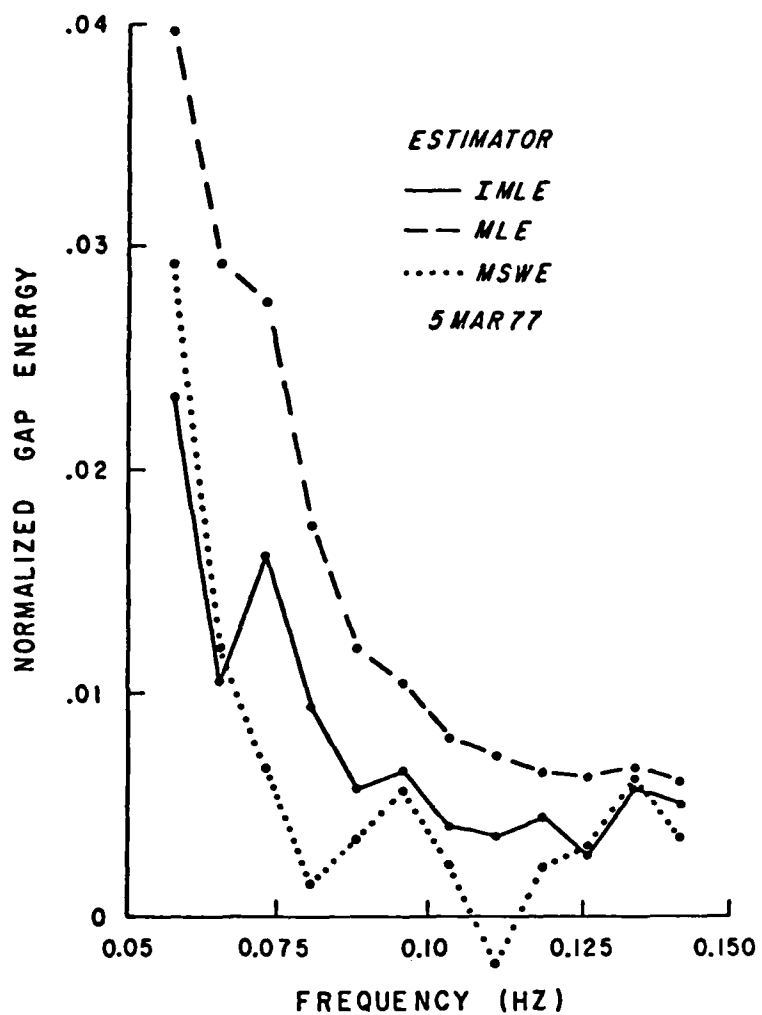


Figure 22. Normalized gap energy density on 5 March 1977. The gap energy $E_g(f)$, is normalized by the total band energy, $E_{tp}(f)$. The results are averaged over 14.3 hours on continuous data. The directional bandwidth is 1° and the frequency bandwidth is 0.0078125 Hz.

was roughly equal to the average over all 45 runs. The mean value of N required for stability was 5 runs with the MLE and 8 for the IMLE method. The MSWE estimates required averaging over 13-20 runs for stability. This result eliminated the possible use of the MSWE estimates in the investigation of trends of gap energy level over 8-10 hour data runs.

There were 10 high quality data runs sampled during the West Coast Experiment which had sufficient length to make stable estimates with the MSWE method. The results of the gap energy estimates averaged over the 10 continuous directional sample (CDS) days are shown in Figure 23. The sample variance of the gap energy estimates was calculated for the three frequency bands with average results roughly equal to zero. These variances were very consistent and were used to estimate the standard error bars shown on the plot. The average results significantly exceed the standard error bars in both the low and high frequency sections.

There is a trough which corresponds to SCI in the majority of the low frequency (0.059-0.074 Hz) directional spectra (Figure 24). The results shown in Figure 23 indicate a relatively high gap energy level for these frequencies. However, it is expected that resolution problems will be the most severe in this frequency range. Additionally, the expected directional gap in 10 meters depth is narrowed due to refraction over the local shelf. This process is most significant at low frequency.

The three directional spectrum estimators were tested for their response to typical directional forms obtained from the island

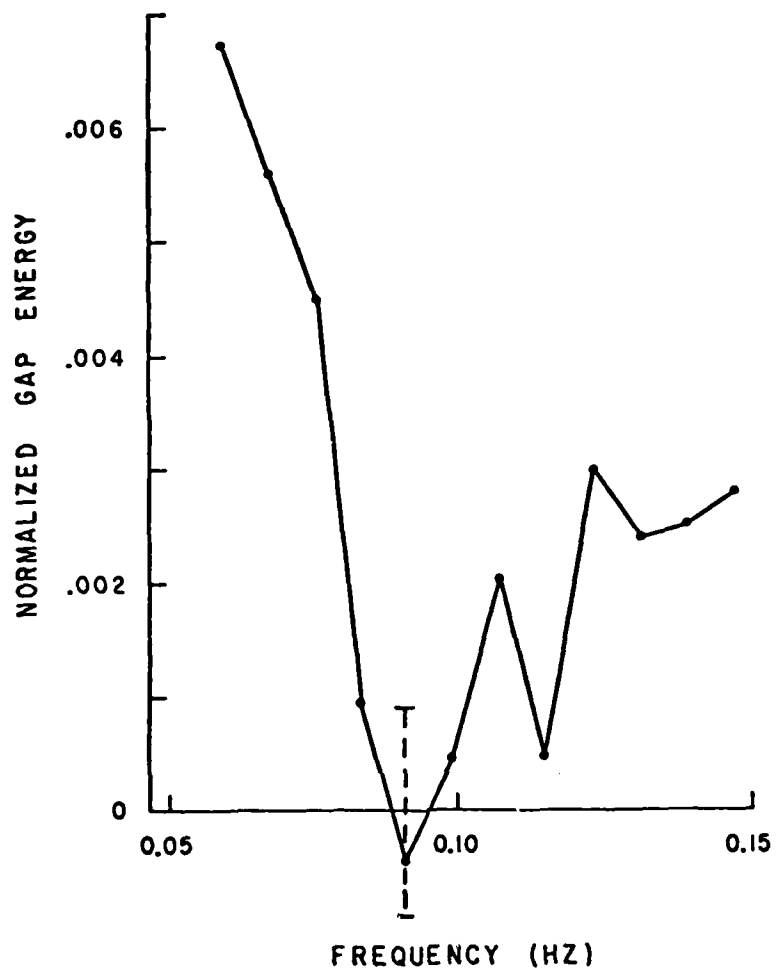


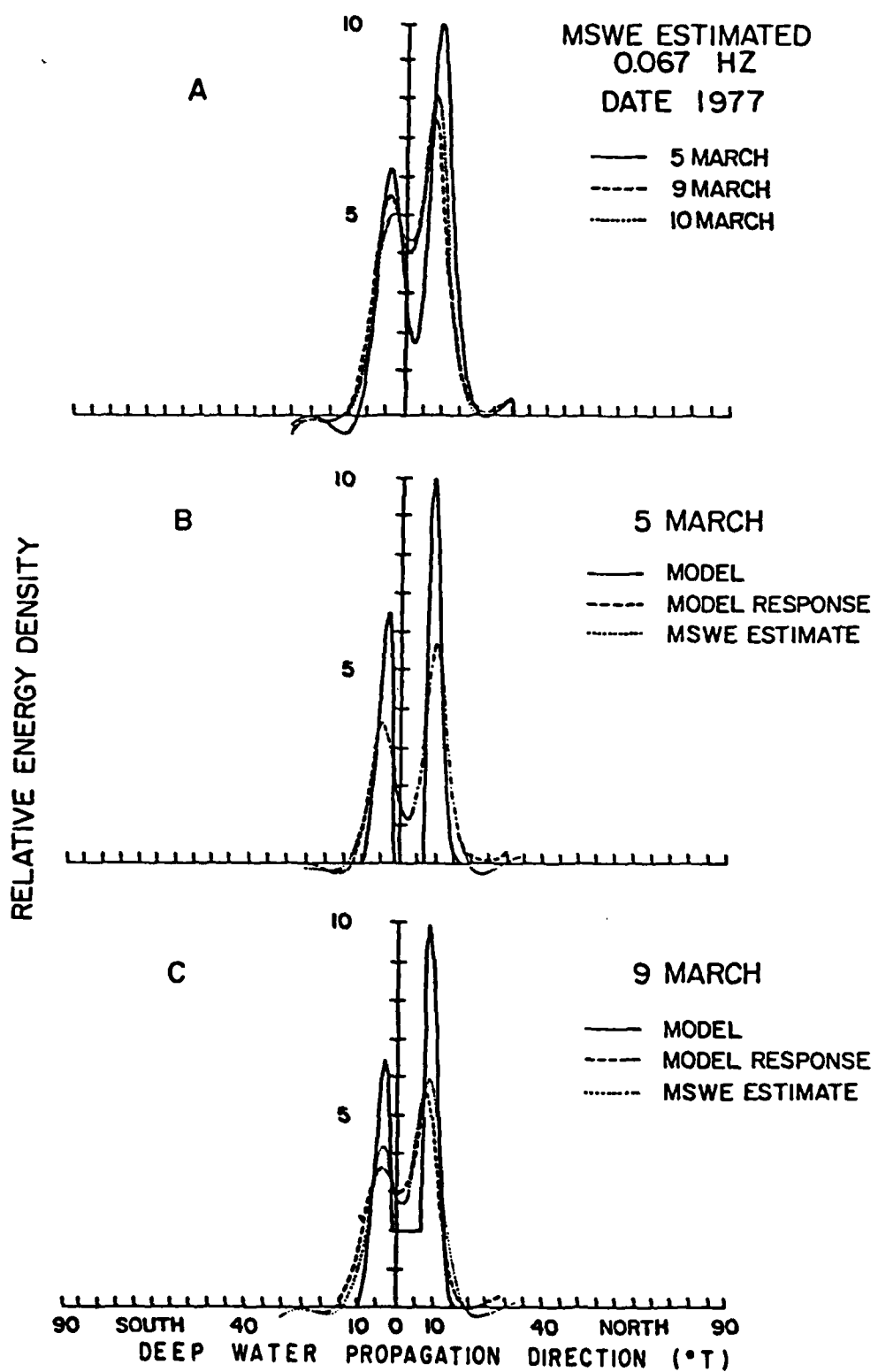
Figure 23. MSWE estimates of normalized gap energy (see Figure 22) averaged over 10 sample days of the West Coast Experiment. The error bars were obtained from the standard deviation of the estimates at 0.090 and 0.098 Hz. The bars reflect an estimate of the standard deviation of a null result.

model. These tests show incomplete definition of the gap at low wave frequencies. These problems are further complicated when significant south swell is present. The addition of a third directional mode increases the expected windowing errors. In fact, the spectra measured in the field at 0.059 Hz for several south swell dominated days (Figure 19) do not evidence a gap at all.

The directional spectra on 5, 9, and 10 March contain no significant south swell energy. The MSWE directional spectra at 0.067 Hz, shown in Figure 24a, have similar peak structure on these days. However, the definition of the directional gap does vary significantly. The gap is most evident on 5 March, the day with the least total wave energy and low frequency band energy. The MSWE directional spectrum in 10 m depth on 5 March is consistent with the simulated response to a directional model with an extremely low energy density level in the expected 8° gap. This comparison is shown in Figure 24b. Any narrowing of the gap or rise of gap energy density significantly alters the simulated response. Figure 24c shows the response to a model which has a gap energy density which is 20% of the peak value. An almost identical result is obtained with a narrowed gap that has the same integrated energy in the original gap directions. The response to the raised gap model compares well with $E_{tw}(\alpha)$ at 0.067 Hz on 9 March (Figure 24c).

Model testing of this sort is at best suggestive and does not verify the details of the true directional spectrum. However, extensive tests were performed using model directional spectra with various peak locations and widths. The level of the gap energy

Figure 24. a) MSWE estimates of the directional spectrum sampled in 10 m depth at Torrey Pines Beach. The data lengths for the runs are 14.3 hours on 5 March, 7.4 hours on 9 March, and 5.1 hours on 10 March. Also shown are the comparison of model spectra and the MLE filtered response to these models with the measured directional spectra on b) 5 March and c) 9 March. The spectra are normalized to equivalent area under the curves. The direction normal to the array is 264.5° T. The associated bandwidth of the frequency spectra was 0.0078125 Hz.



density on 5 March was consistently lower than the response to any model which had non-negligible gap levels. On the other hand, the MSWE spectra on 9 and 10 March could not be matched with models containing negligible gap energy density. It is judged that these measurements represent reliable observations of negligible and non-negligible levels of gap energy density in the low frequency wave regime. The limited number of observations does not allow for the investigation into the likely causes (e.g. nonlinear transfer) of the variability of the gap level. However, the indicated gap energy density values of roughly 20% are much greater than the expected values of wave reflection from the beach.

The averaged directional spectra in the frequency range 0.082-0.114 Hz evidence very low gap energy density. The MSWE spectrum at 0.114 Hz averaged over the 10 CDS runs, $\langle E_{tw}(\alpha) \rangle_{CDS}$ (Figure 25), shows negligible values for the deep water directions 269-271°T. These angles are close to the center of the SCI shadow (271°T) at these wave frequencies. $E_g(f)/E_{tp}(f)$ does vary over the sample but does not correlate with total wave energy, band energy, or wind speed. Additionally, the marked change in the results between 5 March and 9-10 March which occurred at the low frequencies was not evident in the mid frequency range. These results indicate a negligible level of gap energy density for the mid frequencies during these sample days which is consistent with the quantitative confirmation of the refraction/blocking model discussed previously.

The average level of gap energy density increases in the high frequency region of the spectrum. The normalized energy in the gap is

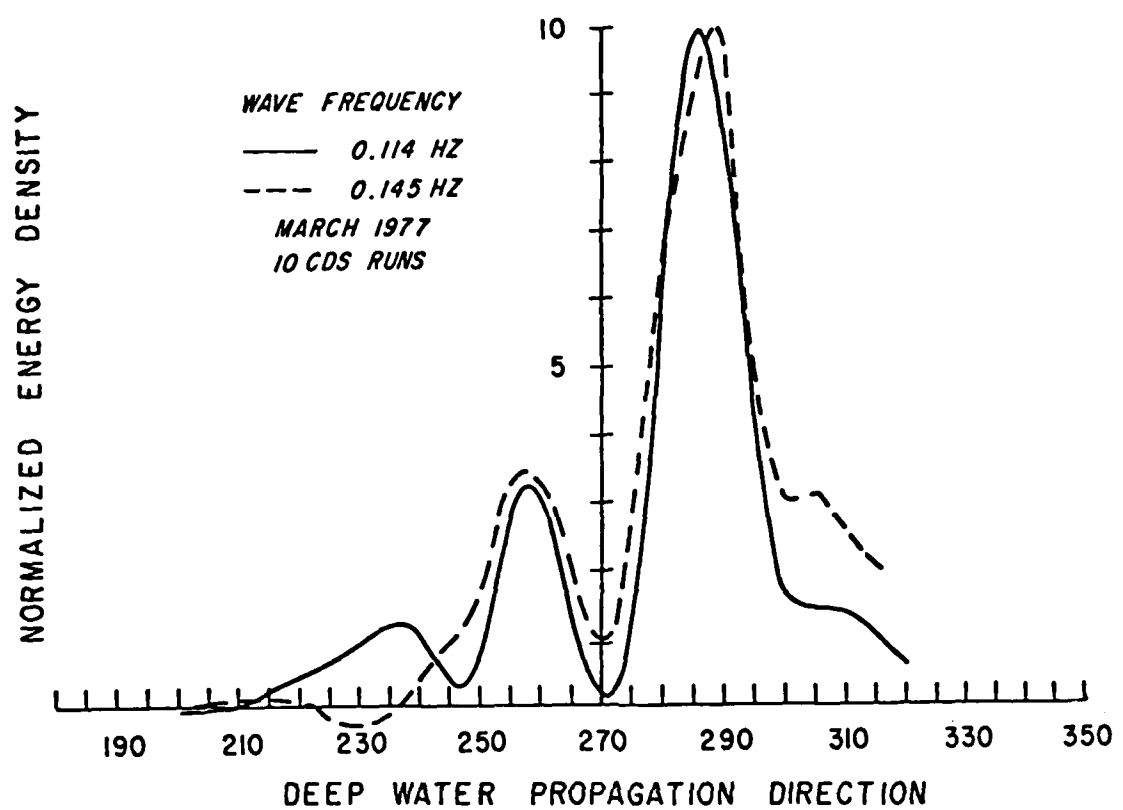


Figure 25. Average MSWE direactional spectrum estimates for the 10 CDS runs of the March 1977 experiment. The runs have a cumulative length of about 64 hours. The spectra are each normalized to a maximum value of 10 (relative units).

the most significant at 0.145 Hz, which is the highest frequency of routine analysis. $\langle E_{tw}(\alpha) \rangle_{CDS}$ at 0.145 Hz, also shown in Figure 25, has a trough centered on roughly $268^\circ T$. The location of this minimum is shifted slightly south of the mid frequency result.

The comparision of coastal and deep ocean frequency spectra on 25 March, discussed earlier, indicated the existence of local wave generation in the range 0.121-0.145 Hz. It was hypothesized that this generation resulted from energy supplied by the wind. The gap energy density values for frequencies 0.137-0.145 Hz do show a correlation of 0.80 with the NOSC wind speeds. This value is significant at the 99% level for a 10 point correlation. For these frequencies, the average correlation of the band energy with the wind is 0.45. The corresponding correlation of $E_g(f)$ with the winds at SCI is roughly 0.3. All of these correlation values drop to insignificant values at the mid frequency range. These observations are indicative of some control of the local winds over the high frequency energy in the gap.

25 March was the sample day which had the most high frequency energy density in the gap directions. The wind speeds were fairly uniform over the borderland region with averages of roughly 7 m/sec. Kitaigorodskii's relationship (equation II.12) for limited fetch generation yields an expected frequency of maximum energy density of 0.179 Hz for the 120 Km fetch from SCI to TPB. Using the maximum recorded values (10 m/sec), instead of the means, shifts this result to 0.155 Hz. The frequency- directional spectrum in the gap directions has a maximum value of $110 \text{ cm}^2/\Delta\alpha\Delta\text{Hz}$ at 0.149 Hz. The energy density drops sharply at lower frequency reaching values of 8

$\text{cm}^2/\Delta\alpha\Delta\text{Hz}$ at 0.125 Hz. The highest frequency analyzed, 0.153 Hz, had gap energy density of $90 \text{ cm}^2/\Delta\alpha\Delta\text{Hz}$. These peak energy density values are approximately 4 times the average over the 10 CDS runs. Although these peak frequencies are somewhat lower than the limited fetch values, the difference is not large compared to the spread of field observations summarized in Hasselmann et al (1973).

The effects of local generation on 25 March as indicated by the comparison of measured and predicted energy at the coastal sites, peaks at 0.137 Hz. This was also the peak frequency of $E_{tp}(f)$, shown in Figure 17, while the Begg Rock buoy had maximum values at 0.161 Hz. It is not surprising that this peak is at lower frequency than the peak of gap energy (0.145 Hz) because of the relatively large fetches (~300km) available at some of the directional sectors. This suggests a fundamental difference between local generation in a partially sheltered region and most typical cases of "limited fetch" which are concerned with wave growth away from an infinite wall. The growth of energy in the gap directions may well be affected by the energy in the unsheltered directional quadrants. In fact, the gap energy density at high frequency does trend (correlation, defined Table 9, $r=0.6$) with the ratio of the secondary to primary directional peak energy. However, this ratio is not independent from the local wind ($r=0.4$) so it is not certain if the relationship is causal. A larger data sample is required to investigate the functional dependence of gap energy on multiple parameters. All of these correlations drop to insignificant values at mid frequency.

The Stanford HF radar measurements support the general

observations at TPB on 25 March. These wave field maps, shown by Veseycky et al. (1980), display a distinct shadow of SCI. The center of the trough is on the southern side of the expected gap. The unsheltered energy coming through the northern window is the dominant peak. Veseycky concluded that HF measurements were consistent with non-negligible energy levels in the shadow. The energy density in the gap directions is shown to grow with distance leeward of the island. The trough/peak ratio increases from 0.05 at 50 km from the coast to 0.14 at 25 km. The corresponding value of that ratio (MSWE estimate) at TPB was 0.20. These trough/peak ratios are the maximum values recorded over the CDS runs of this experiment. Therefore, although the occurrence of high frequency energy in the gap directions has been demonstrated, the energy density is roughly an order of magnitude lower than the unsheltered values. However, wind events with roughly 2-3 times the speeds recorded on 25 March do occasionally occur in the region. These local storms are shown by Pawka et al. (1976) to be important features in the yearly wave climate and may exhibit further smearing of the island shadows.

IV.3 Northern Quadrant Window (270-295°T)

The primary window exposing TPB to the Northern Pacific wave generation regions is between SCI and the Santa Rosa Island group (Figure 1). The limits imposed by the islands' borders constrain the local directional spectrum to the range 277.5-291.5°T. San Nicolas Island partially blocks the window as it subtends the angles 280-282°T. The upper limit of this window cuts off a significant portion of the active storm regions of the North Pacific. However, the

refraction model indicates that some low frequency wave energy will spread into the window for deep ocean directions up to approximately 320°T.

The array data analysis showed the northern "window quadrant peak" to be a persistent feature in the spectrum at all wave frequencies (see e.g. Figure 25). The spectra for the 10 CDS runs were analyzed for the location and width (FWHM) of the window quadrant peak. The MSWE spectra resolve the peaks for a higher percentage of the available data than either the MLE or IMLE spectra. The average mode angles obtained from the three methods typically agree to 1-2°. The mode widths , analyzed for the 5 March data, agree to within 5° with the ordering MLE>MSWE>IMLE (Figure 26).

The average value and standard deviation of the MSWE estimates of the window quadrant peak parameters are listed in Table 10. Resolution problems at low frequency did not always allow for separation of peaks at FWHM. The results show the average mode direction to be in the very narrow range of 284-287°T. There seems to be little trend with frequency. The unaveraged mode directions have a range of 278-291°T which is consistent with the anticipated window limits.

The average and range in value of the percentage of band energy contained in the window quadrant sector, $E_w(f)/E_{tp}(f)$ (where $E_w(f) = \sum_{\alpha=275}^{295} E_{tp}(f, \alpha) \Delta \alpha$) are listed in Table 10. The importance of this peak varies as a function of frequency. The peak is most dominant in the mid frequency range. The island sheltering causes a very simple directional spectrum at TPB in the mid frequency range.

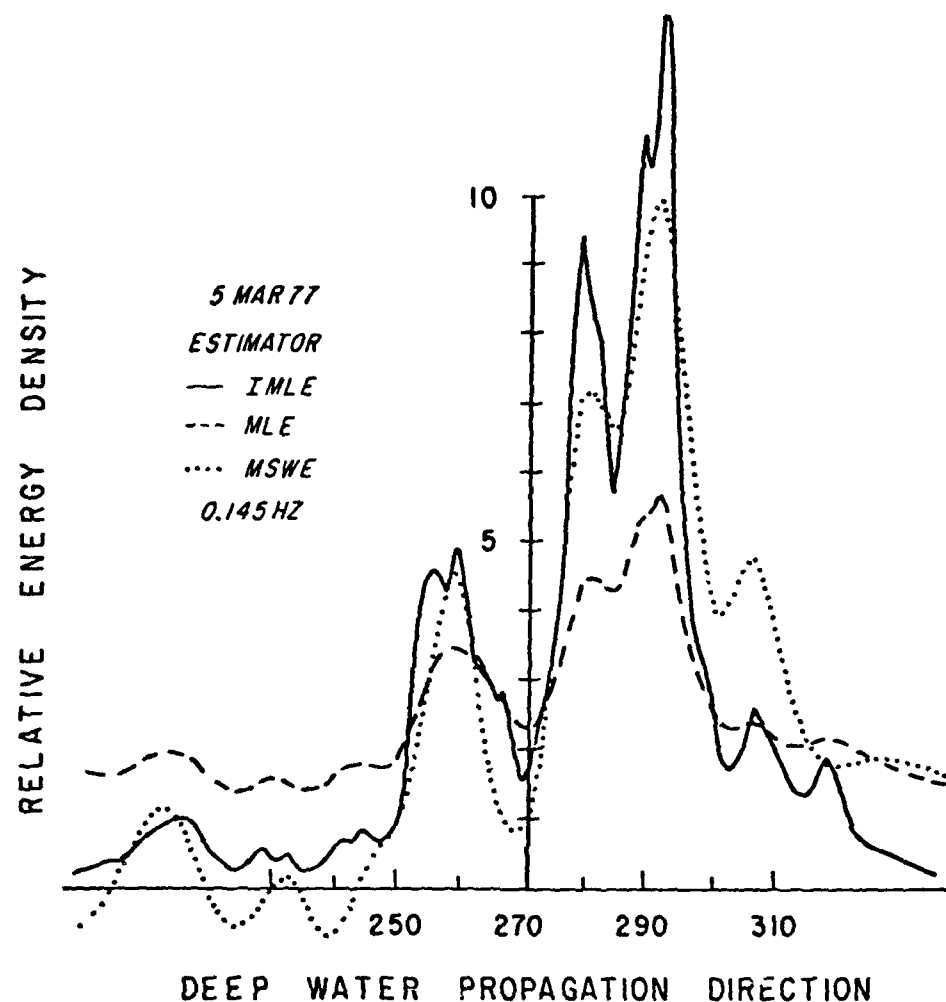


Figure 26. Estimates of high frequency directional spectrum using the MSWE, IMLE, and MLE methods. The data is averaged over 14.3 hours. The spectra are normalized to the same band energy.

Frequency (Hz)	$\langle \alpha_m \rangle$	Std(α_m)	$\langle \Delta\alpha_m \rangle$	Std($\Delta\alpha_m$)	Average	$E_w(f)/E_{tp}(f)$
0.059	292	3.9	-	-	-	-
0.067	286	2.5	26	3.9	29	11-46
0.074	288	2.8	21	3.8	45	14-57
0.082	288	2.9	16	1.6	65	31-83
0.090	288	2.8	14	2.3	74	56-94
0.098	287	2.5	13	2.8	70	64-82
0.106	287	3.1	14	2.6	63	56-80
0.114	286	3.2	14	3.7	60	51-72
0.121	286	4.6	16	4.6	64	55-75
0.129	287	4.0	15	4.4	63	48-74
0.137	288	3.5	16	4.4	62	49-76
0.145	287	4.9	16	5.5	61	51-82

Table 10. Statistics of the mode parameters of the northern window quadrant peak for the 10 cos runs. α_m is the mode angle, $\Delta\alpha_m$ is the width (FWHM), and Std is the standard deviation. All angles are given in degrees. Also given is the average and range of the percentage of band energy contained in the quadrant. The analysis was performed on MSWE directional spectrum estimates.

The expected limits to the northern quadrant window are actually a function of frequency due to refraction effects at the island edges. The theoretical window width varies from 14° at 0.145 Hz to a value of 9° at 0.067 Hz (neglecting San Nicolas Island). Also, refraction at low frequencies tends to concentrate energy density at particular directions within the window limits. These two factors should decrease the variance of the mode directions at lower frequency. This is roughly observed in the data. Departures from this trend may be due to changes with frequency of the variability of the deep ocean spectral properties.

The mid frequency directional spectra tend to have the smallest average window quadrant peak widths. The increase of peak width from mid to high frequency is consistent with the larger effective window width and broader deep ocean directional spectrum at higher frequencies. The average widths for wave frequencies 0.090-0.114 Hz are within $2-3^\circ$ of the expected window size. The variance of the peak widths increases sharply with frequency. This is consistent with the general decrease of refractive effects at higher wave frequency. Refraction not only reduces the maximum peak width but also tends to broaden very narrow directional peaks. The latter effect was discussed by Munk, et al. (1963). The shoals interior to the window will refract some wave energy to the site regardless of the deep ocean directionality. Therefore, the refraction effects have a tendency to make the peak width constant.

The average peak widths for the low frequency spectra are very much broader than the expected window size. Model testing suggests

that the increase of average width from mid to low frequency may be due to resolution problems. In particular, the width of a narrow secondary peak is consistently overestimated. This situation occurs frequently at the low frequencies when the northern component is small relative to the south swell. There is a strong linear relationship ($r=0.90$) between the standard deviation of the mode angles and the average mode width for wave frequencies 0.098-0.145 Hz. The low frequency values do not follow this trend.

The refraction model shows multiple sources of wave energy within the limits of the northern quadrant window (Figure 19). The sources are associated with energy refracted to the site by various shoal regions. The maximum separation of these peaks is 2-3° (deep water) which is not resolvable at these wave frequencies. Resultantly, the observed window quadrant energy is primarily contained in a smooth unimodal peak (see e.g. Figure 18). Therefore, the measurements are not generally adequate to investigate the directional fine structure indicated by the refraction results.

There is an infrequent occurrence of a split window quadrant peak at higher wave frequencies. Examples of this observation are shown in Figure 26. All three spectral estimators show the same basic structure in the primary mode. This spectral form was observed on 5, 9, and 10 March in the frequency range 0.129-0.145 Hz. The observed locations of these spectral features were averaged to yield values of 276°T and 287°T for the peaks and 280°T for the trough. These directions are roughly consistent with the expected blocking pattern (centered on 281°T) of San Nicolas Island. It is hypothesized that

resolution problems limit the observations of this apparent shadow to infrequent occurrences at higher wave frequencies. Closely spaced peaks are more readily resolved if they are of roughly equivalent amplitude. If the peaks are of dissimilar magnitude, there is a tendency for a smaller secondary peak to be smeared into the primary.

IV.4 Refraction Banks Quadrant (250-269°T)

The TPB directional spectra frequently have a significant secondary peak in the range 250-261°T (example, Figure 26). These directions correspond to the banks south and west of SCI which should be relatively strong sources of refractive wave energy. The analysis presented here is a statistical description of the "banks quadrant" peak characteristics. The results are checked for consistency with the island refraction analysis.

There are three banks quadrant peak characteristics which are of particular interest. These are peak location, width (FWHM), and energy relative to the window quadrant peak energy, $E_b(f)/E_w(f)$. The three directional spectrum estimators were intercompared for their relative performance in the analysis for these peak characteristics for 0.090 Hz waves on 5 March (a data set of 50 consecutive 17.1 minute runs). The average peak angle was 254°T for all three estimators. The average peak width was 8.9° for the IMLE, 12.4° for the MSWE, and 14.4° for the MLE. The ratio $E_b(f)/E_w(f)$ as a function of frequency is plotted in Figure 27. The same basic trends are shown by all three estimators. There is good agreement of the MSWE and IMLE methods in the frequency range 0.074-0.145 Hz while the MLE yields a relatively biased estimate. This tendency is consistent with the

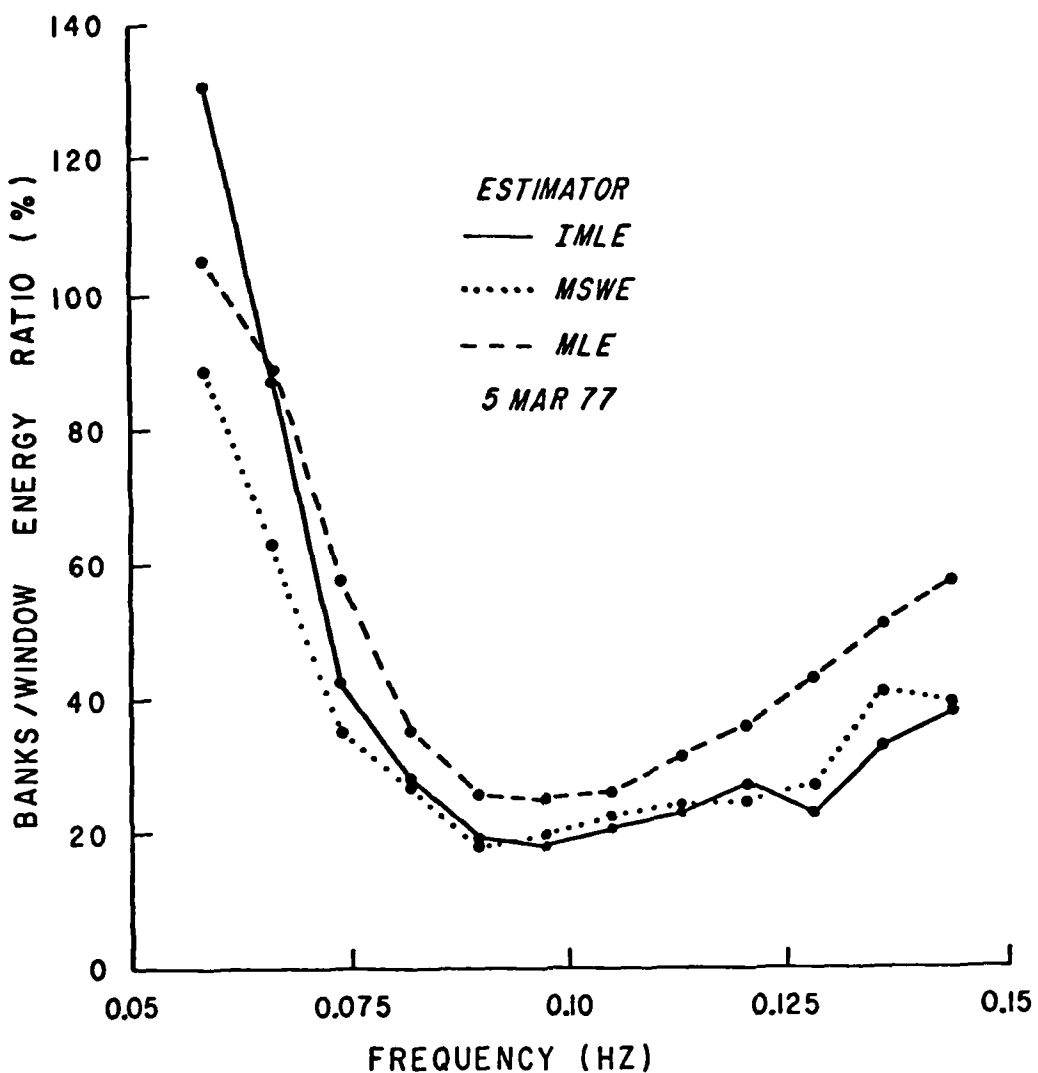


Figure 27. Ratio of the banks quadrant ($250-269^{\circ}$ T) to northern window quadrant ($270-296^{\circ}$ T) energy for the various directional spectrum estimators. The data were averaged over 14.3 hours on 5 March.

model testing of the estimators. The MSWE estimates were judged adequate for the analysis of peak characteristics.

The values of $E_b(f)/E_w(f)$ obtained from the island refraction/blocking model predictions are compared with the measured values in the frequency range 0.082-0.114 Hz in Table 11. This was the frequency range which showed good agreement of the measured band energy at TPB with that predicted with the unimodal approximation of the deep ocean directional spectrum. The predictions made with the full SAR spectrum, $E_r(a)$, yield a strong overemphasis of the banks quadrant (Table 11). The average unimodal prediction of $E_b(f)/E_w(f)$ shows close agreement with the measured values, particularly those estimated with the MSWE and IMLE methods. However, the predicted values do not show the same trends with frequency as the measured values. The ratio of southern/northern energy in the deep ocean radar spectra has a distinct minimum near 0.090-0.098 Hz on the two sample days. This is reflected to some degree in the full spectrum predictions of $E_b(f)/E_w(f)$. This apparent change in the deep ocean spectrum is not adequately accounted for by the unimodal representations.

The MSWE directional spectra for the 10 CDS runs were analyzed for the banks quadrant peak characteristics and the results are displayed in Table 12. The peak was resolved in 83% of all the spectra and in 100% of the spectra for frequencies greater than 0.09 Hz. Resolution of the banks quadrant peak was lost at low frequency when a significant south swell peak, with offshore directions of about $230^\circ T$, was present in the spectrum. The average peak angle was around

BANKS/WINDOW ENERGY RATIO

Date	Frequency (Hz)	PREDICTED		MEASURED		
		$E_r(\alpha)$	$E_u(\alpha)$	IMLE	MSWE	MLE
25 March	0.082	109.	59.2	18.2	21.9	25.4
	0.090	41.5	17.1	17.1	19.8	26.6
	0.098	93.9	15.4	19.6	17.2	28.2
	0.106	79.5	6.8	24.2	29.3	29.6
	0.114	77.3	5.4	31.9	29.4	35.3
	AVERAGE	80.2	20.8	22.2	23.5	29.0
28 March	0.082	136.	16.9	12.2	10.9	20.1
	0.090	136.	4.7	8.6	9.2	15.0
	0.098	93.5	12.2	9.3	15.6	14.4
	0.106	111.	9.8	8.6	17.8	15.5
	0.114	96.1	5.9	13.3	14.4	20.8
	AVERAGE	114.5	9.9	10.4	13.5	17.2

Table 11. Comparison of the predicted and measured values of the banks/window energy ratio (%), $E_b(f)/E_w(f)$. The predictions were made using the SAR spectrum, $E_r(\alpha)$, and a unimodal approximation, $E_u(\alpha)$, as the deep ocean inputs into the island refraction/blocking model. The measured values were obtained with three directional spectrum techniques.

Frequency (Hz)	$\langle \alpha_m \rangle$	std(α_m)	$\langle \Delta\alpha_m \rangle$	std($\Delta\alpha_m$)	$\langle \alpha_c \rangle$	std(α_c)
0.059	254	-	-	-	240	-
0.067	251	-	-	-	240	-
0.074	252	1.4	20	-	241	-
0.082	254	1.9	17	2.0	247	1.8
0.090	255	3.5	16	3.2	248	4.2
0.098	257	3.3	16	3.1	249	3.8
0.106	256	2.3	14	3.3	249	3.6
0.114	257	2.4	14	5.0	250	5.6
0.121	258	2.6	14	4.9	251	5.1
0.129	258	3.1	15	6.9	249	6.5
0.137	258	3.4	16	8.5	249	8.0
0.145	257	3.1	13	5.3	250	5.0

Table 12. Statistics of mode parameters for the banks quadrant peak and the 10 cds runs. α_m is the mode angle, $\Delta\alpha_m$ is the width (FWHM), and α_c is the southern cutoff at half maximum (all in degrees). std indicates the standard deviation and the brackets indicate the mean value. The analysis was performed with the MSWE directional spectrum estimator.

252°T for the wave frequencies. This is consistent with the anticipated strong refraction over Cortez Bank. This result shifts to roughly 257°T for wave frequencies greater than 0.090 Hz.

The mean and standard deviation of the ratio $E_b(f)/E_w(f)$ are also listed for the various frequencies in Table 12. The mean ratios have the same basic trend with frequency as displayed in the 5 March data. The drop in $E_b(f)/E_w(f)$ with increasing frequency in the range 0.067-0.098 Hz is an expected feature of the refraction of high angle north swell. All indications, which include current meter data at Tanner Bank, aerial photography, and the SAR spectra show the approximate mode angle of the deep ocean waves to be in the range 295-310°T throughout the experiment. However, the sharp rise in $E_b(f)/E_w(f)$ at 0.106 Hz is not anticipated with a constant (with frequency) deep ocean spectrum.

The analysis results for each sample day show a distinct minimum in the ratio $E_b(f)/E_w(f)$ in the mid frequencies. The frequency of the minimum varies from 0.082-0.121 Hz but is usually in the vicinity of a local minimum in $E_{tp}(f)/E_{br}(f)$. Consistency of these observations with the refraction model results requires a broadening or southern shift in direction of the north swell at frequencies higher than the local minimum.

Figure 5 shows that the ratios $E_b(f)/E_w(f)$ and $E_{tp}(f)/E_{br}(f)$ may trend in the same or opposite sense as a function of the characteristics of $E_{do}(\alpha)$. The SAR spectra on 25 and 28 March indicate a relatively narrow average offshore distribution with mode directions near 300°T. For these conditions, the ratios $E_b(f)/E_w(f)$

and $E_{tp}(f)/E_{br}(f)$ vary strongly in the opposite sense in response to both changes in offshore mode direction and width. The correlation of the ratios was calculated over the 10 CDS runs. The results show values of roughly -0.3 in the range 0.074-0.082 Hz, -0.7 for 0.090-0.098 Hz, and values near 0.0 to 0.2 at higher frequency. The lower frequency values are assumed to be contaminated with south swell. The values for 0.090-0.098 Hz are felt to be mild confirmation of the expected refraction trends. Any one of three factors, a southern shift or broadening of $E_{do}(\alpha)$, or a decrease in the importance of the refractive energy, may cause the relatively abrupt change of correlation at 0.106 Hz. As mentioned previously, the ratio of the southern to northern quadrant energy in the SAR directional spectra does show a distinct minimum near 0.090 Hz on both sample days.

The banks quadrant peak widths are greatest at the lower wave frequencies. As with the window quadrant peak, resolution problems are the expected cause of this result. There is no real trend to the widths at mid to high frequencies. The average width for these frequencies is 14.8° , which is slightly greater than the expected $10-12^\circ$ spread due to refraction. The variance of the peak widths increases sharply at 0.114 Hz. This result evidences the decrease of refractive control over the banks quadrant peak shape. This conclusion can best be shown by considering the southern cutoff of the peak at a value half the peak maximum. The average southern cutoff is in the range $248-251^\circ T$ and has little trend with frequency. However, the standard deviation of the cutoff is 2.9° below 0.114 Hz and 6.1° above. The low frequency results are more consistent with the purely

refracted wave spectrum which cuts off sharply at 251°T.

Both the theory discussed in Section II and the data presented here have shown the occurrences of values of $E_b(f)/E_w(f)$ greater than 1.0 at lower wave frequencies. The 0.059 Hz spectrum on 5 March has a peak structure very similar to the curves shown in Figure 24 except that the southern mode is actually dominant. The measured values of $E_{tp}(f)/E_{br}(f)$ of roughly 0.05 indicates that the bulk of the deep ocean energy is shadowed. Mode angles obtained from the Tanner Bank current meter indicate directions of 305-320°T throughout the low frequency range. The island refraction analysis indicated that a southern dominated bimodel form at TPB can be caused by high angle ($\alpha_{do} > 300^\circ T$) north swell. The southern mode may also be in response to low levels of deep ocean energy in the directional range 250-270°T. This second explanation is rejected due to the relatively low energy levels at Oceanside and Imperial Beach which have significantly more open exposure in these quadrants than the TPB site.

IV.5 Inter-Island Fetch (296-320°T)

The coastline and borderland islands are configured so that there is no direct exposure at TPB to deep ocean swell with angles greater than 291°T. Refraction theory and data analysis discussed earlier show that some of the high angle ($\alpha_{do} > 291^\circ T$) northern energy is refracted to the site from various banks and shoals. Inspection of the refraction "cross-sections" indicate that all of the significant refracted wave energy is contained within the angles 250-291°T. A sharp cutoff at 291°T is seen in most of the local directional spectra, see e.g. Figure 25.

There is a possibility of wind generation of waves in the ocean east of the borderland islands. TPB has a 13° sector, bounded by Santa Catalina Island (298°T) and San Pedro Point (311°T) for which the fetch has a minimum length of roughly 240 km (Figure 1). The directions 301.5-308°T have the maximum fetch values of 280 km. The available fetch drops off rapidly for directions greater than 311°T.

There was a common occurrence of significant peaks in the directional range 298-311°T in the higher frequency spectra. On five of the ten CDS runs the 0.137 Hz spectra contained a peak near 303°T with energy density values at least 30% of the spectral maximum. This direction is roughly the center of the sector with maximum available fetch. The peak widths (FWHM) fall in the range 16-20°. Figure 28 is a plot of 0.137 Hz spectra analyzed with the MLE, IMLE, and MSWE methods. All three estimates indicate a well defined peak at 302°T. The IMLE and MSWE spectra agree well in the partition of energy amongst the various peaks.

The average energy associated with the directions 296-320°T, $E_f(f)$, is plotted as a function of frequency in Figure 29. This plot shows relatively high average values in the high and low frequency regions. $E_f(f)$ at low frequency is primarily due to the broadening of the primary mode, discussed earlier, rather than the occurrence of a separate peak. This effect is most likely due to resolution problems. The values of $E_f(f)$ in the frequency range 0.124-0.145 Hz correlate well ($r=0.7$) with the wind speeds at SCI. This correlation drops to insignificant values at lower frequencies ($f<0.114$ Hz). $E_f(f)$ at high frequency is less correlated ($r=0.3$) with the NOSC winds. These

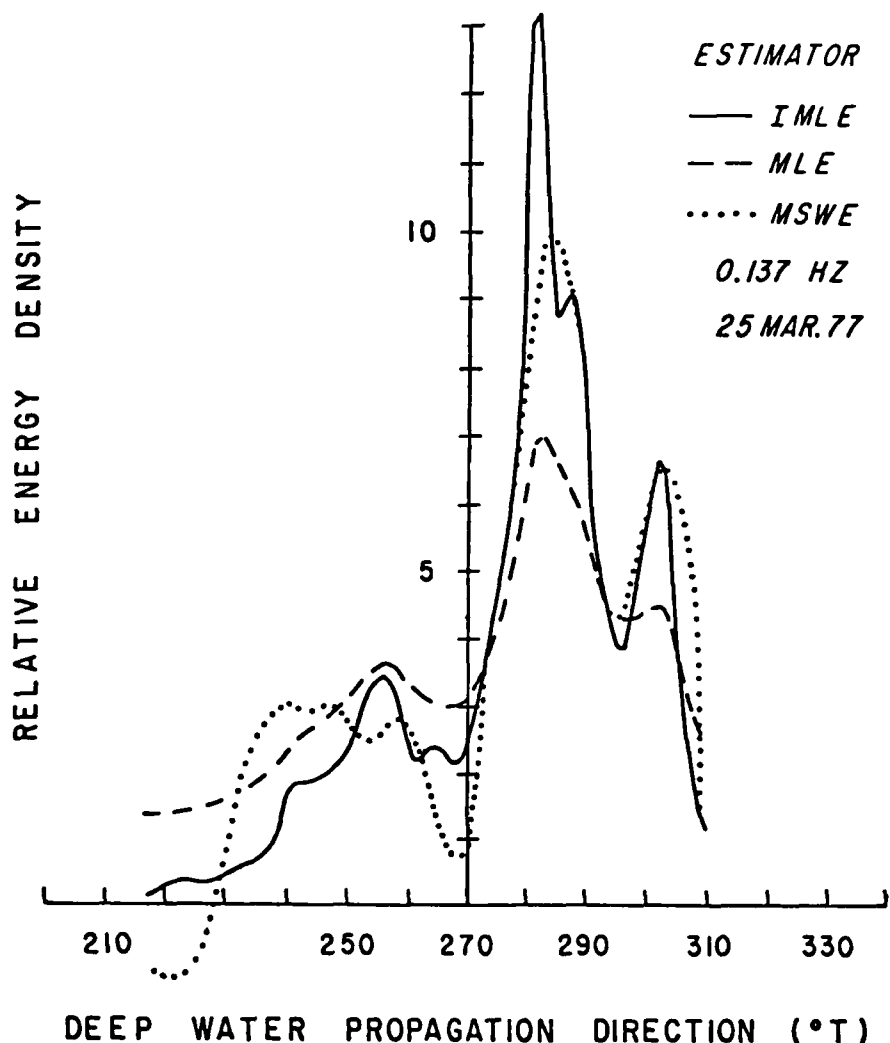


Figure 28. Directional spectrum estimates for the various methods.

The estimates are averaged over 6.8 hours with a frequency spectrum bandwidth of 0.0078125 Hz. The area under the curves is normalized to the same band energy.

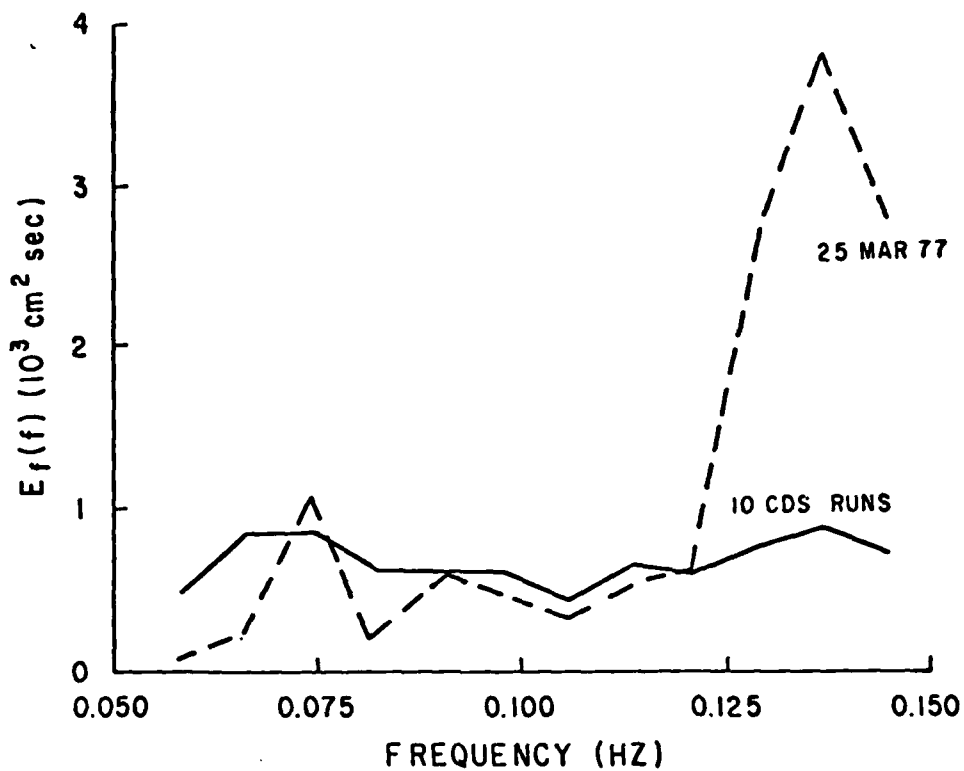


Figure 29. Wave energy associated with the inter-island fetch ($296\text{-}320^\circ T$) for 25 March and the average over the 10 CDS runs. The data were averaged over 6.8 hours on 25 March and about 64 hours for the 10 CDS runs. The frequency spectrum bandwidth is 0.0078125 Hz. MSWE directional spectrum estimates were used for the analysis.

trends follow the results developed earlier for the relationship of $E_{tp}(f)$, TPB band energy, with the general wind field.

The high frequency values of $E_f(f)$ are greater than their average on only two sample days, 10 March and 25 March. The ratio $E_f(f)/E_{tp}(f)$ is in the range 0.2-0.3 for the high frequency spectra on these days. The Kitagorodskii relationship (equation II.12) for an unrestricted fetch of 250 km yields a peak frequency of 0.14 Hz for the 25 March wind conditions. This compares well with the peak frequency of $E_f(f)$, also shown in Figure 29. $E_f(f)$ at the peak frequency (0.137 Hz) is equal to $3.7 \times 10^2 \text{ cm}^2/\Delta\text{Hz}$.

The trough located at roughly 293°T in the spectra of Figure 28 corresponds with the location of Santa Catalina Isl. There is more apparent energy density in these directions than in the SCI shadow (270°T). However, the expected gap at 293°T is only 40% as wide as the one at 270°T . There is not a trough associated with Santa Catalina Isl. evident in the HF spectrum sampled on this day at San Mateo Pt. (see Vesecky, et al., 1980). This is suggestive that the measured differences in the gap levels at TPB are significant.

IV.6 Southern Quadrant ($180-249^\circ\text{T}$)

The site at TPB is partially sheltered from the southern quadrant by Pt. La Jolla (Figure A.1). Refraction analysis shows that the 0.059 Hz deep ocean energy in the directional range $180-230^\circ\text{T}$ is funneled into the deep water directions $238-245^\circ\text{T}$ at the site. This local topography, coupled with the banks and shoals in the island region, leave only the directions $250-251^\circ\text{T}$ open to unaffected exposure at 0.059 Hz. The theoretical southern cutoff due to the

point varies monotonically from 238°T at 0.059 Hz to 200°T at 0.145 Hz.

Low frequency south swell ($\alpha_{d0} < 250^{\circ}\text{T}$) is significant in the wave climate at TPB during all the seasons (Pawka et al., 1976). South swell is generated by high latitude storms in the South Pacific and typhoons in the equatorial region. The typhoons are active in the eastern part of the ocean in the late summer and in the west during the winter. Typical distances to the tropical disturbances off Baja California of 1-3 10 km represent the shortest propagation path for south swell energy to the local coast.

Southern quadrant energy at TPB, $E_s(f)$, was dominant in the 0.059-0.067 Hz directional spectra on 7 of the 10 CDS runs of the West Coast Experiment. The southern limit of the mode directions did vary monotonically from 236°T at 0.059 Hz to 227°T at 0.082 Hz. The peak frequency of $E_s(f)$ varied from 0.059-0.074 Hz. $E_s(f)$ drops markedly in the range 0.082-0.098 Hz. This is consistent with the observation of a sharp increase in propagation "attenuation" for $f > 0.08$ Hz observed by Snodgrass et al (1966). It was hypothesized that this attenuation is due to nonlinear transfer of energy in the near storm region. The directional spectra for several wave frequencies on 25 March are plotted in Figure 30. The southern shift in the peak directions from 0.059 Hz to 0.074 Hz is expected with a deep ocean source at 220°T , an observed mode in the deep ocean SAR spectrum. $E_s(f)$ generally increases slightly at frequencies higher than 0.098 Hz. The IMLE directional estimates (Figure 30) show that $E_s(f)$ is not contained in a well directed peak at higher wave frequencies, but

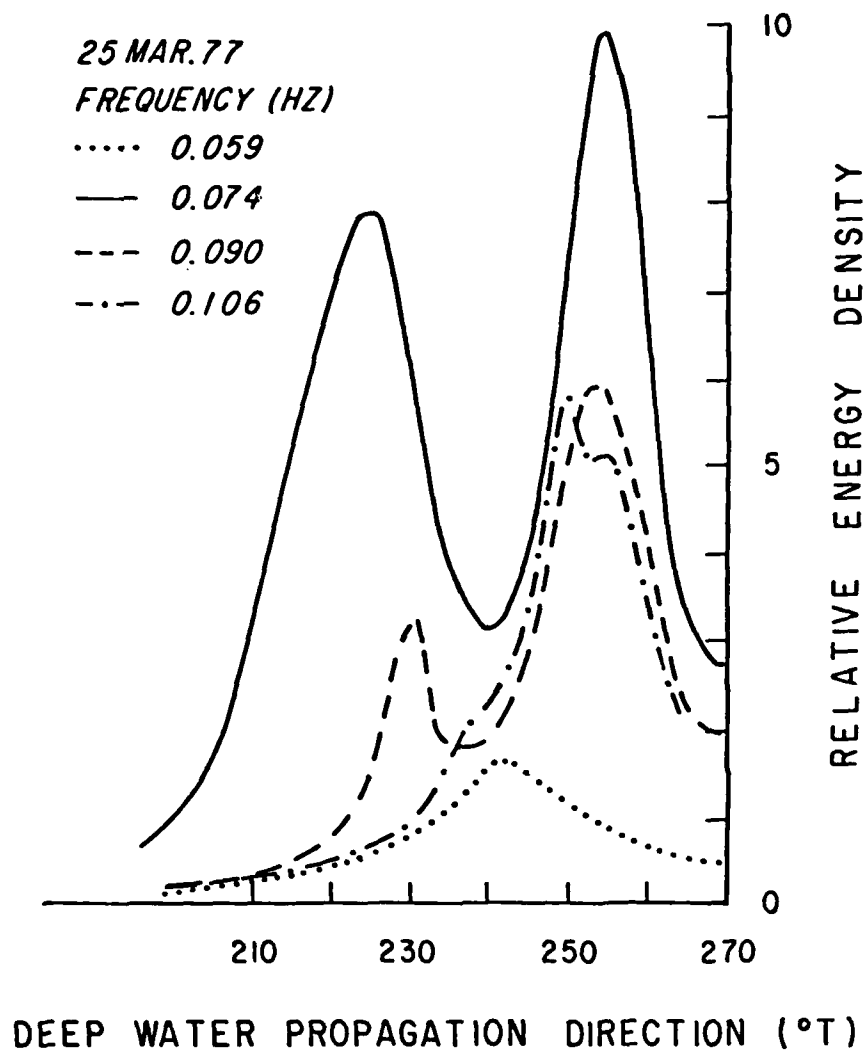


Figure 30. IMLE estimates of directional spectra for various frequencies on 25 March. The spectra are normalized by their respective band energy.

rather is due to a broad background level.

The IMLE directional spectrum at 0.059 Hz on 25 March does not resolve a peak in the banks directions from the south quadrant mode. Therefore, the distribution is broader than expected for waves from a fairly distant source. These two peaks are resolved at 0.074 Hz which yields a distinct trimodal directional form. A very narrow southern peak is measured at times. An example of a very narrow low frequency south swell is treated later in this work (see Figure 33).

IV.7 Conclusions

The borderland islands are shown to have a profound effect on the coastal wave conditions. The wave energy at the coast is typically an order of magnitude lower than in the deep ocean. The data also showed significant variations in the comparative energy levels. The general comparisons of the field data with the transformations of deep ocean to coastal wave conditions obtained from the island refraction/blocking model were not good. The low quality of the comparisons is linked with the relatively high noise level in the SAR directional spectra which were used as estimates of the deep ocean conditions.

A unimodal representation of the deep ocean SAR spectrum was also used as an input to the island refraction/blocking model. The unimodal predictions of both total band energy and directional structure (relative strength and location of directional modes) at TPB agreed well with the data in the frequency range 0.082-0.114 Hz. This agreement is viewed as a first order confirmation of the island refraction model in this frequency range. South swell and local wind

effects restrict the application of the unimodal approximations to this frequency range.

No tested representation of the deep ocean directional spectra yielded predictions which agreed well with the measured data at Oceanside. Blocking of the north swell at this site makes the local spectrum at this site very sensitive to low background levels in the southern quadrant. The general quantitative verification of the island refraction/blocking modeling of the transformation of deep ocean to coastal wave conditions will require stable, high resolution directional spectra in the region west of the islands. A unimodal approximation of the deep ocean directional spectrum is not generally adequate for use in wave predictions on this partially sheltered coast.

The qualitative effects of wave refraction by the island topography are confirmed for the low frequency wave regime. In particular, strongly bimodal directional distributions at Torrey Pines Beach are shown in response to north swell. The southern mode, which is due to refraction of the north swell to the site by Cortez and Tanner Banks, is occasionally the dominant peak. The low frequency refraction can theoretically supply up to 5-20% of the deep ocean energy that would have otherwise be sheltered. The qualitative evidence shows no significant refraction effects for wave frequencies higher than 0.106 Hz. At these frequencies, the refraction process can theoretically spread only 1% of the deep ocean energy for sheltered deep ocean directions.

The windowing and refraction effects of the island topography

tend to channel the mid to low frequency wave energy into certain well defined quadrants at Torrey Pines Beach. These effects cause persistent energetic modes at 280-287°T (northern quadrant window) and 251-258°T (refractive banks peak) in response to north swell. In one sense this ordering represents a large decrease in the potential randomness of the local directional spectrum. The directional spectra at 0.098 Hz are consistently dominated by the narrow window quadrant mode. On the other hand, strongly bimodal spectra, centered on near normal incidence, are virtually guaranteed at low frequency in response to north swell. These spectral forms result in complicated forcing of surf zone dynamics, as will be discussed in Section VI.

Analysis with the MSWE estimator showed consistently negligible energy density in the shadowed quadrant corresponding to San Clemente Island for wave frequencies 0.082-0.114 Hz. These observations are compatable with coastal wave prediction models which consider only the interaction of waves with island topography. There is evidence of significant levels of energy density in the shadowed directions in both the high and low frequency regions of the spectrum. The high frequency "gap energy density" correlates well with the local wind. The maximum level of energy denisty in the shadowed directions is seen to be roughly 20% of the peak level in the directional spectrum.

Wave generation by winds in the borderland region is shown to be important in this data set for frequencies greater than 0.12 Hz. The high frequency band energy at the coast can actually exceed the deep ocean values during periods of local front activity. The most

important qualitative feature of the local wave generation is the formation of a high angle peak in the northern quadrant of the directional spectrum. This peak is due to generation of waves in the inter-island fetch. These high angle waves are of particular importance in the longshore transport of sand.

Several nearshore wave characteristics, including the southern cutoff of the banks quadrant peak, the relative size of the southern quadrant energy, and the ratios $E_b(f)/E_w(f)$ and $E_{tp}(f)/E_{br}(f)$, all indicate a broadening deep ocean source for frequencies greater than 0.098 Hz. These observations are consistent with the general increase of the ratio of southern to northern quadrant energy in the SAR directional spectra (due to the demphasis of the north swell peak) at roughly the same frequency. The high frequency cutoff of the well directed south swell was also near this wave frequency.

The three directional spectrum estimators employed, the MLE, MSWE, and IMLE methods, intercompare well on the location of significant modes in the spectrum. Up to four distinct modes in a single spectrum are located in a consistent fashion by all three methods. Additionally, the mode distributions are consistent to within 2-3° with the physical limits of the directional windows. This agreement is consistent with the uncertainty in the array alignment. The MLE method biases the relative size of a secondary mode in the spectrum. The IMLE and MSWE methods agree well in the partition of band energy amongst the various spectral peaks for wave frequencies greater than 0.067 Hz. Both the MLE and IMLE methods bias high the estimate of the energy density in a deep spectral trough. However,

the IMLE method does show marked improvement over the MLE method in the estimation of this spectral property. All three estimators show the same basic trends of the various spectral properties with wave frequency. The anticipated resolution problems at the lowest wave frequencies ($f < 0.074$ Hz) degrades the quantitative performance of all three estimators.

V MOMENTUM FLUX ESTIMATION

V.1 Introduction

The longshore transport of sand by wind generated waves is a phenomenon of considerable importance in the dynamics of shoreline evolution. The problem of deriving a relationship between the energy supplied by the waves and the resulting longshore currents and sediment transport has been approached both theoretically and empirically. Bowen (1969) and Longuet-Higgins (1970a,b) relate longshore currents to on-offshore variations in the onshore flux of longshore directed momentum, S_{yx} . Several investigators, including Komar and Inman (1970), have worked empirically with the relationship for longshore transport

$$I_1 = K_0 (C S_{yx})_b \quad (V.1)$$

where I_1 is the immersed weight transport rate, K_0 is a constant, and b denotes evaluation of the parameters at depth of wave breaking. Good quality field data is fairly rare because both the sediment transport rate and S_{yx} are difficult quantities to measure.

The onshore flux of onshore directed momentum, S_{xx} , is also an important forcing function in surf zone dynamics. For example, Dorrestein (1961) showed that wave set-up and set-down are associated with on-offshore gradients in S_{xx} . However, accurate estimates of S_{xx} are readily obtained from integration of crude directional spectrum measurements when the waves are near normal incidence to a linear array (generally true for nearshore arrays). Therefore, attention is focused on the more difficult problem of making accurate estimates of

S_{yx} .

S_{yx} can be expressed as a function of frequency and related to the following moment of the frequency-directional spectrum

$$S_{yx}(f) = n(f) \int_{\alpha} E(f, \alpha) \sin \alpha \cos \alpha d\alpha \quad (V.2)$$

$$S_{yx} = \rho g \sum_f S_{yx}(f) \Delta f \quad (V.3)$$

where the ratio of group to phase speeds is expressed as a function of frequency, $n(f)$, and ρ = the density of seawater. There are significant sampling problems involved in the measurement of the directional spectrum (see e.g. Barber, 1963) and many approximate forms have been used for the estimation of $S_{yx}(f)$. Several investigators, including Caldwell (1956) have used visual observations of the breaker angle in the estimate

$$S_{yx} = \rho g n(f_0) E \cos \alpha_b \sin \alpha_b \quad (V.4)$$

where f_0 is the observed "average" wave frequency. There is no known mathematical relationship between this estimate and the definition given in equations V.2 and V.3. Komar and Inman (1970) used the phase difference between pairs of wave sensors for the estimation of breaker angle used in equation V.4. The weighting of this average angle, however, is not the same as the directional weighting in the spectral moment of equation V.2 and significant errors are expected with complicated directional spectra. More accurate results are expected with the use of this technique if the waves are approximately unidirectional.

Many analysis techniques have been used for the calculation of the directional spectrum from wave array data. Dean (1974) compared the use of the Barber window (equation II.29) with the W2 smoothed scheme (Panicker,1971) for the estimation of $S_{yx}(f)$ (equation V.2). His results indicated the superiority of the Barber window with expected errors of less than 10% for unidirectional waves. Pawka (1977) demonstrated $S_{yx}(f)$ estimation errors in the range 5-40% for the Barber window with directional spectra of finite width. These results indicated better relative performance of the MLE method. This data adaptive estimator was shown to be particularly accurate in the estimation of $S_{yx}(f)$ with the conditions of narrow directional spectra.

The directional moment given in equation V.2 can be obtained directly (independent of a directional spectrum estimate) from sensor systems which measure orthogonal components of wave velocity or sea surface slope (see e.g. Longuet-Higgins,1963). Examples of these systems include the tilt buoy, orthogonal axis current meter, and the slope array introduced by Seymour and Higgins (1977). These "orthogonal component" systems have relatively poor resolution power for the definition of the directional spectrum. The poor resolution would render these systems inadequate for the detailed study of the directional wave properties discussed in Section IV. Therefore, an investigation was made into the methods of extraction of accurate values of $S_{yx}(f)$ from a linear array of sensors.

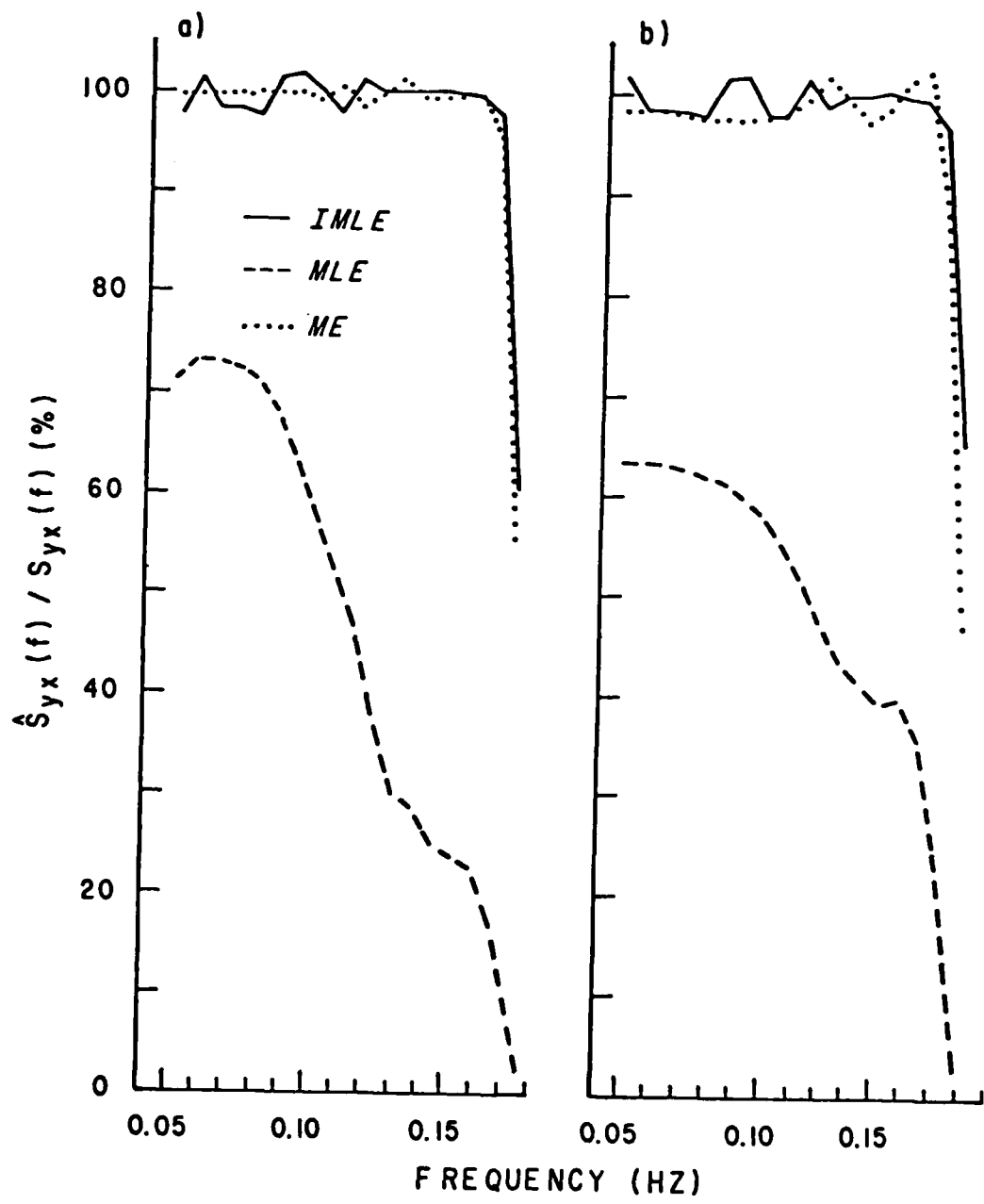
$S_{yx}(f)$ can be obtained from a linear array by integration of the various directional spectrum estimators (equation V.2).

Additionally, the ME_v method was introduced in Section II.2.4 as a processing technique for accurate estimates of $S_{yx}(f)$ from linear array data. The various linear array methods were subjected to extensive deterministic and random simulation tests to compare their relative error in $S_{yx}(f)$ estimation. The results of these tests are reported in this section and in Appendix B. The simulation test results indicate extremely accurate results from the IMLE and ME_v methods while the MLE method yields biased estimates. Below, two field tests are used for the comparison of the various $S_{yx}(f)$ estimates obtained from the linear array with results from other systems (slope array and current meter). Although these systems theoretically yield low bias estimates of $S_{yx}(f)$, they have not been previously field tested.

V.2 Field Comparisons with a Slope Array

In June of 1977 a slope array was aligned within a 1-2-4-5 linear array, see Figure 13, for the intercomparison of the $S_{yx}(f)$ estimates obtained from the two systems. The 1-2 configuration subarray was used for the primary comparisons to the slope array to minimize bias from possible spatial homogeneities in the wave field. However, comparisons of the 3 and 5 sensor linear systems were made for selected sets of the data. The response of the MLE, IMLE, and ME_0 (no noise rejection) methods was tested for various deterministic spectral forms and the results showed roughly equivalent accuracy of the 3 and 5 sensor systems. Figure 31 shows the model response of the various $S_{yx}(f)$ estimators to a typical directional form. The IMLE and ME_0 methods show similar accuracy while the MLE results are biased

Figure 31. Estimates of $S_{yx}(f)$ made with the MLE, IMLE, and ME_0 methods in response to a strongly bimodal test spectrum (TS-2, Figure B.7). The estimates are normalized by the true test value of $S_{yx}(f)$. The results are for: a) 1-2-4-5 linear array of length 396 m, and b) 1-2 linear array of length 99 m.



tow. The three estimators were also tested in response to simulated random cross-spectra (the procedure is discussed in Appendix B). The random simulation tests showed approximately the same variance for all three methods. The variance of the ME_v estimates with this array configuration decreased slowly with the increasing values of v_n .

The directional moment associated with $S_{yx}(f)$ is directly proportional to the cross-spectrum of the orthogonal components of sea surface slope

$$C_{n_x n_y}(f) = K^2 \int_a E(f, \alpha) \cos \alpha \sin \alpha d\alpha \quad (V.5)$$

where $C_{n_x n_y}(f)$ is the co-spectrum of the x and y components of slope. The slope array uses short sensor lags (~6m) for the estimation of the orthogonal slope components. The only fundamental bias in this measurement is the finite difference approximation of the sea surface slopes. The expected errors associated with this approximation are a function of K versus the size of the sensor lags but should be very small (less than 1%) for the wave frequencies considered in these comparisons. Higgins et al.(1981) analyze the expected errors of the slope array system.

A high quality continuous data run lasting 2.6 hours was taken on 10 June. The average frequency spectrum for this run is dominated by a very narrow low frequency peak (Figure 32). There is a wide variety in forms of $E(f, \alpha)$ as a function of frequency. Figure 33 is a plot of the MLE and IMLE estimates of the directional spectra for 2 wave frequencies on 10 June. The data set was divided into 9 segments of length 1024 seconds for the analysis of the frequency spectra,

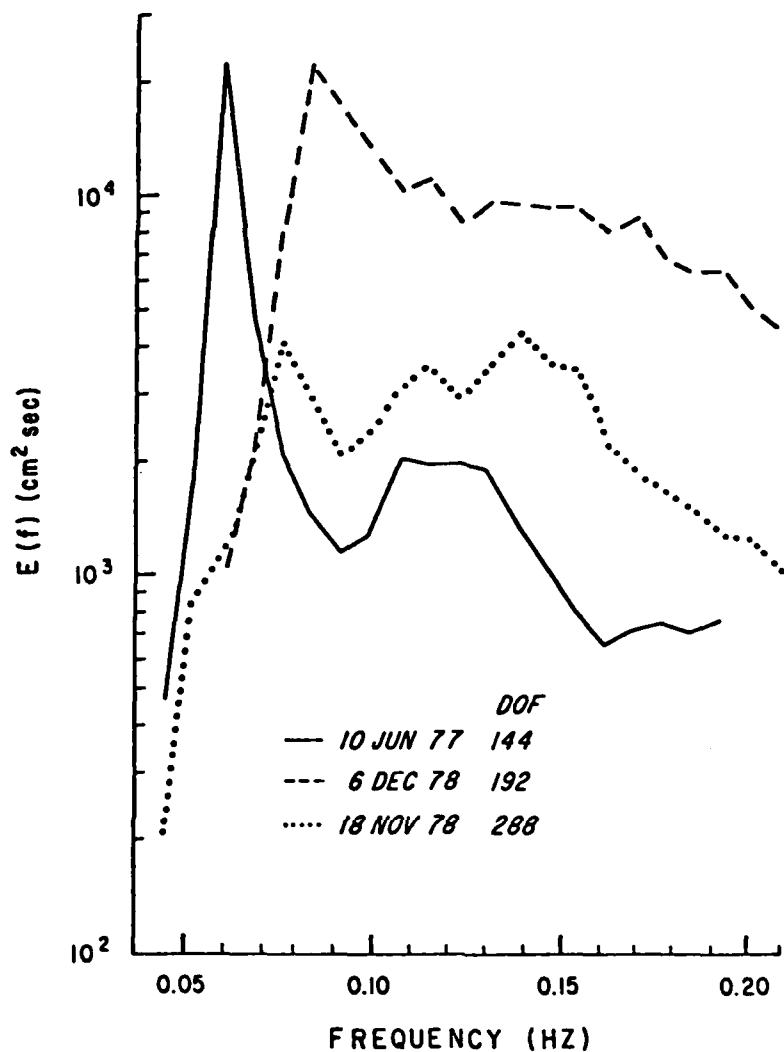
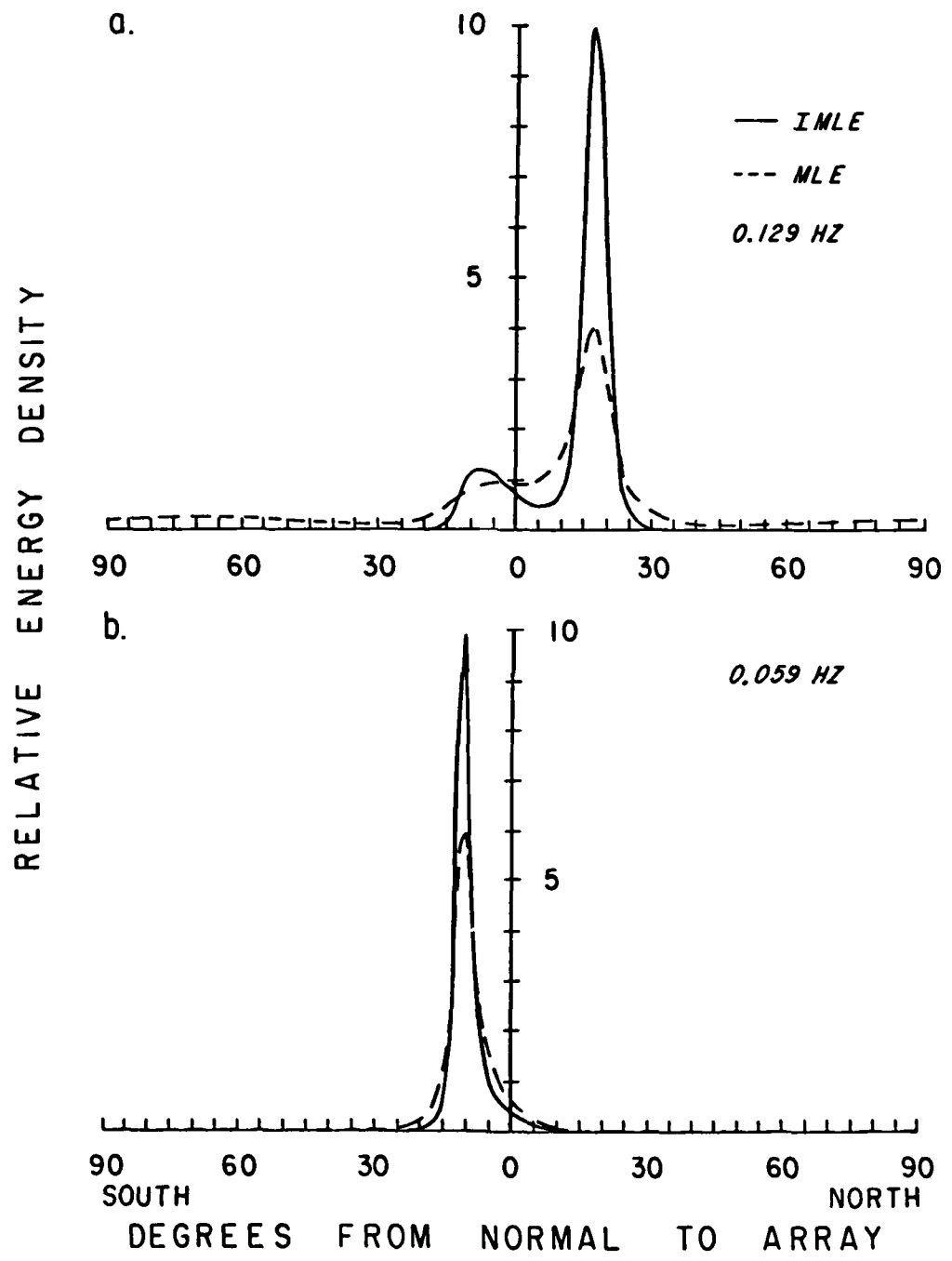


Figure 32. Average frequency spectra for the $S_{yx}(f)$ estimation comparison data sets. The 10 June data was sampled at the 9.6 m array depth while the Nov.-Dec. 1978 runs were obtained from the 5.7 m depth pressure gage. DOF indicates the degrees of freedom resulting from the spectral averaging.

Figure 33. IMLE directional spectrum estimates from the 1-2 linear array for the average of 9 consecutive 17.1 minute data segments on 10 June 1977. The estimates are for a mean depth of 9.6 m.



directional spectra, and $S_{yx}(f)$. The spectral smoothing employed yielded 16 DOF with a bandwidth of 0.0078 Hz.

The original analysis of the 10 June data, presented in Higgins et al.(1981), showed a relatively poor general agreement between the "slope" estimates of $S_{yx}(f)$ and the linear array results analyzed with the MLE method. Figure 34 shows the comparison of the $S_{yx}(f)$ estimates for wave frequencies ranging from 0.051-0.168 Hz. The discrepancy between the results of the two systems is particularly large for the higher wave frequencies.

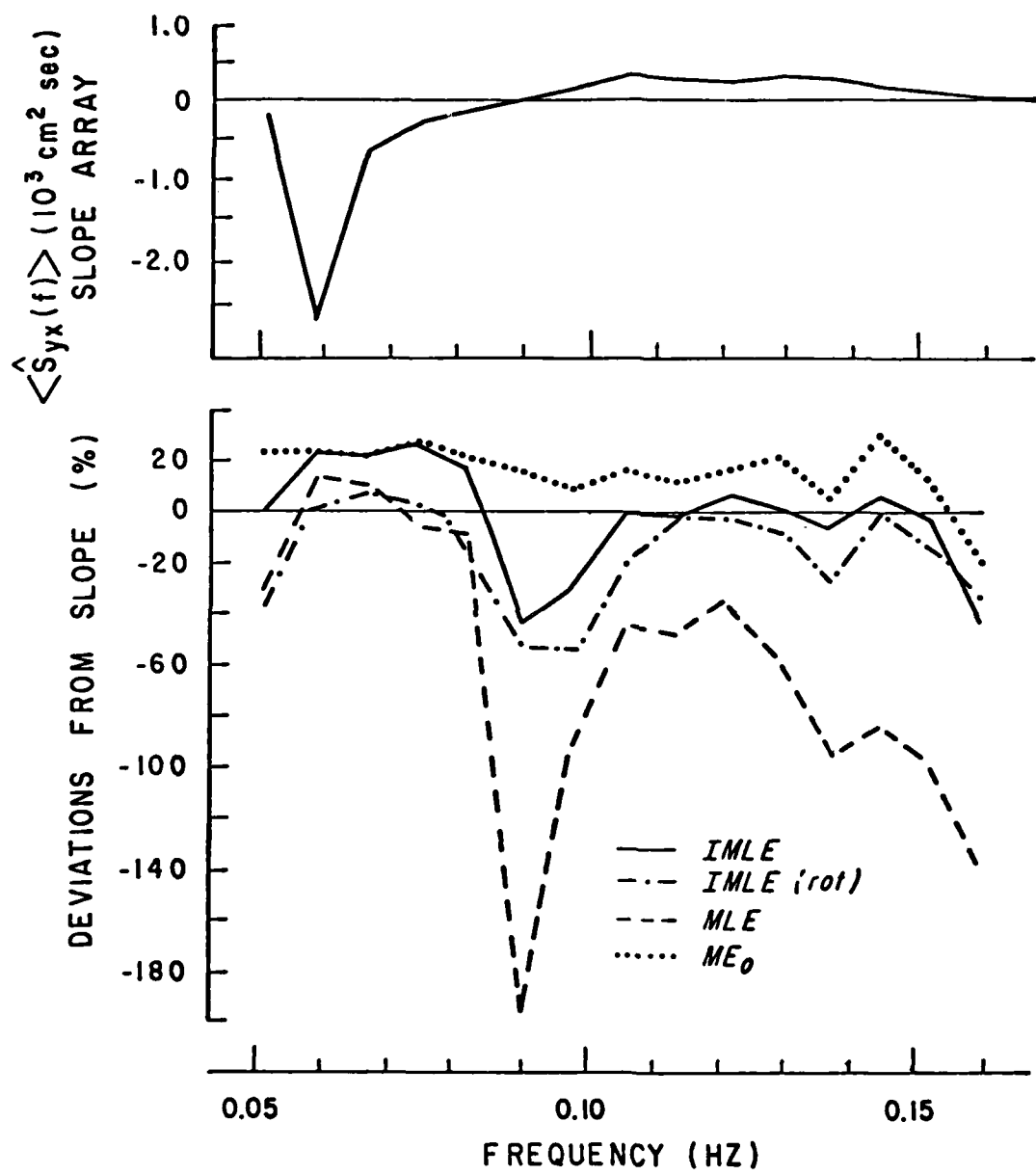
The results obtained from the IMLE and ME_0 methods are also shown in Figure 34 and show much closer general agreement with the slope estimates. The most dramatic improvement is in the high frequency region of the spectrum. The ME_0 estimates appear to be slightly biased high in this frequency range. The normalized square deviation (NSD) of any two estimates is defined

$$NSD = \left(\frac{E_1 - E_2}{E_1 + E_2} \right)^2 \quad (V.6)$$

where E_1 and E_2 are the two estimates. The values may also be compared by the rms deviation which equals $(NSD)^{\frac{1}{2}}$ given in %. The quantitative intercomparisons of the various $S_{yx}(f)$ estimates for wave frequencies 0.098-0.145 Hz are listed in Table 13. The ME_v estimates show increasing correlation with the slope results for increasing values of v_n up to 3.5. However, the rms deviation of these estimates shows a minimum for $v_n=1.0$. This is in rough agreement with the results from the simulation tests reported in Section II. Too much noise rejection degrades the resolution to the extent that $S_{yx}(f)$ is

Figure 34. a) Slope array estimaes of $S_{yx}(f)$ for the average of 9 consecutive 17.1 minute data runs on 10 June 1977.

b) Deviations of the various linear array $S_{yx}(f)$ estimates from the slope results. The deviations are defined as (array estimate-slope estimate)/average estimate given in percent. The results are shown for the MLE, IMLE, and ME_0 methods. Also shown are the IMLE deviations with a 2 degree rotation in the 33 m lag of the array.



not well estimated. The high frequency estimates of the ME₁, slope, and IMLE methods agree to an average of roughly 7-8%. Note that the MLE estimates are biased significantly low with rms deviations of 40-100% throughout this frequency range.

The average sample variance of the various estimates is also shown in Table 13. The IMLE, slope, and ME₁ estimates show approximately the variability. The MLE estimates are much more stable. However, the MLE estimates do not correlate as well with the slope results as either the IMLE or ME_v estimates.

The intercorrelation of the estimates from the various methods is very high ($r \sim .99$) at the peak of the frequency spectrum ($f=0.059$ Hz). However, the various linear array methods show significant bias relative to the slope estimates. The average directional spectrum for the 0.059 Hz waves, shown in Figure 33, is a very narrow unimodal distribution. The MLE should provide fairly accurate $S_{yx}(f)$ estimates with this form of the directional spectrum. As expected with these conditions, there is not much relative change in the IMLE and ME_v results compared to the MLE estimates. The correlation of the ME_v and slope estimates peaks at values of v_n equal to 0.3. The ME₃ estimates at 0.059 Hz fall between the MLE and IMLE values.

The deterministic and random tests of unimodal spectral forms, discussed in Appendix B, showed the MLE estimates of $S_{yx}(f)$ to always be biased low. The fact that the MLE estimates of $S_{yx}(f)$ are greater than the slope estimates for 0.059-0.067 Hz (Figure 34) coupled with the very close agreement of the various array estimates in this range suggests possible errors in the experimental set-up creating a bias

	Estimator Pairs					
	MLE-S	IMLE-S	ME ₀ -S	ME _{1.} -S	ME _{2.} -S	ME _{1.} -IMLE
RMS Deviation	69.2	4.7	17.9	6.8	14.2	4.9
Correlation	0.77	0.91	0.81	0.83	0.84	0.93
$\hat{S}_{yx}(f)$	Estimator					
	S	MLE	IMLE	ME ₀	ME _{1.}	ME _{2.}
Mean ($10^2 \text{ cm}^2 \text{ sec}$)	2.36	1.27	2.35	2.78	2.35	2.08
Variance ($10^4 \text{ cm}^4 \text{ sec}^2$)	0.63	0.43	0.58	0.68	0.63	0.42

Table 13. Quantitative comparison of various linear array estimates of $\hat{S}_{yx}(f)$ with slope array (S) results for 10 June 1977.
 RMS Deviation = $(\text{NSD})^{1/2}$ where NSD is defined in equation V.6
 All quantities are averaged over the frequency range 0.106-0.153 Hz.

between the slope and linear systems. One possible source of bias between the sensor systems is the relative orientation of the sensor lags. The slope array was physically aligned with the 66 m lag of the linear array, see Figure 13, leaving only the orientation of the 33 m lag as a possible source of error. The directional spectra and $S_{yx}(f)$ estimates were calculated for different assumed orientations of the 33 m lag to test the sensitivity of the estimates. The changes in the $S_{yx}(f)$ estimates for the IMLE estimates are shown in Figure 33 and indicate relatively strong sensitivity in the low frequency region. The rotation significantly improves the low frequency comparisons while causing relatively small changes in the high frequency tail.

Although it is not desired to estimate the expected errors of the systems with this rotated configuration, it is a strong possibility that this rotation explains the discrepancies in the low frequency range. An error of roughly 1 m in the location of either sensor in the 33 m lag will cause a discrepancy of 2° in orientation. This is the approximate accuracy of the sensor locations.

Relatively low values of $S_{yx}(f)$ result when the directional spectrum is strongly bimodal and centered about normal incidence to the coast. This spectral condition exists for the frequency range 0.082-0.090 Hz where the emphasis in the spectrum is shifting from southern to northern dominance (Figure 33). The IMLE and MLE methods have particular problems in the estimation of $S_{yx}(f)$ with these spectral forms. The IMLE estimates in this range deviate from the slope results by values up to 30%. The MLE results have deviations up to 100%. The ME₀ and ME₁ estimates show significantly improved

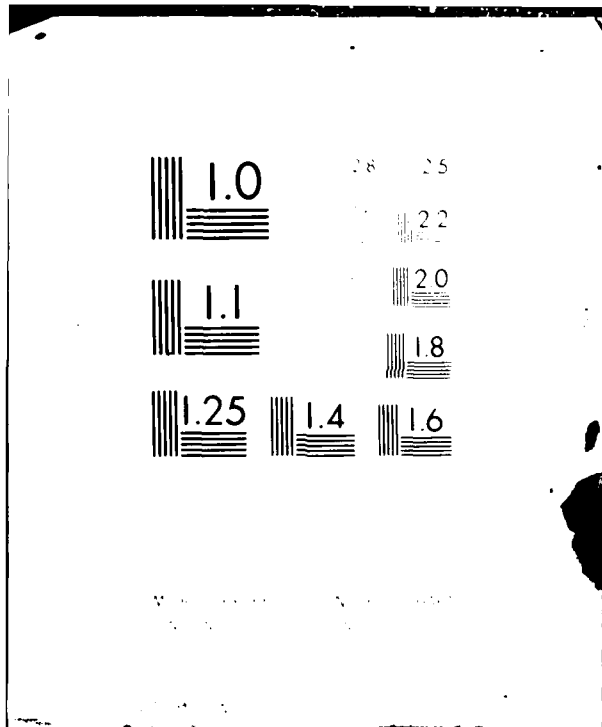
AD-A113 385 SCRIPPS INSTITUTION OF OCEANOGRAPHY LA JOLLA CA SHOR--ETC F/G 8/3
WAVE DIRECTIONAL CHARACTERISTICS ON A PARTIALLY SHELTERED COAST--ETC(U)
1982 S S PAWKA N00014-75-C-0300

UNCLASSIFIED

3 of 3

AD A

END
DATE
FILED
105-82
DTIC



agreement with deviations within the values of 20% and 10% respectively.

There is a design problem in the decision of what value of v_n to use in the general application of the ME_v method. The numerical simulation tests and field data comparisons indicate that the value of v_n which results in minimum bias with the slope system varies with wave frequency and directional spectrum form. However, the value of v_n which yields the minimum bias with the slope estimates was close to 1.0 for most of the mid to high frequency range. Also, the ME_1 results at low frequency differ from the ME_0 estimates by only 10%. Therefore, a constant value of v_n can result in accurate estimates of $S_{yx}(f)$ for a variety of wave frequencies and spectral forms with this array configuration.

The 1-2-4-5 sensor array was also used for the analysis of directional spectra for selected frequency bands. The MLE estimates of $S_{yx}(f)$ obtained from the 2 linear arrays (1-2 and 1-2-4-5) deviated by a mean value of 8.4% for the frequencies dominated by south swell (0.059-0.074 Hz) and 15.8% for the higher frequency northern waves (0.106-0.153 Hz). The IMLE analysis of the directional spectra for the 2 arrays at frequencies 0.059 and 0.158 Hz yielded somewhat closer agreement of the $S_{yx}(f)$ estimates. The rms deviation of the IMLE estimates of $S_{yx}(f)$ with the 2 arrays is 3.4% (for these two frequencies) as compared to 7.9% for the MLE results. There is a small amount of spacial inhomogeneity indicated as the 5 sensor directional results are always shifted south relative to the 3 sensor estimates. The measured bias in $S_{yx}(f)$ estimates correspond to

angular differences of less than 1°.

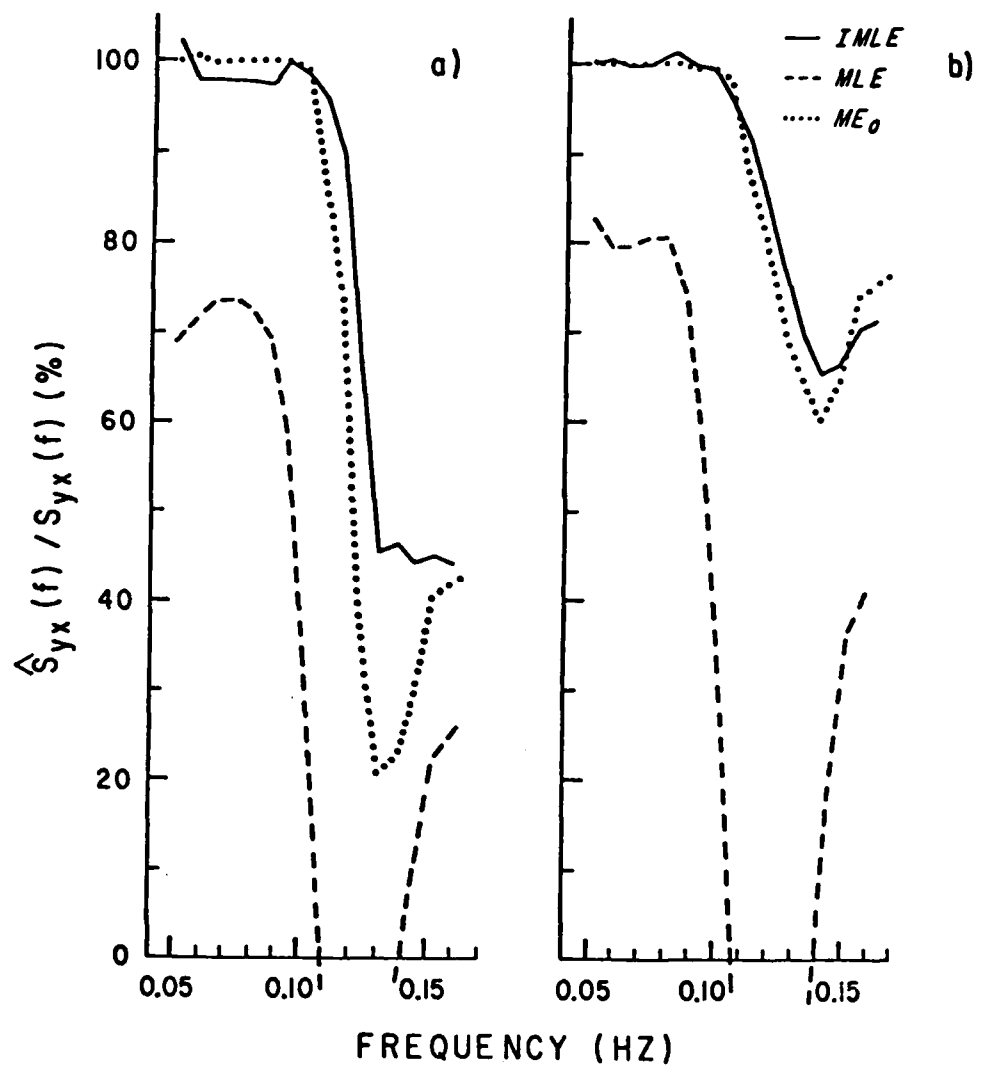
V.3 Field Comparisons with a Current Meter

The Nearshore Sediment Transport Study (NSTS) conducted an intensive field experiment at the TPB site during the month of November 1978. Approximately 60 instruments, including pressure sensors, wavestaffs, and current meters, covered the shelf region from 10 meters depth to the swash zone. The experiment was designed for the investigation of fluid dynamics and water-sediment interaction in the surf zone. Gable (1980) gives the details of the experimental set-up, sensors employed, and the data recorded.

Detailed statistics of the incident wave field were necessary for support data to the surf zone study. These "offshore" wave measurements were made by a linear array of pressure sensors in 10 meters of water and a biaxial electromagnetic current meter and pressure sensor in a mean depth of 5.7 meters. The layout of the sensors is shown in Figure 13. The array had a 2-2-2-5 configuration with an integral lag equal to 33 meters. A shorter lag was planned but not realized because of errors in sensor placement.

The expected directional performance of the 2-2-2-5 array is seriously degraded in the higher frequency bands relative to the 1-2-4-5 array. Figure 35 is a plot of the $S_{yx}(f)$ estimates obtained from the MLE, IMLE, and ME_0 methods with the NSTS array configuration for two test spectra. The performance of all the estimators drops off at a relatively low frequency for this array configuration (compare to Figure 31). The analysis indicates a slight superiority of the IMLE method over the ME_0 method in the frequency range where the general

Figure 35. Linear array estimates of $S_{yx}(f)$ for a 2-2-2-5 configuration with a) strongly bimodal test spectrum (TS-1, Figure B.7) and b) unimodal test spectrum (TS-2, Figure B.7). The deterministic response of the various methods is normalized by the true test value of $S_{yx}(f)$ and the normalized values are given in percent.



performance of both methods begins to drop (0.113-0.153 Hz). Numerical experiments were run with 50 realizations of random cross spectra with a strongly bimodal test spectrum (TS-1, Figure B.7). The results show an increase of estimator variance for both methods (20-30%) and a decrease in test correlation of the two methods for the 2-2-2-5 system relative to the 1-2.

The average wave conditions during the November experiment had significant wave energy at frequencies above the usable range for directional analysis of the 2-2-2-5 array. It was necessary to use the current meter-pressure sensor pair in 5.7 meters for the complete directional coverage of the energetic wave frequencies. The co-spectrum of the 2 orthogonal components of orbital velocity is related to the frequency-directional spectrum

$$C_{uv}(f) = \left(\frac{gk}{\sigma}\right)^2 \frac{\cosh^2 Kz'}{\cosh^2 Kh} \int_a E(f, \alpha) \cos \alpha \sin \alpha d\alpha \quad (V.7)$$

where z' is the height of the sensor off the bed, and $C_{uv}(f)$ is the co-spectrum of the cross-shore velocity, u , and the longshore velocity, v . This moment is directly proportional to $S_{yx}(f)$, which was a desired parameter for the longshore current studies.

The major problem with the current meter was a relatively large uncertainty in its absolute orientation. The estimated confidence in the current meter orientation was roughly 3-5° compared to the uncertainty of, at most, 1° for the larger lags in the array. The orientation of the current meter was checked in a preliminary way by the comparison of the mean direction, at a particular frequency, with the modal direction of the directional spectrum estimated at the

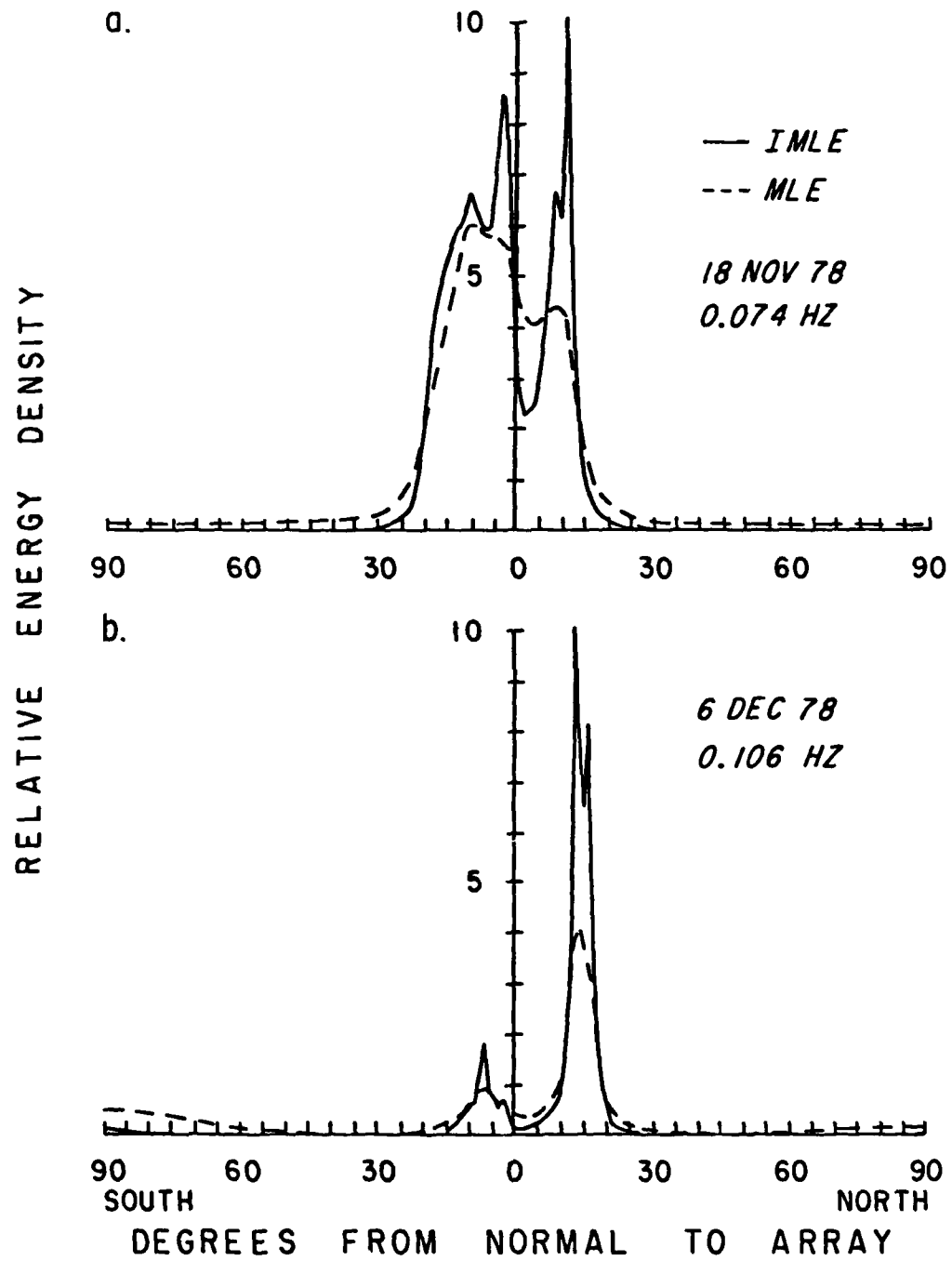
10 m array. These comparisons are only meaningful for a very narrow, unimodal directional spectrum. The directional spectra of the array were refracted to 5.7 m depth for the directional comparisons with the current meter. The results showed a consistent discrepancy of 5° in the assumed orientation of the current meter.

There was only a small number of cases available for the modal directional comparisons. Therefore, another approach was adopted for the orientation computations. Array estimates of $S_{yx}(f)$ were made usng the IMLE method and transformed, with the use of the refraction of the directional spectra, to the 5.7 meter contour. The assumed orientation of the current meter was then rotated to yield the best fit, in the least squares sense, to the $S_{yx}(f)$ values in the frequency range 0.051-0.106 Hz. The array has a relatively good expected performance in this range.

Data runs from 5 separate days spanning the month long experiment were selected for the orientation analysis. The "optimal" rotation angles of all 5 runs fell within a range of 1.7° and the mean of these angles was only 0.5° different from the result of the modal directional analysis. The mean rotation angle was then used for a constant current meter orientation angle for all the data runs of the November experiment.

A relatively energetic north swell dominated the wave field on 6 December. The average frequency spectrum and sample directional spectra obtained from the linear array are shown in Figures 32 and 36 respectively. The comparative $S_{yx}(f)$ estimates obtained from the ME.8 and IMLE methods and the current meter (CM) system are shown in Figure

Figure 36. IMLE directional spectrum estimates from the 2-2-2-5 linear array for a) the average of 18 consecutive 17.1 segments on 18 Nov. 1978 and b) 12 consecutive 17.1 minute segments on 6 Dec. 1978. The estimates are for a mean depth of 9.6 m.



37. The various estimates intercompare well in the frequency range 0.074-0.106 Hz. The ME.₈ estimates drop off sharply for wave frequencies above 0.106 Hz. This result was demonstrated in the deterministic model testing of the estimators. No tested value of v_n suppressed this sharp dropoff. The $S_{yx}(f)$ estimates obtained from the IMLE method agree well with the CM results for frequencies up to 0.129 Hz. The MLE estimates show a considerable bias (low), particularly at higher frequencies.

The sample variances of the $S_{yx}(f)$ estimates are listed in Table 14. These results show the relative instability of the ME₀ estimates. The IMLE estimates show considerably more variability than the ME.₈ results, which have roughly the same variance as the CM estimates. The value of $v_n = 0.8$ achieved the best fit of the average ME_v estimates with the CM results in the frequency range 0.074-0.106 Hz. However, the mean ME.₅ estimates varied by only a few percent from the average ME₁ values in this frequency range.

The $S_{yx}(f)$ estimates on 6 December are all of the same sign (longshore component of the momentum flux is to south). The intercomparison of bias in these estimates is somewhat suspect due to the current meter orientation procedure. The wave field on 18 November contains significant southern and northern components. In fact, the lower frequency directional spectra (Figure 36) show a complicated mixture of these components. The comparative estimates of $S_{yx}(f)$ for 18 November are shown in Figure 38. The IMLE and CM estimates compare very well from 0.051-0.129 HZ. The ME.₁ estimates ($v_n = 0.1$ yields the minimum low frequency bias) also compare well with

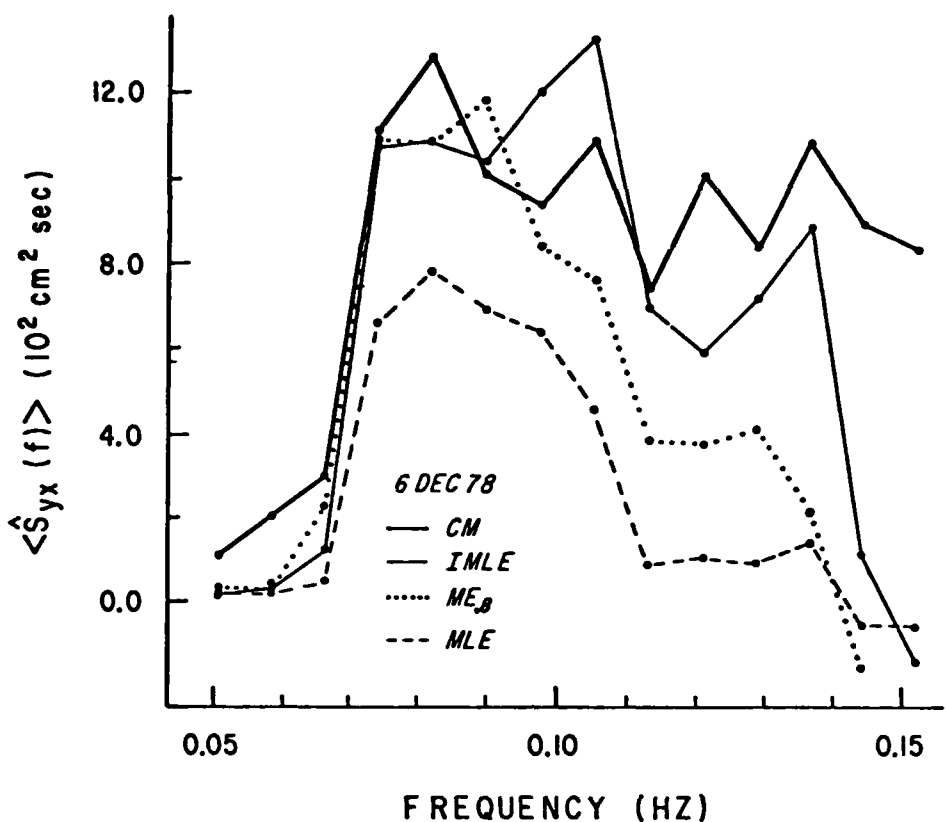
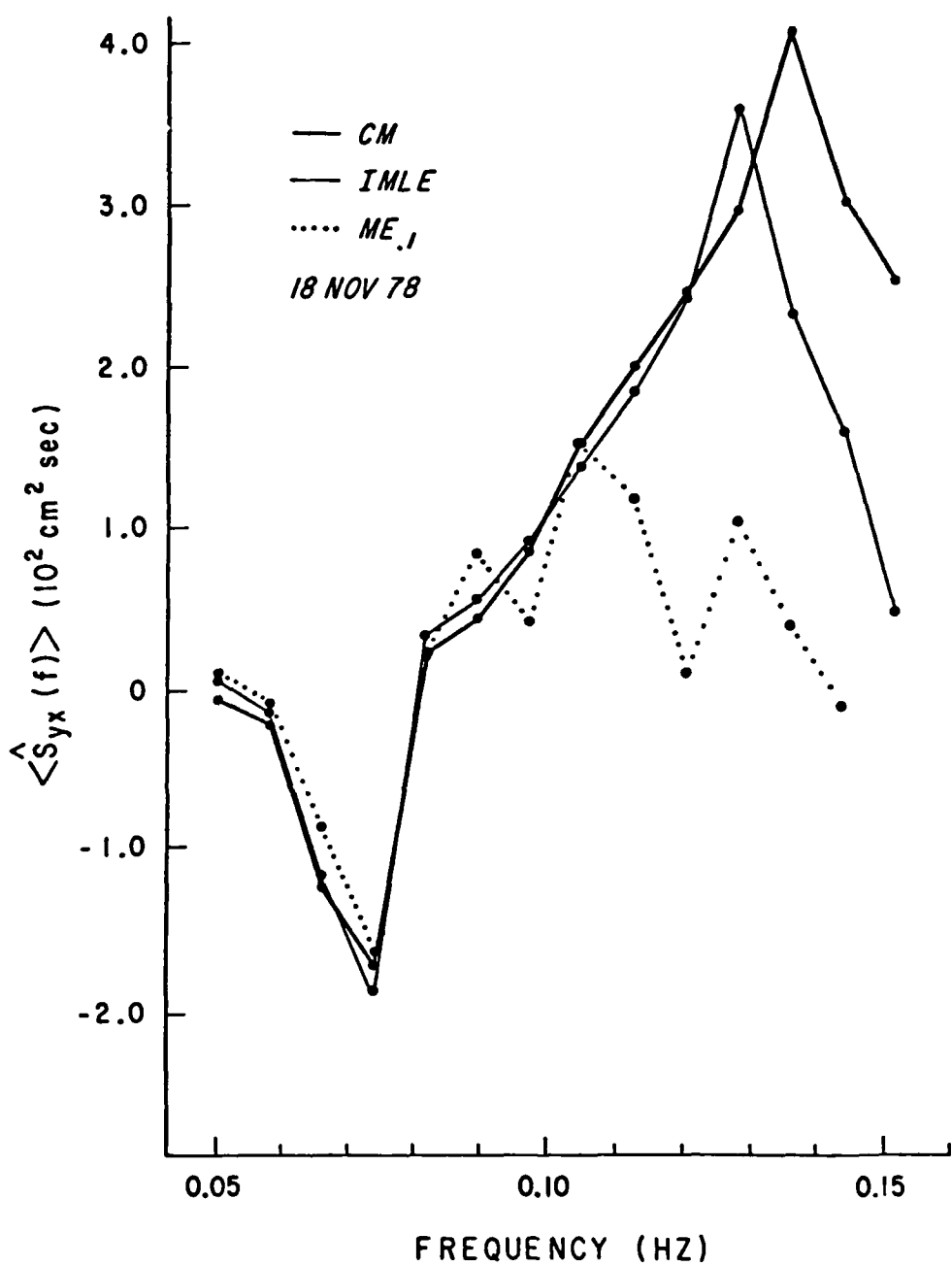


Figure 37. Estimates of $S_{yx}(f)$ for 3 methods with the 2-2-2-5 linear array and the 2 axis current meter (CM). The data averaged over 12 consecutive 17.1 minute runs. The value of $v_n = 0.8$ yielded the best fit of the ME_v estimates to the current meter results in the frequency range 0.074-0.106 Hz.

Figure 38. Estimates of $S_{yx}(f)$ for 2 methods with the 2-2-2-5 linear array and the 2 axis current meter (CM). The data were averaged over 18 consecutive 17.1 minute segments. The value of $\nu_n = 0.1$ yielded the best fit of the ME_v results with the current meter in the low frequency (0.059-0.074 Hz) range.



$\hat{S}_{yx}(f)$ Variance ($\text{cm}^4 \text{ sec}^2 10^4$)

18 NOV 1978

Frequency (Hz)	CM	IMLE	ME_0	$ME_{.1}$	$ME_{.8}$	$ME_{1.}$
0.074-0.106	35.2	43.4	232.	37.8	27.7	26.7

6 DEC 1978

	CM	IMLE	ME_0	$ME_{.1}$	$ME_{.4}$
0.074	1.43	2.95	41.9	10.8	2.75
0.082-0.106	1.10	1.03	2.34	1.56	1.15
0.114-0.129	2.44	3.39	1.70	1.67	1.38

Table 14. Variance of the $S_{yx}(f)$ estimates obtained from 18 consecutive 17.1 minute runs on 18 Nov. 1978 and 12 consecutive 17.1 minute runs on 6 Dec. 1978. Estimates from two linear array methods are compared with results from a current meter (CM).

the other estimates in the range 0.051-0.106 Hz.

The sample variance of the various $S_{yx}(f)$ estimates are listed in Table 14. The $ME_{.1}$ estimates are more variable than the IMLE and CM results, particularly at lower wave frequency. The $ME_{.4}$ estimates show comparable variance to the other methods and good average agreement in range 0.082-0.106 Hz. The low frequency $ME_{.4}$ estimates are biased low in values. As with the 6 December data, no tested value of v_n prevents the sharp dropoff of the ME_v estimates at 0.114 Hz.

V.4 CONCLUSIONS

Results from deterministic and random computer simulation tests and field comparisons with a slope array and current meter show the MLE method to be deficient in the estimation $S_{yx}(f)$. The MLE method performs well only for very narrow, unimodal distributions with low background noise levels.

The IMLE and ME_v methods show significant improvement over the MLE method in the deterministic and random simulation tests of the $S_{yx}(f)$ estimates. The response of the 1-2-4-5 array to random cross-spectra showed no instabilities for either the IMLE or ME_v estimates in the frequency range 0.051-0.160 Hz.

The field comparisons of a 1-2 linear array of length 99.0 m with a slope array show roughly equivalent comparisons of the IMLE and ME_v estimates with the slope results. The deviation of the estimates from either method from the slope estimates is in the range 10-20% compared to values up to 100% for the MLE comparisons. The ME_v showed the most stable comparisons with the slope array with low values

(relative to band energy) of $S_{yx}(f)$. The useful range of the 1-2 array was shown to be approximately 0.051-0.153 Hz.

Simulation tests showed degraded performance of the array methods with the 2-2-2-5 configuration, particularly at higher wave frequencies. The IMLE estimates of $S_{yx}(f)$ compared well with the current meter results in the range 0.059-0.129 Hz. However, the IMLE estimates showed consistently higher variance. The ME_v ($v_n=0.5-1.0$) estimates compared well with the other methods in the range 0.059-0.106 Hz. The severe degradation of the ME_v estimates above 0.106 Hz was demonstrated in the simulation test and shown to be independent of v_n .

The variance of the ME_v estimates drops with increased values of v_n . However, the value of v_n which minimized the bias of the ME_v estimates relative to the results from the other methods varied from 0.1-1.0. The simulation tests and field comparisons show the minimum bias v_n to vary as a function of array configuration, directional spectrum, and wave frequency. However, values of v_n from 0.5-1.0 yield reasonable bias and estimator variance for most of the frequency range and both arrays. Some attention will have to be paid to this parameter in the application of the ME_v method with other array configurations and directional spectral forms.

These experiments also represent the first attempts at field verification of the $S_{yx}(f)$ measurement capability of the slope array and biaxial current meter. The comparative results yield confirmation of accurate performance of these systems over the entire frequency range of usable data provided by the linear array.

VI STATISTICAL PROPERTIES OF MOMENTUM FLUX

Estimates of $S_{yx}(f)$ in the ocean are realizations of a random process. The analysis discussed in Section V showed significant fluctuations in the time sequences of the $S_{yx}(f)$ estimates. There are active wave climatology programs designed to sample $S_{yx}(f)$ in the field (Seymour and Higgins, 1977). However, the derivation of the theoretical probability density function for $S_{yx}(f)$ estimates has not been specifically addressed. A direct estimate of $S_{yx}(f)$ is obtained from the co-spectrum of orthogonal velocity components (or sea surface slope). The statistics of co-spectrum estimates has been addressed by Goodman (1957), which will now be referred to as Goodman.

Goodman's work was concerned with the joint distribution of estimates of the frequency spectrum and cross-spectrum in a 2 dimensional Gaussian random field. The density function for the frequency spectrum estimates, $\hat{E}(f)$, is a χ^2 (Chi-square) distribution. This result was probably first introduced to ocean sciences by Tukey (1949). The density function for estimates of $E(f)$ obtained from FFT coefficients is a textbook result. The sea surface elevations and Fourier coefficients are assumed to be zero mean Gaussian. $\hat{E}(f)$, which is a sum of squares of the coefficients, is therefore a χ^2 random variable. This distribution approximation has been widely used in the field for the description of the variability of $E(f)$ estimates. Borgman (1972,74) tested the assumptions and the resulting fit of the χ^2 distribution with field measurements. His conclusion was that although the sea surface elevations were significantly non-Gaussian, the FFT coefficients were roughly normally distributed and the

estimates of $E(f)$ were x^2 .

An outline of Goodman's derivation of the probability density function for co-spectral estimates will be presented here. This distribution will then be compared to field measurements of $S_{yx}(f)$ obtained from a linear array. Lastly, the theoretical distributions will be studied for their dependence on the structure of the directional spectrum.

VI.1 Characteristic and Density Function of Cross-Spectral Estimates

Goodman approaches the derivation of the cross-spectral density function by first solving for the joint characteristic function for the spectral estimators. The characteristic function of the variable x is defined

$$\phi_x(\theta) = \langle e^{i\theta x} \rangle = \int_{-\infty}^{\infty} e^{i\theta x} p(x) dx \quad (\text{VI.1})$$

where θ is the transformation variable of x , $p(x)$ is the associated density function, and the brackets denote the expected value.

Consider the complex Gaussian random variables

$$U = U_r + iU_i \quad (\text{VI.2})$$

$$V = V_r + iV_i$$

which are zero mean and have the variance-covariance matrix

$$V_a = \begin{bmatrix} \sigma_U^2 & 0 & \Lambda\sigma_U\sigma_V & 0 \\ 0 & \sigma_U^2 & 0 & \Lambda\sigma_U\sigma_V \\ \Lambda\sigma_U\sigma_V & 0 & \sigma_V^2 & 0 \\ 0 & \Lambda\sigma_U\sigma_V & 0 & \sigma_V^2 \end{bmatrix} \quad (\text{VI.3})$$

where σ_U^2 = variance of U , U and V represent the complex Fourier

transforms of the horizontal velocity components normalized so that

$$\begin{aligned}\sigma_U^2 &= \int_{\alpha} \cos^2 \alpha E(\alpha) d\alpha \\ \sigma_V^2 &= \int_{\alpha} \sin^2 \alpha E(\alpha) d\alpha \\ \Lambda \sigma_U \sigma_V &= \int_{\alpha} \cos \alpha \sin \alpha E(\alpha) d\alpha\end{aligned}\quad (\text{VI.4})$$

Working with the dimensionless variables

$$\begin{aligned}u_{rj} + iu_{ij} &= (U_{rj} + iU_{ij})/\sigma_U \\ v_{rj} + iv_{ij} &= (V_{rj} + iV_{ij})/\sigma_V\end{aligned}\quad (\text{VI.5})$$

where j denotes the frequency band, a new variable list can be generated

$$\begin{aligned}a &= \frac{1}{2n_e} \sum_{j=1}^{n_e} u_{rj}^2 + u_{ij}^2 = A/A_0 \\ b &= \frac{1}{2n_e} \sum_{j=1}^{n_e} v_{rj}^2 + v_{ij}^2 = B/B_0 \\ c &= \frac{1}{2n_e} \sum_{j=1}^{n_e} u_{rj}v_{rj} + u_{ij}v_{ij} = C/C_0\end{aligned}\quad (\text{VI.6})$$

and

$$\begin{aligned}A_0 &= \sigma_U^2 \\ B_0 &= \sigma_V^2 \\ C_0 &= \Lambda \sigma_U \sigma_V\end{aligned}\quad (\text{VI.7})$$

where n_e is the number of ensembles and A, B, and C are the horizontal frequency and cross-spectral estimates. Define the following vectors

$$\underline{S} = \begin{bmatrix} u_{rj}^2 \\ u_{ij}^2 \\ v_{rj}^2 \\ v_{ij}^2 \\ u_{rj} u_{ij} \\ u_{rj} v_{rj} \\ u_{rj} v_{ij} \\ u_{ij} v_{rj} \\ u_{ij} v_{ij} \\ v_{ri} v_{ij} \end{bmatrix} \quad \underline{\theta} = \begin{bmatrix} \theta_{11} \\ \theta_{22} \\ \theta_{33} \\ \theta_{44} \\ \theta_{12} \\ \theta_{13} \\ \theta_{14} \\ \theta_{23} \\ \theta_{24} \\ \theta_{34} \end{bmatrix} \quad (\text{VI.8})$$

where some of these components, u_{ij} and v_{rj} for example, are identically equal to zero. The joint characteristic function of the vector \underline{S} is

$$\phi_{\underline{S}}(\underline{\theta}) = \langle e^{i\underline{\theta}^T \underline{S}} \rangle = \langle e^{i\underline{x}^T \tilde{\underline{\theta}} \underline{x}} \rangle \quad (\text{VI.9})$$

where $\tilde{\underline{\theta}}$ is a matrix with elements $\tilde{\theta}_{ij} = \theta_{ij}(1 + \delta_{ij})$ and \underline{x} is defined

$$\underline{x} = \begin{bmatrix} u_{rj} \\ u_{ij} \\ v_{rj} \\ v_{ij} \end{bmatrix} \quad (\text{VI.10})$$

The whole point of these manipulations is that the joint distribution of \underline{x} is known (joint normal). Therefore, we have

$$\phi_{\underline{S}}(\underline{\theta}) = \int_{\underline{x}} \frac{e^{i\underline{x}^T \underline{\theta}}}{(2\pi)^2 |V_a|^{\frac{1}{2}}} e^{-\frac{1}{2} \underline{x}^T V_a^{-1} \underline{x}} d\underline{x} \quad (\text{VI.11})$$

where V_a^{-1} and $|V_a|$ are the inverse and determinant of the variance-covariance matrix. Further manipulation shows

$$\phi_{\underline{S}}(\underline{\theta}) = |V_a|^{\frac{1}{2}} |V_a^{-1} - 2i\underline{\theta}|^{\frac{1}{2}} \int_{\underline{x}} \frac{e^{i\underline{x}^T \underline{\theta}}}{(2\pi)^2 |V_a^{-1} - 2i\underline{\theta}|} e^{-\frac{1}{2} \underline{x}^T V_a^{-1} \underline{x}} d\underline{x} \quad (\text{VI.12})$$

where the integral is equal to unity. Thus,

$$\phi_{\underline{S}}(\underline{\theta}) = |V_a|^{-\frac{1}{2}} |V_a^{-1} - 2i\underline{\theta}|^{-\frac{1}{2}} \quad (\text{VI.13})$$

see Borgman (1976). The remaining manipulations involve repeated transformations of the variables of \underline{S} to achieve the characteristic function of the new variables

$$\begin{aligned} a' &= n_e a / \psi \\ b' &= n_e b / \psi \\ c' &= n_e c / \psi \end{aligned} \quad (\text{VI.14})$$

where $\psi = 1 - \Lambda^2$. These steps are carefully discussed by Goodman and they involve the invocation of several identities of characteristic functions. These transformations yield the joint characteristic function

$$\phi(\theta_a, \theta_b, \theta_c) = \psi^n e \left[(1-i\theta_a)(1-i\theta_b)(\Lambda+i\theta_c) \right]^{-n_e} \quad (\text{VI.15})$$

This characteristic function may now be inverse Fourier transformed to yield the joint density function. Here we are only interested in the density function of the co-spectrum, C. The associated characteristic function is

$$\phi(\theta_{C'}) = \phi(0,0,\theta_{C'}) = \Psi e^{\left[1-(\Lambda+\theta_{C'})\right]^{-n_e}} \quad (\text{VI.16})$$

Goodman employs known Fourier transform relationships (Erdelyi, 1955) to solve for the density function

$$p(c') = \frac{\Psi e^{\Lambda c'} |c'|^{n_e^{-\frac{1}{2}}} K_{n_e^{-\frac{1}{2}}}(|c'|)}{2^{n_e^{-\frac{1}{2}}} \pi^{\frac{1}{2}} \Gamma(n_e)} \quad (\text{VI.17})$$

where $\Gamma(n_e)$ is the gamma, $K_{n_e^{-\frac{1}{2}}}$ is the Bessel function of the third kind. $K_{n_e^{-\frac{1}{2}}}$, with n_e = positive integer, can be reduced to yield

$$p(c') = 2^{-n_e} \Psi e^{\Lambda c'} |c'|^{n_e^{-1}} e^{-|c'|} \sum_{k=0}^{n_e-1} \frac{1}{2|c'|^{-k}} \frac{\Gamma(n_e+k)}{k! \Gamma(n_e-k)} \quad (\text{VI.18})$$

$S_{yx}(f)$ is proportional to the co-spectrum

$$\langle \hat{s}_{yx}(f) \rangle = \frac{C_0}{n(f)} \quad (\text{VI.19})$$

Thus

$$\langle \hat{s}_{yx}(f) \rangle = \frac{C}{n(f)} \quad (\text{VI.20})$$

$$\hat{s}_{yx}(f) / \langle \hat{s}_{yx}(f) \rangle = \frac{C\Psi}{n_e}$$

This distribution is degenerate with perfectly coherent velocity

components (unidirectional waves). Some sample analytic density functions are plotted in Figure 39. The distributions are relatively wide and asymmetric for low values of n_e . These results also show that a narrowing of the directional spectrum causes a decrease in the variance of the $S_{yx}(f)$ estimates.

VI.2 Comparisons with Field Data

The density function given in equation VI.18 is not directly applicable to linear array measurements which have spatial averaging of the wave field. The array estimators (IMLE and ME_v) of $S_{yx}(f)$ showed good comparison to the slope array (Table 13). This comparison included close agreement of the estimator variance. Therefore, this family of distributions may be useful in the description of array estimate variability.

IMLE estimates of $S_{yx}(f)$ obtained from the 1-2 and 1-2-4-5 array configurations were compared for the limited section of 10 June data described in Section V. The directional spectra from the 2 arrays were normalized to the energy density from the 3 sensors of the 1-2. The average normalized variance of the estimates ($\sigma_n^2(S_{yx}(f))$) over the frequency range 0.059-0.145 Hz from the 2 arrays agreed to within 2%. Therefore, the 1-2-4-5 array, which has higher directional spectrum resolution, was used for the analysis. Two long data sets of high quality were available for the intercomparison of the field data and the theoretical distributions. 8.0 hours of continuous array data were sampled on 10 June 1977 and 14.2 hours (equivalent to 50 consecutive 17.1 minute segments) were obtained on 5 March 1977.

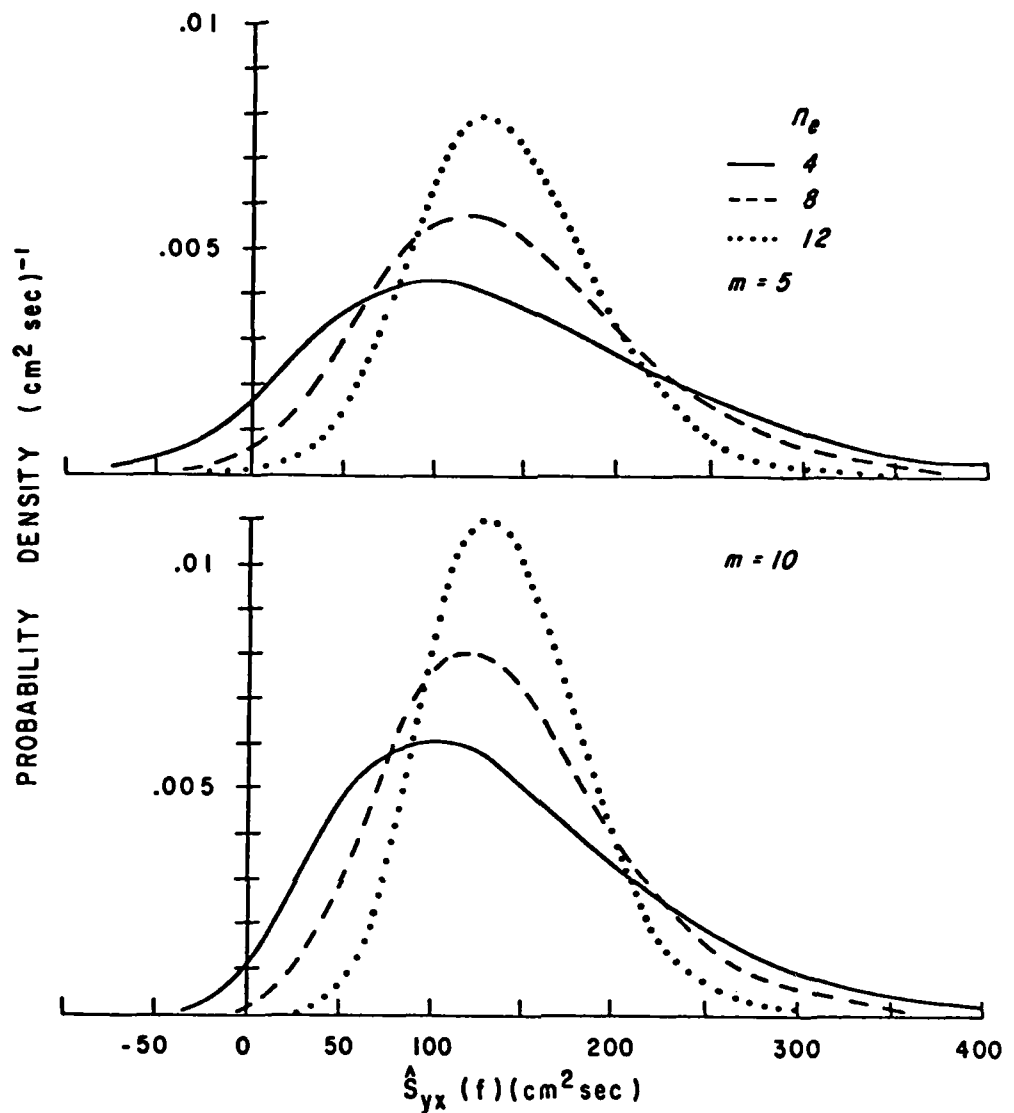


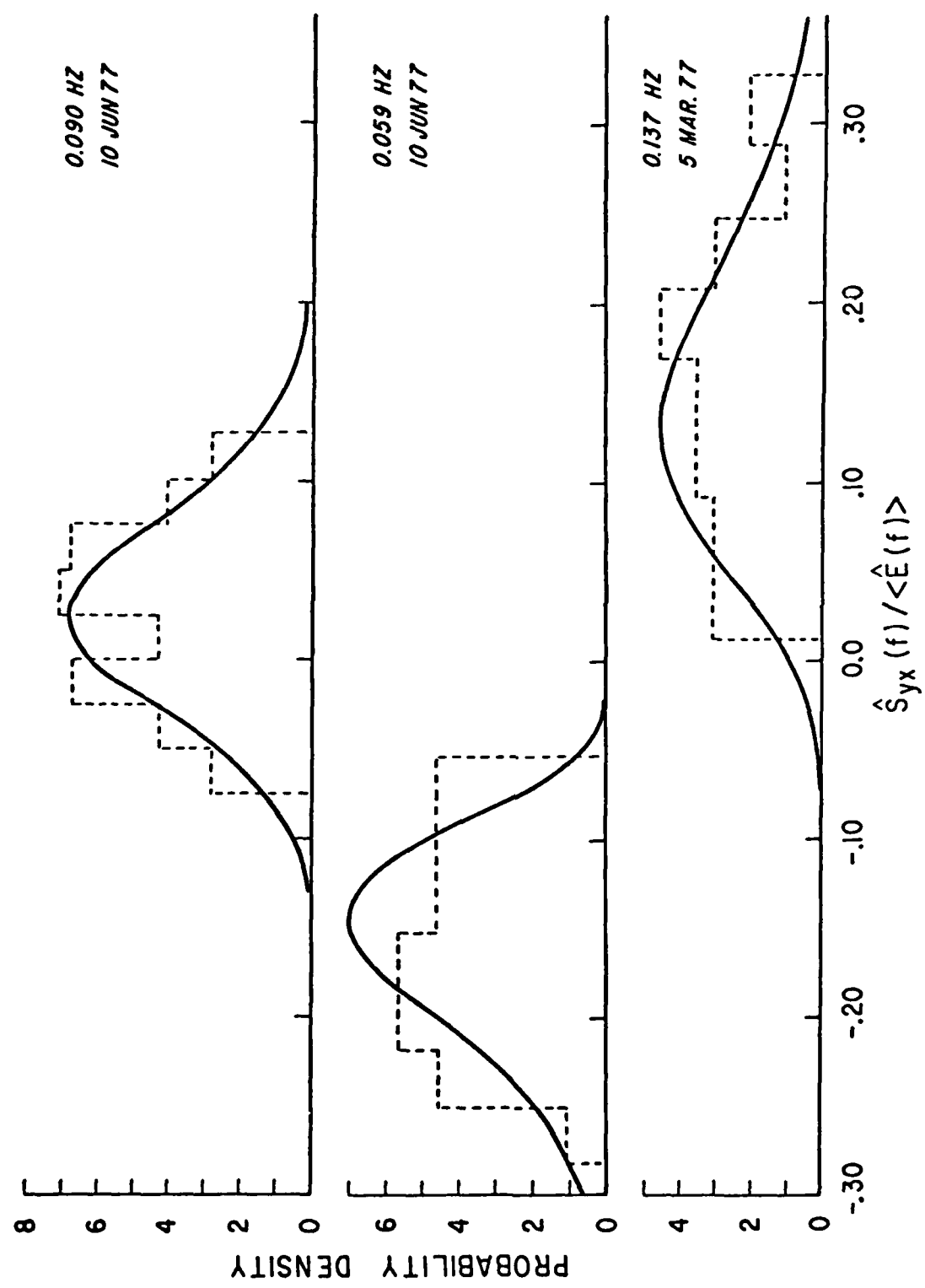
Figure 39. Analytic density functions for estimates of $S_{yx}(f)$. The distributions are calculated for several values of ensemble averaging, n_e , and powers of the spectrum $E(\alpha)=\cos^m(\alpha-20^\circ)$.

The time sequences of $S_{yx}(f)$ values were studied in order to reject obvious "nonstationary" conditions. The mean length of "runs" between crossings of the median value of a random variable has a probability distribution which is independent of the statistics of the variable. The sample value of the mean run length can be used as an indication of the stationarity of the sequence, see e.g. Bendat and Piersol (1971). Sample mean run lengths which exceeded the 95% confidence region for either the $\hat{S}_{yx}(f)$ or the associated $\hat{E}(f)$ time sequences were used to reject the data. Also, if the number of $\hat{E}(f)$ outliers of the 90% confidence range (χ^2) exceeded 20% of the sample population, the sequence was rejected. These tests left 10 frequency bands (out of a total of 12 in the range 0.059-0.145 Hz) suitable for analysis on 10 June and only 3 bands on 5 March. The accepted sequences of 5 March were generally more marginal than the 10 June sequences.

Figure 40 shows the comparison of 3 sample distributions of $\hat{S}_{yx}(f)$ with the associated analytic density functions. The analytic functions were generated with the use of the IMLE directional spectra (shown in Figure 32 and 41). These comparisons show examples of a good distribution fit (Figure 40a) and relatively poor agreement (Figure 40b). Note that the sample variability of $\hat{S}_{yx}(f)$ for the 0.090 Hz band on 10 June is very large compared to the mean (near zero) value. This results from the bimodal directional distribution which is roughly centered on normal incidence to the coast.

The moments of the distributions can be compared to evidence the quantitative usefulness of the linear statistical theory. It is

Figure 40. Comparison of analytic density functions with sample distributions of $S_{yx}(f)$ analyzed with the IMLE method (1-2-4-5 array). The IMLE directional spectra were used in the generation of the analytic distributions.



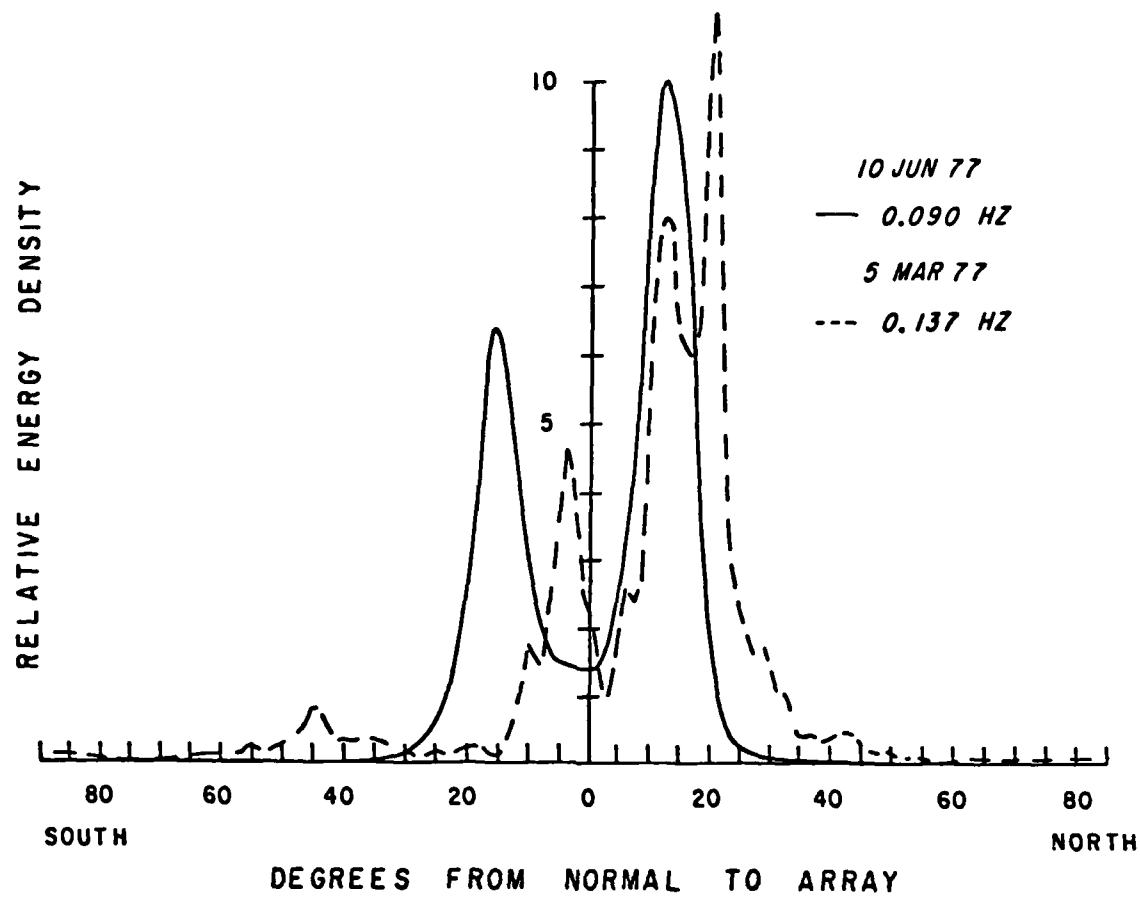


Figure 41. Directional spectrum estimates associated with the sample $S_{yx}(f)$ distributions plotted in Figure 40. The IMLE method was used for the analysis on data from the 1-2-4-5 array. The 10 June cross-spectrum had 448 DOF while the 5 March had 800 DOF.

expected that the validity of the moment comparisons will degrade with increasing order due to the limited resolution of the sample distributions. Comparisons of sample variances of $\hat{S}_{yx}(f)$ with the results from the analytic density functions are shown in Figure 42. The estimates were generated with the IMLE method using normalization to a single sensor (consistent with the comparison work with slope array and current meter) and to 3 sensors. The spectral averaging parameter, n_e , was strictly interpreted as the number of ensembles averaged. This is consistent with the rectangular window (no tapering) estimates of the cross-spectrum.

The model variances describe well the trends in the sample distributions ($r \sim 0.999$ for both normalizations). The sample variances are biased somewhat high. The average value of sample/model variance ratio is 1.13 for the 3 sensor normalization and 1.42 for the single sensor. The sample/model ratio of the energy density variances for the same data set had an average value of 1.18. This may evidence some "nonstationarity" to the data set.

Table 15 shows the comparisons of the skewness and kurtosis (normalized third and fourth moments defined in the table) of the theoretical and sample distributions. The higher order moment comparisons are more scattered than the variance results. The correlation of the theoretical and sample skewness is 0.87. A considerable range in the skewness values is evidenced by both the model and sample values. The correlation of the theoretical and sample estimates of kurtosis is only 0.5. The intercomparisons are more variable than the theoretical departures from a normal value

Date	Frequency (Hz)	DATA		THEORY	
		Skewness	Kurtosis	Skewness	Kurtosis
5 Mar 77	0.090	.52	2.7	0.69	3.7
	0.137	0.19	2.3	0.55	3.6
	0.145	0.75	4.0	0.54	3.6
	0.090-0.145	0.49	3.0	0.56	3.6
10 Jun 77	0.059	0.02	1.8	-0.50	2.8
	0.067	-0.86	2.8	-0.57	3.1
	0.074	-1.7	6.9	-0.69	3.7
	0.082	-0.55	3.3	-0.44	3.5
	0.090	-0.04	2.1	0.19	3.4
	0.098	0.68	2.9	0.41	3.4
	0.106	0.32	2.7	0.49	2.9
	0.114	0.48	2.5	0.42	2.8
	0.137	0.40	2.4	0.43	2.8
	0.145	0.43	2.3	0.52	3.2
	0.059-0.090	-0.78	3.7	-0.55	3.3
	0.098-0.145	0.38	2.5	0.41	3.0

Table 15. Comparison of theoretical and sample values of skewness and kurtosis of the $\hat{S}_{yx}(f)$ distributions. The parameters are defined in the standard fashion

$$\text{normalized moment} = \frac{\int x^n p(x) dx}{(\int x^2 p(x) dx)^{n/2}}$$

where $n=3$ for skewness and $n=4$ for kurtosis and $p(x)$ is the density function.

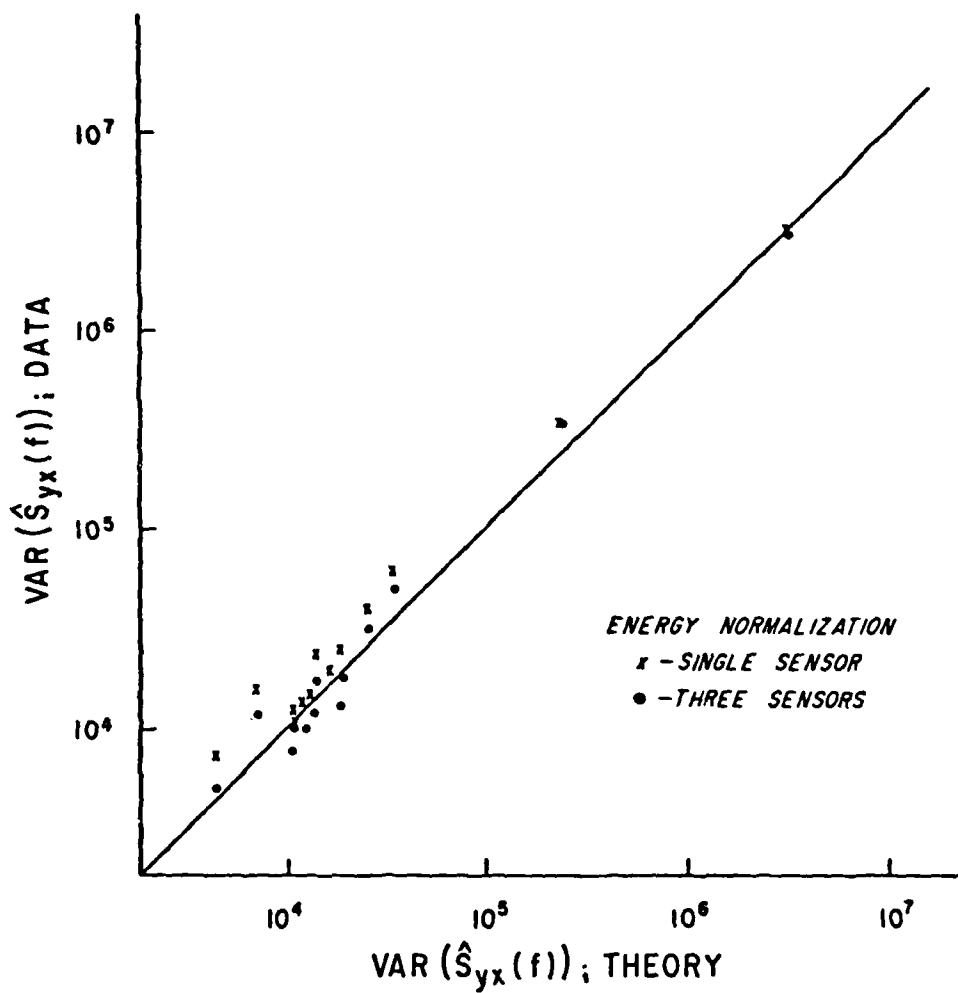


Figure 42. Comparison of sample variances of $S_{yx}(f)$ estimates from a 1-2-4-5 array (IMLE method) with theoretical values for point measurements. The variances have the units $\text{cm}^4 \text{ sec}^2$. x 's are for the array energy normalized to a single sensor while the \cdot 's are for normalization to the average of 3 sensors.

(3.0). However, the averaged sample kurtosis values for relatively broad frequency ranges do appear to track with the theoretical results. It should be noted that the high frequency region of the 10 June data shows reasonable comparisons of all 3 spectral moments.

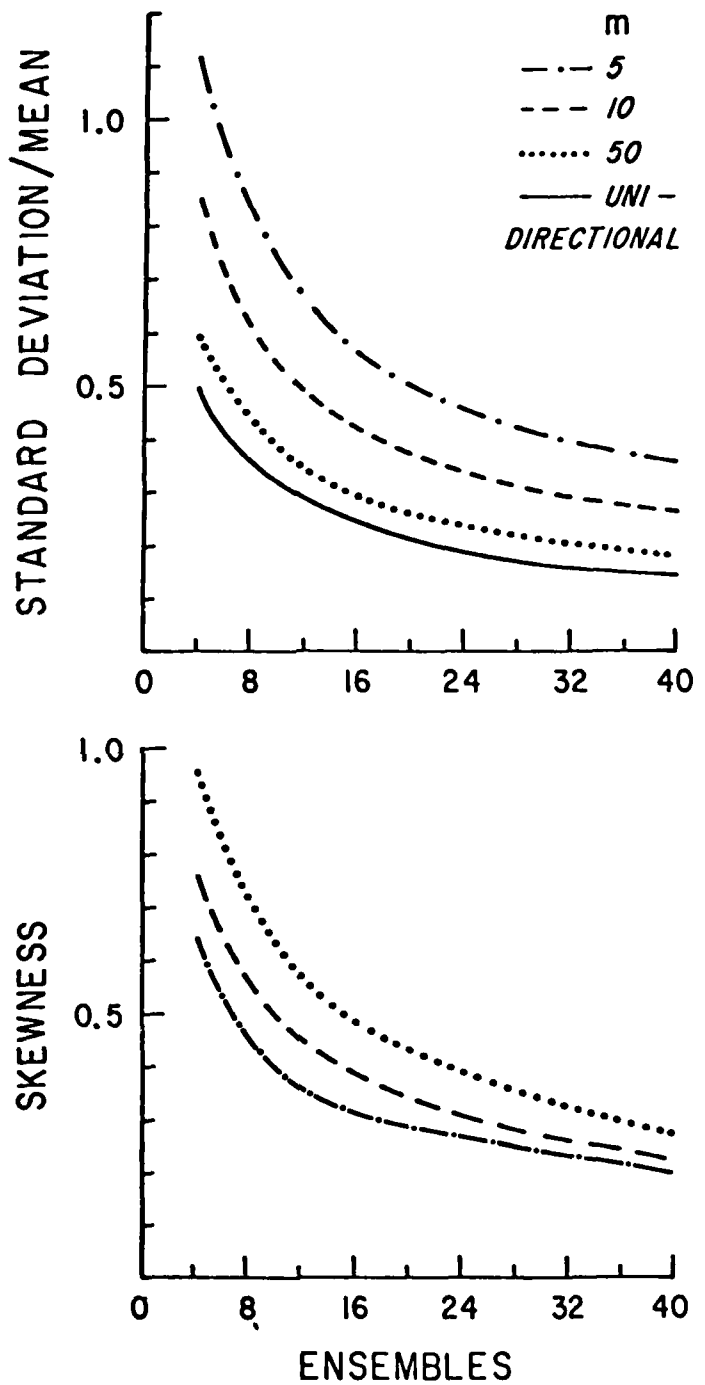
VI.3 Distribution Variability

The shape of the theoretical and sample distributions was shown above to vary as a function of the directional spectrum (Figures 39,40). The dependence of the distribution moments on the directional spectrum characteristics is an important factor in experimental design. Appriori knowledge of the directional wave characteristics can be used in the sampling specifications.

The variance and skewness properties of various unimodal distributions are shown in Figure 43. The normalized variance, σ_n^2 , is shown to decrease sharply with decreasing width of the directional mode. For distributions of equal width, the normalized variance drops for increasing mode angles up to 45° . This change with mode angle is most significant for broad distributions. The normalized variance for unidirectional waves, shown in Figure 43, does not vary with direction. Note that this result is valid even though the distribution in equation VI.18 is degenerate with perfectly coherent waves. The flucuations in $\hat{S}_{yx}(f)$ are, in this case, directly associated with the variability in $\hat{E}(f)$.

An approximate analytic expression for the estimator variance can be obtained with the representation of a random process with white noise fed through linear filters (see e.g. Jenkins and Watt, 1968). The resulting expression for the normalized variance is

Figure 43. Dependence of the normalized 2nd and 3rd order moments of $\hat{S}_{yx}(f)$ distributions on the width of unimodal directional spectra and the number of ensembles averaged. The directional distribution employed was $E(\alpha) = \cos^m(\alpha - 10^\circ)$.



$$\frac{\text{VAR}(\hat{S}_{yx}(f))}{\langle \hat{S}_{yx}(f) \rangle^2} = \frac{1}{n_e} \left[\frac{\sigma_U^2(f) \sigma_V^2(f)}{C_{UV}^2(f)} + 1 \right] \\ = \frac{1}{n_e} \left[\frac{\int_{-\pi}^{\pi} \cos^2 \alpha E(f, \alpha) d\alpha \int_{-\pi}^{\pi} \sin^2 \alpha E(f, \alpha) d\alpha}{\left(\int_{-\pi}^{\pi} \cos \alpha \sin \alpha E(f, \alpha) d\alpha \right)^2} \right] \quad (\text{VI.21})$$

An integral limit to Schwartz's inequality ($\sum A^2 \sum B^2 \geq (\sum AB)^2$) shows that this expression takes a minimum value for the case when $\sigma_U^2 \sigma_V^2 = C_{UV}^2(f)$. This is only satisfied by the condition of unidirectional waves.

The skewness of the $\hat{S}_{yx}(f)$ distributions for unimodal waves is shown (Figure 43) to decrease with increasing mode width. Increasing values of n_e , the ensembles averaged, also causes a sharp decrease in the skewness of the distributions (for a small number of ensembles averaged). The skewness of narrow unimodal waves does not vary significantly with mode direction. However, relatively broad modes have increasing skewness for angles up to 45° . The symmetry of the error bars associated with the $S_{yx}(f)$ estimates is to a large part determined by the skewness of the distribution.

Longshore currents and sediment transport are thought to be proportional to $S_{yx} = (\sum_i S_{yx}(f_i) \Delta f_i)$. The statistical nature of this parameter is therefore of considerable practical concern. The probability distribution of S_{yx} is derived on the assumption that the frequency band values are independent of each other. The

characteristic function of \hat{S}_{yx} is then equal to the product of the characteristic functions for $\hat{S}_{yx}(f)$. also, the density function $p(\hat{S}_{yx})$ is obtained

$$p(\hat{S}_{yx}) = p(\hat{S}_{yx}(f_1) * p(\hat{S}_{yx}(f_2) * \dots * p(\hat{S}_{yx}(f_N)) \quad (VI.22)$$

where * denotes the convolution and there are N bands. The convolution of any two bands yields a result with increased absolute variance. However, if $\langle \hat{S}_{yx}(f) \rangle$ is of the same sign for both bands, the normalized variance (σ_n^2) decreases. For illustrative purposes, consider the sampling time required to obtain an estimate which is within 25% of the true mean. Given the sampling specifications used, this time is about 1.7 hours for $\hat{S}_{yx}(f)$ at the frequency maximum on 6 Dec. 1977 (Figure 37). However, only 0.5 hours are required for similar stability of \hat{S}_{yx} on this day. If the bands averaged are comprised of components which are of opposite sign, the normalized variance may increase dramatically. $\hat{S}_{yx}(f)$ at the frequency maximum on 10 June 1977 (Figure 34) requires 1.7 hours sampling time for the desired stability while roughly 3.1 hours are needed for \hat{S}_{yx} .

The variability of \hat{S}_{yx} should be of physical significance as well as being a sampling consideration. The difference between a relatively steady and a wildly fluctuating version of this forcing function may be important in the dynamics of the surf zone. Several investigators, including Inman and Quinn (1951) and Guza and Thorton (1978), have shown that relatively large temporal fluctuations are an important characteristic of longshore currents in the surf zone.

Inspection of the data presented in Guza and Thorton (1978) shows that the normalized variance of the longshore currents and \hat{S}_{yx} are close in magnitude, with the currents being slightly more variable. However, the authors were unable to correlate the associated time sequences of these variables. The directional spectra in this experiment (Nov. 1978 experiment discussed in Section V) were complicated bimodal distributions. This resulted in large temporal and spacial variability in the physical parameters. Additionally, it was hypothesized that long waves may account for some of the current variability. Investigation of a data set with simpler wave conditions (NSTS Santa Barbara,Gable,1981) should provide more useful information on the statistical link between the incident waves and resulting processes.

VI.4 Conclusions

Theoretical probability density functions for $S_{yx}(f)$ estimates from a "orthogonal component" system are related to the statistics of the co-spectrum. These distributions are studied for their adequacy in describing the variability of array measurements of $\hat{S}_{yx}(f)$. The theoretical density functions describe well the trends in the sampled values of distribution variance and skewness. However, there is a bias in the variance of the sample estimates that is a function of the spacial averaging (sensors averaged in the array). The high correlation of the theoretical and sample values of distribution variance and skewness lends hope for the direct applicability of these analytic functions to the statistics of current meter and slope array estimates. The comparison of higher order moments, e.g. kurtosis,

were inconclusive because of the limited scope of the data.

Energy density estimates, which have a χ^2 distribution, have a variability which is a function of only the mean value of the estimate and the number of ensembles averaged. This is not true for $\hat{S}_{yx}(f)$ estimates. Near zero estimates of $\hat{S}_{yx}(f)$ may have relatively large absolute variances. The other spectral moments which determine the variance are σ_U^2 and σ_V^2 which are directly measured by a orthogonal component system. Therefore, both an estimate of $\hat{S}_{yx}(f)$ and its expected variance can be determined from a limited data set.

REFERENCES

- Arthur,R.S.,1946,"Refraction of water waves by islands and shoals with circular bottom-contours", Trans. Am. Geophys. Union, vol 27, pp 168-177
- Arthur,R.S.,1951,"The effect of islands on surface waves", SIO Bulletin, vol 6, no 1, pp 1-26
- Barber,N.F.,1954,"Finding the direction of travel of sea waves", Nature, vol 174, pp 1048-1050
- Barber,N.F.,1958,"Optimal arrays for direction finding", New Zea. Jour. of Science, vol 1, pp 35-51
- Barber,N.F.,1963,"The directional resolving power of an array of wave detectors", Ocean Wave Spectra, Prentice-Hall Inc, Englewood Cliffs, N.J., pp 137-150
- Barrick,D.E.,1978,"HF radio oceanography-a review", Boundary-Layer Meteorology, vol 13, pp 23-44
- Bendat.R.S. and A. Piersol,1966, Measurement and Analysis of Random Data, Wiley-Interscience, New York
- Blair,P.M.,1974,"Buoy for recording ocean wave height and period", Proc. Int. Symp. on Ocean Wave Measurement and Analysis, ASCE, New Orleans, La., pp 254-271
- Borgmann,L.E.,1972,"Confidence intervals for ocean wave spectra", Proc. 13th Int. Conf. on Coastal Engin., ASCE, Vancouver, B.C., pp 237-250
- Borgmann,L.E.,1973,"Computer simulation of multivariate normal vectors applied to the reliability of spectral-based computations", Stat. Lab. Rep. No. 2007, Univ. of Wyoming, Laramie
- Borgmann,L.E.,1974,"Statistical reliability of computations based on wave spectral relations", Proc. Int. Symp. on Ocean Wave Measurement and Analysis, ASCE, New Orleans, La. pp
- Borgmann,L.E.,1976,"Statistical properties of FFT coefficients computed from real-valued, covariance-stationary, periodic random sequences", Tech. Paper No. 76-9, Coastal Engin. Res. Center, U.S. Army of Engin., Ft. Belvior, Va.
- Bowen,A.J.,1969,"The generation of longshore currents on a plane beach", Jour. of Marine Res., vol 27, no 2, pp 206-225
- Brainard,E.C. and R.J.Lukens,1975,"A comparison of the accuracies of various continuous recording current meters for offshore use", OTC Paper 2295, 7th Offshore Technology Conf., pp 485-492
- Caldwell,J.M.,1956,"Wave action and sand movement near Anaheim Bay, California", U.S. Army Beach Erosion Board, Tech. Memo. No. 68, 21 pp
- Capon,J.,1969,"High-resolution frequency-wavenumber spectrum analysis", Proc. IEEE, vol 57, no 8, pp 1408-1418
- Collins,J.I.,1972,"Prediction of shallow-water spectra", Jour. of Geophys. Res., vol 77, no 15, pp 2693-2707
- Davis,R.E. and L.A.Regier,1977,"Methods for estimating directional wave spectra from mulit-element", Jour. of Marine Res., vol 35, no 3, pp 453-477

- Dean,R.G.,1974,"Directional wave spectra: some applications and storage", Proc. Int. Symp. on Ocean Wave Measurement and Analysis, ASCE, New Orleans, La. pp
- Dobson,R.S.,1967,"Some applications of digital computer to hydraulic engineering problems", Tech. Rep. No 80, Dept. of Civil Engin., Stanford Univ.
- Dorrestein,A.,1960,"Simplified method of determining refraction coefficients for sea waves", Jour. Geophys. Res., vol 65, no 2, pp 637-642
- Dorrestein,R.,1961,"Wave set-up on a beach", Proc. 2nd Tech. Conf. Hurricanes, 230
- Erdelyi,A.,1955, Table of Integral Transforms, Vols 1&2, McGraw Hill, New York
- Emery,K.O.,1958,"Wave patterns off Southern California", Jour. of Marine Res., vol 17, pp 133-140
- Evans,D.D. and O.H.Shemdin,1980,"An investigation of the modulation of capillary and short gravity waves in the open ocean", Jour. of Geophys. Res., vol 85, no C9, pp 5019-5024
- Fett,R.W. and K.M.Rabe,1976,"Island barrier effects on sea state as revealed by a numerical wave model and DMSP satellite data", Jour. of Phys. Ocean., vol 6, pp 324-334
- Forristall,G.Z.,J.R.Kreider and A.M. Reece,1979,"Semi-submersible rig motion studies offshore of Alaska and Southern California", OTC Paper 3557, 11th Offshore Tech. Conf., pp 1755-1763
- Gable,C. G.,1979,"Report on data from the NSTS experiment at Torrey Pines Beach, California, November-December 1978", IMR Ref No. 79-8, Inst. of Marine Resources, Univ. of Calif., San Diego
- Gable,C. G.,1979,"Report on data from the NSTS experiment at Santa Barbara, California, Jan-Feb 1980" IMR Ref No. 81-5, Inst. of Marine Resources, Univ. of Calif., San Diego
- Goodman,N.R.,1957,"On the joint estimation of the spectra, cospectrum, and quadature spectrum of a two-dimensional stationary gaussian process", Ph.D Thesis, Scientific Paper No. 10, New York University, New York
- Guza,R.T. and E.B. Thorton,1978,"Variability of longshore currents", Proc. 16th Conf. on Coastal Engin., ASCE, pp 756-775
- Hasselmann,K.,T.P.Barnett,E.Bouws, H.Carlson,D.E.Cartwright, K.Enke,J.A.Ewing,H.Gienapp,D.E.Hasselmann,P.Kruseman, A.Meerburg,P.Muller,D.J.Olbers,K.Richter,W.Sell, and H. Walden,1973,"Measurements of wind-wave growth and swell decay during the Joint North Sea Project (JONSWAP)", Erganzungsheft zur Deutschen Hydrographischen Zeitschrift, Reihe, A(8),No 12, 99 pp
- Haubrich,R.A.,1965,"Earth Noise 5 to 500 Millicycles Per Second, 1. spectral stationarity, normality, and non-linearity", Jour. of Geophy. Res., vol 70, pp 1415-1427
- Higgins,A.L.,R.J.Seymour, and S.S.Pawka,"A compact representation of ocean wave directionality", in press, Jour. of Applied Ocean Res.
- Hom-ma,M.,K. Horikawa, and Y. Chao,1966,"Sheltering effects of Sado Island on wind waves off Niigata Coast",Coastal Engin. in Japan, vol 9, pp 27-44

- Inman,D.L. and W.H. Quinn,1951,"Currents in the surf zone", Proc. 2nd Conf. on Coastal Engin.,ASCE, pp 24-36
- Inman,D.L. and B.M.Brush,1973,"The coastal challenge", Science, vol 181, pp 20-32
- Keller,J.B.,1978,"Rays,waves, and asymptotics", Bull. AM. Math. Soc., vol 84, pp 727-750
- Kitaigorodskii,S.A.,1962,"Application of the theory of simularity to the analysis of wind-generated wave motion as a stochastic process", Bull. Acad. Sci. USSR Geophys. Ser No. 1, vol 73
- Komar,P.D. and D.L. Inman,1970,"longshore sand transport on beaches", Jour. of Geophys. Res., vol 75, no 30, pp 5914-5927
- Long,R.B.,1973,"Scattering of surface waves by an irregular bottom", Jour. of Geophys. Res., vol 78, no 33, pp 7861-7870
- Longuet-Higgins,M.S.,1957,"On the transformation of a continuous spectrum by refraction", Proc. Camb. Phil. Soc., vol 53 , pp 226-229
- Longuet-Higgins,M.S.,D.E.Cartwright, and N.D.Smith,1963, Observations of the directional spectrum of sea waves using the motions of a floating buoy", Ocean Wave Spectra, Prentice- Hall, Englewood Cliffs,N.J., pp 111-136
- Longuet-Higgins,M.S.,1970 a&b,"longshore currents generated by obliquely incident sea waves", Jour. of Geophys. Res., vol 75, no 33, pp 6778-6789
- Lugwig,D.,1966,"Uniform asymptotic expansions at a caustic", Comm. Pure and Applied Math., vol 19, no 2, pp 215-250
- Ludwig,D.,1968,"Strength of caustics", Jour. Acoust. Soc. Am., vol 43, no 2, pp 1179-1180
- McLeish,W.,D.Ross,R.A.Scuchman,P.G.Teleki,S.V.Hsiao,O.H.Shemdin, and W.E.Brown Jr., "Synthetic aperture radar imaging of ocean waves: comparison with wave measrments", Jour. of Geophys. Res., vol 85, no C9, pp 5003-5011
- Munk,W.H. and R.S.Arthur,1952,"Wave intensity along a refracted ray", Gravity Waves, U.S. Dept. of Commerce, National Bureau of Standards, cir. 521, pp 95-108
- Munk,W.H.,F.E.Snodgrass, and M.J.Tucker,1959,"Spectra of low-frequency ocean waves", SIO Bull., vol 7, pp 283-361
- Munk,W.H.,G.R. Miller,F.E.Snodgrass, and N.F.Barber,"Directional recording of swell from distant storms", Phil. Trans. of R. Soc. Lond. (A), vol 255, no 1062, pp 505-584
- National Marine Consultants,1960,"Wave statistics for seven deepwater stations along the California coast", U.S. Army Corps of Engin., L.A. District
- Newman,J. N.,1965,"Propagation of water waves past 2-dimensional obstacles", Jour. of Fluid Mech., vol 23, pp 23-29
- Panicker,N.N.,1971,"Determination of directional spectra of ocean waves from gage arrays", Tech. Rep. HEL 1-18, Univ. of Calif., Berkeley 315 pp
- Panicker,N.N.,1974,"Review of techniques for directional wave spectra", Proc. Int. Symp. on Ocean Wave Measurement and Analysis, ASCE, New Orleans, La. pp 669-688
- Pawka,S.S.,D.L.Inman,R.L.Lowe, and L.C.Holmes,1976,"Wave climate at Torrey Pines Beach, California", Tech. Paper 76-5,Coastal Engin.

- Res. Cen., Ft Belvoir, Va.
- Pawka,S.S.,1977,"Linear arrays", Proc of a Workshop on Coastal Processes Instrumentation, La Jolla, Ca., Univ. of Calif., San Diego, Sea Grant Pub. No. 62, IMR ref No. 78-102, pp 97-112
- Penney,W.G. and A.T. Price,1952,"The diffraction theory of sea waves by breakwaters, and the shelter afforded by breakwaters", Phil. Trans. of R. Soc. Lond. (A), vol 244, pp 236-253
- Peregrine,D.H. and R. Smith,1979,"Nonlinear effects upon waves near caustics", Phil. Trans. of R. Soc. Lond. (A), vol 292, pp 341-370
- Pierson,W.J.,1951,"The interpretation of crossed orthogonals in wave refraction phenomena", U.S. Army Beach Erosion Board, Tech. Memo. No. 21, 83 pp Phillips,O.M.,1966, The Dynamics of the Upper Ocean, Cambridge Univ.Press, London
- Putnam,J.A. and R.S.Arthur,1948,"Diffraction of water waves by Breakwaters", Trans. Am. Geophys. Union, vol 29, no 4, part 1, pp 481-490
- Putnam,J.A. and J.W.Johnson,1948,"The dissipation of wave energy by bottom friction", Univ. of Calif. Fluid Mech. Lab. Tech. Rep. HE-116-275
- Regier,L.A.,1975,"Observations of the power and directional spectrum of oceanic surface waves",Ph.D. Dissertation, Univ. of Calif., San Diego
- Ross,D.B.,B.Au,W.Brown, and J.Mcfadden,1974,"A remote sensing study of Pacific hurricane Ava", Proc. Int. Symp. Remote Sensing Environ., 9th, pp 163-180
- Seymour,R.J.,1977,"Estimating wave generation on restricted fetches", Jour. of the Waterways Port Coastal and Ocean Div., ASCE, vol 103, WW2, pp 251-264
- Seymour,R.J. and M.H. Sessions,1976,"A regional network for coastal engineering data", Proc. 15th Int. Conf. on Coastal Engin., ASCE, Honolulu, Haw.
- Seymour,R.J. and A.L.Higgins,1977,"A slope array for measuring wave direction", Proc. of a Workshop on Coastal Processes Instrumentation, La Jolla,Ca.,Univ. of Calif., San Diego, Sea Grant Pub. No. 62, IMR Ref. No. 78-102, pp 133-142
- Shemdin,O.H.,D.L.Inman, and J.E.Blue,1977,"West Coast Experiment Test Plan", Jet Propulsion Lab. Rep. 900-765, CIT, Pasadena, Ca.
- Shemdin,O.H.,1980,"The West Coast Experiment: a review", Jour. of Geophys. Res., vol 85, no C9, after 4145
- Shemdin,O.H.,K.Hasselmann,S.Y.Hsiao, and K.Herterich,1978, "Nonlinear and linear bottom interaction effects in shallow water", in Turbulent Fluxes through the Sea Surface, Wave Dynamics, and Prediction, Nato Conference, pp 347-372, Plenum, New York
- Snodgrass,F.E.,G.W.Groves,K.F.Hasselmann,G.R.Miller,W.H.Munk, and W.H.Powers,1966,"Propagation of ocean swell across the Pacific", Phil. Trans. of R. Soc. of Lond. (A), vol 259, pp 431-497
- Stillwell,D. Jr and R.O.Pilon,1974,"Directional spectra of surface waves from photographs", Jour. of Geophys. Res., vol 77, no 9, pp 1277-1284

- Thompson,E.F.,1980,"Energy spectra in shallow U.S. waters", Tech. Paper No. 80-2, Coastal Engin. Res. Cen., U.S. Army Corps of Engin., Ft. Belvoir, Va.
- Tunstall,E.B., and D.L.Inman,1975,"Vortex generation by oscillatory flow over rippled surfaces", Jour. Geophys. Res., vol 80, no 24, p 3475-3484
- Tyler,G.L.,C.C.Teague,R.H.Stewart,A.M.Peterson,W.H.Munk, and J.W.Joy,"Directional spectra from synthetic aperture observations of radar scatter", Deep Sea Res., vol 12, pp 989-1016
- Vesecky,J.F.,S.Y.Hsiao,C.C.Teague,O.H.Shemdin, and S.S.Pawka, "Radar observations of wave transformations in the vicinity of islands", Jour. of Geophys. Res., vol 85, no C9, pp 4977-4986
- Wilson,S.W.,D.G. Wilson, and J.A.Michael,1973,"Analysis of swell near the island of Aruba", Jour. of Geophys. Res., vol 78, no 33, pp 7834-7844

Appendix A. Comparison of SAR and Linear Array

Comparisons Between Wave Directional Spectra From SAR and Pressure Sensor Arrays

S. S. PAWKA

Shore Processes Laboratory, Scripps Institution of Oceanography, La Jolla, California 92093

S. V. HSIAO AND O. H. SHEMDIN

Jet Propulsion Laboratory, California Institute of Technology, Pasadena, California 91103

D. L. INMAN

Shore Processes Laboratory, Scripps Institution of Oceanography, La Jolla, California 92093

Simultaneous directional wave measurements were made at Torrey Pines Beach, California, by a synthetic aperture radar (SAR) and a linear array of pressure sensors. The measurements were conducted during the West Coast Experiment in March 1977. Quantitative comparisons of the normalized directional spectra from the two systems were made for wave periods of 6.9–17.0 s. The comparison results were variable but generally showed good agreement of the primary mode of the normalized directional energy. An attempt was made to quantify the physical criteria for good wave imaging in the SAR. A frequency band analysis of wave parameters such as band energy, slope, and orbital velocity did not show good correlation with the directional comparisons. It is noted that absolute values of the wave height spectrum cannot be derived from the SAR images yet and, consequently, no comparisons of absolute energy levels with corresponding array measurements were intended.

INTRODUCTION

A central objective of the West Coast Experiment is to establish a rational basis for verifying the capabilities and limitations of remote sensing systems equivalent to those deployed in Seasat 1. This study focuses on the surface truth verification of the synthetic aperture radar (SAR) for detecting wavelengths and directions of surface gravity waves in the ocean. A SAR system equivalent to that on board Seasat 1 was flown aboard the NASA aircraft CV-990 over the southern California test area as part of the West Coast Experiment.

Wave patterns have been observed frequently in SAR images of the ocean surface. Normally, surface waves can be distinguished from internal waves by the crescent-shaped and packetlike configuration of internal waves versus the long-crested nature associated with swell. The deepwater lengths of internal waves are of the order of 750 m, while swell lengths are commonly in the range 150–450 m. In shallow waters, however, internal waves become more long crested, and their wavelengths may decrease to 300 m. Therefore one cannot always distinguish between surface and internal waves without some surface truth information.

It is only recently that attempts have been staged to carefully verify the nature of these wavelike patterns observed in SAR images. The first comprehensive attempt was made during the Marineland Experiment, where wave measuring sensors were placed over the continental shelf at three stations along a transect normal to shore in the area offshore of Marineland, Florida. A capillary sensor was also deployed at the station closest to shore to study the modulation of short waves, detected by radar waves, along the profile of long waves. A preliminary report on these results was given by Shemdin [1978]. A series of papers describing the results in detail appear in this issue of the *Journal of Geophysical Research*. It is of interest to note that the Marineland results did provide

Copyright © 1980 by the American Geophysical Union.

Paper number 80C0483.
0148-0227/80/080C-0483\$01.00

positive confirmation on the SAR capability to measure the dominant wave length and the dominant wave direction accurately.

In this paper, comparisons are made between wave directional spectral properties derived from SAR images and those computed from a pressure sensor array. The primary surface wave measuring system used was the linear pressure gauge deployed at Torrey Pines by the Shore Processes Laboratory (SPL) of Scripps Institution of Oceanography.

Quantitative comparisons were made of the wave directional spectra sampled with the SAR and pressure array systems.

SPL LINEAR PRESSURE ARRAY

The surface measurements of wave directional spectra were obtained by using a linear array of five pressure sensors located in a mean water depth of 9.5 m. The sensors were spaced in a 1-2-4-5 configuration (see Figure 1), where the unit spacing was 33 m. The overall array length of 396 m was designed for directional resolution of waves coming around the north and south ends of San Clemente Island. This requires a directional resolution of peaks separated by 5°–10° in 10 m of water. Pawka *et al.* [1976] discuss the local wave climate and fundamental directional spectra analysis techniques.

The pressure sensor data were processed in consecutive 34.1-min time segments and analyzed to yield frequency spectra with 32 degrees of freedom and a bandwidth of 0.0078125 Hz. The spectra were corrected for depth attenuation of the pressure signal to yield estimates of sea surface height spectra. The range of high-quality spectral estimates, limited by resolution in the low frequencies and by depth attenuation in the high frequencies, spans wave periods of 4–25 s. Figure 2 is a plot of a typical frequency spectrum estimate obtained from the SPL pressure array.

The pressure sensor data were analyzed for wave direc-

PAWKA ET AL. COMPARISON OF SAR AND PRESSURE SENSOR ARRAY

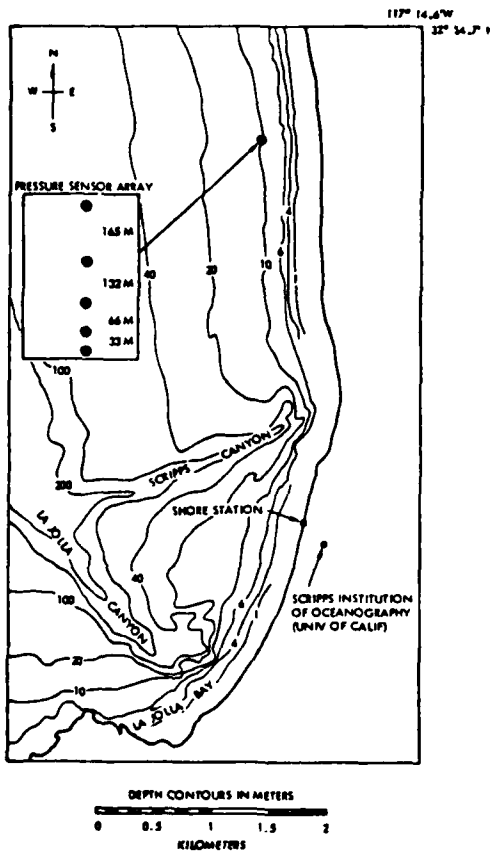


Fig. 1. Location map for SPL pressure sensor array at Torrey Pines Beach. The array axis points 4.5° west of north, which is roughly parallel to the near-plane contours.

tional spectra by using the maximum likelihood estimator (MLE), as given by Capon [1969]. This estimator performs well in the analysis of narrow directional spectra. Davis and Ringer [1977] discuss the performance of the MLE with various forms of the directional spectrum. Figure 3 shows the response of the SPL array and MLE to narrow and broad unimodal directional spectra. The width and location of the narrow spectrum are accurately defined by this method of analysis. However, the broad peak is 'overresolved,' with the result that multiple peaks appear in the spectrum. Also shown in Figure 3 is the good response of the SPL array and analysis techniques to a typical form of bimodal directional spectrum found in the region.

The wave period range for high-quality directional spectra is approximately 7–20 s. Longer-period waves are not well resolved by the array. Problems develop at the short-period region of the spectrum because of the relatively large size of the smallest lag in the array compared to the length of the waves. This effect causes ambiguity of wave approach angle, which creates false 'alias' peaks in the directional spectrum. Because

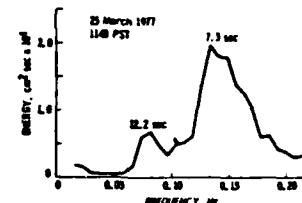


Fig. 2. Frequency spectrum estimated from SPL pressure sensor array. The mean depth of the sensors during the measurement was 9.3 m. The total variance for this run is 1407 cm², which corresponds to a significant height of approximately 1.5 m.

of these sampling problems the frequency range for comparisons of directional spectra was set with limits of 6.9–17.0 s. The Torrey Pines site was selected for nearshore wave measurements because of the relatively plane depth contours in the vicinity. This type of topography is necessary for spatial homogeneity of the wave field over the length of the array. The measurements of the directional spectra in 10 m of water were refracted out to deep water for comparison with the SAR spectra. A numerical refraction model patterned after the one

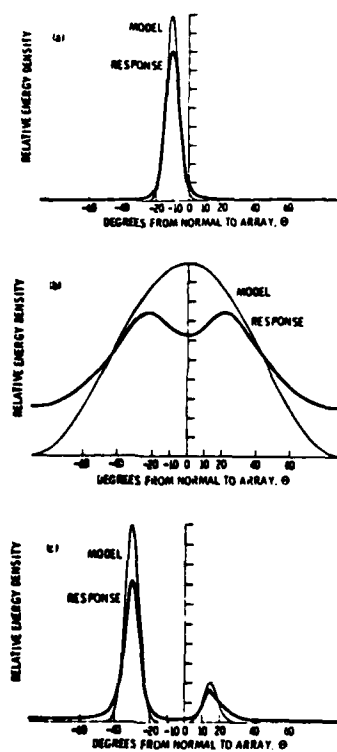


Fig. 3. Response of the SPL array and analysis techniques (MLE) to several model directional spectra: (a) $\cos^{200}(\theta + 10^\circ)$, (b) $\cos^2(\theta)$, and (c) $10.0 \cos^{200}(\theta + 30^\circ) + 2.0 \cos^{200}(\theta - 10^\circ)$. The plot shows the good response of the array system to narrow input directional spectra.

PAWKA ET AL. COMPARISON OF SAR AND PRESSURE SENSOR ARRAY

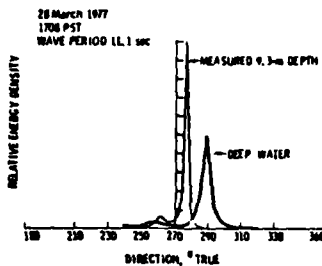


Fig. 4. Measured directional spectrum and deepwater estimate obtained from refraction analysis. The nearshore spectrum was sampled by the SPL pressure sensor array. The directionally integrated energy density in 9.3-m depth is $1.00 \times 10^4 \text{ cm}^2 \text{ s}$, while the estimated deepwater value is $1.15 \times 10^4 \text{ cm}^2 \text{ s}$.

developed by Dobson [1967] was used for the estimation of the shoaling transformation of the wave directional spectrum. An example of the refractive effects on the directional spectrum is shown in Figure 4, which displays the spectrum measured in 10 m along with the deepwater estimate obtained from the refraction model.

SAR SYSTEM AND IMAGE PROCESSING

The SAR is an imaging radar which operates at an electromagnetic frequency of 1.36 GHz, corresponding to a wavelength of 23 cm [see Brown et al., 1976; Shemdin et al., 1978]. It provides its own illumination so it can be operated during day or night and independently of clouds. The SAR uses the Doppler history or the change in phase associated with motion of a scatterer with respect to the moving aircraft in the processing of images. The phase and amplitude of the back-scattered energy from a surface roughness element are both recorded on a signal film in a manner that improves the azimuth (along track) resolution of an image. The latter is also directly proportional to the antenna length of the radar. The range or cross-track resolution of the SAR is determined by the width of short pulses or the width of coded pulses, which are compressed to equivalent short pulses by match-filtering techniques. Figure 5 is a schematic of the SAR illuminating a patch on the ocean surface. The SAR system used in the West Coast Experiment had an estimated resolution of $25 \times 25 \text{ m}$.

For each scattering point on a scene being imaged the phase and amplitude of the backscatter appears on the signal film as a Fresnel zone pattern. The pattern is determined in the azimuth direction by the phase history produced by the relative motion between the sensor and scatterer and in the range direction by the structure of transmitted pulses.

The signal film is thus composed of many Fresnel zone patterns corresponding to each scatterer on the scene. The signal film is used as input into an optical processor which is designed to convert the film to the original scene being imaged by Fourier transform techniques.

In order to process the image digitally the raw image was digitized at a spacing of 10.8 m in the azimuth direction. The scale in range direction of the raw image is the radar slant range instead of the surface distance. To convert the range scale to surface distance, the range dimension is divided by $\sin \gamma$, where γ is the incidence angle. Then the samples are reformatted by interpolation. This process is called geometric correction.

An example of the corrected image which was taken on March 28, 1977, near Torrey Pines is shown in Figure 6. Because of the small incidence angle the geometrically corrected image is distorted near nadir.

A subsection of 512×512 samples of the geometrically corrected image was chosen far enough from nadir to avoid the distortion effect (see Figure 6). The area of the subsection is approximately $5.5 \times 5.5 \text{ km}^2$. A two-dimensional fast Fourier transform (FFT) was performed on the subsection image to obtain a two-dimensional wave number spectrum, shown in Figure 7.

The directional distribution of wave energy at wave number k was then plotted by tracing along a circle centered at zero in the wave number plane with a radius k on the two-dimensional spectrum. Because of the 180° ambiguity in the image, there are two peaks 180° apart in the directional distribution when only one wave train is present in the image. This ambiguity can be resolved by assuming that all waves are propagating shoreward.

There is a distortion in the wave image due to the wave propagation during the imaging process. The amount of the distortion depends on the angle between wave direction and radar flight direction and the ratio of wave phase speed to radar flight speed. A schematic sketch of the distortion is shown in Figure 8. In this figure, V is the velocity of the aircraft, k is the true wave number, and k' is the observed wave number. It can be shown through simple geometric relations that

$$\begin{aligned} k = k' \cos \theta / \cos \beta &\quad \theta \neq \pm 90^\circ \\ k = k' V / (V \mp C) &\quad \theta = \pm 90^\circ \end{aligned} \quad (I)$$

and

$$\beta = \theta + \arcsin (C \cos \theta / V)$$

where C is the wave phase velocity and θ and β are the observed and real wave directions, respectively, as defined in Figure 8. These equations give maximum wave number distortion at $\theta = \pm 90^\circ$ (azimuth waves) and maximum wave direction distortion at $\theta = 0^\circ$ or 180° (range waves). In the West Coast Experiment the aircraft speed was 470 km (235 m/s). For 15.0-s deepwater waves the largest wave directional distortion is 5.6° , and the largest wave number distortion is 9.8%.

The SAR data used in this study are centered at $32^\circ 59' \text{N}$,

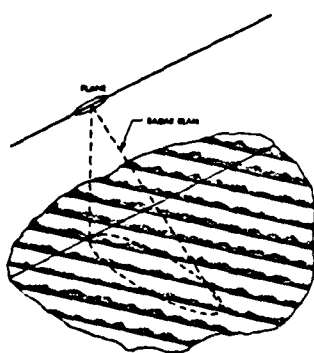


Fig. 5. Schematic of the SAR illuminating a patch on the ocean surface [after Elachi and Brown, 1977].

PAWKA ET AL.: COMPARISON OF SAR AND PRESSURE SENSOR ARRAY

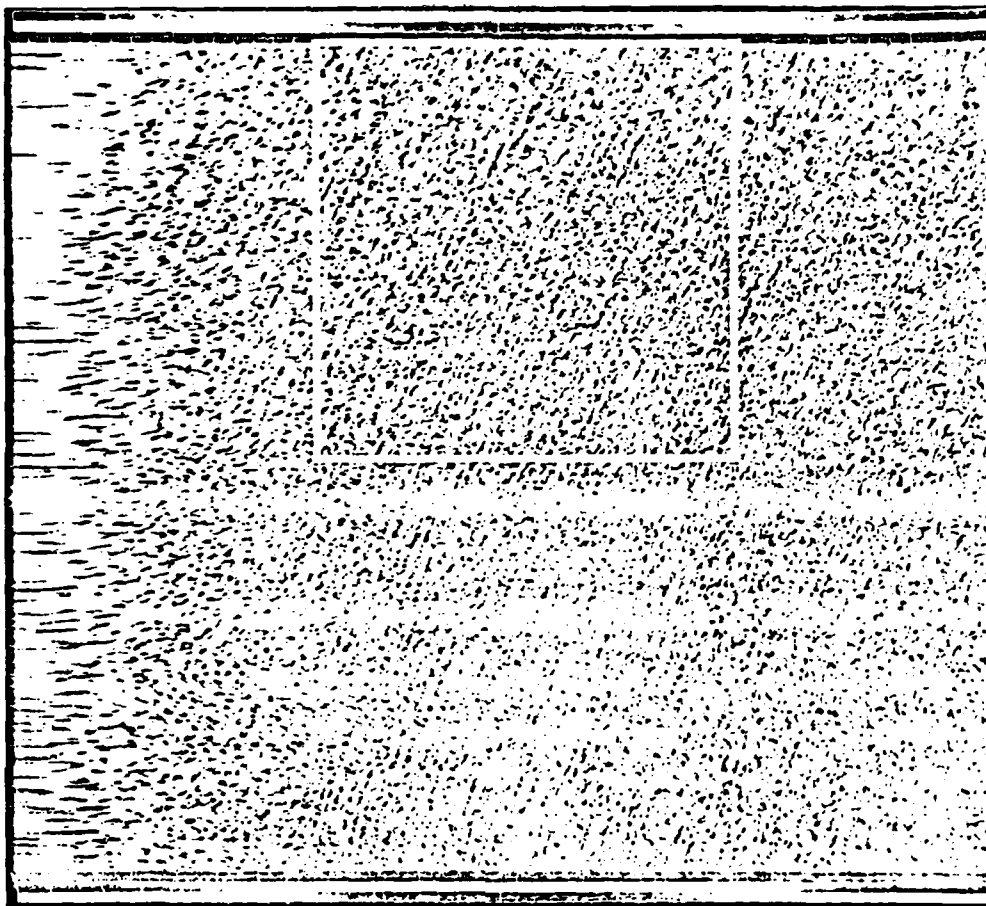


Fig. 6. Geometrically corrected SAR imagery near Torrey Pines Beach taken on March 28, 1977. The subsection is the area where a two-dimensional FFT was performed. Each small division is approximately 54 m.

117°20'W, where the water depth is 200 fathoms (370 m). Since it is close to the SPL array site (~1 km apart), any variations in wave directional distributions due to island shadowing are expected to be negligible.

COMPARISONS OF DIRECTIONAL SPECTRA DERIVED FROM SAR AND SPL ARRAY

Simultaneous wave measurements were made by the SAR and the SPL array on March 25 and 28, 1977. The general wave conditions were quite different on the two days, as was evidenced by the frequency spectra shown in Figure 2 (March 25) and Figure 9 (March 28). The March 25 data run had a total variance of 1407 cm², which was divided between a small swell peak centered on 12.2 s and a locally generated wind wave peak which had a maximum at 7.3 s. The waves of March 28 had a unimodal frequency spectrum with a peak period of 11.1 s and a total variance of 602 cm².

The directional spectra from the two measurement systems were normalized to the same frequency band energy for comparison. That is,

$$\int_{\alpha_s}^{\alpha_n} S_d(f_0, \alpha) d\alpha = \int_{\alpha_s}^{\alpha_n} S_a(f_0, \alpha) d\alpha \quad (2)$$

where $S_d(f_0, \alpha)$ and $S_a(f_0, \alpha)$ are the SAR and SPL array directional spectra for the frequency band centered on f_0 , α is the direction of wave propagation, and α_n and α_s are the north and south cutoffs of the refraction analysis for the shoaling transformation of the array directional spectrum.

The comparative directional spectra for six different frequency bands of the March 25 data run are shown in Figure 10. Figure 11 displays the spectral comparisons for March 28. The agreement of the directional spectra obtained from the two systems is quite variable. Some of the frequency bands,

PAWKA ET AL.: COMPARISON OF SAR AND PRESSURE SENSOR ARRAY

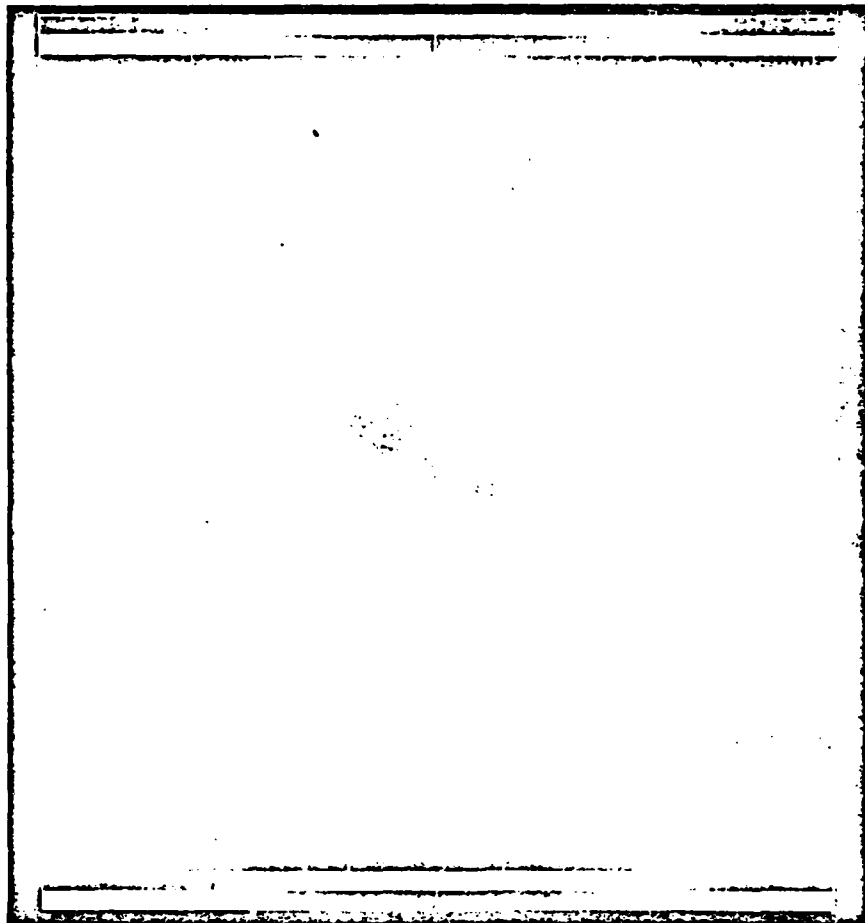


Fig. 7. Two-dimensional FFT of the subsection in Figure 6. The wave number scale in each small division is approximately 0.0057 m^{-1} .

such as the 8.8-s waves on March 28 (Figure 11b) show very close agreement, while other bands, the 12.2-s waves on March 28 (Figure 11c), for example, show no common features. In general, there appears to be more scatter and a higher noise level in the SAR directional spectra. Also, there appears to be a persistent secondary peak in the SPL array spectra centered on 250° - 260° T and some south swell ($\sim 230^\circ$ T) (Figure 11a) which are not well represented in the SAR spectra. However, the primary mode of most of the spectra, a peak located around 280° - 290° T, is indicated in the results from both systems.

In an attempt to quantify the comparison of the primary modes of the spectra of the SAR and SPL array a parameterization of the modes is made in terms of α_m , the direction of maximum energy density, and $\Delta\alpha_m$, the full width at half maximum. Table I lists the results for this modal analysis for both

data runs. The comparisons of the mode directions and widths estimated by the two systems were good except in the longest-period bands which have low energy and significant southern components. The modal directions agree to within 6° for 79% of the directional spectrum comparisons.

The average mode parameters were calculated for the spectra with dominant northern components, waves with periods of 6.9-11.1 s. The average mode direction and width for each data run, also listed in Table I, indicate good agreement between the two measurement systems. Both the SAR and SPL array results indicate a shift of mode direction and a decrease in mode width between March 25 and 28.

Many computational uses of directional wave data involve various moments of the directional spectrum. The first and second moments of the spectrum are important quantities and are defined as follows:

PAWKA ET AL. COMPARISON OF SAR AND PRESSURE SENSOR ARRAY

TABLE I. Mode Parameters

Wave Period, s	March 25, 1977		March 28, 1977		SPL Array		SAR	
	α_m	$\Delta\alpha_m$	α_m	$\Delta\alpha_m$	α_m	$\Delta\alpha_m$	α_m	$\Delta\alpha_m$
17.0	244	64	306	20	283	49	290	10
15.0	285	55	291	16	227	14	266	42
13.3	291	15	291	13	291	14	275	17
12.2	288	16	325	10	288	9	257	9
11.1	286	9	284	7	289	6	288	16
10.2	288	9	284	14	291	10	290	9
9.5	287	10	283	10	288	6	291	7
8.8	283	11	279	14	288	13	289	9
8.2	293	10	265	16	288	8	290	9
7.7	286	23	287	30	291	10	290	8
7.3	280	15	286	15	291	8	289	7
6.9	286	9	284	15	290	12	290	14
Average	286	13	282	15	290	9	290	10

Parameters α_m and $\Delta\alpha_m$ are the direction of maximum energy density of primary mode and full width at half maximum of primary mode, respectively. The average is computed for periods of 6.9–11.1 s.

$$\hat{\alpha}_x = \frac{\int_{-\pi}^{\pi} \alpha S_x(f_x, \alpha) d\alpha}{\int_{-\pi}^{\pi} S_x(f_x, \alpha) d\alpha} \quad (3)$$

$$\sigma_x^2 = \int_{-\pi}^{\pi} (\alpha - \hat{\alpha}_x)^2 S_x(f_x, \alpha) d\alpha \quad (4)$$

where x is a subscript denoting the system used (R and A for SAR and SPL array, respectively), $\hat{\alpha}_x$ is the average angle, $S_x(f_x, \alpha)$ is the directional spectrum, and σ_x^2 is the dispersion. The calculated values for these moments for the two systems and the various frequency bands are listed in Table 2. Although the mean angle estimates tend to be more stable than the mode results in the lower-frequency region of the spectrum, the agreement is less good than the mode comparisons in the energetic bands. The region of the spectrum which is dominated by northern quadrant energy, wave periods of 6.9–11.1 s, has an average difference in the estimation of the mode direction of 3.9°, while the average mean angle difference is 7.8°. This is due to the fact that although the primary mode is well located in the SAR spectra, the high noise level and lack of detection of secondary modes degrade the SAR estimates of the mean angle. The dispersion values are generally higher

for the SAR directional spectra, particularly in the medium frequency range, where the SAR noise level is relatively high and the secondary mode in the array spectra is low (see Figures 10 and 11). The dispersion values agree well for the short-period (6.9–8.2 s) region of the spectrum. It is interesting to note that both systems indicate a dramatic increase in the value of σ^2 between the 7.3-s and the 6.9-s bands.

A more general quantitative comparison between the directional spectra of the SAR and SPL array is a normalized mean square difference (MSD), defined as follows:

$$MSD = \frac{\int_{-\pi}^{\pi} [S_A(f_A, \alpha) - S_R(f_R, \alpha)]^2 d\alpha}{\int_{-\pi}^{\pi} S_A^2(f_A, \alpha) d\alpha} \quad (5)$$

The MSD was computed for all of the comparative spectra, and the results are included in Table 2. As with the other comparisons of the spectra, this parameter shows a wide range in its values. Also, there is little correlation (-0.23 on March 25 and 0.13 on March 28) between the band energy and the MSD. Figure 12a is a plot of the MSD as a function of the band energy. Included as Figure 12b is a plot of the relationship between the MSD and a slope parameter Ek^2 , where E is the band energy and k is the magnitude of the wave number. Although the correlation is somewhat higher with Ek^2 (-0.25 on March 25 and -0.38 on March 28), it does not support well the anticipated enhancement of the imaging process of waves with increasing wave slope. Another process to consider is the modulation of the short waves (23 cm) by interaction with the

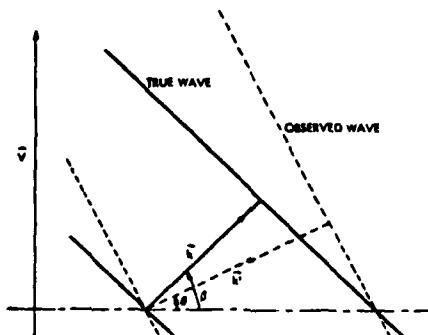


Fig. 8. Schematic sketch of the SAR image distortion due to wave motion

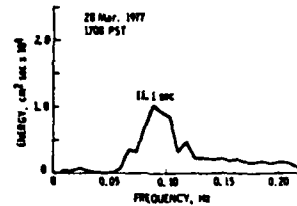


Fig. 9. Frequency spectrum estimated from the SPL pressure sensor array. The mean depth of the sensors during the measurement was 9.4 m. The total variance for this run is 602 cm², which corresponds to a significant height of 0.98 m.

PAWKA ET AL.: COMPARISON OF SAR AND PRESSURE SENSOR ARRAY

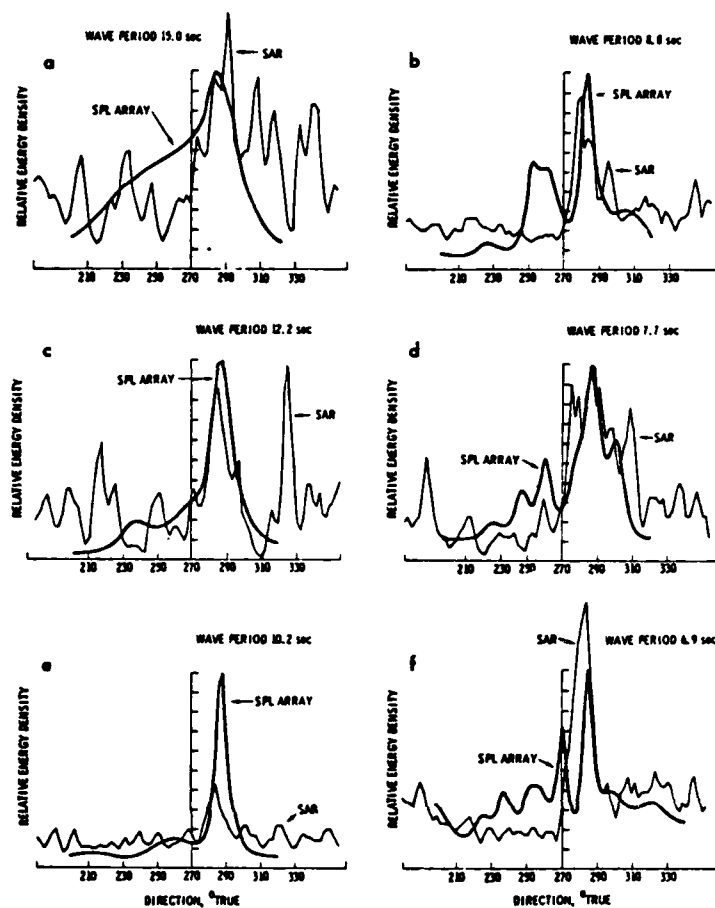


Fig. 10. Comparison plots of directional spectra estimated by the SAR and SPL array for indicated wave periods. These results are for the data run at 1140 PST on March 25, 1977. The spectra show good agreement of the primary mode of directional energy.

TABLE 2. Estimates of Spectral Moments

Wave Period, s	March 25, 1977				March 28, 1977							
	SPL Array		SAR		SPL Array		SAR					
	$\bar{\alpha}$	σ^2	$\bar{\alpha}$	σ^2	Energy	MSD	$\bar{\alpha}$	σ^2	$\bar{\alpha}$	σ^2	Energy	MSD
17.0	257	0.82	267	1.2	3.6	46.2	260	0.93	265	0.81	4.0	35.3
15.0	266	0.77	272	1.1	12.0	27.4	248	0.73	262	0.81	23.3	56.6
13.3	267	0.89	276	0.98	47.9	39.2	263	0.85	265	1.1	25.4	59.3
12.2	275	0.55	261	0.98	54.7	24.2	281	0.33	260	1.0	60.2	69.6
11.1	274	0.48	266	1.1	41.7	31.6	283	0.29	262	1.1	90.2	63.1
10.2	273	0.73	264	1.1	31.0	36.6	284	0.30	267	1.0	88.0	33.5
9.5	274	0.70	271	0.93	46.0	30.2	284	0.27	269	1.0	85.4	24.6
8.8	272	0.70	268	1.1	49.7	26.7	278	0.50	271	0.95	31.9	13.4
8.2	270	0.84	274	0.67	59.7	54.7	280	0.40	277	0.65	49.6	11.5
7.7	272	0.72	280	0.68	144.0	20.4	277	0.34	281	0.60	22.3	35.0
7.3	271	0.74	278	0.69	197.0	35.8	273	0.79	281	0.70	21.7	43.8
6.9	273	1.3	280	1.2	193.0	30.4	278	1.2	279	1.3	21.7	15.1
Average	270	0.77	271	0.98		33.6	274	0.59	270	0.94		38.4

The mean angle $\bar{\alpha}$ is defined in equation (3). The dispersion σ^2 is defined in equation (4). Values are in $\text{deg}^2 \times 10^3$ (divided by band energy). Energy is bond energy in $\text{cm}^2 \cdot S(\text{Hz}) \Delta f$. Values are refracted to deep water. MSD is the mean square difference of the SPL array and SAR spectra defined in equation (5). Values are given in percent.

PAWKA ET AL.: COMPARISON OF SAR AND PRESSURE SENSOR ARRAY

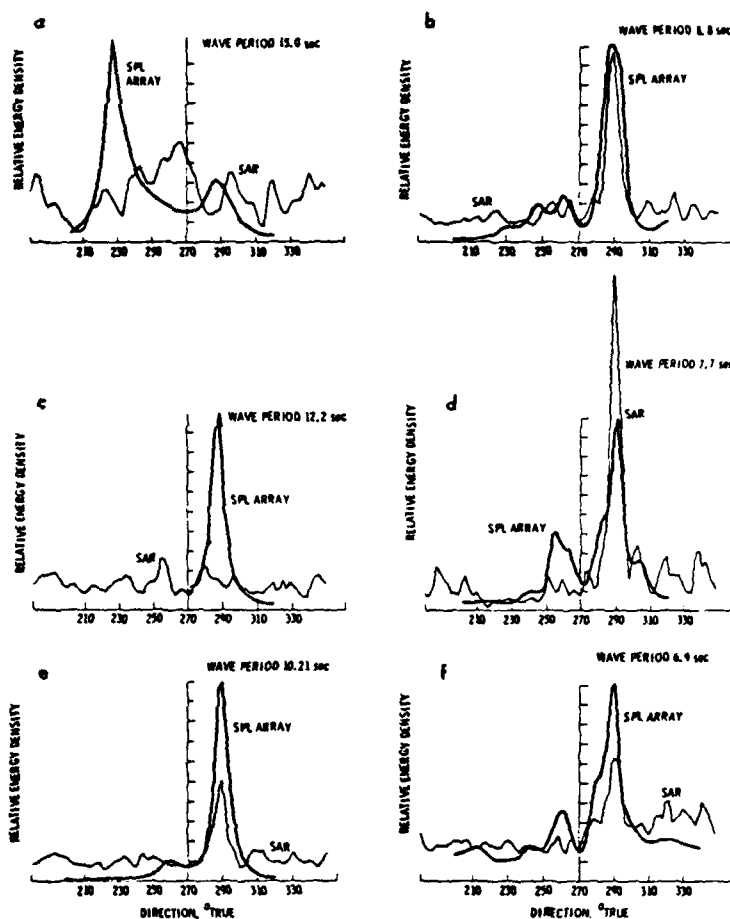


Fig. 11. Comparison plots of directional spectra estimated by the SAR and SPL array for indicated wave periods. These results are for the data run at 1708 PST on March 28, 1977. The spectra show a highly variable degree of comparison.

orbital velocity field of the long waves as discussed by Shemdin [1978]. This mechanism should increase the imaging process with higher orbital velocity, which is proportional to $E^{1/2}\alpha$, where α is the radian frequency. Once again the correlation with MSD (-0.20 on March 25 and -0.29 on March 28) is not significant. A more quantitative discussion of the modulation processes is given by Wright et al. [this issue].

The lack of correlation of the MSD with the various parameters of wave intensity suggests that either there are other factors that are significant in the imaging process or the concept of individual frequency band values for these parameters is not valid in this case. The integrated values of E , EK^2 , and $E^{1/2}\alpha$ are all greater on March 25 than on March 28, which corresponds to several indications of generally better spectral agreement on March 25. There is a slight increase in the average MSD and a large increase in the scatter of the MSD values on March 28 as compared to March 25. Also, the aver-

age difference in the estimated mean angle is 7.3° for March 25 contrasted to the value of 9.8° for March 28. It may be noted that there were stronger winds during the March 25 run ($7-9$ m/s) than during the March 28 run ($4-5$ m/s). Also, it should be noted that the spectra for waves in the range $6.9-8.2$ s compared well on both days which had dramatically different energy levels for these bands.

DISCUSSION OF RESULTS

The resolution of both measurement systems appears to be consistent in the definition of the narrow (approximately $10^\circ-15^\circ$ full width at half maximum) northern quadrant peak in the directional spectrum. However, the SAR does not always detect this peak, which is consistently present in the SPL array spectra for wave periods of $7-12$ s. It is suggested that the imaging processes trend with some parameter of the wave intensity and that conditions exist for which waves are not un-

PAWKA ET AL.: COMPARISON OF SAR AND PRESSURE SENSOR ARRAY

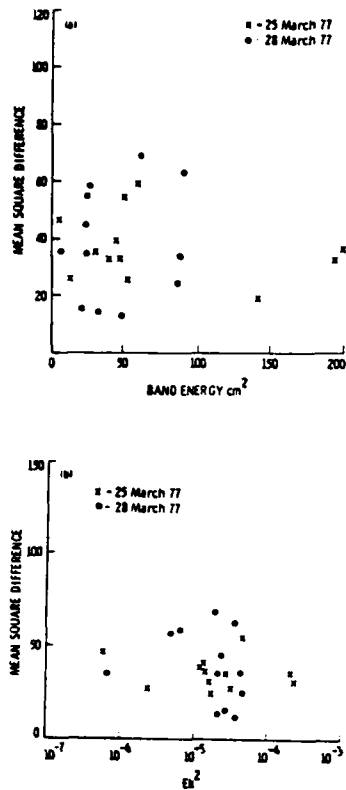


Fig. 12. Relationship between the mean square difference of the directional spectra from SAR and the SPL array as a function of frequency band values of wave parameters: (a) band energy E and (b) band slope Ek^2 , where k is the magnitude of the wave number.

aged. For example, the low-frequency southern swell and the small secondary peak in the medium frequency spectra are not imaged by the SAR system. Theory suggests that wave slope and orbital velocity should be important in the imaging process, but this was not well demonstrated in this experiment.

A modal analysis of the directional spectra indicates good agreement of the modal direction and width estimates of the two systems when the SAR has imaged the waves (a noticeable peak appears in the spectrum). Because of the similarity of the directional spectra of well-imaged waves it appeared that the SAR may have been yielding only information on the dominant directions of the wave field. The mode directions and width for the 7- to 12-s waves with low MSD (below 35%) were correlated with these parameters obtained from the array analysis. The correlations of 0.84 for mode directions and 0.88 for widths indicate that the SAR system is defining variable wave information with frequency.

The relatively high noise level and poor detection of low secondary modes in the SAR spectra cause difficulties in the

estimation of spectral moments. The two systems have an average difference in estimation of mean angle of 8.5°. In general, the SAR estimates of dispersion were higher than the results from the SPL array. The estimates of mean angle and dispersion agreed well for waves in the period range 6.9–7.7 s.

CONCLUSIONS

The SAR can provide useful information on the normalized directional spectra of wind-generated waves when the wave intensity is sufficient for imaging. The experiment was conducted in relatively low wave conditions, the significant heights ranging from 1.0 to 1.5 m. It is suggested that the SAR performance would significantly improve in the open ocean environment. This is also the region where conventional surface directional measurements are difficult to obtain.

It is important that further investigation be made into the nature of the imaging mechanisms in order to understand the physical criteria of accurate SAR images of waves. The ultimate goal of this research would be to provide a complete description of the SAR system transfer function, which would also allow the determination of wave energy levels in the wave height directional spectrum. At present, only the relative directional distribution of the wave height spectrum can be derived from SAR images.

Acknowledgments. The ground truth data acquisition was sponsored by the Jet Propulsion Laboratory under contract 954672 (D. L. Inman). Support for the analysis of the pressure sensor array data and interpretation of the spectral comparisons was provided by the Office of Naval Research, Geography Branch, under contract N00014-75-C-0300 (D. L. Inman). The staff of the Shore Processes Laboratory, SIO, installed and maintained the array and data acquisition system. The JPL contributions were supported by the National Aeronautics and Space Administration under contract NAS 7-100.

REFERENCES

- Brown, W. E., Jr., C. Elachi, and T. W. Thompson, Radar imaging of ocean surface patterns, *J. Geophys. Res.*, 81(15), 2657–2667, 1976.
- Capon, J., High resolution frequency-wavenumber spectrum analysis, *Proc. IEEE*, 57, 1408–1418, 1969.
- Davis, R. E., and L. A. Regier, Methods for estimating directional wave spectra from multi-element arrays, *J. Mar. Res.*, 35(3), 453–477, 1977.
- Dobson, R. S., Some application of a digital computer to hydraulic engineering problems, *Tech. Rep. 80*, Dep. of Civil Eng., Stanford Univ., Stanford, Calif., 1967.
- Elachi, C., and W. E. Brown, Jr., Models of radar imaging of the ocean surface waves, *IEEE Trans. Antennas Propagat.*, AP-25(1), 84–93, 1977.
- Pawka, S. S., D. L. Inman, R. L. Lowe, and L. C. Holmes, Wave climate at Torrey Pines Beach, California, *Tech. Pap. 76-5*, Coastal Eng. Res. Center, U.S. Army Corps of Eng., Fort Belvoir, Va., 1976.
- Shemdin, O. H., Modulation of centimeter waves by long gravity waves: Progress report on field and laboratory results, in *Turbulent Fluxes Through the Sea Surface, Wave Dynamics, and Prediction*, edited by A. Favre and K. Hasselmann, pp. 235–253, Plenum, New York, 1978.
- Shemdin, O. H., W. E. Brown, Jr., F. G. Staudhammer, R. Shuchman, R. Rawson, J. Zelenka, D. B. Ross, W. McLeish, and R. A. Berles, Comparison of in situ and remotely sensed ocean waves off Marineland, Florida, *Boundary Layer Meteorol.*, 13, 193–202, 1978.
- Wright, J. W., W. J. Plant, W. C. Keller, and W. L. Jones, Ocean wave-radar modulation transfer functions from the West Coast Experiment, *J. Geophys. Res.*, this issue.

(Received July 24, 1979;
revised March 7, 1980;
accepted April 4, 1980.)

Appendix B Model Tests of MLE and IMLE Methods

B.1 Deterministic Model Tests

The theory of operation of the IMLE method is lacking due to the complexity of the data adaptive (MLE) transformation and the renormalization performed after each iterative modification. As a result, it can not be analytically shown when the IMLE estimates converge to the true spectrum. Due to this lack of theoretical justification, the responses of the MLE and IMLE methods were obtained for an extensive set of test spectra. Both unimodal and bimodal directional spectra were used in the deterministic numerical simulation testing of the estimators. The array configuration used for the simulation tests was the 1-2-4-5 linear array, see Figure 13.

The unimodal test analysis was performed for 5 wave frequencies ranging from 0.051-0.137 Hz. The associated wavelengths were calculated assuming an array depth of 10 m. 192 unimodal test spectra had the basic form

$$E(\alpha) = \cos^{P1}(\alpha - \alpha_1) + \kappa_u \int_{\alpha'} \cos^{P1}(\alpha' - \alpha_1) d\alpha' \quad (B.1)$$

where $P1$ ranged from 2 to 2000, κ_u adjusted a uniform background level with values from 0.01-0.15, α_1 , the mode angle, varied from 10° (from normal to array) to 70° . A relatively slow approach path ($\beta=1.0, \gamma=5.0$) with 50 iterations was used for the model testing. The relative performance of the two methods can be viewed in terms of the ratio of the associated NSE (equation II.20)

$$RSE = \frac{\sum_{\alpha} (\hat{E}_j(\alpha) - E(\alpha))^2}{\sum_{\alpha} (\hat{E}_0(\alpha) - E(\alpha))^2} \quad (B.2)$$

where $E_i(\alpha)$ is the IMLE directional spectrum estimate, $E_0(\alpha)$ is the MLE estimate, and RSE is defined as the relative square error. The average value of RSE for the 960 unimodal tests was 0.130. Values of RSE greater than 1.0, indicating a degradation of the spectrum with iterative modifications occurred for only 3.5% of the unimodal test cases. The test case with the worst relative performance of the IMLE had a RSE value of 2.96. The trends in the NSE, shown in Figures B.1 and B.2, indicate improving performance of the IMLE method (and degrading MLE performance) with increasing wave frequency and increasing background level (κ_u). In fact, there were no cases of RSE greater than 1.0 for values of κ_u greater than 0.01. Table B.1 displays the square error of the IMLE method as a function of wave frequency and unimodal peak width. The low frequency performance of the IMLE method was best for relatively broad directional forms. The high frequency range had a minimum NSE for medium directional widths (P1-20-100).

One spectral problem that is encountered with the IMLE modifications is the over-resolution of spectral peaks. Figure B.3 is a plot of a peak which is defined in form by the MLE method but was over-resolved by the MLE. This splitting of the unimodal peak occurred for approximately 8.3% of the unimodal test cases. Over-resolution is particularly a problem with spectra that have low background levels. This is evidenced by the fact that 53% of the cases encountered were for tests with $\kappa_u=0.01$. The existence of over-resolution in the IMLE spectrum does not appear to degrade the relative improvement offered in the estimation of low order spectral

Frequency (Hz)	Cos Power P1										
	2000	999	500	200	100	50	20	10	5	2	
0.051	.070	.061	.054	.036	.024	.009	.004	.004	.003	.003	
0.067	.075	.062	.047	.028	.026	.008	.003	.003	.002	.002	
0.082	.075	.055	.040	.023	.014	.007	.003	.002	.002	.004	
0.098	.063	.041	.029	.018	.010	.005	.003	.002	.004	.008	
0.122	.053	.031	.022	.012	.007	.004	.002	.004	.010	.012	
0.137	.032	.011	.006	.002	.001	.001	.008	.024	.042	.064	
AVERAGE	.061	.044	.033	.020	.014	.006	.004	.007	.010	.016	

Table B.1. Normalized square error, NSE defined in equation II.20, of the IMLE estimates for the deterministic unimodal model tests. All combinations of the following parameter values, see equation B.1, were tested:

$$\alpha_1 = 10, 20, 40, 70$$

$$\kappa_u = 0.01, 0.05, 0.10, 0.15$$

yielding 16 test cases for each wave frequency-cos power pair. There were 960 test cases.

Figure B.1 Normalized square error, NSE of equation II.20, for directional spectrum estimates; and $S_{yx}(f)$ estimation error, SYXE of equation B.5, for the average of the unimodal deterministic tests. 160 test spectra with varying widths, location, and background level were used for each frequency band result.

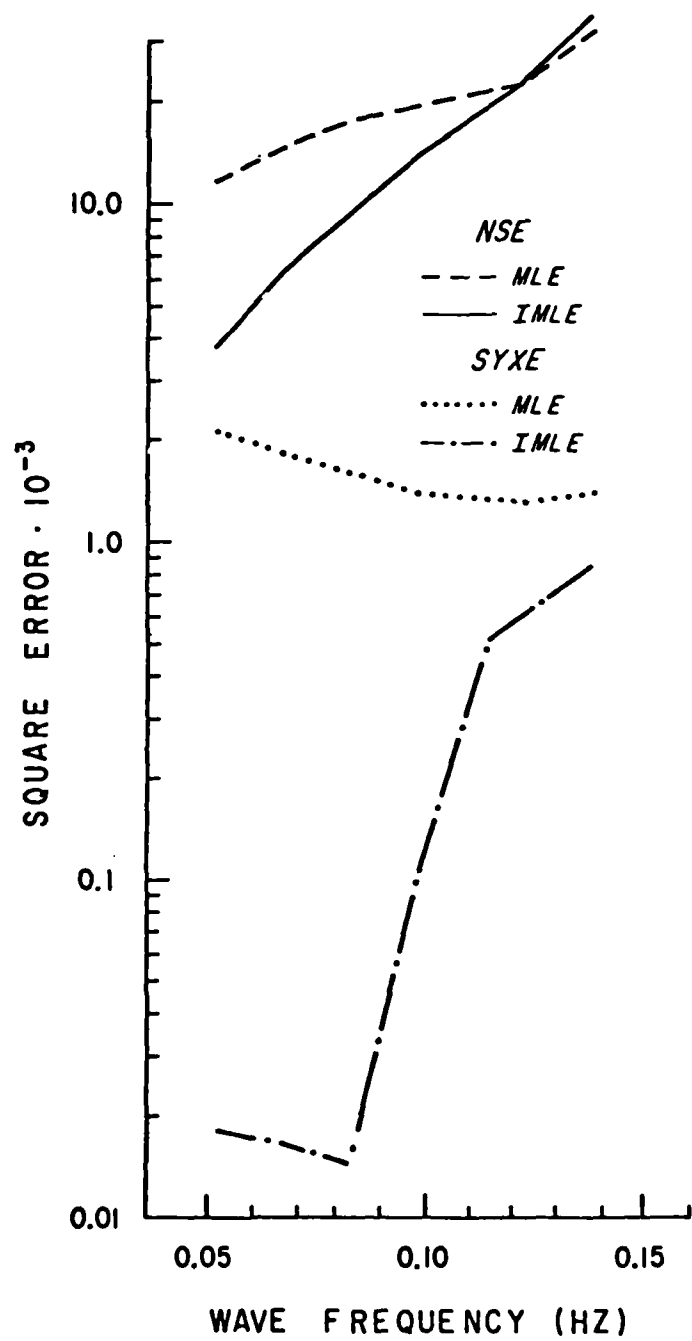
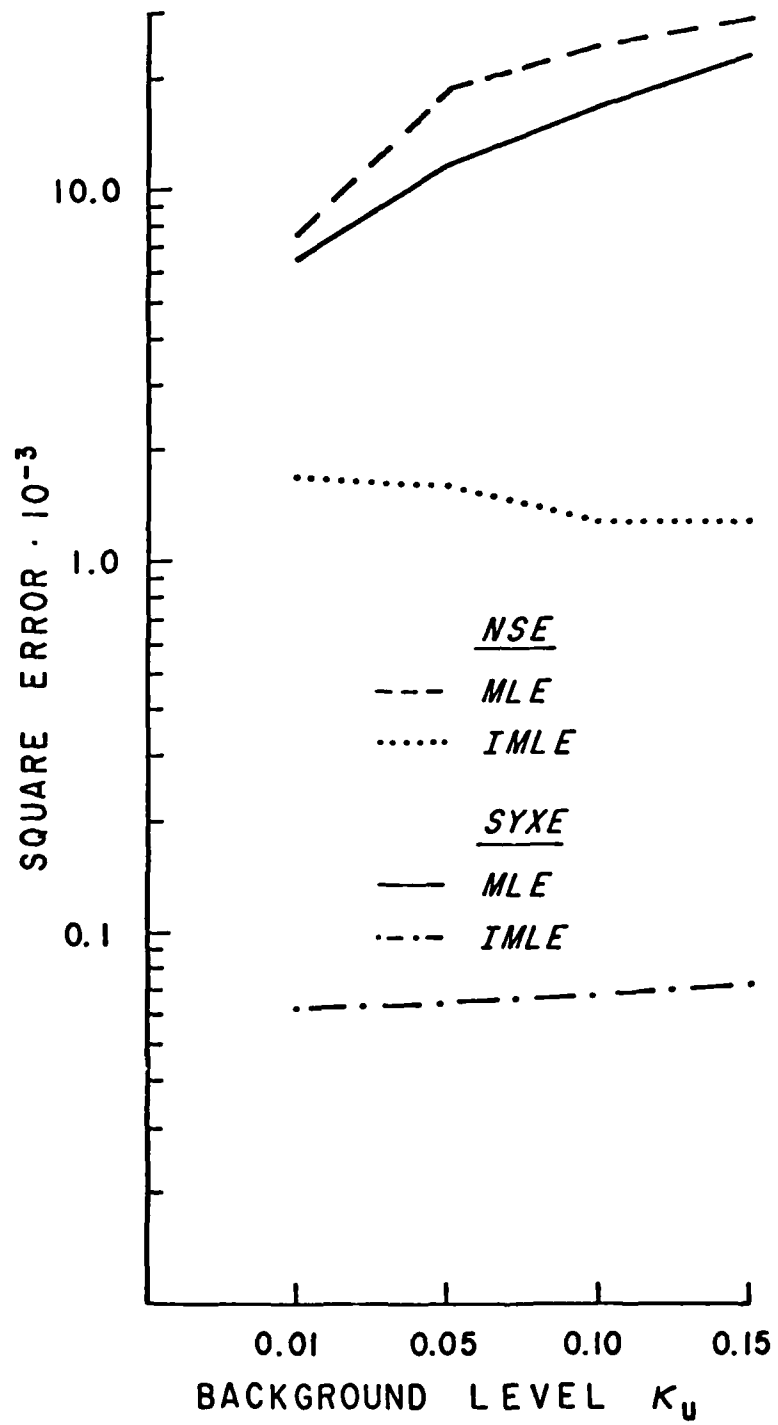


Figure B.2 Normalized quare error, NSE of equation II.20, for directional spectrum estimates; and SYXE, $S_{yx}(f)$ estimation error (equation B.5), for the average of the unimodal deterministic tests. 240 test spectra with varying peak width, location, and wave frequency were tested for each background level, κ_u .



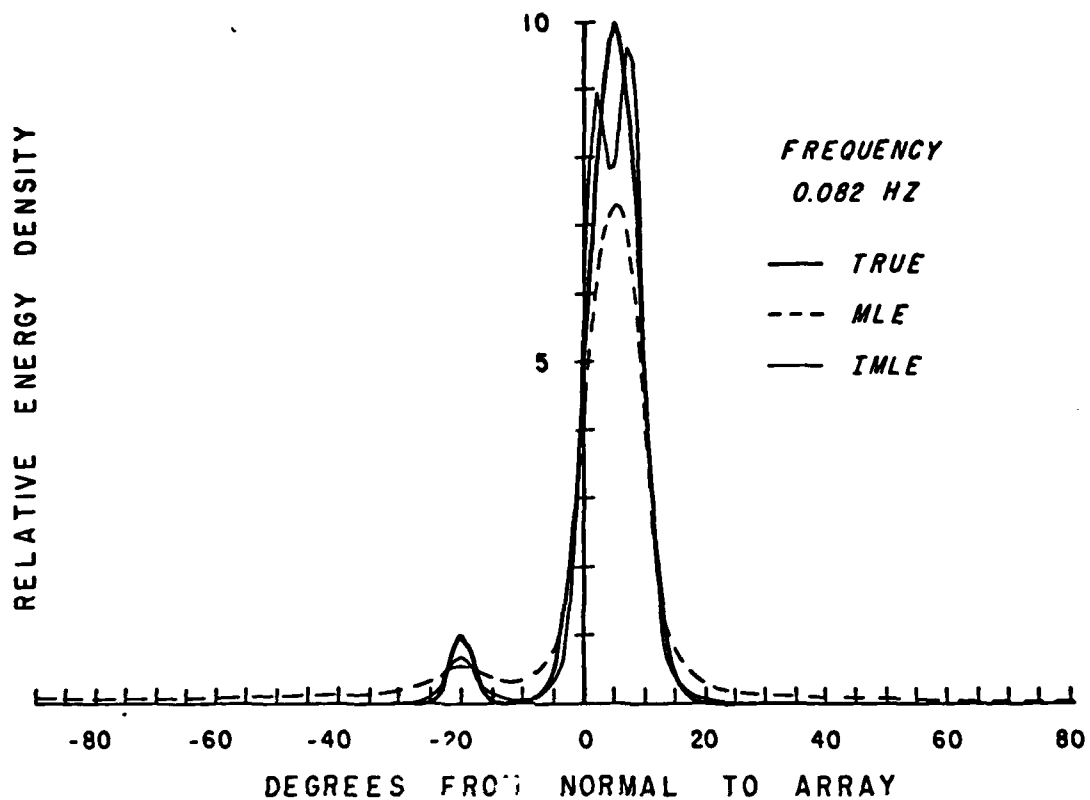


Figure B.3 MLE and IMLE ($\beta=0.5, \gamma=5.0$) estimates of the directional spectrum for a deterministic bimodal test distribution. The IMLE estimate "over-resolves" the major peak.

moments. The use of $E_{30}(\alpha)$ from Figure B.3 for the estimation of $S_{yx}(f)$ yields a result that is 0.1% greater than the true value while $E_0(\alpha)$ leads to a result 25.4% low. Also, the over-resolved peaks are stable at high iterations, see Appendix C.

The bimodal deterministic testing of the estimators was performed using the basic spectral form

$$E(\alpha) = D_2 \cos^{P_2}(\alpha - \alpha_2) + D_3 \cos^{P_3}(\alpha - \alpha_3) \\ + \kappa_b \int_{\alpha'} \left[D_2 \cos^{P_2}(\alpha' - \alpha_2) + D_3 \cos^{P_3}(\alpha' - \alpha_3) \right] d\alpha' \quad (B.3)$$

where P_2 and P_3 had 4 possible values (999, 200, 50, 10), the ratio D_2/D_3 ranged from 10.0-0.01, κ_b had values from 0.01-0.05, $\alpha_2 = +6.0^\circ$, and α_3 had values ranging from -40° to $+30^\circ$ with 10° increments. A total of 400 bimodal test spectra were tested for wave frequencies 0.067 and 0.123 Hz. The resulting mean value of RSE, 0.011, is an order of magnitude lower than the average of the unimodal results, indicating improved relative performance of the IMLE method with bimodal spectra. RSE was greater than 1.0 for only 0.1% of the test cases, the maximum value being 1.42. Table B.2 displays the RSE as a function of the test parameters and shows the same basic trends as the unimodal results. The average value of NSE for 0.067 Hz bimodal test conditions was 0.010 as compared to a value of 0.018 for the unimodal cases with the same wave frequency. The occurrences of over-resolved spectral peaks was significantly lower for the bimodal test spectra.

Several spectral forms were tested with a more dense coverage of the wave frequency range 0.051-0.20 Hz. Figure B.4 is a plot of

		<u>0.067 Hz</u>				<u>0.122 Hz</u>			
		P3		$\kappa_b = 0.01$		P3			
		999	200	50	10	999	200	50	10
P2	999	0.590	0.381	0.226	0.121	0.121	0.064	0.031	0.031
	200	-	0.252	0.149	0.029	-	0.028	0.019	0.025
	50	-	-	0.080	0.023	-	-	0.017	0.024
	10	-	-	-	0.021	-	-	-	0.027
$\kappa_b = 0.05$									
P2	999	0.240	0.112	0.131	0.093	0.071	0.030	0.020	0.026
	200	-	0.112	0.058	0.015	-	0.013	0.012	0.019
	50	-	-	0.024	0.008	-	-	0.011	0.019
	10	-	-	-	0.008	-	-	-	0.022

Table B.2. Values of RSE, ratio of square error of the IMLE directional spectra estimates to the square error of the MLE estimates defined in equation B.2, for bimodal model spectrum parameters (equation B.3). All combination of the following parameter values were used:

$$\alpha_2(^{\circ}) = +5$$

$$\alpha_3(^{\circ}) = -40, -30, -20, -10, 0, 10, 20, 30$$

$$D_2/D_3 = 0.1, 0.5, 1.0, 2.0, 10.0$$

yielding 40 test cases for each value of RSE shown in the table. The analysis was done for two wave frequencies and two background levels, κ_b .

the square error of the MLE and IMLE methods for a narrow unimodal directional spectrum. The IMLE method uniformly outperforms the MLE, but has particularly good results for the frequency range 0.08-0.17 Hz. Two approach paths were tested with the IMLE method and show similar results. The peak of square error for the IMLE results in the low frequency region is characteristic for all the spectral forms tested. It is interesting to note that the square error for the MLE method smoothly increases through the occurrence of spatial aliasing (at approximately 0.179 Hz) while the IMLE errors show a dramatic jump at that point.

B.2 Moment Estimation

As mentioned previously, the iterative modifications to the MLE estimates tend to increase the consistency of the directional spectrum with the measured cross-spectral moments. It is not unreasonable to expect that there would be a similar improvement in the estimation of other low order moments, such as $S_{yx}(f)$. The unimodal and bimodal deterministic tests showed on the average a significant increase of accuracy in the estimation of the moments

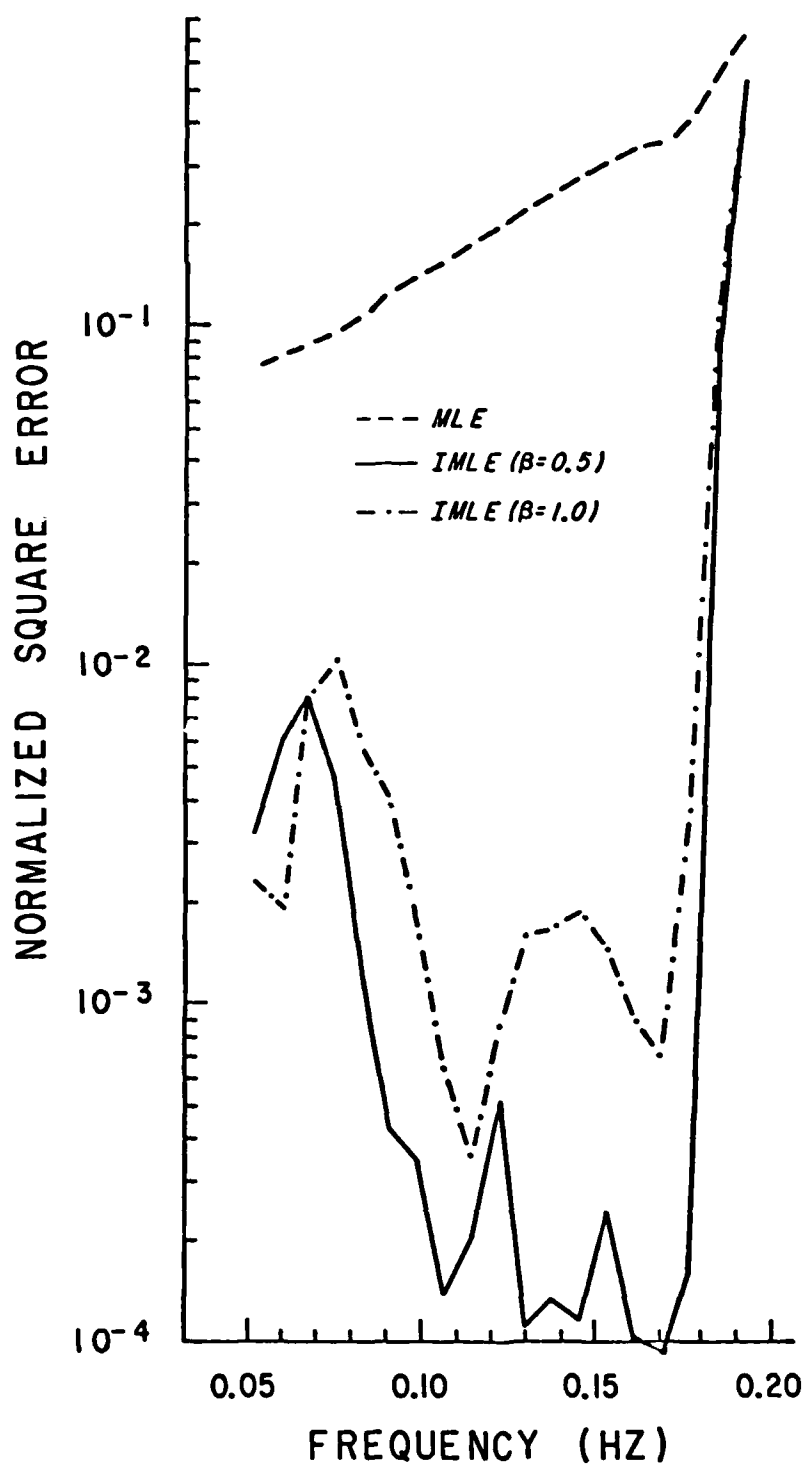
$$M_{1m}(f) = \int_0^{\pi} \cos^1(\alpha) \sin^m(\alpha) E(f, \alpha) d\alpha \quad (B.4)$$

where $M_{1m}(f)$ are the low order harmonic moments, 1 and m take the values of 0, 1, and 2. A normalized square error of the $S_{yx}(f)$ estimates is defined, $S_{yx}(f) = M_{11}(f)$

$$SYXE = \frac{(S_{yx}(f) - S_{yx}(f))^2}{S_{yx}^2(f)} \quad (B.5)$$

The average value of SYXE for the unimodal tests was 0.0006 for the

Figure B.4 Normalized square error, NSE of equation II.20, for directional spectrum estimates of the MLE and IMLE (2 different approach paths) methods. 50 iterations were used with the relatively slow approach path ($\beta = 1.0$) and 30 iterations with the fast method. The unimodal test directional spectrum, TS-2, is shown in Figure B.7.



IMLE method and 0.118 for the MLE method. The IMLE result corresponds to an average magnitude of error of 2.4% while the MLE result is 34.4%. The trends shown in Figures B.1 and B.2 show an increase in $S_{yx}(f)$ estimation error with the IMLE method for increasing wave frequency but no significant effect of increasing background level. The errors with the MLE method increase rapidly with a raised background level in the spectrum.

The bimodal tests (Table B.3) yield the same basic trends in $S_{yx}(f)$ estimation errors as the unimodal results. The average value of SYXE for the bimodal test spectra was 0.0018 for the IMLE method and 0.20 for the MLE method. A relatively slow approach method was used in the deterministic tests and it is felt that the values listed here for the improvement in $S_{yx}(f)$ estimation are conservative. There is a strong tendency for the MLE estimates of $S_{yx}(f)$ to be biased low in magnitude. The MLE estimate of $S_{yx}(f)$ was low in magnitude for 95.1% of the bimodal tests and 100.0% of the unimodal cases. Therefore, the relatively large errors associated with this method will not tend to average out with increased data.

B.3 Random Spectral Tests

The responses of the MLE and IMLE methods were tested with numerically simulated random cross-spectra to investigate the stability of the estimators. The random cross-spectra were generated using multivariate-Gaussian Fourier coefficients following Borgman (1974). The intent of the random tests was to determine whether the mean estimate spectrum, averaged over many cases (usually 50), closely approximated the "true" spectrum used in the generation of the cross-

Table B.3. Values of $(SYXE)^{\frac{1}{2}}$, the normalized error of $S_{yx}(f)$ estimation defined in equation B.6, for bimodal spectral parameters. Each value is an average over 40 test spectra listed in Table B.2. Analysis was performed for two wave frequencies, two background levels (κ_b), and the MLE and IMLE estimators.

		0.067 Hz				0.122 Hz			
		MLE							
		P3		$\kappa_b = 0.01$				P3	
		999	200	50	10	999	200	50	10
P2	999	15.7	20.1	20.3	23.5	36.7	47.1	53.7	76.5
	200	-	12.7	17.1	26.6	-	50.3	58.5	76.0
	50	-	-	13.8	25.5	-	-	62.5	73.5
	10	-	-	-	23.6	-	-	-	74.4
$\kappa_b = 0.05$									
P2	999	33.3	33.5	32.3	30.0	54.0	60.6	64.8	79.4
	200	-	25.0	25.0	34.5	-	61.0	63.2	77.1
	50	-	-	22.7	30.8	-	-	67.7	74.8
	10	-	-	-	33.3	-	-	-	75.4
IMLE									
		$\kappa_b = 0.01$							
P2	999	0.2	0.4	0.6	1.1	0.4	1.1	1.0	0.9
	200	-	0.2	0.2	1.2	-	0.4	0.3	1.0
	50	-	-	0.2	0.7	-	-	0.5	0.4
	10	-	-	-	0.4	-	-	-	0.5
$\kappa_b = 0.05$									
P2	999	5.4	9.0	10.2	7.5	9.0	8.5	8.1	7.7
	200	-	7.6	8.6	7.6	-	8.5	8.1	7.5
	50	-	-	9.0	7.2	-	-	8.0	7.0
	10	-	-	-	9.0	-	-	-	9.0

spectra. The relative performance of the MLE and IMLE methods is shown in Tables B.4 and B.5 for 4 test spectra and smoothing over 6-16 ensembles. The relative performance of the IMLE decreases with less spectral smoothing evidencing some noise sensitivity problems. However, these examples do not display any gross stability problems with any estimator. There was an instability noted for both methods for less than 6 ensembles averaged, particularly on test spectra with low background levels.

Figure B.5 is a plot of the range of the estimated directional spectrum values for the responses of the MLE and IMLE methods on 2 sets of random cross-spectra. The range is defined

$$\text{Range} = \frac{\hat{E}^{95}(\alpha_0) - \hat{E}^5(\alpha_0)}{\langle \hat{E}(\alpha_0) \rangle} \quad (\text{B.6})$$

where $\hat{E}^{95}(\alpha_0)$ and $\hat{E}^5(\alpha_0)$ are the 95% and 5% points of the distribution of spectral estimates at look angle α_0 , and $\langle \hat{E}(\alpha_0) \rangle$ is the mean spectral estimate.

The analysis was done for several different directional locations relative to the peaks in the test spectra. The results indicate a greater relative variability of the IMLE estimates, particularly in the low tail regions of the spectrum. It should be noted, however, that the MLE result for the spectrum level in the tail is biased high and the absolute range of the MLE estimates can be as large or larger than the range of the IMLE estimates in this region. The trends of variability of the IMLE estimates suggest a desired smoothing of at least 8-12 ensembles for the spectral forms tested.

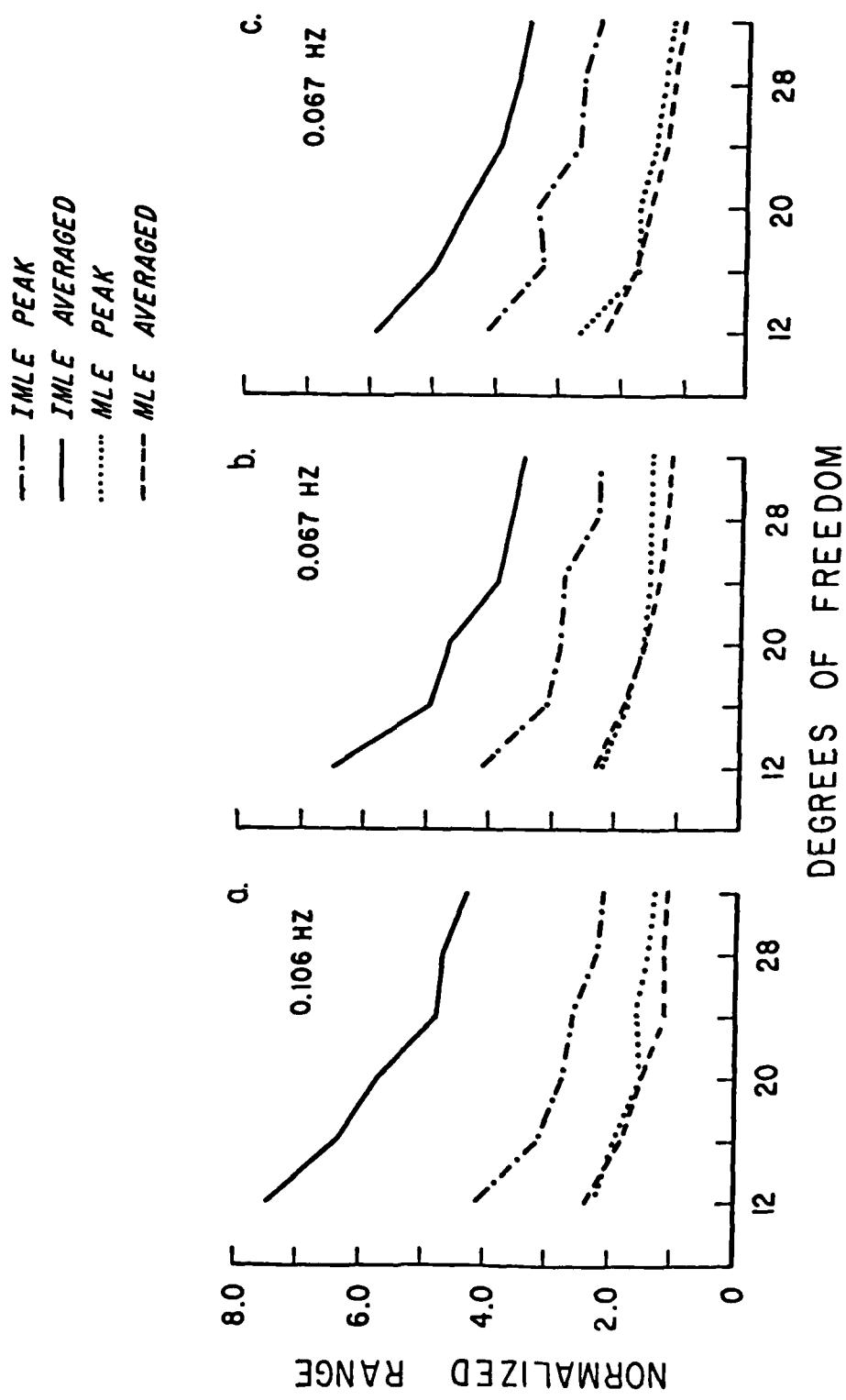
Test Spectrum	Frequency (Hz)	Ensembles Averaged						
		6	8	10	12	14	16	800
TS-2	0.067	0.420	0.320	0.527	0.271	0.240	0.263	0.216
TS-2	0.106	0.137	0.045	0.045	0.054	0.056	0.048	0.029
TS-3	0.121	0.337	0.247	0.172	0.139	0.112	0.084	0.032
TS-4	0.067	1.12	0.639	0.367	0.326	0.290	0.181	0.236

Table B.4. Relative square error, RSE of Equation B.2, of the MLE and IMLE methods in response to numerically simulated random cross-spectra. 50 cases were averaged for each spectral comparison to the mean value. TS-2 and TS-3 are shown in Figure B.7 while TS-4 is the model spectrum of Figure B.6a.

Estimator	Test Spectrum	Frequency (Hz)	Ensembles Averaged						
			6	8	10	12	14	16	800
IMLE	TS-2	0.067	3.2	1.2	0.3	1.5	0.9	0.1	0.7
IMLE	TS-2	0.106	3.8	0.6	0.6	1.4	1.1	0.9	0.2
IMLE	TS-3	0.121	55.0	54.0	47.3	40.3	35.7	28.3	15.7
IMLE	TS-4	0.067	19.1	13.8	6.5	4.7	4.0	4.0	0.0
MLE	TS-2	0.067	26.6	24.7	24.2	25.7	26.4	25.2	25.7
MLE	TS-2	0.106	29.4	28.8	28.4	28.9	28.5	29.4	29.4
MLE	TS-3	0.121	83.3	87.2	88.0	86.6	87.5	85.9	87.3
MLE	TS-4	0.067	33.0	34.7	32.3	32.6	33.0	34.0	34.3

Table B.5. $S_{yx}(f)$ estimation errors, $(SYXE)^{1/2}$ of Equation B.5 given in %, for the IMLE and MLE methods in response to random cross-spectra. The average value obtained for 50 spectra was compared with the true value (calculated from the deterministic test spectrum used to generate the random cross-spectra). TS-2 (narrow unimodal) and TS-3 (bimodal) are shown in Figure B.7 while TS-4 (broad unimodal) is the model spectrum of Figure B.6a.

Figure B.5 Normalized range in the directional spectrum estimates, defined in equation B.6, obtained from the MLE and IMLE methods in response to numerically simulated random cross-spectra. The average range (over all angles) is shown as well as a peak range, averaged over 5 degrees around the test spectrum mode. The associated mean test spectra are: a,b) a narrow unimodal form (TS-1, Figure B.7) and c) the broad form shown in Figure B.6a.



There were no cases tested which exhibited stability problems of estimates due to the occurrence of an over-resolved peak. Figure B.6a is a plot of the responses of the two methods to both deterministic and random cross-spectra with a very broad test spectrum. The improvement of the IMLE method over the MLE is less dramatic with the random inputs, but is still substantial (see also Table B.4). This example emphasizes the dependence of the IMLE estimate on a reasonably accurate structure of the MLE spectrum. Other processing techniques, e.g. the MO estimator developed by Regier (1975), will outperform these methods for this broad spectral form.

There were cases where the over-resolution problem existed in the deterministic testing of a spectrum but was smeared out in the averaging of the random estimates (see Figure B.6b). The analysis of range of spectral estimates did not indicate any marked increase in variability in the region of the over-resolved peaks.

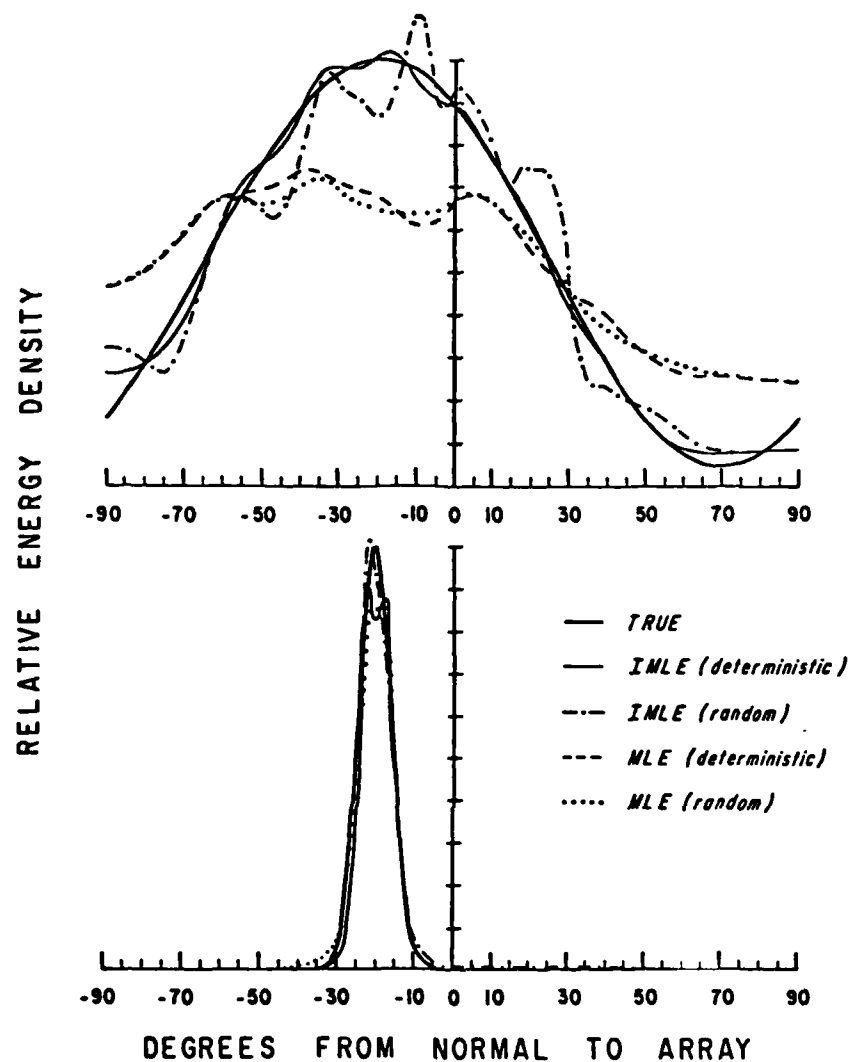


Figure B.6 Directional spectrum estimates of the MLE and IMLE ($\beta=1.0, \gamma=5.0$) methods for deterministic and random inputs.
The random estimates are an average of 50 cases with 32 DOF.

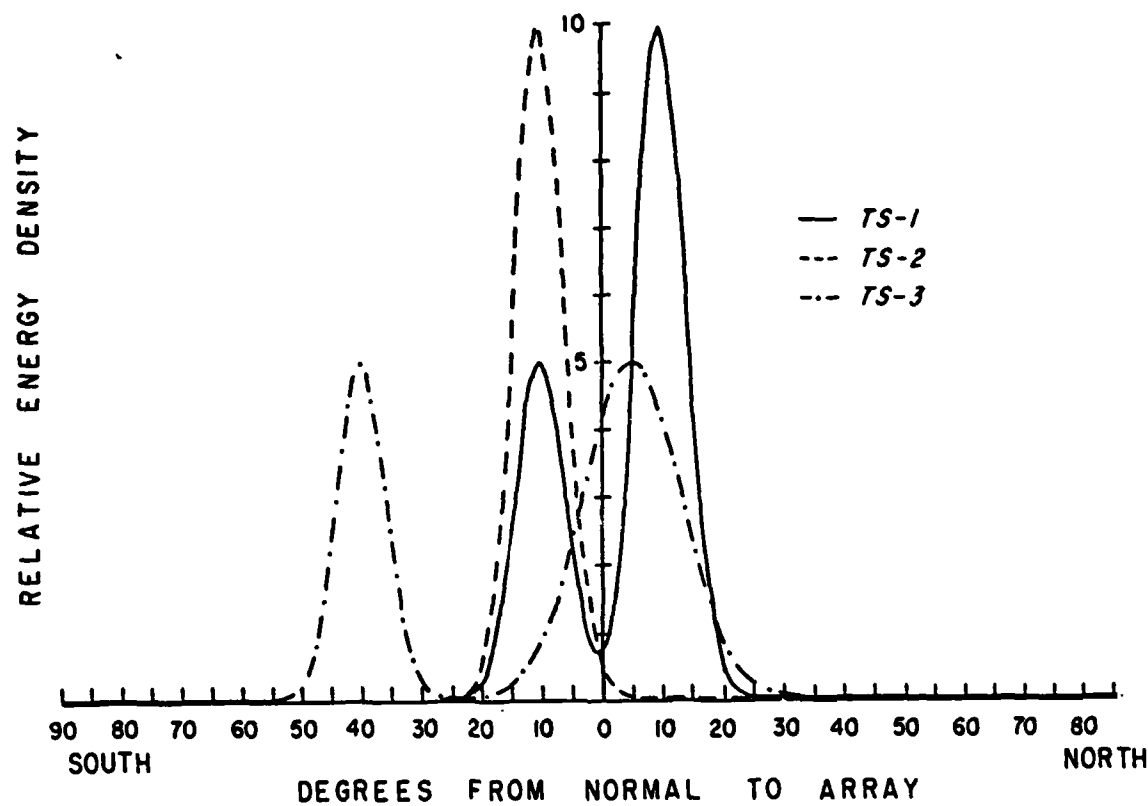


Figure B.7. Test directional spectra used for the analysis of the MLE, IMLE, and ME methods. The background level, κ_u (equation B.1) and κ_b (equation B.3) is equal to 0.5 for all 3 spectra.

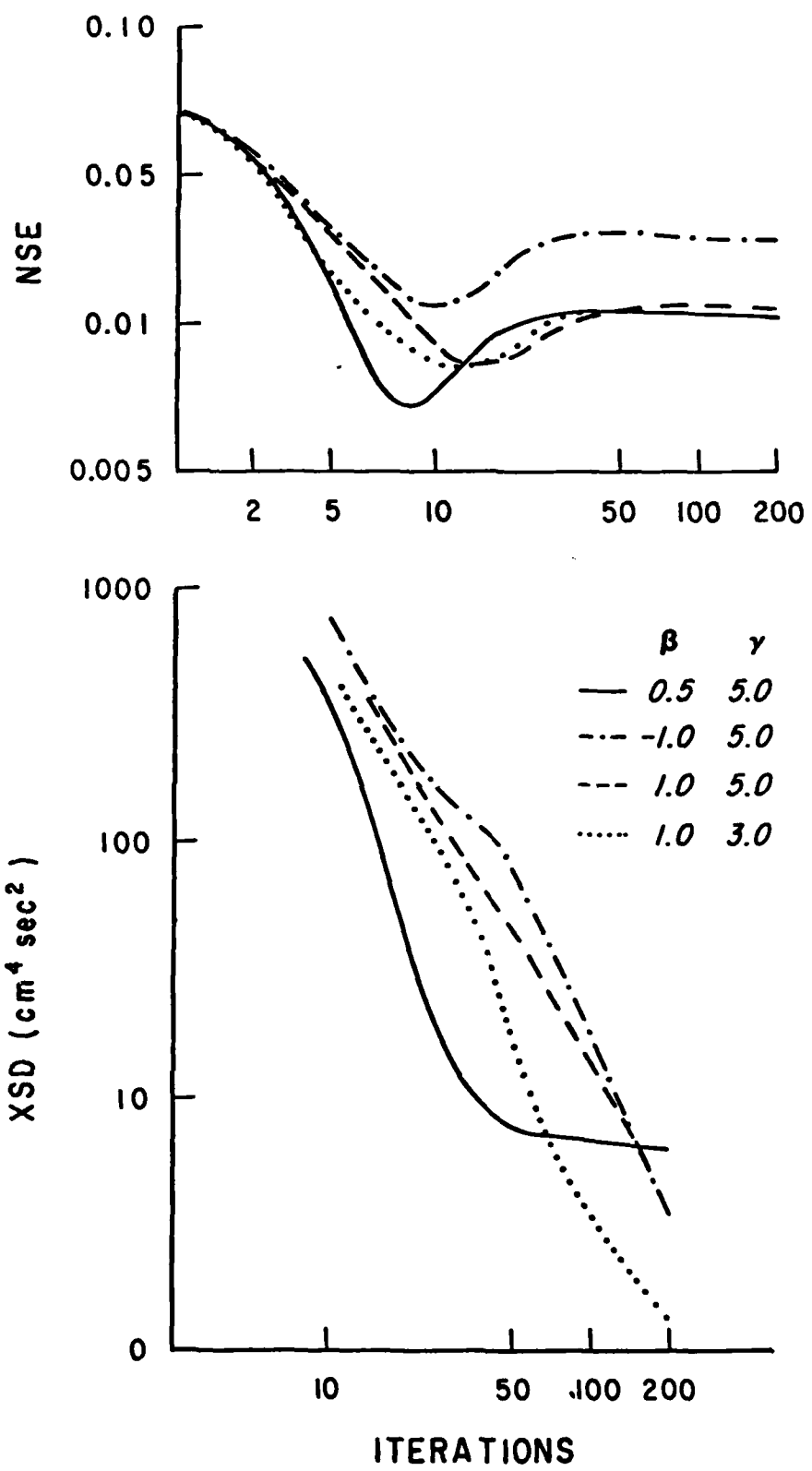
Appendix C IMLE Approach Paths

Various approach paths of the IMLE method were used in the numerical testing of the directional spectrum estimators. The general form of these paths is given in equation II.19. It would be undesirable if different approach paths "converged" to markedly different directional spectrum estimates. Even though it will be demonstrated that the IMLE modifications decrease with iterations for certain spectral forms, no analytic proof of convergence is offered.

A spectrum which was over-resolved by the IMLE method was chosen for the intercomparison of the approach paths. The quantitative value of the spectrum is expressed in terms of the normalized square error of the spectrum estimates, the cross-spectral error (XSD of equation II.22), and $S_{yx}(f)$ estimation accuracy. These parameters are plotted as a function of iteration for 4 different approach paths in Figures C.1 and C.2. Although the results of the different paths vary at low iterations, there is a close agreement of the NSE and $\hat{S}_{yx}(f)$ values at high iteration counts. There is a general monotonic decrease in XSD with iteration for all 4 paths.

The IMLE estimates for each approach path were iterated to a constant value of XSD for the comparison of the directional spectrum forms. The iteration count required had a range of 42-150. The directional spectrum estimates of the 4 approach paths are shown in Figure C.3. There are differences as to the degree of over-resolution, but the spectra are qualitatively similar. The approach path which has the most pronounced "false" peak also stabilizes to the highest values of square error. The comparative estimates of the

Figure C.1 Trends of the normalized square error, NSE of equation II.20, and cross-spectral error, XSD of equation II.17, versus iteration for 4 approach paths of the IMLE method. The test directional spectrum is shown in Figure C.3.



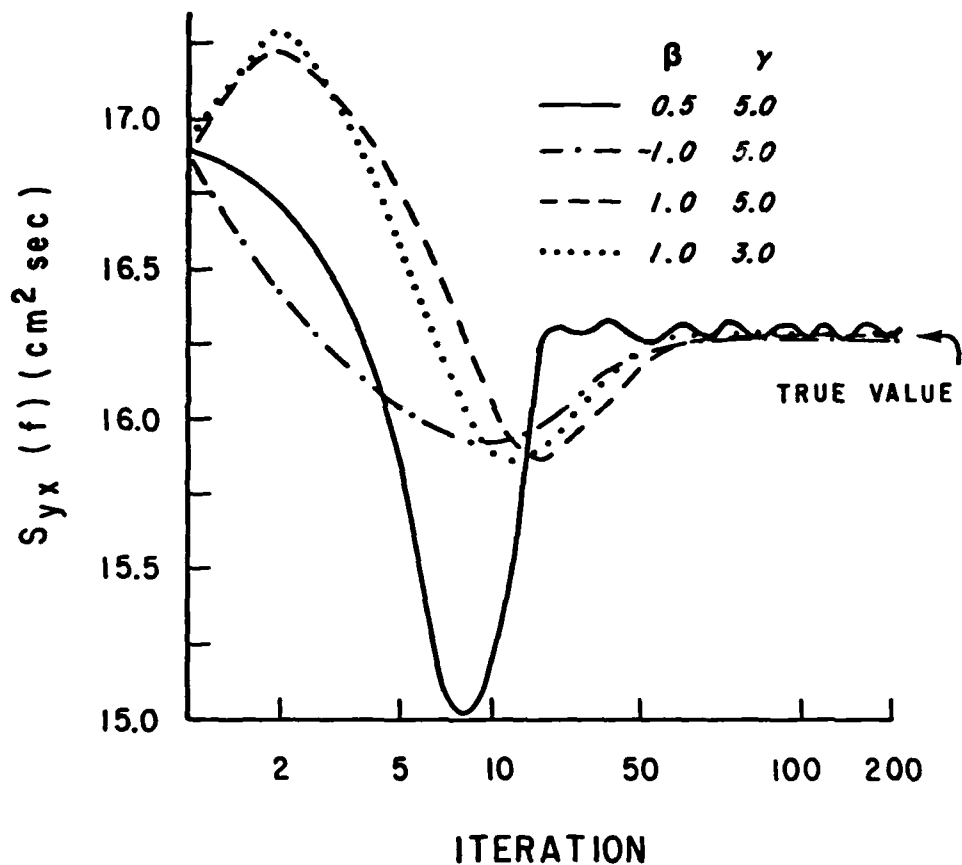
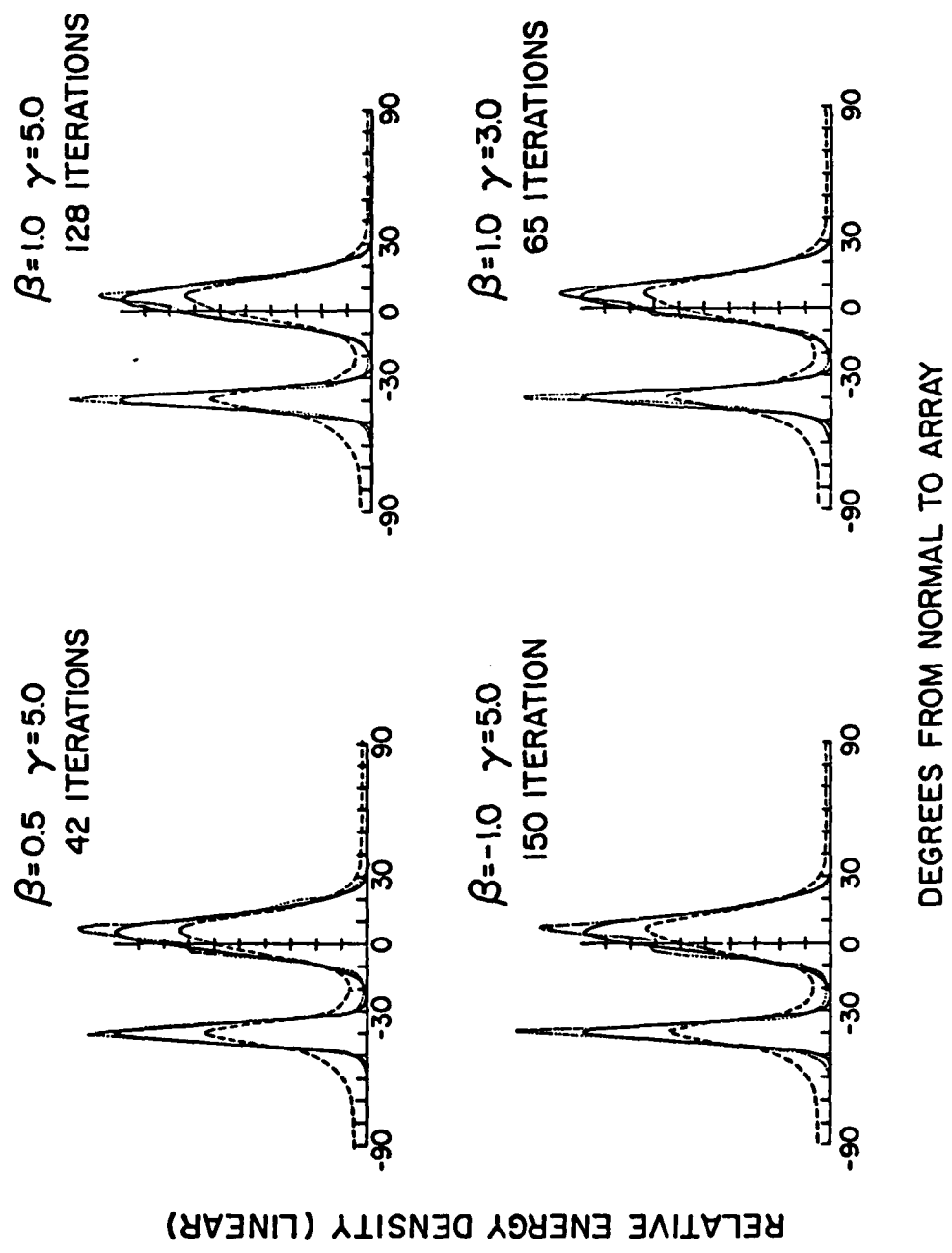


Figure C.2. Values of the $S_{yx}(f)$ estimate versus iteration for 4 approach paths of the IMLE method. The test directional spectrum is shown in Figure C.3.

Figure C.3 Estimates of the directional spectrum with 4 approach paths for a bimodal test spectrum. Each estimate is iterated to a constant value of XSD. The analysis was done for 0.059 Hz with a 1-2-4-5 array (unit lag = 33.0 m). The IMLE estimates (dotted line) and the MLE estimates (dashed lines) are both shown.



harmonic moments, equation B.5, with different approach methods are shown in Table C.1. These estimated moments agree well and show significant improvement over the MLE estimates.

The trends of NSE with iteration shown in Figure C.1 were common to many of the spectral forms tested. The only other trend observed was a monotonically decreasing value of NSE for all iterations. The relative maximum in the NSE values is associated with the overshoot of the spectral peaks (see Figure C.3). The iterations were carried out to a count of 4000 and no secondary minimum was encountered.

A clear problem with the IMLE method is the uncertainty as to when to cease the iterations. The trends of $\hat{S}_{yx}(f)$ with iteration show many turning points. Since there are varying forms to the trend of $\hat{S}_{yx}(f)$ with iteration, the termination of iteration with a low slope ($\Delta \hat{S}_{yx}(f)/\text{iteration}$) criterion can lead to poor results. Although a constant value of 50 iterations of a slow method ($\beta=1.0$) showed good general results with the simulation tests and comparative field data (Section V), some test spectra showed very slow convergence. The faster approach path ($\beta=0.5$) shows marked improvement in the $S_{yx}(f)$ estimates at low iterations. Also, the trend of $S_{yx}(f)$ estimates shown in this example show an onset of oscillations for the $\beta=0.5$ path after which there is little change in the spectral parameter.

The analysis of field data showed that the IMLE estimates stabilize at low iteration counts. Table C.2 displays the comparison of the IMLE estimates for 0.129 Hz waves on 10 June 1977. The two

		Estimate Error (%)		
Power	m	IMLE (range)		MLE
		max.	min.	
1	1	+0.0	-0.2	-2.5
1	0	+0.1	-0.0	+8.2
0	1	+0.2	-1.1	-15.6
2	0	+0.1	-0.0	+11.5
0	2	+0.2	-0.8	-60.4

Table C.1. Percentage errors of the harmonic moment estimates, Equation B.5, normalized by the true value. The estimates are in response to the test spectrum shown in Figure C.3. The maximum and minimum estimates obtained from the 4 approach paths of the IMLE listed in Figure C.3 are given as well as the MLE result. The moments are: $\int_{\alpha} \cos^1(\alpha) \sin^m(\alpha) E(\alpha) d\alpha$

	MLE	IMLE ($\beta=1.0$)					IMLE ($\beta=0.5$)	
		Iterations						
		5	10	20	50	250	XSD min.	XSD min.
Difference (%)	-43.9	-16.9	-7.6	-0.8	+1.2	+0.4	-2.8	-2.8
Correlation	0.72	0.80	0.76	0.86	0.87	0.87	0.84	0.84

Table C.2. Comparisons of the linear and slope array estimates of $S_{yx}(f)$ for 0.129 Hz on 10 June 77. The values are averaged over the results obtained from 9 consecutive 17.1 minute data runs. The array analysis was performed with a 1-2 array. The IMLE results are shown for several iterations including the iteration for minimum cross-spectral error (XSD, equation II.22). The Difference is defined as:

$$200 \cdot (\text{linear-slope}) / (\text{linear+slope}).$$

systems for 0.129 Hz waves on 10 June 1977 with the results of a slope array. The two systems show good agreement after only 10-20 iterations of a slow approach path. Although the correlation of the $S_{yx}(f)$ estimates of the two systems increases monotonically with iteration, the mean value of the IMLE estimate overshoots the slope estimate at about 40 iterations. This effect was seen in the numerical testing of the estimators.

The cross-spectral error showed a minimum for some of the field data, see Figure C.4. This was not predicted by the deterministic model tests. The $S_{yx}(f)$ estimates for the IMLE iterations terminated at this XSD minimum, also show in Table C.2, agree well with the slope array results. The results of a relatively fast approach path ($\beta=0.5$) agreed well with the slow path ($\beta=1.0$) with termination at the XSD minimum. However, the $\beta=0.5$ path reached the XSD minimum at an average of 24 iterations while the slow path took roughly 40 iterations. Due to the large amount of computations required, termination at the XSD minimum or at approximately 30 iterations with the fast approach path is recommended.

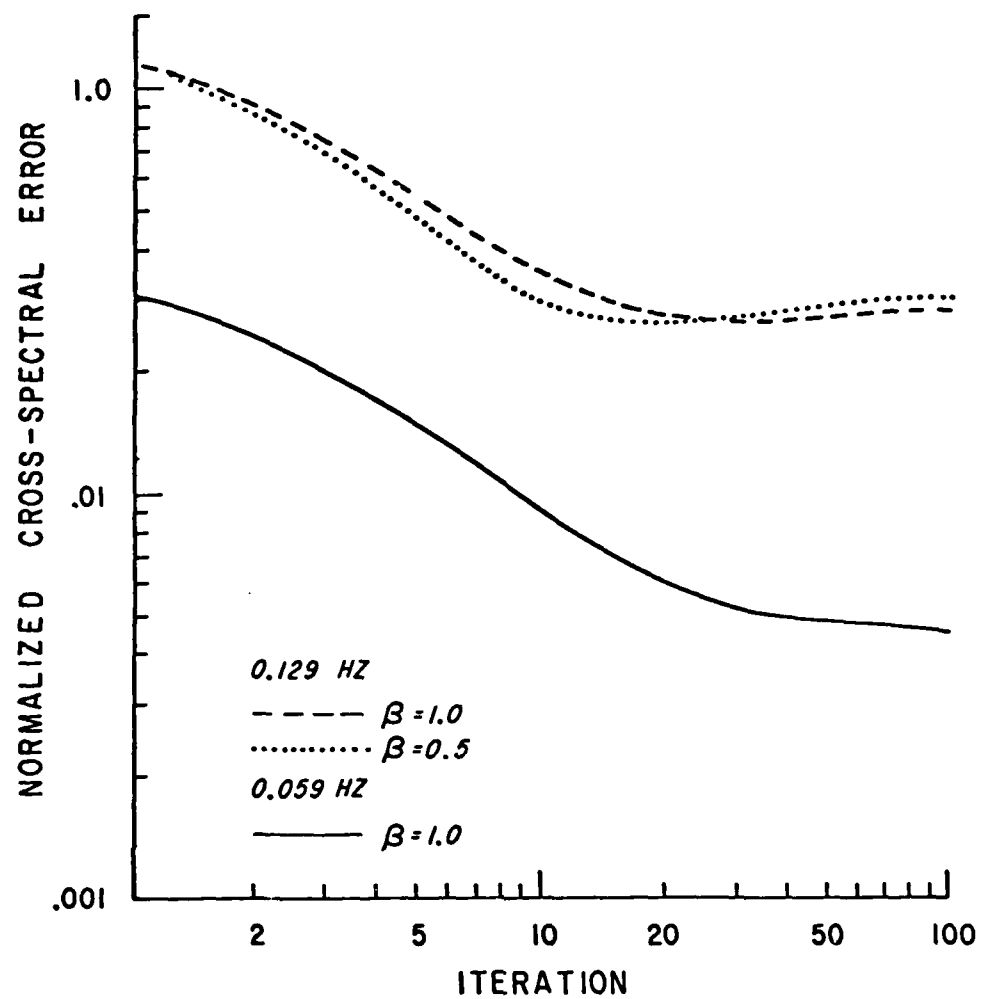


Figure C.4 Normalized cross-spectral error, $XSD/E^2(f)$, versus iteration of the IMLE method for field data sampled on 10 June 1977.
The measured cross-spectra have 448 DOF.

DATE
FILMED

105-8